Single Channel Kondo Physics In Triple Quantum Dots

Thomas F. Jarrold
University College
University of Oxford

A thesis submitted for the degree of
Doctor of Philosophy
at the University of Oxford, Trinity 2012

Single Channel Kondo Physics in Triple Quantum Dots

Thomas Furnley Jarrold
University College

A thesis submitted for the degree of

Doctor of Philosophy

at the University of Oxford, Trinity 2012

Abstract

In this thesis we investigate a system of three tunnel-coupled quantum dots, arranged in a triangular geometry and attached to a single metallic conduction band, using both analytic and semi-analytic methods and the numerical renormalisation group technique. This is the simplest coupled quantum dot system to exhibit frustration. We study three different models of the triple quantum dot device: a mirror symmetric arrangement of dots in which only one dot is connected to the conduction band, a triple quantum dot system in which only one dot is connected to the conduction band without a plane of mirror symmetry and a mirror symmetric arrangement of quantum dots in which all three dots are coupled to the conduction band. We study these models over a wide range of parameter space, and in both the presence and absence of a magnetic field.

Both antiferromagnetic and ferromagnetic Kondo effects are observed, and in all three models we find that the system contains at least two phases, and so a number of quantum phase transitions may be observed, associated in some cases with significant changes in the low temperature conductance through the triple quantum dot device. In addition to zero-field Kondo physics, a number of field induced Kondo effects are also observed. Both first order quantum phase transitions and Kosterlitz-Thouless phase transitions are observed. We use both symmetry arguments and low energy effective models which we derive to explain and understand both the position of and type of phase boundary that is observed in each case, and perturbative methods are used to accurately predict Kondo temperatures for a wide range of systems.

Acknowledgements

First and foremost, I would to thank my supervisor, Professor David Logan, for the unique and valuable contribution he has made to my academic development over the past five years. I would also like to recognise the other members of the Logan group — particularly Martin and Andrew, but also Anne, Chris, Fred, Adam and Phil — to whom I an indebted for many fruitful and interesting discussions.

I would also like to thank my parents, Christine and Kevin, for their unflagging, unconditional support throughout my DPhil, without which this thesis would not have been completed. Likewise, I would like to thank my siblings, Fiona and David, and my friends and housemates — including (although this could never be an exhaustive list) Cat, Zino, Jess, Gam, Maris, Dave, Alex, Chrissy, Neil, Carolina, Shell, Blath, Abi and Pete — both for their support and sympathy, and for the pleasure of their company. Finally, I would like to thank my students, the chemists at Jesus and Teddy Hall, for reminding me what a wondrous thing science can be.

Date: Signature:

Contents

1 Introduction **1**

2 Theoretical Models Of Quantum Dots **15**

2.1 The Anderson Model and the Schrieffer-Wolff Transformation 15

2.2 The Kondo Model and Poor Man's Scaling 20

3 The Numerical Renormalisation Group **27**

3.1 Initial Transformations 28

3.2 Logarithmic Discretisation 29

3.3 Iterative Diagonalisation and the Recursion Relation 32

3.4 Fixed Points 36

3.5 Thermodynamics 39

3.6 Dynamical Properties, the Density Matrix and the Self Energy 43

3.7 NRG Results For The Single Anderson Impurity Model 52

3.8 Magnetic Fields and the Single Impurity Anderson Model 56

4 The Apex Coupled Trimer Model Part I: Mirror Symmetry **61**

4.1 The Apex Coupled Trimer Hamiltonian 62

4.2 Parity and Other Symmetries 63

4.3 Effective Spin Model 64

4.4 Conductance and the Friedel-Luttinger Sum Rule 65

4.5 The Phase Diagram 66

4.6 Regime II: $J > 10T_{\mathrm{K}}$ 68

4.6.1 Effective Low Energy Model 68
4.6.2 Thermodynamics 71
4.6.3 Dynamics 73
4.7 Regime I: $J < 10T_K$ 75
4.7.1 Effective Low Energy Model 75
4.7.2 Thermodynamics 79
4.7.3 Dynamics 82
4.8 Regime III: The Orbital Regime 85
4.8.1 Effective Low Energy Model 85
4.8.2 Thermodynamics 92
4.8.3 Dynamics and the Friedel-Luttinger Sum Rule 94
4.9 Magnetic Fields 96
4.10 Magnetic Fields: Regime II: $J > 10T_K$ 96
4.10.1 Effective Low Energy Models 96
4.10.2 Thermodynamics 101
4.10.3 Dynamics 104
4.11 Magnetic Fields: Regime I: $J < 10T_K$ 106
4.11.1 Effective Low Energy Models 106
4.11.2 Thermodynamics 108
4.11.3 Dynamics 110
4.12 Magnetic Fields: Regime III: The Orbital Regime 111
4.12.1 Effective Low Energy Models 111
4.12.2 Thermodynamics 116
4.12.3 Dynamics 119
4.13 Summary 120

5 The Apex Coupled Trimer Model Part II: Breaking Mirror Symmetry 123

5.1 The Asymmetric Apex Coupled Trimer Hamiltonian 124

5.2 The Spin Model . . . 125
5.3 Conductance and the Friedel-Luttinger Sum Rule . . . 126
5.4 The Phase Diagrams . . . 127
5.4.1 Uncertainty in the Position of the Phase Boundary . . . 131
5.5 Regime II: $J > 10T_{\mathrm{K}}$ . . . 132
5.5.1 Effective Low Energy Model . . . 132
5.5.2 Thermodynamics . . . 137
5.5.3 Dynamics . . . 142
5.6 Regime I: $J < 10T_{\mathrm{K}}$ . . . 144
5.6.1 Thermodynamics . . . 147
5.6.2 Dynamics . . . 150
5.7 Regime III: The Orbital Regime . . . 152
5.7.1 Thermodynamics . . . 157
5.7.2 Dynamics . . . 159
5.8 Magnetic Fields . . . 160
5.9 Magnetic Fields: Regime II: $J > 10T_{\mathrm{K}}$ . . . 161
5.9.1 Effective Low Energy Model . . . 161
5.9.2 Thermodynamics . . . 163
5.9.3 Dynamics . . . 166
5.10 Magnetic Fields: Regime I: $J < 10T_{\mathrm{K}}$ . . . 166
5.10.1 Thermodynamics . . . 167
5.10.2 Dynamics . . . 168
5.11 Magnetic Fields: Regime III: The Orbital Regime . . . 169
5.11.1 Effective Low Energy Model . . . 169
5.11.2 Thermodynamics . . . 172
5.11.3 Dynamics . . . 174
5.12 Inducing Asymmetry By Other Means . . . 175
5.13 Summary . . . 177

6 The Trimer in Parallel **179**

6.1 The Trimer in Parallel Hamiltonian 180

6.2 The Effective Spin Model and the Absence of Regime I 181

6.3 Symmetries of the Bare and Effective Hamiltonians 184

6.4 Conductance and the Friedel-Luttinger Sum Rule 184

6.5 The Phase Diagram 186

6.6 The Spin Regime 190

6.6.1 Effective Low Energy Models 190

6.6.2 Thermodynamics 198

6.6.3 Dynamics 211

6.7 The Orbital Regime 221

6.7.1 Effective Low Energy Model 222

6.7.2 Thermodynamics 224

6.7.3 Dynamics 225

6.8 The Intermediate Regime 226

6.8.1 Thermodynamics 229

6.8.2 Dynamics 230

6.9 Magnetic Fields 231

6.10 Magnetic Fields: The Spin Regime 232

6.10.1 Effective Low Energy Models 232

6.10.2 Thermodynamics and Dynamics 236

6.11 Magnetic Fields: The Orbital Regime 241

6.11.1 Effective Low Energy Models 242

6.11.2 Thermodynamics and Dynamics 246

6.12 Summary 248

7 Conclusion **251**

A Elements of the $\mathbf{F}_\sigma$ Matrix **255**

B Parity Operators **259**

C The Friedel Sum Rule **261**

D Perturbation Theory In The Orbital Regime **267**

E Schrieffer-Wolff Transformations with Numerically Evaluated Elements **273**

F Scaling in the Anisotropic Kondo Model **277**

G Scaling in the Anisotropic Kondo Model II **281**

Bibliography **285**

Chapter 1

Introduction

The Kondo effect is one of the enduring paradigms of condensed matter physics [1]. It was initially observed in the 1930s as an unexpected increase in the resistivity of metals containing magnetic impurities at low temperatures [1, 2], an increase which was ultimately understood to be the result of correlations between impurity spin states and conduction band orbitals [3, 4]. In the years since Wilson's first explanation of the Kondo effect [4] theoretical and experimental interest in this fascinating area of many body physics has remained high [1, 2], with Kondo physics being observed in systems very different from the impure metals in which it was first described, including, most importantly from the perspective of this work, quantum dots [5].

The initial observation of increased resistivity in impure metals at low temperatures was surprising as resistivity was expected to decrease as the temperature fell; with fewer phonons excited in the metal, less electron scattering and therefore a lower resistivity was predicted [2]. Initial observations were particularly puzzling, as the correlation between a resistivity minimum and the presence of magnetic impurities was not understood. Once the connection between the presence of magnetic impurities within the metal and the presence of the resistivity minimum was known, work on the problem began in earnest: as the impurities in these systems made a contribution to the magnetic susceptibility which was described well by the Curie

law at high temperatures, it was clear that the presence of magnetic impurities must give rise to local moments under some conditions. Anderson suggested [6] that these local moments might arise as a result of electron correlation on the impurities themselves, and derived a model (the single impurity Anderson model, SIAM), which modelled an impurity within a bulk metal as a single level coupled to the wider conduction band by a hopping matrix element V. This level has both a level energy, ϵ, and an on-site Coulomb repulsion (or charging energy), U, which disfavours double occupation of the level, and hence allows the formation of a local moment.

This deceptively simple model was first proposed in 1961, but a solution of the SIAM at all energy scales was not available until the publication of the papers by Krishnamurthy *et al.* in 1981 [7, 8], which applied Wilson's Numerical Renormalisation Group [4] to the Anderson model. In the Anderson model the impurity is coupled to all the states of the conduction band, and the need to consider all of the macroscopically large number of conduction electrons renders *ab initio* methods impractical. Perturbation theory in U, the interaction strength, is, of course, only valid in the limit where U is small, whilst most of the interesting physics displayed by the Anderson model occurs in regimes in which U is large compared to the other energy scales of the problem [9–11]. Perturbation theory in the hopping matrix element, V, on the other hand suffers because the ground state contains correlated electrons, and as such Wick's theorem is not applicable [2], meaning that the standard diagrammatic techniques cannot be used. A number of methods have nevertheless been developed which involve performing perturbation theory in V, most notably the '1/N' expansion technique [2], which produces accurate results for a modified Anderson model with an N-fold spin degeneracy. However, this method involves taking the limit $N \to \infty$, and so is not reliable when applied to the non-degenerate Anderson model, which we discuss here.

Anderson initally attempted to solve the SIAM using the unrestricted Hartree-Fock approach (UHF) [6]; however this approach also proved unsuccessful, as it

predicts the presence of a phase transition between magnetic and non-magnetic ground states — whilst subsequent work [4, 7, 8] has shown that the ground state is non-magnetic in all cases. The UHF approach is however qualitatively correct at high temperatures.

Further progress was made with a model even simpler than the SIAM — the so-called Kondo model, also known as the s-d model. This model was first proposed in 1951 by Zener [12] for bulk transition metals, but was later adapted for the case of a magnetic impurity in a metal. This model treats the impurity as a single spin, coupled to the conduction band by a Heisenberg exchange coupling, J. A negative J indicates a ferromagnetic correlation between the impurity and conduction band spins, whilst a positive J indicates an antiferromagnetic correlation; it is the latter which most interests us, as it can be shown that the region of the SIAM in which the impurity is singly occupied at low temperature can be mapped directly onto the antiferromagnetic Kondo model using what is known as a Schrieffer-Wolff transformation [13].

By performing perturbation theory in J on the Kondo model, Jun Kondo was able to derive an expression for the total resistivity of the system [3];

$$R(T) = a + bT^5 + c \ln\left(\frac{k_B T}{D}\right), \tag{1.1}$$

where D is the conduction band width. This third order calculation gives a minimum in the resistivity at low temperature, due to the logarithmic term. However, whilst this calculation explained the presence of a resistivity minimum, and agreed very well with experimental results in the region around the resistivity minimum [3], in many ways it raised as many questions as it answered: the logarithmic term in $R(T)$ diverges as $T \to 0$, giving rise to a completely unphysical prediction of an infinite resistivity at zero temperature.

The question of how the Kondo model behaves in the limit $T \to 0$ continued to exercise physicists for another decade, and became known as the 'Kondo problem'.

The Kondo problem defied all attempts at solution using conventional perturbation theory methods, but Anderson made considerable progress applying the newly developed renormalisation group techniques within a perturbational framework — work which culminated in the development of his 'Poor Man's Scaling' method [14]. This technique, which is discussed in detail in Chapter 2, gives a full solution of the ferromagnetic Kondo model, but, as with all perturbational approaches, breaks down at low temperature in the antiferromagnetic case. Poor Man's Scaling does however predict the existence of an exponentially small low energy scale, known as the Kondo temperature, in the antiferromagnetic Kondo model. This scale may be shown to depend non-analytically upon the parameters of the bare model (J for the Kondo model; V, ϵ and U for the Anderson model in the region where the Schrieffer-Wolff transformation is valid).

Further progress had to await the development of a truly non-perturbative approach to the problem. This came with Wilson's development of the numerical renormalisation group (NRG) [4]; Wilson's crucial advance was to discretise the conduction band *logarithmically*, thus ensuring that all of the energy scales of the system — from the bandwidth to the Kondo temperature and below — were equally well sampled. This allowed all of the parameters of the system to be treated non-perturbatively, permitting a full solution of the Kondo problem, albeit one which had to be evaluated numerically rather than analytically. The low temperature behaviour of the antiferromagnetic Kondo model was in all cases found to depend solely upon a single low energy scale, corresponding to the Kondo temperature of Poor Man's Scaling, the knowledge of which allows all of the low temperature behaviour of a given system to be predicted. The NRG method was later extended to the Anderson model by Krishnamurthy *et al.* [7, 8]. We discuss the NRG in rather more detail in Chapter 3.

Attempts to find a truly analytical solution of the Kondo and Anderson Hamiltonians culminated in the development of the Bethe *ansatz*, which gave exact an-

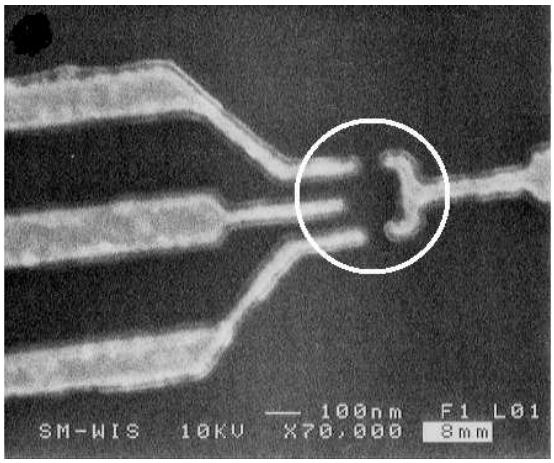


Figure 1.1: A scanning electron microscope image of a quantum dot on the surface between wafers of GaAs and $Al_xGa_{1-x}As$. Reprinted from Ref. [5]. The white circle highlights the quantum dot; the lighter regions are the electrodes.

alytical results for the thermodynamic properties of both the Kondo [15–17] and Anderson [18,19] models. However, the Bethe *ansatz* method cannot be used to calculate spectra exactly (although approximate spectra may be calculated using the 'spinon approximation' [2,20]), and is moreover restricted to integrable models; as a result the NRG remains a popular, and more general tool for the study of quantum impurity systems.

A number of other techniques have also been used to study quantum impurity systems, including Fermi Liquid theory [2,21,22], slave boson mean field theory [2,23] and Conformal Field Theory [24], as well as the Local Moment Approach (LMA) [25–27] and the Renormalised Perturbation Theory (RPT) [2, 28–31] method, both of which have been developed and extended in recent years.

Interest in the Kondo effect has recently been rekindled by the observation of the Kondo effect in quantum dot systems [1,5]. Quantum dots are mesoscopic 'droplets' of electrons attached to a large electron reservoir (conduction band), and have been realised in many different systems; on semiconductor interfaces [5], as adatoms on the surfaces of metals [1] and inside carbon nanotubes [33, 34]. All these diverse systems share two properties; a small size (of the order of 100nm — as shown in Fig. 1.1), leading to quantised energy levels, and tunable parameters. It is this

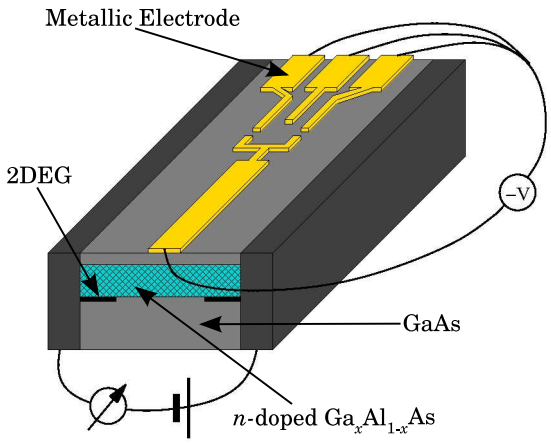


Figure 1.2: A schematic illustration of a semiconductor quantum dot, such as the one shown in Fig. 1.1, described in the main text, and studied in Ref. [5]. Reproduced with permission from Ref. [32].

combination of quantum behaviour with tunability in experiment that has given rise to such a high degree of scientific interest, both theoretical and experimental, in this area of condensed matter physics. As the behaviour of single quantum dots has become well understood, focus has switched to systems of coupled quantum dots: individual quantum dots have been dubbed 'artificial atoms' [35], and if that is the case, we may consider systems of coupled quantum dots as 'artificial molecules', and we might anticipate that a much wider range of behaviour could be observed in coupled quantum dot systems, in much that same way that chemical compounds exhibit a much wider variety of physical properties than pure elements.

Fig. 1.1 is a scanning electron microscope image of a semiconductor quantum dot (taken from Ref [5]); Fig. 1.2 is a schematic illustration of the same system. The quantum dot is defined in a two-dimensional electron gas (2DEG), created by the interface between two semiconductors (GaAs and $Al_xGa_{1-x}As$ in this case). Metallic electrodes are deposited on the surface of the semiconductor, and charging these electrodes (the pale regions in Fig. 1.1) creates regions of depleted electron density in the 2DEG. This is used to define the quantum dot (circled in Fig. 1.1), which is in this case connected to two metallic leads (at the top and bottom of the micrograph), which permits electron flow through the quantum dot (and therefore measurement of

the electron transport through the quantum dot device). By adjusting the potential applied to the various 'gates' (electrodes) the physical properties of the dot, including the size, level energy, charging energy and couplings to the leads, can be adjusted in experiment [36].

Recent advances in scanning tunneling microscopy allowing the manipulation of objects on atomic lengthscales permit the accurate fabrication of coupled quantum dot systems [33, 37–43]. There is an extensive literature on double quantum dots [34, 44–57] in a variety of geometries and in different substrates, and in both the theoretical and experimental fields. Until recently, triple quantum dots have been less well studied: although there are a number of theoretical papers [58–77] on triple quantum dots, using various techniques and investigating many geometries and occupation regimes, theory does appear to be leading experiment by quite a considerable margin; there are relatively few experimental papers on triple quantum dots [33, 39–41, 43, 78–85], and the first report of a triple quantum dot with a manipulable spin on each dot (as we shall see, one of the major focuses of this thesis) was very recent [42, 84, 86].

Triple quantum dots offer the opportunity to observe an extremely wide range of diverse physics, including a number of phenomena which are completely inaccessible in double quantum dot systems, and this is what has motivated much of the recent work on triple quantum dots. For example the triangular quantum dot system studied in this thesis is the simplest quantum dot system to exhibit frustration, which naturally arises from the ring structure of the triple quantum dot device. As we shall see, this gives rise to a number of quantum phase transitions and other interesting properties of the triple quantum dot system which have no analogue in smaller systems of coupled quantum dots.

Kondo physics in quantum dot systems have been a subject of particlar interest [1], partly due to the exquisite tunability possible in quantum dot systems, which opens the door to a more thorough experimental probing of the Kondo effect than

has previously been possible, but primarily due to the impact of the Kondo effect on the low temperature conductance through quantum dot systems. As discussed above, the Kondo effect in metals gives rise to a decrease in the conductance through the system at low temperature, as electrons are scattered off impurity states [1, 2]. By contrast, the Kondo effect in quantum dots gives rise to an enhancement of conductance at low temperature [1, 5] (electrons scattering off the dot leads to an increase in electron flow through the dot). This has led to considerable interest in quantum dot systems as nanoelectronic components [1], and is also one of the major motivations for this work; one consequence of frustration in triple quantum dot systems is that small changes in the bare parameters of the system can translate into large changes in the conductance through the triple quantum dot device at low temperature. In this thesis we investigate a triangular triple quantum dot coupled to a single conduction band, a model which has received much less theoretical study than the case where two [62, 70, 71, 74, 77, 87, 88] or more [61, 69, 89] leads are attached to the quantum dot device. We consider two distinct models; in the first ('the apex coupled trimer model') only a single quantum dot is coupled directly to the conduction band. In the second ('the trimer in parallel model') all three dots couple to the conduction band. These models are shown schematically in Fig. 1.3 and 1.4, respectively.

Both of these models have been the subject of previous research, although the trimer in parallel has received more attention. For the apex coupled trimer model, we note the work published by Wang [72], and that some of our results were previously published in Ref. [90]; similar behaviour was also subsequently seen by Chiappe *et al.* [75]. All of these works focus upon a small region of the model parameter space however. Our paper and that of Wang consider only systems which are mirror symmetric and in which all three dots are singly occupied at low temperature, meaning that the system can be modelled at low energies by an effective spin model. In addition, they explicitly investigate only systems in which interdot couplings dwarf

the interactions between the dots and the conduction band. Chiappe *et al.* focus on a linear system with an artificially inserted Heisenberg exchange coupling, and utilise the logarithmic discretization embedded cluster approximation, rather than the NRG. Wang considers Aharonov-Bohm effects in such a system, but there is no other investigation of the effects of magnetic fields upon a triple quantum dot in this geometry. In this thesis we consider the apex coupled trimer in both mirror symmetric and asymmetric configurations, and over a much wider parameter space. We also investigate the effect of an applied field upon the triple quantum dot. In addition, we derive a number of low energy effective models which may be used to both understand and predict the low temperature behaviour of the triple quantum dot device over a wide parameter range.

The trimer in parallel has been more extensively studied, and in particular we note papers again by Wang [66] and Žitko and Bonča [52, 53], both of which use the NRG. Although these works consider a wider range of parameters than has been the case in the literature on the apex coupled trimer model there has been a general focus on the C_{3v} symmetric case of the 'parallel triple quantum dot', where all three interdot couplings are equal, and all three dot-lead couplings are equal. As we discuss in this thesis, this is a special case of the trimer in parallel Hamiltonian, and not entirely representative of the behaviour of the system when it does not possess a C_{3v} symmetry. Indeed, we are aware of only two works which do not restrict themselves to this symmetry, Refs [91] and [92], and these use the non-equilibrium Green function technique, in such a way that the effect of Kondo physics on the system is entirely neglected, and also assume a C_{3v} symmetry with respect to the coupling between the triple quantum dot and the conduction band. In this thesis we consider the effects of breaking the C_{3v} symmetry of the model Hamiltonian in detail, and examine the triple quantum dot system in a much larger parameter space (although, unlike with the apex coupled trimer model, we do restrict ourselves to the mirror symmetric case). We investigate the effect of an applied field upon the

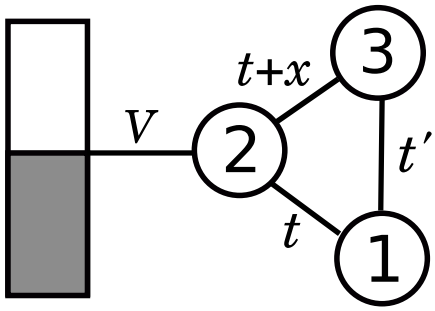


Figure 1.3: A schematic representation of the asymmetric version of the apex coupled trimer model.

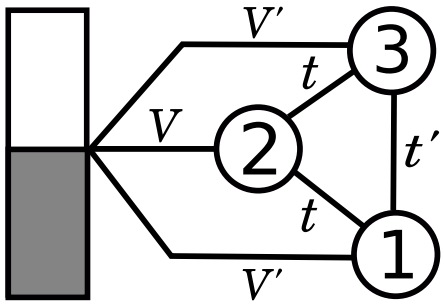


Figure 1.4: A schematic representation of the trimer in parallel model.

triple quantum dot in this geometry, and derive a number of low energy effective models which both explain and predict the low temperature behaviour of the triple quantum dot device. The trimer in parallel has recently been realised experimentally in a GaAs/Al_xGa_{1-x}As semiconductor system [80, 85], although there has been (to our knowledge) no explicit experimental investigation of the Kondo effect, or of the consequences of frustration in this system as yet.

We conclude this introduction with a brief plan of the thesis. In Chapter 2 we discuss the models commonly used for single quantum dot systems — the Anderson and Kondo Hamiltonians — and discuss the derivation of the Schrieffer-Wolff transformation which may be used to map the low temperature behaviour of the Anderson model onto the Kondo model. We also describe the Poor Man's Scaling technique of Anderson and (briefly) the concept of fixed points, both of which are used later in the thesis to understand the results of our numerical renormalisation group calculations.

Chapter 3 contains a detailed explanation of the numerical renormalisation group (NRG) method which is used throughout this thesis to model systems of coupled quantum dots. We describe the basic underlying principles behind the NRG — logarithmic discretisation and iterative diagonalisation — as well as how the NRG may be used to calculate both thermodynamic and dynamic properties of strongly correlated systems. The discussion of fixed points given in the previous chapter is expanded upon. The refinements of the basic NRG technique used in this thesis, the full density matrix and direct calculation of the electron self-energy, are also explained, and the chapter concludes with an examination of the results of the NRG when applied to the Anderson model (a model which describes the behaviour of a single quantum dot attached to a metallic conduction band) in the presence and absence of a magnetic field. This is used to illustrate the scaling properties which make the NRG such a powerful and widely applicable technique.

In Chapter 4 we consider the mirror symmetric case of the apex coupled trimer Hamiltonian. We begin by discussing the model Hamiltonian and the symmetry properties it possesses, before examining the effective spin model which may be derived from it in the case where all three dots are single occupied at low temperature. We then consider the phase diagram of this model. Three regimes may be identified, each exhibiting a distinct physics. We label these regimes I, II and III, and then investiate the behaviour of each regime in turn, using both analytic and semi-analytic methods and the NRG to examine both the thermodynamic and dynamic properties of the system. Regimes I and II lie within the parameter space where the effective spin model is valid, whilst regime III lies outside this region. In all three cases we find that the system has two phases with distinct parities, and that a first order quantum phase transition may be observed between them. When the system lies exactly upon the phase boundary, it is frustrated and the system is described down to zero temperature by a distinct transition fixed point. In regimes I and II the quantum phase transition is associated with a discontinuous change in the

zero-temperature zero-bias conductance through the system. In all three regimes we derive low energy effective models which explain the low temperature behaviour of the system well. We conclude with an investigation of the effect of an applied magnetic field upon the system in all three regimes, and we find that for certain parameter sets a field-induced Kondo effect may be observed.

Chapter 5 expands upon the work of Chapter 4, examining the effect of breaking mirror symmetry upon a triple quantum dot where a single dot is connected to the conduction band (the 'asymmetric apex coupled trimer model'). This chapter follows much the same plan as Chapter 4, focusing initially upon the bare model Hamiltonian, and the spin model which may be derived from it, before moving on to discuss the phase diagram for this model. We again find that three different regimes may be identified, each exhibiting distinct physics, and in all three a quantum phase transition is observed, associated in regimes I and II with a change in the zero temperature conductance through the system. However, rather than first order quantum phase transitions, all of the quantum phase transitions in this case are found to be Kosterlitz-Thouless transitions. This means that we cannot generally specify the position of the phase boundary with as much precision as was possible in Chapter 4, and the consequences of this are discussed in the section immediately following the phase diagrams. A further consequence of this is that a system lying exactly on the phase boundary is no longer described by a transition fixed point down to zero temperature. We consider the behaviour of the system in each regime in turn, using analytic and semi-analytic techniques and the NRG, and considering both thermodynamic and dynamic properties, and again find that a dramatic change in the zero-temperature conductance is seen across the phase boundary in both regimes I and II. The chapter ends with a discussion of the effect of an applied field upon the system in all three regimes, and we again find that field-induced Kondo effects may be observed.

Chapter 6 discusses the trimer in parallel model. We initially consider the model

Hamiltonian and the effective spin model that may be derived from it, before discussing the symmetry properties of these models; we also explain at this juncture that the effective spin model in this case is found to contain RKKY interactions and this leads directly to the suppression of 'regime I' physics. We next discuss the phase diagram of this model. As 'regime I' is suppressed, we find that the phase diagram may be divided into two distinct regions: the first, the 'spin regime', corresponding to the region where all three dots are singly occupied at low temperature and the second, the 'orbital regime', corresponding the the parameter space outside the spin regime. We see in both regimes a number of quantum phase transitions — both first order and Kosterlitz-Thouless transitions being observed — and we find that the behaviour of the system may be understood if one considers the underlying symmetry properties of the Hamiltonians. We investigate the spin and orbital regimes in turn, using both analytic and semi-analytic methods as well as the NRG. Both the thermodynamic and dynamic properties of the system are examined, and a number of low energy effective models are derived, which we use to better understand the low temperature physics of the system. The chapter concludes with an examination of the effect of an applied magnetic field upon the triple quantum dot device in both the spin and orbital regimes. We again find that field-induced Kondo effects may be observed under certain conditions.

The thesis proper ends with Chapter 7, which summarises the key results of this work. Chapter 7 is followed by seven appendices: Appendix A defines the elements of the $\mathbf{F}_\sigma$ matrix used in the direct calculation of the electron self energy matrix for a triple quantum dot device, Appendix B discusses the derivation and properties of the parity operator which we may use to classify states of mirror symmetric triple quantum dot devices and Appendix C contains a derivation of the Friedel-Luttinger sum rule for a triple quantum dot device attached to a single conduction channel. Appendix D describes the perturbation theory calculation used to determine the energies of states in the orbital regime (regime III) for our low energy effective

model, whilst Appendix E describes the technique we use to numerically calculate the exchange couplings arising from the Schrieffer-Wolff transformations which we use to derive low energy effective models. Appendix F uses the Poor Man's Scaling method of Anderson to derive an expression for the Kondo temperature for the anisotropic Kondo model which is one of the low energy effective models that arises when a magnetic field is applied to regime II of the apex coupled trimer model. Appendix G gives a derivation of an expression for the Kondo temperature for the anisotropic Kondo model which arises in the corresponding case for the trimer in parallel.

Chapter 2

Theoretical Models Of Quantum Dots

We discuss here the models commonly used to represent systems of single quantum dots, the Anderson [6] and Kondo Hamiltonians [2, 12], as these are the 'building blocks' from which we construct models of more complex, coupled quantum dot systems. The Schrieffer-Wolff transformation [13] which may be used to relate the Kondo Hamiltonian to the low energy behaviour of the Anderson model, and the Poor Man's Scaling technique of Anderson [14], which provides crucial insights into the basic ideas of renormalisation and scaling that we will develop further in the next chapter, are also discussed. Both these techniques are used in the study of the triple quantum dot connected to a single conduction channel, which forms the main body of this thesis.

2.1 The Anderson Model and the Schrieffer-Wolff Transformation

We consider first the Anderson model [6], which is ubiquitous in theoretical treatments of quantum impurity systems [2]. The Anderson Hamiltonian models the

quantum dot as a single level which may contain no, one or two electrons, coupled to a single metallic conduction band.

As a quantum dot contains a great many energy levels, it might initially appear that a model as simple as Anderson's could not possibly explain the physics of such a system. However, the gate voltage applied to the quantum dot may be tuned such that almost all of the energy levels lie either sufficiently far below the Fermi level that they are fully occupied or sufficiently far above it that they are empty. It is, indeed, possible to tune the gate voltage in such a way that only a single orbital lies sufficiently close to the Fermi level that it is neither definitely empty or definitely full[1] [5,35]. We may therefore neglect the high and low lying dot levels, and focus all our attention upon the level which lies closest to the Fermi level. The Hamiltonian for this system is then the single impurity Anderson model (SIAM), given by [6]

$$\hat{H} = \hat{H}_d + \hat{H}_L + \hat{H}_{hyb}, \tag{2.1a}$$

$$\hat{H}_d = \sum_{\sigma} \epsilon c^{\dagger}_{d\sigma} c_{d\sigma} + U c^{\dagger}_{d\uparrow} c_{d\uparrow} c^{\dagger}_{d\downarrow} c_{d\downarrow}, \tag{2.1b}$$

$$\hat{H}_L = \sum_{\mathbf{k},\sigma} \epsilon_{\mathbf{k}} c^{\dagger}_{\mathbf{k}\sigma} c_{\mathbf{k}\sigma}, \tag{2.1c}$$

$$\hat{H}_{hyb} = \sum_{\mathbf{k},\sigma} V(c^{\dagger}_{d\sigma} c_{\mathbf{k}\sigma} + H.c), \tag{2.1d}$$

where $\epsilon_{\mathbf{k}}$ is the energy of an electron in the conduction band with wavevector $\mathbf{k}$, ϵ is the one-electron energy of the quantum dot level, U is the Coulomb repulsion incurred when the dot level is doubly occupied (also known as the charging energy) and $c^{\dagger}_{\mathbf{k}\sigma}$ ($c_{\mathbf{k}\sigma}$) is the creation (destruction) operator for an electron in the conduction band with wavevector $\mathbf{k}$ and spin σ ($\sigma = \uparrow$ / $\downarrow$). $c^{\dagger}_{d\sigma}$ ($c_{d\sigma}$) is the creation (destruction) operator for an electron on the quantum dot with spin σ. V is the hopping matrix element between the dot and the conduction band, taken for simplicity to be independent of $\mathbf{k}$. Eq. 2.1d couples the correlated quantum dot level to every

[1]The gate voltage may also be tuned in such a way that two (or more) levels on the quantum dot lie close to the Fermi level, but this is beyond the scope of the current work.

state in the conduction band; this means that solving the Anderson impurity model is a true many-body problem, and a deeply non-trivial one at that. However, a question naturally arises; if one wishes to study the electronic transport through the quantum dot device, what useful information can one possibly obtain from a model which contains only a single conduction band? The answer is simple: under certain (fairly general) conditions a two lead problem may be reduced to a model of the form of Eq. 2.1, containing only a single conduction band. This can be easily understood. Consider an Anderson model where the dot level is connected to two conduction bands, one ('L') on the left side of the dot, and another ('R') on the right. The Hamiltonian for this system is $\hat{H} = \hat{H}_d + \hat{H}_L + \hat{H}_{hyb}$ with $\hat{H}_d$ unchanged from Eq. 2.1a. The other terms in the Hamiltonian may be written

$$\hat{H}_L = \sum_{\mathbf{k},\sigma} \epsilon_{\mathbf{k}} c^\dagger_{\mathbf{k}L\sigma} c_{\mathbf{k}L\sigma} + \sum_{\mathbf{k},\sigma} \epsilon_{\mathbf{k}} c^\dagger_{\mathbf{k}R\sigma} c_{\mathbf{k}R\sigma}, \tag{2.2a}$$

$$\hat{H}_{hyb} = \sum_{\mathbf{k},\sigma} V_L (c^\dagger_{d\sigma} c_{\mathbf{k}L\sigma} + H.c.) + \sum_{\mathbf{k},\sigma} V_R (c^\dagger_{d\sigma} c_{\mathbf{k}R\sigma} + H.c.). \tag{2.2b}$$

Assuming that V_L and V_R are independent of $\mathbf{k}$ — an assumption which we make implicitly in Eq. 2.1 as given — linear combinations of the left and right leads may be taken, defining new 'odd' (o) and 'even' (e) leads:

$$c^\dagger_{\mathbf{k}e\sigma} = \frac{1}{\sqrt{V_L^2 + V_R^2}} (V_L c^\dagger_{\mathbf{k}L\sigma} + V_R c^\dagger_{\mathbf{k}R\sigma}), \tag{2.3a}$$

$$c^\dagger_{\mathbf{k}o\sigma} = \frac{1}{\sqrt{V_L^2 + V_R^2}} (V_R c^\dagger_{\mathbf{k}L\sigma} - V_L c^\dagger_{\mathbf{k}R\sigma}). \tag{2.3b}$$

Using these linear combinations $\hat{H}_L$ and $\hat{H}_{hyb}$ may be written in the following form;

$$\hat{H}_L = \sum_{\mathbf{k},\sigma} \epsilon_{\mathbf{k}} (c^\dagger_{\mathbf{k}e\sigma} c_{\mathbf{k}e\sigma} + c^\dagger_{\mathbf{k}o\sigma} c_{\mathbf{k}o\sigma}), \tag{2.4a}$$

$$\hat{H}_{hyb} = \sum_{\mathbf{k},\sigma} \sqrt{V_L^2 + V_R^2} (c^\dagger_{d\sigma} c_{\mathbf{k}e\sigma} + H.c.). \tag{2.4b}$$

As the odd linear combination is entirely decoupled from the quantum dot, it may be

neglected and the system may be treated as if it contained only a single conduction band — the even combination of the left and right leads. The result presented here is generally true for any system at zero bias where only a single level is connected to the conduction bands. It may be generalised to the case where more than one level is coupled to the conduction band (we discuss such a case in Chapter 6) although in this case it is necessary to specify that the ratio V_L/V_R be fixed for all levels [55].

Now, when $\epsilon < \epsilon_F < U + \epsilon$ (where $\epsilon_F = 0$ is the Fermi level of the system), the singly occupied states of the dot lie lowest in energy. Under these conditions excitations to the empty and doubly occupied states of the dot may be perturbatively eliminated (to second order in V). This process is known as a Schrieffer-Wolff transformation [2,13]. One begins by defining a unity operator for the reduced local Hilbert space of the dot, which spans the singly occupied states of the quantum dot,

$$\hat{1}_{red} = |\uparrow\rangle\langle\uparrow| + |\downarrow\rangle\langle\downarrow| \tag{2.5}$$

and also a further operator,

$$\hat{P} = \hat{1} - \hat{1}_{red}, \tag{2.6}$$

which spans the remainder of the basis states of the full dot Hilbert space. We define E_0 as the energy of the ground state of the system (the singly occupied dot level and conduction band) under $\hat{H}_0 = \hat{H}_d + \hat{H}_L$, and so the effective low energy Hamiltonian for this system to second order in V is $\hat{H}_{red} = \hat{1}_{red}\hat{H}_{hyb}(E_0 - \hat{H}_0)^{-1}\hat{P}\hat{H}_{hyb}\hat{1}_{red} + \hat{H}_L$. This expression may (after some prolonged algebra) be written

$$\hat{H}_{red} = \sum_{\mathbf{k},\mathbf{k}'} J(\tfrac{1}{2}S^+ c^\dagger_{\mathbf{k}\downarrow}c_{\mathbf{k}'\uparrow} + \tfrac{1}{2}S^- c^\dagger_{\mathbf{k}\uparrow}c_{\mathbf{k}'\downarrow} + S^z\tfrac{1}{2}[c^\dagger_{\mathbf{k}\uparrow}c_{\mathbf{k}'\uparrow} - c^\dagger_{\mathbf{k}\downarrow}c_{\mathbf{k}'\downarrow}]) + \sum_{\mathbf{k},\mathbf{k}',\sigma} K c^\dagger_{\mathbf{k}\sigma}c_{\mathbf{k}'\sigma}. \tag{2.7}$$

Here $S^+ = |\uparrow\rangle\langle\downarrow|$, $S^- = |\downarrow\rangle\langle\uparrow|$ and $S^z = \frac{1}{2}(|\uparrow\rangle\langle\uparrow| - |\downarrow\rangle\langle\downarrow|)$ are spin-$\frac{1}{2}$ operators

for the dot, whilst

$$J = 2V^2 \left(\frac{1}{\epsilon + U} - \frac{1}{\epsilon} \right), \tag{2.8a}$$

$$K = -\frac{1}{2} V^2 \left(\frac{1}{\epsilon + U} + \frac{1}{\epsilon} \right), \tag{2.8b}$$

retardation effects being neglected [2]. The first term in Eq. 2.7 couples the spin of the quantum dot to the lead, whilst the second term (which vanishes in the particle-hole symmetric limit where $\epsilon = -U/2$) is potential scattering. We may recast Eq. 2.7 in the following form;

$$\hat{H}_{red} = J_{\mathrm{K}} \hat{\mathbf{S}} \cdot \hat{\mathbf{S}}(0) + \kappa f^{\dagger}_{0\sigma} f_{0\sigma} + \hat{H}_L, \tag{2.9}$$

with $J_{\mathrm{K}} = NJ$ and $\kappa = NK$, N being the number of $\mathbf{k}$ states in the conduction band, and where $\hat{\mathbf{S}}(0)$ is the spin density of the conduction band at the dot given by

$$\hat{\mathbf{S}}(0) = \sum_{\sigma,\sigma'} f^{\dagger}_{0\sigma} \boldsymbol{\sigma}_{\sigma\sigma'} f_{0\sigma'}. \tag{2.10}$$

$\boldsymbol{\sigma}$ are the Pauli matrices; $f^{\dagger}_{0\sigma}$ ($f_{0\sigma}$) is the creation (destruction) operator for an orbital which couples directly to the dot (this is known as the 0-orbital of the Wilson chain [4], and is discussed further when we examine the Numerical Renormalisation Group in detail — see Chapter 3) and is given by

$$f^{\dagger}_{0\sigma} = \frac{1}{\sqrt{N}} \sum_{\mathbf{k}} c^{\dagger}_{\mathbf{k}\sigma}. \tag{2.11}$$

As we will see in the next section, Eq. 2.9 is the isotropic Kondo model. We may therefore say that when $\epsilon < \epsilon_F < U + \epsilon$ the Kondo Hamiltonian is the effective low energy model for the Anderson impurity model, and the two models exhibit identical low temperature behaviour in this region [2, 7, 8].

2.2 The Kondo Model and Poor Man's Scaling

The Kondo model [2, 12] (also known as the s-d model) is conceptually simple, but study of it is nevertheless extremely useful, and theoretically enlightening: as we have already shown, the Kondo Hamiltonian is the effective low energy model for the Anderson model in the region $\epsilon < \epsilon_F < U + \epsilon$, and we find that the vast majority of the low energy effective models derived in this thesis take the form of a Kondo model. The general Hamiltonian for the Kondo model may be written;

$$\begin{aligned}\hat{H} =& \sum_{\mathbf{k},\mathbf{k}'} J_\perp (\tfrac{1}{2} S^+ c^\dagger_{\mathbf{k}\downarrow} c_{\mathbf{k}'\uparrow} + \tfrac{1}{2} S^- c^\dagger_{\mathbf{k}\uparrow} c_{\mathbf{k}'\downarrow}) \\ &+ \sum_{\mathbf{k},\mathbf{k}'} \tfrac{1}{2} J_z S^z (c^\dagger_{\mathbf{k}\uparrow} c_{\mathbf{k}'\uparrow} - c^\dagger_{\mathbf{k}\downarrow} c_{\mathbf{k}'\downarrow}) + \sum_{\mathbf{k},\sigma} \epsilon_{\mathbf{k}} c^\dagger_{\mathbf{k}\sigma} c_{\mathbf{k}\sigma}\end{aligned} \tag{2.12}$$

where $J_\perp$ and J_z are the perpendicular and z components of the exchange coupling, respectively. We consider here the more general, anisotropic case of the Kondo model (i.e. $J_\perp \neq J_z$). The (renormalisation group irrelevant) potential scattering is neglected. Eq. 2.12 represents a true many-body problem, and one which, as we have seen (Chapter 1), defied all attempts at solution via conventional perturbative methods. We must, therefore, use inherently *non-perturbative* methods to solve this problem. As discussed in Chapter 1 the Poor Man's Scaling technique of Anderson [14] was an important first step in this direction. In addition to the historical importance of the Poor Man's Scaling technique in developing the concepts of renormalisation, fixed points and scaling used within the Numerical Renormalisation Group (discussed in Chapter 3), we have also found it to be very useful in both analysing and understanding the models of coupled impurities studied in this thesis, and so we provide here a brief overview of the derivation and results of Poor Man's Scaling, as applied to the spin-anisotropic Kondo model.

In the Kondo model, the magnetic impurity is coupled to a conduction band of width $2D$, where $-D < \epsilon_{\mathbf{k}} < D$, with the Fermi level $\epsilon_{\mathrm{F}} = 0$. Now, in the ground state the region of the conduction band within δD of D contains no electrons, whilst

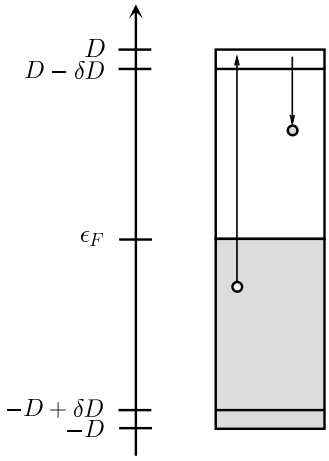


Figure 2.1: The division of the conduction band used in Poor Man's Scaling [14]. Excitations to the upper and lower band edges are perturbatively eliminated.

the region within δD of $-D$ contains no holes. The essence of Poor Man's Scaling is to perturbatively eliminate excitations to both the upper and lower band edges (UBE and LBE — the regions defined by $D - \delta D < \epsilon_{\mathbf{q}} < D$ and $-D < \epsilon_{\mathbf{q}} < -D + \delta D$, respectively), resulting in a Hamiltonian of the same form, with a smaller conduction band width and *renormalised* couplings. This is shown schematically in Fig. 2.1. This process of shrinking the conduction band may be considered as equivalent to reducing the *temperature* of the system; as the temperature falls, the range of accessible excitations is also reduced.

One begins by splitting the conduction band. Two indices, $\mathbf{p}$ and $\mathbf{q}$, are defined such that $-D + \delta D < \epsilon_{\mathbf{p}} < D - \delta D$ and $-D < \epsilon_{\mathbf{q}} < -D + \delta D$ or $D - \delta D < \epsilon_{\mathbf{q}} < D$ (i.e. $\epsilon_{\mathbf{p}}$ lies within the reduced conduction band; $\epsilon_{\mathbf{q}}$ lies within the perturbatively

eliminated regions). One then defines the following Hamiltonians

$$\hat{H} = \hat{H}_L + \hat{H}_{sd} + \hat{H}_{1a} + \hat{H}_{1b}, \tag{2.13a}$$

$$\hat{H}_L = \sum_{\mathbf{k},\sigma} \epsilon_{\mathbf{k}} c^\dagger_{\mathbf{k}\sigma} c_{\mathbf{k}\sigma}, \tag{2.13b}$$

$$\hat{H}_{sd} = \sum_{\mathbf{p},\mathbf{p}'} J_\perp (\tfrac{1}{2} S^+ c^\dagger_{\mathbf{p}\downarrow} c_{\mathbf{p}'\uparrow} + \tfrac{1}{2} S^- c^\dagger_{\mathbf{p}\uparrow} c_{\mathbf{p}'\downarrow}) + \sum_{\mathbf{p},\mathbf{p}'} \tfrac{1}{2} J_z S^z (c^\dagger_{\mathbf{p}\uparrow} c_{\mathbf{p}'\uparrow} - c^\dagger_{\mathbf{p}\downarrow} c_{\mathbf{p}'\downarrow}), \tag{2.13c}$$

$$\hat{H}_{1a} = \sum_{\mathbf{p},\mathbf{q}} J_\perp (\tfrac{1}{2} S^+ c^\dagger_{\mathbf{q}\downarrow} c_{\mathbf{p}\uparrow} + \tfrac{1}{2} S^- c^\dagger_{\mathbf{q}\uparrow} c_{\mathbf{p}\downarrow}) + \sum_{\mathbf{q},\mathbf{p}} \tfrac{1}{2} J_z S^z (c^\dagger_{\mathbf{q}\uparrow} c_{\mathbf{p}\uparrow} - c^\dagger_{\mathbf{q}\downarrow} c_{\mathbf{p}\downarrow}), \tag{2.13d}$$

$$\hat{H}_{1b} = \sum_{\mathbf{p},\mathbf{q}} J_\perp (\tfrac{1}{2} S^+ c^\dagger_{\mathbf{p}\downarrow} c_{\mathbf{q}\uparrow} + \tfrac{1}{2} S^- c^\dagger_{\mathbf{p}\uparrow} c_{\mathbf{q}\downarrow}) + \sum_{\mathbf{q},\mathbf{p}} \tfrac{1}{2} J_z S^z (c^\dagger_{\mathbf{p}\uparrow} c_{\mathbf{q}\uparrow} - c^\dagger_{\mathbf{p}\downarrow} c_{\mathbf{q}\downarrow}), \tag{2.13e}$$

such that $\hat{H}_{1a}$ creates an electron in the UBE, and $\hat{H}_{1b}$ creates a hole in the LBE. (Processes which occur purely within the band edge, or connect one band edge to another are neglected). The effective Hamiltonian is then evaluated via Brillouin-Wigner perturbation theory [93] to second order, viz;

$$\hat{H}_{eff} = \hat{1}(\hat{H}_L + \hat{H}_{sd} + \hat{H}_1 + \hat{H}_1 (E_0 - \hat{H}_L)^{-1} \hat{P} \hat{H}_1) \hat{1}, \tag{2.14}$$

where $\hat{H}_1 = \hat{H}_{1a} + \hat{H}_{1b}$ and E_0 is the energy of the ground state under $\hat{H}_L$. $\hat{1}$ is a unity operator, spanning the reduced Hilbert space of $\hat{H}_{sd}$ and $\hat{P} = \hat{1}_{full} - \hat{1}$, where $\hat{1}_{full}$ is the unity operator for the complete Hilbert space. Trivially $\hat{1}\hat{H}_1\hat{1} = 0$, but $\hat{1}\hat{H}_1(E - \hat{H}_0)^{-1}\hat{P}\hat{H}_1\hat{1} \neq 0$. This term may be evaluated diagrammatically, in a process which is lengthy, but not overly complex [2, 14]. This leads to an effective Hamiltonian which has the same form as Eq. 2.12, but renormalised values of $J_\perp$ and J_z. This gives rise to the differential equations;

$$\frac{\mathrm{d}J_\perp}{\mathrm{d}\ln D} = -\rho_0 J_\perp J_z, \tag{2.15a}$$

$$\frac{\mathrm{d}J_z}{\mathrm{d}\ln D} = -\rho_0 J_\perp^2, \tag{2.15b}$$

which describe how $J_\perp$ and J_z evolve as the conduction band states are progressively

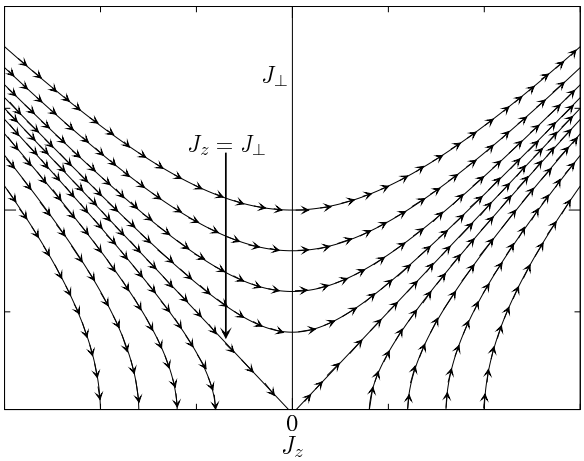


Figure 2.2: The scaling trajectories for an anisotropic Kondo model, as derived from Anderson's Poor Man's Scaling [14].

eliminated. $\rho_0 = N\rho$ is the total density of states in the conduction band, with N the number of $\mathbf{k}$ states in the conduction band and ρ the conduction band density of states per orbital (all the systems investigated in this thesis have a conventional wide, flat band and we therefore set $\rho = 1/2D$ throughout). Dividing Eq. 2.15a by Eq. 2.15b and then integrating between the initial coupling constants (J_z^0 and $J_\perp^0$) and some renormalised coupling constants ($\tilde{J}_z$ and $\tilde{J}_\perp$) gives rise to the scaling trajectory equation for this problem,

$$J_z^2 - J_\perp^2 = C, \tag{2.16}$$

with C a constant. Fig. 2.2 shows the scaling trajectories that result from Eq. 2.16. The scaling trajectories are found to be a function of $|J_\perp|$, and so only the positive $J_\perp$ axis is shown. For each trajectory it is possible to define a scaling invariant, which does not change as the bandwidth is reduced. For the isotropic Kondo model (where $J_z = J_\perp = J$), this scale may be found by integrating

$$\frac{\mathrm{d}J}{\mathrm{d}\ln D} = -\rho_0 J^2 \tag{2.17}$$

between the initial bandwidth, D_0, and $\tilde{D}$, the renormalised bandwidth (Eq. 2.17 is

the isotropic case of Eq. 2.15). This gives rise to the expression

$$k_B T_{\mathrm{K}} \sim D_0 \exp \frac{-1}{\rho_0 J^0} = \tilde{D} \ \exp \frac{-1}{\rho_0 \tilde{J}}, \tag{2.18}$$

for the scaling invariant (also known as the Kondo temperature) where J^0 and $\tilde{J}$ are the initial and renormalised exchange couplings, respectively. We define $J_{\mathrm{K}} = NJ^0$, and therefore write Eq. 2.18 as

$$k_B T_{\mathrm{K}} \sim D \exp \frac{-1}{\rho J_{\mathrm{K}}}, \tag{2.19}$$

where J_{K} may be calculated from the Schrieffer-Wolff transformation of the Anderson model, as described above. Systems which lie on the same scaling trajectory (and hence have the same T_{K}) will exhibit the same low temperature behaviour, although they may have very different bare parameters.

The calculation of the Kondo temperature for the more general spin-anisotropic case of the Kondo model is somewhat more complex. The majority of the models studied in this thesis are found to be described at low temperature by an isotropic Kondo model, but in some cases we find that the low energy effective model takes the form of a spin-anisotropic Kondo model. Expressions for the Kondo temperatures for these models are derived using Poor Man's Scaling in Appendices F and G.

The behaviour of the Kondo model under Poor Man's Scaling may be understood in terms of fixed points. These are sets of parameters for which further reduction in the bandwidth causes no additional renormalisation of the parameters $J_\perp$ and J_z. Fixed points may be classified as attractive (stable), repulsive (unstable) or marginal; we will discuss the formal language used to classify them further in Chapter 3. In general terms, a system close to a stable fixed point will flow towards it upon further renormalisation, whilst a system near to an unstable fixed point will flow away from it. As we can see from Figure 2.2, when $J_z > 0$ the stable fixed point is $J_z = J_\perp = \infty$, the so-called strong coupling fixed point. This is also the fixed

point the system flows to when $J_z < 0$, as long as the condition $|J_\perp| > |J_z|$ is also satisfied. When $J_z < 0$ and $|J_\perp| \leq |J_z|$ the system will ultimately flow to a stable fixed point which lies along the line $J_\perp = 0$. These are the so-called local moment fixed points. There is a second line of (unstable) local moment fixed points which can be found along the line $J_\perp = 0$ when $J_z > 0$. Being unstable these fixed points are only accessible when the initial parameters of a system place it directly upon the line $J_\perp = 0$.

The Poor Man's Scaling technique we have described here is a perturbative method, and implicitly assumes that the coupling constants J_z and $J_\perp$ are small, relative to the initial bandwidth. This presents no conceptual difficulties when dealing with the local moment fixed point, but it is clear that flow towards the strong coupling fixed point quickly takes us outside the regime of validity of Poor Man's Scaling. We must therefore adopt a new, entirely non-perturbative approach, to solve the Kondo problem in that regime.

Chapter 3

The Numerical Renormalisation Group

In this thesis we study models of coupled quantum impurity systems using the Numerical Renormalisation Group (NRG), and so a summary of the derivation and application of this method is provided here. The NRG was initially developed by Wilson for the Kondo Model [4], and subsequently applied by Krishnamurthy, Wilkins and Wilson to the Anderson impurity model [7,8]. We will draw heavily upon these papers in this chapter. The NRG has subsequently been extended to a wide range of quantum impurity systems including two channel physics [88, 94–96], models of coupled impurities — both dimers [50, 96–101] and trimers [52, 60, 66, 72, 74, 88, 90] — as well as impurities connected to ferromagnetic [102, 103] and superconducting [104–106] leads. A wide range of modifications to allow quicker and more accurate calculation have been developed. Interested readers are directed to the recent review by Bulla *et al.* [107]. In this thesis we restrict ourselves to the study of a triple quantum dot system attached to a single, metallic conduction channel.

The NRG is a procedure whereby the Hamiltonian of a quantum impurity system, coupled to a conduction band, is transformed into the form of a linear chain, via a logarithmic discretization of the conduction band, such that the problem may be solved iteratively, each successive iteration revealing information about a lower en-

ergy scale — temperature, for thermodynamic data, or frequency, for dynamic data. The great strength of the NRG is that it provides accurate information about both static and dynamic properties over a wide temperature range. The full derivation of the NRG is lengthy and it will therefore not be attempted here. We will confine ourselves to presenting the key features of the NRG with illustrative examples taken from the application of the NRG to the Anderson impurity model, and we direct interested readers to the papers by Wilson [4] and Krishnamurthy *et al.* [7, 8] and the review by Bulla *et al.* [107], where full details of the derivation may be found.

3.1 Initial Transformations

One begins with the Anderson impurity model Hamiltonian [6] — Eq. 2.1. It is assumed that the conduction band is isotropic (i.e. $\epsilon_{\mathbf{k}}$ depends only upon $|\mathbf{k}|$) and the conduction band is then written in terms of a series of spherical (s-wave) orbitals about the impurity. The discrete momentum variable $\mathbf{k}$ is replaced with a continuous energy variable, ϵ_e (the subscript 'e' is introduced to distinguish this variable from the level energy, ϵ, appearing in Eq. 2.1). This process recasts Eq. 2.1 into a one dimensional form [7, 8], viz.

$$\begin{aligned}\hat{H} =& D\left(\int_{-1}^{1} k a^{\dagger}_{k\sigma} a_{k\sigma} dk + \frac{1}{D}(\epsilon + \tfrac{1}{2}U) c^{\dagger}_{d\sigma} c_{d\sigma}\right. \\ &\left. + \frac{1}{2}\frac{U}{D}(c^{\dagger}_{d\sigma} c_{d\sigma} - 1)^2 + \left(\frac{\Gamma}{\pi D}\right)^{1/2} \int_{-1}^{1} dk (a^{\dagger}_{k\sigma} c_{d\sigma} + c^{\dagger}_{d\sigma} a_{k\sigma})\right),\end{aligned} \tag{3.1}$$

where $k = \epsilon_e/D$ and $a^{\dagger}_{k\sigma} = \sqrt{D} a^{\dagger}_{\epsilon_e\sigma}$; $a^{\dagger}_{\epsilon_e\sigma}$ creates an electron in the spherical orbital with energy ϵ_e and spin σ. $\Gamma = \pi\rho V^2$, and in this chapter we assume a conventional wide flat band, for convenience, but as shown in Ref. [7, 8] this is not strictly necessary. Eq. 3.1 contains only dimensionless parameters, and is now in a suitable form for discretisation. The convention of Ref. [7, 8] has been adopted, where repeated spin indices (σ) are implicitly summed over.

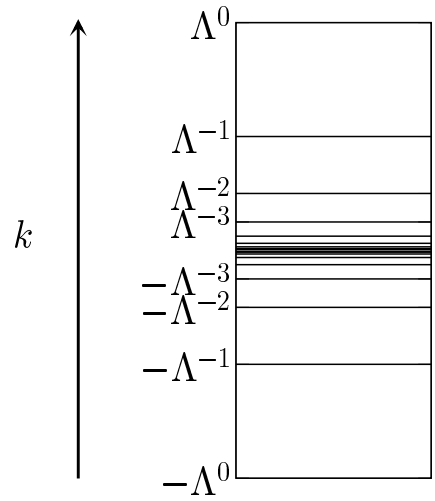


Figure 3.1: The logarithmic discretisation of a conduction band.

3.2 Logarithmic Discretisation

The next step is to discretise the conduction band. This however presents a difficulty: as discussed in Ref. [4], excitations on all energy scales, from that of the bandwidth to the exponentially small Kondo Temperature, T_{K}, must be considered in order to fully understand the physics of the problem. Dividing the conduction band linearly, such that energy scales of the order of T_{K} and smaller are well sampled, would lead to an impractically large number of conduction band states, whilst a division which gave a more manageable number of states would not sample the low energy behaviour of the system well enough to give useful results; for example, with a linear discretisation scheme, to resolve energies on the scale of $T = 10^{-8}D$ would require a conduction band divided into $\sim 10^9$ intervals. As each interval corresponds to an iteration of the NRG clearly this is not computationally feasible. The solution is to discretise the conduction band *logarithmically* [2, 4], thus ensuring that all energy scales are well sampled, whilst the number of intervals that need to be considered is sufficiently small that a calculation is computationally viable. A discretisation parameter, Λ, is defined such that the nth interval of the conduction band is the region $\Lambda^{-(n+1)} < \pm k < \Lambda^{-n}$; this is illustrated in Fig. 3.1. A complete set of orthonormal functions which span the whole k-space may then be defined by setting

up a Fourier series in each interval;

$$\psi^{\pm}_{np}(k) \equiv \begin{cases} \frac{\Lambda^{-n/2}}{(1-\Lambda^{-1})^{1/2}} e^{\pm i\omega_n pk} & \text{if } \Lambda^{-(n+1)} < \pm k < \Lambda^{-n} \\ 0 & \text{otherwise} \end{cases} \tag{3.2}$$

where n, the interval index, may take any positive integer value and p the Fourier harmonic index may take any integer value. ω_n is the fundamental Fourier frequency for the nth interval [7, 8], viz.

$$\omega_n = \frac{2\pi}{\Lambda^{-n} - \Lambda^{-(n+1)}} = \frac{2\pi\Lambda^n}{1-\Lambda^{-1}}. \tag{3.3}$$

The operators $a_{k\sigma}$ may then be rewritten in terms of this basis [7, 8],

$$a_{k\sigma} = \sum_{n,p} [a_{np\sigma}\psi^{+}_{np}(k) + b_{np\sigma}\psi^{-}_{np}(k)]. \tag{3.4}$$

Inverting this equation gives expressions for $a_{np\sigma}$ and $b_{np\sigma}$ [7, 8],

$$a_{np\sigma} = \int_{-1}^{1} dk [\psi^{+}_{np}(k)]^* a_{k\sigma}, \tag{3.5a}$$

$$b_{np\sigma} = \int_{-1}^{1} dk [\psi^{-}_{np}(k)]^* a_{k\sigma}, \tag{3.5b}$$

where $a_{np\sigma}$ and $b_{np\sigma}$ are a complete set of discrete operators which obey the usual Fermion anti-commutation relations; $\{a_{np\sigma}, a^{\dagger}_{n'p'\sigma'}\} = \delta_{nn'}\delta_{pp'}\delta_{\sigma\sigma'}$. Combining Eq. 3.5 with Eq. 3.1, it is readily shown that [7, 8],

$$\begin{aligned} \int_{-1}^{1} k a^{\dagger}_{k\sigma} a_{k\sigma} dk =& \frac{1}{2}(1+\Lambda^{-1}) \sum_{n,p} \Lambda^{-n} (a^{\dagger}_{np\sigma} a_{np\sigma} - b^{\dagger}_{np\sigma} b_{np\sigma}) \\ &+ \frac{1-\Lambda^{-1}}{2\pi i} \sum_{n} \sum_{p \neq p'} \frac{\Lambda^{-n}}{p'-p} (a^{\dagger}_{np\sigma} a_{np'\sigma} - b^{\dagger}_{np\sigma} b_{np'\sigma}) \exp\left(\frac{2\pi i(p'-p)}{1-\Lambda^{-1}}\right), \end{aligned} \tag{3.6a}$$

$$\int_{-1}^{1} a_{k\sigma} dk = (1-\Lambda^{-1})^{1/2} \sum_{n} \Lambda^{-n/2} (a_{n0\sigma} + b_{n0\sigma}). \tag{3.6b}$$

Comparing Eq. 3.6b with Eq. 3.1 it is clear that the impurity couples only to the operators $a_{n0\sigma}$ and $b_{n0\sigma}$ (i.e. those operators where $p = 0$). The NRG so far has been exact; the first, and most fundamental approximation of the NRG is now made. It is assumed that the terms in Eq. 3.6 which contain $p \neq 0$ may be neglected. This assumption is strictly only justifiable in the limit $\Lambda \to 1$, where $\omega_n \to \infty$ (Eq. 3.3), but it may be shown [4, 7, 8] that calculated results for Λ as high as $\Lambda = 3$ are accurate, deviating from those found by extrapolating down to $\Lambda \to 1$ by only a few percent. In this work we will use $\Lambda = 3$.

As is evident from the work shown above, it is convenient at this point to define a new operator, $f_{0\sigma}$, such that

$$f_{0\sigma} = \left[\frac{1}{2}(1-\Lambda^{-1})\right]^{1/2} \sum_{n=0}^{\infty} \Lambda^{-n/2}(a_{n0\sigma} + b_{n0\sigma}) = \frac{1}{\sqrt{2}} \int_{-1}^{1} dk a_{k\sigma}. \tag{3.7}$$

From this point forward the index p will be dropped, as only the $p = 0$ operators will be encountered (i.e. $a^{\dagger}_{n0\sigma} \equiv a^{\dagger}_{n\sigma}$). The Hamiltonian is now diagonal in the operators $a^{\dagger}_{n\sigma}$ and $b^{\dagger}_{n\sigma}$. It is possible to perform a unitary transformation upon the Hamiltonian, writing it in terms of a new orthonormal set of operators, $f_{n\sigma}$, with $f_{0\sigma}$ given by Eq. 3.7 [4, 7, 8]. This transformation is complex, and it will not be described here (interested readers are directed to [4], where full details may be found). Generally, the operator $f^{\dagger}_{n\sigma}$ contains only the combination $a^{\dagger}_{n\sigma} + b^{\dagger}_{n\sigma}$ if n is even, and only the combination $a^{\dagger}_{n\sigma} - b^{\dagger}_{n\sigma}$ if n is odd (this ensures that $f^{\dagger}_{n\sigma}$ and $f^{\dagger}_{(n\pm1)\sigma}$ are orthogonal [4]). The end result of this transformation is a Hamiltonian in the form of a linear chain (known as the Wilson chain [4]), where $f_{n\sigma}$ is coupled only to $f_{(n-1)\sigma}$ and $f_{(n+1)\sigma}$. This Hamiltonian is [7, 8]

$$\begin{aligned}\frac{\hat{H}}{D} =& \frac{1}{2}(1+\Lambda^{-1}) \sum_{n=0}^{\infty} \Lambda^{-n/2} \xi_n [f^{\dagger}_{n\sigma} f_{(n+1)\sigma} + f^{\dagger}_{(n+1)\sigma} f_{n\sigma}] + \frac{1}{D}(\epsilon + \tfrac{1}{2}U) c^{\dagger}_{d\sigma} c_{d\sigma} \\ &+ \left(\frac{2\Gamma}{\pi D}\right)^{1/2} (f^{\dagger}_{0\sigma} c_{d\sigma} + c^{\dagger}_{d\sigma} f_{0\sigma}) + \frac{1}{2}\frac{U}{D}(c^{\dagger}_{d\sigma} c_{d\sigma} - 1)^2,\end{aligned} \tag{3.8}$$

where ξ_n is given by

$$\xi_n = (1 - \Lambda^{-n-1})(1 - \Lambda^{-2n-1})^{-1/2}(1 - \Lambda^{-2n-3})^{-1/2}. \tag{3.9}$$

For large n, $\xi_n \to 1$, and so it is clear from Eq. 3.8 that the coupling between $f_{n\sigma}$ and $f_{(n+1)\sigma}$ decreases exponentially as n increases. This exponential decay is the reason that the Anderson Hamiltonian can be solved using the NRG technique. As discussed in the next section, if the couplings did not decay exponentially with chain length, the truncation scheme used to render the calculation tractable would not work.

3.3 Iterative Diagonalisation and the Recursion Relation

Eq. 3.8 gives the Anderson Hamiltonian in a tridiagonal form. It would, in principle, be possible to take the entire expression in Eq. 3.8 and diagonalise it to determine the energies and eigenvectors of the Anderson impurity model. However, the Wilson chain is semi-infinite in extent, and diagonalising a matrix (even a tridiagonal one) of semi-infinite dimensions is in general impossible. A method has therefore been developed for *iterative* diagonalisation [4,7,8]. In this process diagonalisation of the entire matrix in a single step is not attempted; rather the chain length is gradually built up, with the Hamiltonian matrix being diagonalised afresh after each additional orbital is added to the system. One begins by defining a sequence of Hamiltonian operators as follows [7,8],

$$\begin{aligned}\hat{H}_N =& \Lambda^{(N-1)/2}\Big(\sum_{n=0}^{N-1}\Lambda^{-n/2}\xi_n(f^\dagger_{n\sigma}f_{(n+1)\sigma} + f^\dagger_{(n+1)\sigma}f_{n\sigma}) + \tilde{\epsilon}c^\dagger_{d\sigma}c_{d\sigma} \\ &+ \tilde{\Gamma}^{1/2}(f^\dagger_{0\sigma}c_{d\sigma} + c^\dagger_{d\sigma}f_{0\sigma}) + \tilde{U}(c^\dagger_{d\sigma}c_{d\sigma} - 1)^2\Big),\end{aligned} \tag{3.10}$$

where

$$\tilde{\epsilon} = \left(\frac{2}{1+\Lambda^{-1}}\right)\frac{1}{D}(\epsilon + \tfrac{1}{2}U), \tag{3.11a}$$

$$\tilde{U} = \left(\frac{2}{1+\Lambda^{-1}}\right)\frac{U}{2D}, \tag{3.11b}$$

$$\tilde{\Gamma} = \left(\frac{2}{1+\Lambda^{-1}}\right)^2\frac{2\Gamma}{\pi D}, \tag{3.11c}$$

such that Eq. 3.8 is recovered by taking the limit

$$\hat{H} = \lim_{N\to\infty} \tfrac{1}{2}(1+\Lambda^{-1})D\Lambda^{-(N-1)/2}\hat{H}_N. \tag{3.12}$$

Now, Eq. 3.10 may be written in the form of a recursion relation [7, 8], viz.

$$\hat{H}_{N+1} = \Lambda^{1/2}\hat{H}_N + \xi_N(f^\dagger_{N\sigma}f_{(N+1)\sigma} + f^\dagger_{(N+1)\sigma}f_{N\sigma}) \tag{3.13a}$$

$$= \Lambda^{1/2}\hat{H}_N + \xi_N\hat{H}_{NI}. \tag{3.13b}$$

This recursion relation allows an iterative solution of $\hat{H}_N$, and as such is of fundamental importance within the NRG: the energies and eigenstates of $\hat{H}_{N+1}$ may be calculated, given the energies and eigenstates of $\hat{H}_N$. The starting point for this process is the energies and eigenstates of the quantum dot coupled purely to the 0 orbital of the Wilson chain — a problem which can easily be solved analytically. To follow this procedure, let us initially assume that all the energies and eigenstates of a Hamiltonian $\hat{H}_N$ are known. These states may be classified by quantum numbers; all of the Hamiltonians here may be easily shown to conserve total charge Q, spin S and the z-component of the spin, S_z. The Hilbert space may therefore be divided into subspaces with fixed Q, S and S_z which naturally reduces the computational cost of the NRG calculation dramatically. Each eigenstate of $\hat{H}_N$ is labelled as $|l, N\rangle$, where l is an index, used to distinguish eigenstates of the same $\hat{H}_N$. Now, from each

of the eigenstates of H_N, four of the basis states of H_{N+1} may be defined [7,8],

$$|l,N,1\rangle = |l,N\rangle, \tag{3.14a}$$

$$|l,N,2\rangle = f^\dagger_{(N+1)\uparrow}|l,N\rangle, \tag{3.14b}$$

$$|l,N,3\rangle = f^\dagger_{(N+1)\downarrow}|l,N\rangle, \tag{3.14c}$$

$$|l,N,4\rangle = f^\dagger_{(N+1)\uparrow} f^\dagger_{(N+1)\downarrow}|l,N\rangle. \tag{3.14d}$$

Labelling the states of Eq. 3.14 $|l,N,p\rangle$, the next step is to evaluate

$$\begin{aligned}\langle l,N,p|\hat{H}_{N+1}|l',N,p'\rangle =& \Lambda^{1/2}\langle l,N,p|\hat{H}_N|l',N,p'\rangle \\ &+ \xi_n\langle l,N,p|\hat{H}_{NI}|l',N,p'\rangle.\end{aligned} \tag{3.15}$$

Now, as $\hat{H}_N$, by definition, does not affect the $N+1$ site on the Wilson chain, the first term here is easily evaluated,

$$\Lambda^{1/2}\langle l,N,p|\hat{H}_N|l',N,p'\rangle = \Lambda^{1/2}E(l,N)\delta_{ll'}\delta_{pp'}, \tag{3.16}$$

where $E(l,N)$ is the energy of the state $|l,N\rangle$ under $\hat{H}_N$. The second term is a little more complex, but noting that $f^\dagger_{(N+1)\sigma}$ can affect only the $(N+1)$th site of the Wilson chain, and so can connect only states of Eq. 3.14 with the same l, $\langle l,N,p|f^\dagger_{(N+1)\sigma}|l,N,p'\rangle$ may be abbreviated $\langle p|f^\dagger_{(N+1)\sigma}|p'\rangle$, and so the second term in Eq. 3.15 may be split [7,8],

$$\begin{aligned}\xi_n\langle l,N,p|\hat{H}_{NI}|l',N,p'\rangle = \xi_n(&\langle l,N|f^\dagger_{N\sigma}|l',N\rangle\langle p'|f_{(N+1)\sigma}|p\rangle \\ &+ \langle p'|f^\dagger_{(N+1)\sigma}|p\rangle\langle l',N|f_{N\sigma}|l,N\rangle).\end{aligned} \tag{3.17}$$

Diagonalising the matrix represented by Eq. 3.15 will give complete information on the energies and eigenvalues of the Hamiltonian $\hat{H}_{N+1}$. The computational cost of diagonalising the matrix can be reduced by constructing basis states of $\hat{H}_{N+1}$ which are also eigenstates of the operators $\hat{Q}_{N+1}$, $\hat{S}^2_{N+1}$ and $\hat{S}_{(N+1)z}$. This makes the

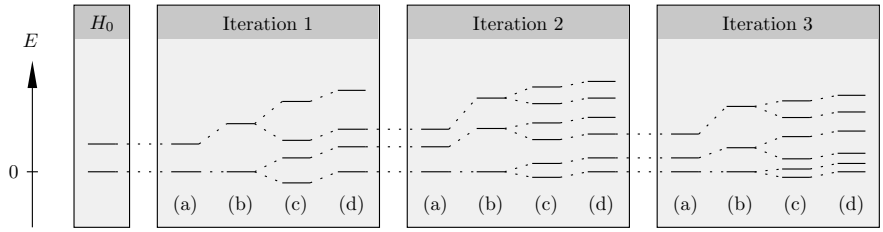


Figure 3.2: A diagrammatic summary of the NRG process, with steps (a)-(d) as described in the text; reproduced with permission from Ref. [32].

matrix $\langle l, N, p|\hat{H}_{N+1}|l', N, p'\rangle$ block diagonal (details on this process may be found in Appendix B of Ref. [7]). However, it is clear from Eq. 3.14 that the size of the Hilbert space will increase by a factor of 4 with each iteration. This exponential growth in the Hilbert space renders the calculation too complex for even modern computers after only a few iterations [107], even if the matrix is block diagonal. However, as discussed in the previous section, the coupling between orbitals on the Wilson chain decreases exponentially with N. As a result each successive iteration will cause a progressively smaller splitting of the energy levels of the system [4]. One may, therefore, discard high energy states at each iteration, confident that, due to the exponentially decreasing coupling along the Wilson chain, states arising from discarded eigenstates cannot change the structure of the eigenstates of later iterations. This process is illustrated in Figure 3.2, which shows the four steps actually followed when performing the NRG. These are (a) retain the lowest N_s states from the previous iteration, (b) rescale their energies by $\Lambda^{1/2}$, (c) couple on an additional site to the chain and (d) express the energies of the system relative to the ground state energy. Steps (b) and (d) ensure that the measured energies are $\mathcal{O}(1)$ for all iterations, so that the same truncation criteria can be used at every step of the NRG. In this work we typically retain a maximum of $N_s = 2000$ states in each iteration, but in some regimes in order to obtain accurate results we have found it necessary to retain more states and we therefore keep a maximum of $N_s = 3000$ states in each iteration in Sec. 4.8, 4.12, 5.7, 5.11, 6.7 and 6.11.

A computationally feasible process for calculating $\hat{H}_N$ for (effectively) arbitrary

N has now been described. However (from Eq. 3.12), $\hat{H}_N$ formally only recovers the full Hamiltonian of the system in the limit $N \to \infty$. Fixed point analysis (described below) provides a theoretical justification for ceasing calculations while N is still finite.

3.4 Fixed Points

The notion of fixed points was discussed briefly in the previous chapter. The concept is now examined more formally. The recursion relation, Eq. 3.13, may be considered as a transformation applied to the Hamiltonian:

$$\hat{H}_{N+2} = \hat{\mathfrak{T}}\hat{H}_N, \tag{3.18}$$

where we consider the transformation from $\hat{H}_N$ to $\hat{H}_{N+2}$ because odd and even iterations within the NRG give different energy levels when flowing to a given fixed point [2, 4, 7, 8], and so they must be considered as separate cases. Now, there exist points in the parameter space of the problem where applying the transformation to the Hamiltonian has no effect upon it — that is

$$\hat{\mathfrak{T}}\hat{H}_* = \hat{H}_*. \tag{3.19}$$

This, formally, is what is meant by a fixed point [4, 7, 8]; a point in parameter space which is invariant under the renormalisation group transformation. Clearly, if one thinks of the iterative NRG process as a transformation, once a fixed point is reached, there is no need for further calculation; as the properties of the system are invariant once it reaches the fixed point, the fixed point must describe the $N \to \infty$ limit required for Eq. 3.10 to recover the full Hamiltonian. An understanding of the fixed points of a given problem will therefore allow us to stop our NRG calculation with a clean conscience after a finite number of iterations. To do this, one must be able

to classify fixed points as stable (attractive), unstable (repulsive) or marginal (see below). The formalism which allows this is quite simple. Consider a Hamiltonian, $\hat{H}_{N=n}$, which lies close to a fixed point $\hat{H}_*$ of the transformation $\mathfrak{T}$ (i.e. $\mathfrak{T}[\hat{H}_*] = \hat{H}_*$) at iteration $N = n$. $\hat{H}_{N=n+2} = \mathfrak{T}[\hat{H}_{N=n}]$ must therefore also lie close to $\hat{H}_*$ [7, 8]. $\delta\hat{H}_{N=n} = \hat{H}_{N=n} - \hat{H}_*$ is defined as the deviation of $\hat{H}_{N=n}$ from $\hat{H}_*$. It then follows that

$$\delta\hat{H}_{N=n+2} = \hat{H}_{N=n+2} - \hat{H}_* = \mathfrak{T}[\hat{H}_* + \delta\hat{H}_{N=n}] - \hat{H}_*, \tag{3.20}$$

and this expression may then be expanded in powers of $\delta\hat{H}_{N=n}$ [7,8]. Retaining only the first two terms gives

$$\delta\hat{H}_{N=n+2} = \mathfrak{L}_*\delta\hat{H}_{N=n}, \tag{3.21}$$

where $\mathfrak{L}_*$ is a linear transformation [2, 4, 7, 8]. Now, there exist some eigenoperators of $\mathfrak{L}_*$, O_l^* [7, 8], with eigenvalues λ_l^* such that

$$\mathfrak{L}_* O_l^* = \lambda_l^* O_l^*, \tag{3.22}$$

and $\delta\hat{H}_{N=n}$ may be expressed in terms of linear combinations of these eigenoperators,

$$\delta\hat{H}_{N=n} = \sum_l C_l\, O_l^*, \tag{3.23}$$

where C_l is a constant. Combining Eq. 3.21 with Eq. 3.23 immediately gives the expression [7, 8]

$$\delta\hat{H}_{N=n+n'} = \sum_l C_l\, \lambda_l^{*n'/2} O_l^* \tag{3.24}$$

for the deviation of the Hamiltonian from the fixed point Hamiltonian, $\hat{H}_*$, after $n + n'$ iterations. As n' is increased, the contribution to $\delta\hat{H}_{N=n+n'}$ from a given eigenoperator will either decrease (if $\lambda_l^* < 1$), increase (if $\lambda_l^* > 1$) or remain the same (if $\lambda_l^* = 1$). An operator with $\lambda_l^* < 1$ is irrelevant, whilst one with $\lambda_l^* > 1$ is relevant; if $\lambda_l^* = 1$ the operator is said to be marginal. A fixed point with only irrelevant operators is a stable fixed point (also known as an attractive fixed point):

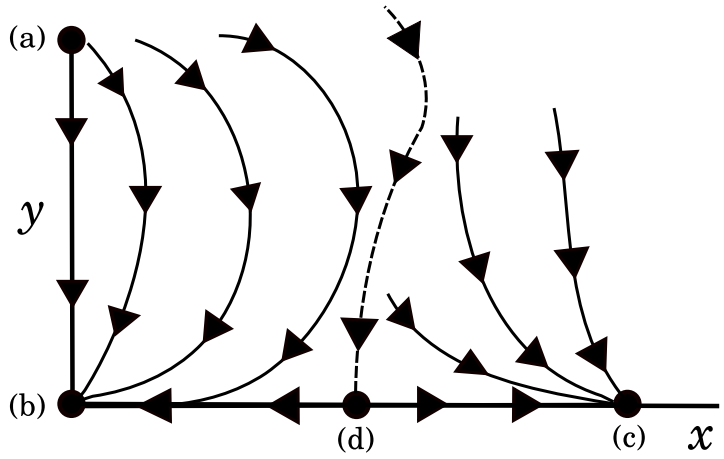


Figure 3.3: Renormalisation group flow for a system with parameters x and y. The system has one unstable fixed point, (a), which is repulsive, two stable fixed points, (b) and (c), which are attractive, and a critical fixed point, (d) which lies at the end of the renormalisation group flow between the basins of attraction of the two stable fixed points.

any Hamiltonian close to the fixed point in parameter space will eventually flow to it. A fixed point which has one or more relevant operators is, by contrast, unstable. Any $\delta\hat{H}_N$ which contains a contribution from one of the relevant operators will ultimately flow away from this fixed point when the transformation is repeatedly applied. If a fixed point has only marginal or irrelevant operators, classification of it is more complex. The most rigorous way in which to deal with a fixed point of this type is to expand Eq. 3.20 in higher powers of $\delta\hat{H}_N$ [4]. However, here we will generally classify fixed points by examining the behaviour of nearby points in parameter space using the NRG.

The behaviour of a system which contains only a single stable fixed point is quite simple; unless the parameters of a given Hamiltonian place it exactly upon an unstable fixed point, it will eventually flow to the stable fixed point of the system. A system with more than one stable fixed point exhibits more complex behaviour [108]. Figure 3.3 shows a system with two stable fixed points, (b) and (c), and a single unstable fixed point, (a). The system here contains two phases, each corresponding to a region of parameter space within which the Hamiltonian will ultimately flow to one of the stable fixed points. The presence of two distinct phases implies that

there must exist a phase boundary between them (represented by the dashed line in Figure 3.3). In this particular case, flow along this line leads to a fixed point (d) which is stable with respect to the boundary line, but unstable with respect to the rest of the parameter space (this is known as a critical fixed point). However, as we shall see, a phase boundary is not necessarily associated with a distinct, critical fixed point. The final, unstable, fixed point, (a), repels renormalisation group flows, and can only be the zero temperature fixed point if the initial parameters place the system directly on it. We also add that whilst the ground state must be one of the stable fixed points, a system may flow close to an unstable fixed point for a great many iterations (and therefore a wide temperature range) before ultimately flowing to a stable fixed point.

3.5 Thermodynamics

We have sketched above how the NRG may be used to calculate the energies and eigenstates of a quantum impurity system attached to a conduction band. In this section, the method used to calculate static quantities for a quantum impurity system from those energies and eigenstates is explained. The subsequent section explains the equivalent process used to calculate dynamic properties. When calculating thermodynamic properties, one starts with the usual statistical mechanical expression for the thermal average of an operator, $\hat{A}$;

$$\langle \hat{A} \rangle (T) = \frac{\mathrm{Tr}\, \hat{A} \exp(-\beta \hat{H})}{\mathrm{Tr} \exp(-\beta \hat{H})}, \tag{3.25}$$

where $\hat{H}$ is the Hamiltonian of the system, and $1/\beta = k_B T$. It is conventional within the NRG to focus on the quantum dot contribution to the thermodynamic properties of the system [107]. This is done by calculating $\langle \hat{A} \rangle_{\mathrm{imp}}$, which is defined

as the difference between $\langle\hat{A}\rangle$ in the presence and absence of the quantum dot[1],

$$\langle\hat{A}\rangle_{\rm imp}(T) = \langle\hat{A}\rangle(T) - \langle\hat{A}^0\rangle_0(T) = \frac{{\rm Tr}\,\hat{A}\exp(-\beta\hat{H})}{{\rm Tr}\exp(-\beta\hat{H})} - \frac{{\rm Tr}\,\hat{A}^0\exp(-\beta\hat{H}^0)}{{\rm Tr}\exp(-\beta\hat{H}^0)}, \quad (3.26)$$

the sub/superscript '0' indicating that the quantity is calculated in the absence of the dot (i.e. for the conduction band alone). Now Eq. 3.26 depends upon the full Hamiltonian of the system. For any given iteration, attempting to solve Eq. 3.26 for too high a temperature will result in errors as relevant, accessible states of the system will have been discarded at earlier iterations during the truncation process [7, 8]. However, attempting to solve Eq. 3.26 for too low a temperature will also give rise to errors, as at low temperature the splitting of the eigenstates caused by later iterations will have an important effect upon the thermodynamics [7,8]. For any given iteration there is, therefore, a modest temperature window within which Eq. 3.26 can be used accurately. However this window is different for each iteration, and so by calculating the thermodynamic properties of the system in *every* iteration one can build up information about the thermodynamics of the system over a wide temperature range. Starting with Eq. 3.12, one may write [7, 8]

$$\beta\hat{H} = \lim_{M\to\infty} \bar{\beta}_M \hat{H}_M, \quad (3.27)$$

where $\beta = 1/k_B T$ and

$$\bar{\beta}_M = \tfrac{1}{2}(1+\Lambda^{-1})\Lambda^{-(M-1)/2}\frac{D}{k_B T}. \quad (3.28)$$

Eq. 3.27 may be divided into three parts [7, 8],

$$\bar{\beta}_M \hat{H}_M = \bar{\beta}_N \hat{H}_N + \bar{\beta}_N \hat{H}_I + \bar{\beta}_M R_{M,N+1}, \quad (3.29)$$

[1]The 'imp' subscript is a relic of the original NRG calculations on impurities in metals. It is retained here for convenience.

where $\hat{H}_N$ is the Hamiltonian for iteration N.

$$\hat{H}_I = \Lambda^{-1/2}\xi_N(f^\dagger_{N\sigma}f_{(N+1)\sigma} + f^\dagger_{(N+1)\sigma}f_{N\sigma}) \tag{3.30}$$

and

$$R_{M,N+1} = \Lambda^{(M-1)/2}\sum_{n=N+1}^{M-1}\Lambda^{-n/2}\xi_n(f^\dagger_{n\sigma}f_{(n+1)\sigma} + f^\dagger_{(n+1)\sigma}f_{n\sigma}), \tag{3.31}$$

are, respectively, the coupling between $\hat{H}_N$ and the rest of the Wilson chain, and the remainder of the Wilson chain. One of the very few approximations required within the NRG is now made: $\hat{H}_I$ is neglected. It has been shown that this approximation introduces an error which is formally $\mathcal{O}(\bar{\beta}_N/\Lambda)$ [7, 8], and we may ensure this error is minimal with an appropriate choice of Λ and $\bar{\beta}_N$. This is typically done by fixing $\bar{\beta}_N = \bar{\beta}$, which allows the definition of an *effective temperature*, T_N, for each iteration [7, 8]:

$$\bar{\beta} = \tfrac{1}{2}(1+\Lambda^{-1})\Lambda^{-(N-1)/2}\frac{D}{k_B T_N}. \tag{3.32}$$

We will, unless otherwise noted, set $\Lambda = 3$ and $\bar{\beta} = 0.7$ in this thesis — values which have been found to provide a reasonable balance between calculation speed and accuracy. If $\hat{H}_I$ is neglected, then the value of $R_{M,(N+1)}$ is the same in the presence or absence of the impurity. As such, this term will vanish from $\langle\hat{A}\rangle_{\text{imp}}$. This gives the expression

$$\langle\hat{A}\rangle_{\text{imp}}(T_N) = \frac{\operatorname{Tr}\hat{A}_N\exp(-\bar{\beta}\hat{H}_N)}{\operatorname{Tr}\exp(-\bar{\beta}\hat{H}_N)} - \frac{\operatorname{Tr}\hat{A}^0_N\exp(-\bar{\beta}\hat{H}^0_N)}{\operatorname{Tr}\exp(-\bar{\beta}\hat{H}^0_N)}, \tag{3.33}$$

which is used to calculate the expectation value of a thermodynamic quantity $\hat{A}$ at the effective temperature T_N. The three thermodynamic quantities we make use of in this work are S_{imp}, the impurity contribution to the entropy, χ_{imp}, the impurity contribution to the magnetic susceptibility, and $n_{\text{imp},\sigma}$, the 'excess' charge with spin σ (in practice, indistinguishable from the charge on the dot itself). S_{imp} may be calculated using a statistical mechanical expression for entropy [109], $S/k_B =$

$\beta\bar{E} + \ln Z$, where Z is the partition function ($\mathrm{Tr}\exp(-\beta\hat{H})$) and $\bar{E}$ the internal energy of the system. This leads to the expression

$$S_{\mathrm{imp}}(T_N)/k_B = \bar{\beta}\langle\hat{H}_N\rangle_{\mathrm{imp}} + \ln\left(\frac{Z_N}{Z_N^0}\right), \tag{3.34}$$

with Z_N^0 the partition function of the system without the dot. χ_{imp} may be calculated from the expression $\chi = \partial M/\partial B|_0$, where M is the magnetization ($\langle S_{tot}^z\rangle$) and B an infinitesimal magnetic field [107],

$$\chi_{\mathrm{imp}}(T_N) = \frac{(g\mu_B)^2}{k_B T_N}(\langle(S_{N,tot}^z)^2\rangle_{\mathrm{imp}} - \langle S_{N,tot}^z\rangle_{\mathrm{imp}}^2). \tag{3.35}$$

Finally, $n_{\mathrm{imp},\sigma}$ may be calculated from the expression

$$n_{\mathrm{imp},\sigma}(T_N) = \langle\hat{Q}(T_N)\rangle_{\mathrm{imp}} + \sigma\langle\hat{S}_z(T_N)\rangle_{\mathrm{imp}}, \tag{3.36}$$

where $\hat{Q} = \sum_{n=0}^{N}(f_{n\sigma}^\dagger f_{n\sigma} - 1) + \sum_i(c_{i\sigma}^\dagger c_{i\sigma} - 1)$ is the charge operator [7,8]; $c_{i\sigma}^\dagger$ ($c_{i\sigma}$) is the creation (destruction) operator for electrons with spin σ on dot level i ($\sigma = \pm$ for spin $\uparrow$ / $\downarrow$, respectively). For the single impurity Anderson model, there is only a single level, and so $i = 1$; we label the creation and destruction operators in this case $c_{d\sigma}^\dagger$ and $c_{d\sigma}$, respectively, for consistency. We also define

$$n_{\mathrm{imp}} = n_{\mathrm{imp},\uparrow} + n_{\mathrm{imp},\downarrow} = \langle\hat{Q}\rangle_{\mathrm{imp}}, \tag{3.37a}$$

$$m = n_{\mathrm{imp},\uparrow} - n_{\mathrm{imp},\downarrow} = 2\langle\hat{S}_z\rangle_{\mathrm{imp}}, \tag{3.37b}$$

and set $g\mu_B = k_B = 1$ from this point onwards.

3.6 Dynamical Properties, the Density Matrix and the Self Energy

In addition to static properties, the NRG may also be used to calculate dynamic properties. The dynamical results presented in this work make use of two major improvements to the basic calculation of dynamics within the NRG — namely the use of the full Anders-Schiller Density Matrix [110,111] and the direct calculation of the self-energy of the quantum dot system [55,107]. Both of these techniques improve the accuracy of the spectra calculated using the NRG. We concentrate in this thesis upon one dynamical function, the single particle spectrum; we also examine the zero-bias differential conductance (henceforth 'the conductance'), a thermodynamic function which may be determined from the single particle spectrum. The starting point for calculating the differential conductance is the Meir-Wingreen formula for the steady-state current through a region containing interacting electrons (such as a coupled quantum dot system), connected to two non-interacting leads [112],

$$\begin{aligned} J = \frac{2ie}{h}\frac{1}{2}\sum_{\sigma}\int_{-\infty}^{\infty} d\omega \left(\mathrm{Tr}\{[f_L(\omega)\mathbf{\Gamma}^I_L(\omega) - f_R(\omega)\mathbf{\Gamma}^I_R(\omega)][\mathbf{G}^r_\sigma(\omega) - \mathbf{G}^a_\sigma(\omega)]\}\right. \\ \left. +\mathrm{Tr}\{[\mathbf{\Gamma}^I_L(\omega) - \mathbf{\Gamma}^I_R(\omega)]\mathbf{G}^<_\sigma(\omega)\}\right), \end{aligned} \tag{3.38}$$

where $f_\nu(\omega) = [e^{\beta(\omega-\mu_\nu)}+1]^{-1}$ are the Fermi functions describing the left (L) and right (R) leads, with μ_ν the chemical potentials of those leads. Couplings to the two leads are given by the $\mathbf{\Gamma}^I_\nu$ matrix, which has elements $[\mathbf{\Gamma}^I_\nu(\omega)]_{ij} = \pi V_{i\nu}V_{j\nu}N\rho$ (with $\rho = 1/2D$ the lead density of states per orbital and i and j denoting the dot levels; $V_{i\nu}$ is the hopping term connecting dot level i to lead ν). $\mathbf{G}^r_\sigma(\omega)$, $\mathbf{G}^a_\sigma(\omega)$ and $\mathbf{G}^<_\sigma(\omega)$ are the retarded, advanced and non-equilibrium Keldysh 'lesser' Green function matrices. $[\mathbf{G}^r_\sigma(\omega)]_{ij} = \langle\langle c_{i\sigma}; c^\dagger_{j\sigma}\rangle\rangle$, where $\langle\langle A; B\rangle\rangle$ is the Fourier transform of the retarded correlator $\langle\langle \hat{A}(t_1); \hat{B}(t_2)\rangle\rangle = -i\theta(t_1-t_2)\langle\{\hat{A}(t_1), \hat{B}(t_2)\}\rangle$, and $c^\dagger_{i\sigma}$ ($c_{i\sigma}$) is the creation (destruction) operator for an electron with spin σ in dot level i. For the single impurity Anderson model, as in the previous section, there is only

one dot level and $c^\dagger_{1\sigma} \equiv c^\dagger_{d\sigma}$. An advanced correlator may be equivalently defined $+i\theta(t_2-t_1)\langle\{\hat{A}(t_1),\hat{B}(t_2)\}\rangle$. The elements of $\mathbf{G}^<_\sigma$ are given by the Fourier transform of $[\mathbf{G}^<_\sigma]_{ij}(t) = i\langle c^\dagger_{j\sigma}(t=0)c_{i\sigma}(t)\rangle_\sigma$ [112]. For the case where couplings to the left and right leads are proportional ($\mathbf{\Gamma}^I_L(\omega) = \lambda\mathbf{\Gamma}^I_R(\omega)$ with λ a constant) Eq. 3.38 simplifies to

$$J = \frac{4ie}{h}\frac{1}{1+\lambda}\frac{1}{2}\sum_\sigma\int_{-\infty}^{\infty}[f_L(\omega)-f_R(\omega)]\mathrm{Tr}[\mathbf{\Gamma}^I_L(\omega)(\mathbf{G}^r_\sigma(\omega)-\mathbf{G}^a_\sigma(\omega)). \tag{3.39}$$

Using the relationship $\mathbf{G}^r_\sigma(\omega)-\mathbf{G}^a_\sigma(\omega) = -2\pi i\mathbf{D}_\sigma(\omega)$, with $\mathbf{D}_\sigma$ the spectral density, gives the result

$$J = \frac{2e}{h}G_0\frac{1}{2}\sum_\sigma\int_{-\infty}^{\infty}[f_L(\omega)-f_R(\omega)]\mathrm{Tr}[\pi\mathbf{\Gamma}^I\mathbf{D}_\sigma(\omega)], \tag{3.40}$$

where $G_0 = 4\lambda/(1+\lambda)^2$ and $\mathbf{\Gamma}^I(\omega) = \mathbf{\Gamma}^I_L(\omega)+\mathbf{\Gamma}^I_R(\omega)$. Differentiating Eq. 3.40 with respect to a bias voltage $V_{sd} = \frac{1}{e}(\mu_L-\mu_R)$ applied between the left (source) and right (drain) leads and then evaluating the limit $V_{sd}\to 0$ immediately gives the expression

$$\frac{G_c(T)}{G_0} = \int_{-\infty}^{\infty} -\frac{\partial f(\omega)}{\partial\omega}\frac{1}{2}\sum_\sigma \mathrm{Tr}[\pi\mathbf{\Gamma}^I\mathbf{D}_\sigma(\omega,T)]d\omega, \tag{3.41}$$

where $f(\omega) = [e^{\beta\omega}+1]^{-1}$ is a Fermi function with chemical potential $\mu = 0$. For a single quantum dot both $\mathbf{\Gamma}^I$ and $\mathbf{D}_\sigma$ are scalar quantities: $D_\sigma(\omega,T)$ is simply the spin-σ single particle spectrum of the dot, and $\Gamma^I = \pi N\rho V^2$ is the coupling of that dot to the conduction band. As we discuss below (Sec. 4.4 and Sec. 6.4), for systems of coupled dots, such as those studied in this thesis, $\mathrm{Tr}[\pi\mathbf{\Gamma}^I\mathbf{D}_\sigma(\omega,T)]$ may be a more complex expression, combining several different single particle spectra.

For the single impurity Anderson model, in order to determine the differential conductance it is clear that the spectral density, D_σ, must be calculated. As noted above, $D_\sigma(\omega) = \frac{i}{2\pi}(G^r_\sigma(\omega)-G^a_\sigma(\omega))$, with $G^r_\sigma(\omega)$ the retarded Green function and $G^a_\sigma(\omega)$ the advanced. The retarded and advanced Green functions are

related by $\mathrm{Re}[G^r_\sigma(\omega)] = \mathrm{Re}[G^a_\sigma(\omega)]$ and $\mathrm{Im}[G^r_\sigma(\omega)] = -\mathrm{Im}[G^a_\sigma(\omega)]$, and as such $D_\sigma(\omega) = -\frac{1}{\pi}\mathrm{Im}[G^r_\sigma(\omega)]$. We concentrate upon the retarded correlator from this point on, and therefore drop the 'r' and 'a' superscripts.

The single particle spectrum may equivalently be written using the Lehmann representation [107],

$$D_\sigma(\omega, T) = \sum_{a,b} \langle b|c_{d\sigma}|a\rangle \frac{\exp(-\beta E_a)}{Z} \langle a|c^\dagger_{d\sigma}|b\rangle \delta(\omega + E_a - E_b), \tag{3.42}$$

with Z the partition function of the system, E_i the energy of state $|i\rangle$ and $\beta = 1/k_B T$. The matrix elements in Eq. 3.42 may be calculated during the NRG process, but one encounters similar issues to those found when attempting to calculate thermodynamic properties (both with truncation and the splitting caused by future iterations), and, just as in that case, one may define an effective *frequency*, analogous to the effective *temperature* used when calculating static properties. However, as is clear from Eq. 3.42, the situation in this case is rather more complex than the analogous case for thermodynamic data, as the spectrum for a given frequency contains contributions from *all* energy scales of the system and therefore the sum in Eq. 3.42 involves terms for *every* iteration of the NRG. It is immediately obvious that this must result in double counting errors, which arise when the spectra is calculated using both the states of an iteration N, and the states derived from them in later iterations. Spectra have been successfully calculated by combining poles from every iteration with a weighting appropriate to the effective frequency [113, 114], but there remain some conceptual difficulties with this approach. Another major problem with this method is that the ground state may not be correctly identified during early iterations, and (as excitations from the ground state make a major contribution to the spectra at all frequencies) this may lead to spectra which are not even qualitatively correct.

Weichselbaum and von Delft [110] and Peters, Pruschke and Anders [111] developed a method of calculating dynamical properties which resolves this issue, and a

number of others (such as the double counting due to overlapping frequency windows) by defining a complete basis set of eigenstates for the system. This method is known as the Full Density Matrix implementation of the NRG (FDM-NRG). In this method, iteration n of the NRG is thought of not as adding the nth orbital to the Wilson chain, but rather as switching on the coupling between orbitals $n-1$ and n in a chain of length P, where P is the total number of iterations in the NRG calculation.

Viewed through this lens, it is clear that a complete basis set of eigenstates can be constructed from the states discarded ('D') during the truncation step of each NRG iteration, the contributions to the basis set from the retained states (also known as 'kept' states — 'K') being included in later iterations[2]. The states of an iteration n, $|s\rangle_n^X$ ($X = K, D$) are related to the K (kept) states of the previous iteration by [110]

$$|s'\rangle_n^X = \sum_{\sigma_n s}^{K} |\sigma_n\rangle \otimes |s\rangle_{n-1}^K [A_{KX}^{[\sigma_n]}]_{ss'} \tag{3.43}$$

with σ_n denoting the possible states of the nth orbital of the Wilson chain ($|\sigma_n\rangle = |0\rangle, |\uparrow\rangle, |\downarrow\rangle, |\uparrow\downarrow\rangle$) and $[A_{KX}^{[\sigma_n]}]$ is a matrix with elements $[A_{KX}^{[\sigma_n]}]_{ss'}$ where $X = K, D$ labels the kept and discarded states at a given iteration (this is an alternative expression for the eigenstates of Eq. 3.15).

The complete basis set, $\{|se\rangle_n^X\}$, known as the Anders-Schiller basis [115], is formed at a given iteration, n, by a direct product of the states of the Wilson chain of length n, $\{|s\rangle_n^X\}$, with a set of 4^{P-n} degenerate 'environmental' states, $\{|e_n\rangle\}$, which span the remainder of the Wilson chain (sites $n+1$ through P) [110]:

$$\{|se\rangle_n^X\} = \{|e\rangle_n \otimes |s\rangle_n^X\}. \tag{3.44}$$

One then makes the 'NRG Approximation' [110] that the states $|se\rangle_n^X$ are ap-

[2]One treats *all* the states of the final iteration as discarded.

proximate eigenstates of the Hamiltonian of the entire Wilson chain:

$$\hat{H}_P|se\rangle_n^X \simeq E_s^n|se\rangle_n^X. \tag{3.45}$$

The complete Anders-Schiller set of basis states [115] is then constructed

$$\hat{1} = \sum_{se} |se\rangle_{n_0}^K \,{}_{n_0}^K\langle se| = \sum_{n>n_0}^{P} \sum_{se} |se\rangle_n^D \,{}_n^D\langle se|, \tag{3.46}$$

where n_0 is the last iteration at which no states are discarded (and all states are therefore kept). The complete set of basis states defined in this way is also a complete set of eigenstates of $\hat{H}_P$ [110] because states discarded at any given iteration, n, are orthogonal to the states kept at that iteration (trivially, as they are all, both kept and discarded, eigenstates of $\hat{H}_n$, the Hamiltonian at that iteration), and also *orthogonal to all states of later iterations*, as these states are derived from the states kept at the current iteration. In addition, as the states discarded at the current iteration are necessarily constructed from the states kept at the previous iteration (Eq. 3.43), it is clear that the discarded states at the current iteration must also be orthogonal to *all states discarded during previous iterations*.

One next considers an operator $\hat{B}$ which acts non-trivially *only* on sites $n < n_0$ (we concentrate on operators which effect the quantum dot levels and so this criteria is automatically fulfilled for all the dynamic quantities studied in this thesis):

$$\hat{B} = \hat{1}\hat{B}\hat{1} \tag{3.47a}$$

$$= \sum_{ss'e} |se\rangle_{n_0}^K \,{}_{n_0}^K\langle se|\hat{B}|s'e\rangle_{n_0}^K \,{}_{n_0}^K\langle s'e| \tag{3.47b}$$

$$= \sum_{ss'e} |se\rangle_{n_0}^K [B_{KK}^{[n_0]}]_{ss'} \,{}_{n_0}^K\langle s'e| = \hat{B}_{KK}^{[n_0]} \tag{3.47c}$$

where

$$[B_{KK}^{[n_0]}]_{ss'} = \,{}_{n_0}^K\langle se|\hat{B}|s'e\rangle_{n_0}^K. \tag{3.48}$$

Noting that all the states of an iteration n are derived from the K subset of the states of iteration $n-1$ (Eq. 3.43), it follows that at a given iteration, any contribution to $\hat{B}$ from the K states of the previous iteration can expressed in terms of the kept and discarded states of the current iteration, and so the contribution from the K states to $\hat{B}$ may be iteratively refined, until at the final iteration all states are discarded;

$$\hat{B}^{[n-1]}_{KK} = \sum_{XX'} \sum_{ss'e} |se\rangle^{X}_{n} [B^{[n]}_{XX'}]_{ss'} \, {}^{X'}_{n}\langle s'e| \tag{3.49a}$$

$$= \sum_{XX'} \hat{B}^{[n]}_{XX'} \tag{3.49b}$$

where $[B^{[n]}_{XX'}]_{ss'} = [A^{[\sigma_n]\dagger}_{XK} B^{[n-1]}_{KK} A^{[\sigma_n]}_{KX'}]_{ss'}$. The operator $\hat{B}$ may therefore be written

$$\hat{B} = \sum_{n>n_0}^{P} \sum_{XX'}^{\neq KK} \hat{B}^{[n]}_{XX'}. \tag{3.50}$$

As the KK term are excluded from this sum, double counting is rigorously eliminated [110]. The density matrix of the system is defined $\hat{\rho} = e^{-\beta \hat{H}}/Z$, with Z the partition function of the system. Using the NRG Approximation in conjunction with the results above leads to [110]

$$\hat{\rho} \simeq \sum_{n>n_0}^{P} \sum_{se} |se\rangle^{D}_{n} \frac{e^{-\beta E^n_s}}{Z} \, {}^{D}_{n}\langle se| \tag{3.51a}$$

$$= \sum_{n>n_0}^{P} w_n \hat{\rho}^{[n]}_{DD} \tag{3.51b}$$

where $w_n = 4^{P-n} Z^D_n / Z$ is a weighting function and $Z^D_n = \sum^D_s e^{-\beta E^n_s}$. The presence of w_n ensures that the correct iterations are sampled at any given temperature — a more rigorous approach to weighting the contributions from different iterations than the system used in the older method. Consider now a dynamic quantity (spectral

function), $\mathcal{A}^{BC}(\omega)$, which may be written as a sum of terms from each iteration [110]:

$$\mathcal{A}^{BC}(\omega) = f(\langle\langle \hat{B}; \hat{C} \rangle\rangle) \tag{3.52a}$$

$$= \sum_n w_n \, \mathcal{A}_n^{BC}(\omega). \tag{3.52b}$$

The Lehmann representation [107] of $\mathcal{A}^{BC}(\omega)$ then follows immediately as

$$\mathcal{A}^{BC}(\omega) = \sum_{a,b} \langle b|\hat{B}|a\rangle\langle a|\hat{\rho}|a\rangle\langle a|\hat{C}|b\rangle \delta(\omega + E_a - E_b). \tag{3.53}$$

Writing this in terms of the expressions for the density matrix and the Anders-Schiller complete basis set derived above leads to the expression

$$\mathcal{A}^{BC}(\omega) = \sum_{m>n_0}^{n} \sum_{ss'} \sum_{XX'}^{\neq KK} [C^{[m]}_{X'X} \rho^{[mn]}_{XX}]_{s's} [B^{[m]}_{XX'}]_{ss'} \delta(\omega - E^m_{ss'}) \tag{3.54}$$

where $E^m_{ss'} = E_s - E_{s'}$ and

$$[\rho^{[m=n]}_{DD}]_{ss'} = \delta_{ss'} \frac{e^{-\beta E^n_s}}{Z_n}, \tag{3.55a}$$

$$[\rho^{[m<n]}_{KK}]_{ss'} = [A^{[\sigma_{m+1}]}_{KK} ... A^{[\sigma_n]}_{KD} \rho^{[nn]}_{DD} A^{[\sigma_n]\dagger}_{DK} .... A^{[\sigma_{m+1}]\dagger}_{KK}]_{ss'}, \tag{3.55b}$$

$$\rho^{[m=n]}_{KK} = \rho^{[m<n]}_{DD} = 0, \tag{3.55c}$$

where the sum over σ_n in Eq. 3.55b is implicit and $Z_n = \sum_s e^{-\beta E^n_s}$. To determine $\mathcal{A}^{BC}(\omega)$ from Eq. 3.54 one first performs a 'forward run' (the normal NRG calculation) during which the matrix elements and energies required in Eq. 3.54 are calculated and then a 'backward run' is used to combine this information to calculate $\hat{\rho}$, the full density matrix, starting with the final iteration P [110]. The reduced density matrix, $\rho^{[m],red}$, is given for an iteration m by

$$\rho^{[m],red}_{XX} = \sum_{n \geq m}^{P} w_n \rho^{[mn]}_{XX} \tag{3.56}$$

where

$$\hat{\rho} = \sum_{n=n_0}^{P} \rho^{[n],red}. \tag{3.57}$$

Once the density matrix has been determined, as one already knows the states of the full Anders-Schiller basis set, evaluation of Eq. 3.54 for a given spectral function $\mathcal{A}^{BC}(\omega)$ is simple. However, the improved accuracy of the FDM-NRG approach does increase the computational cost of the NRG calculation, as in order to perform the 'backward run' the unitary matrices which describe the states of the Hamiltonian $\hat{H}_n$ must be stored at each iteration.

As the conduction band is discretised, spectral functions calculated using the NRG (both those calculated using the Lehmann sum (Eq. 3.42) and those calculated using the FDM-NRG approach (Eq. 3.54)) take the form of a series of discrete poles. In order to view and interpret the spectrum, it is conventional to replace each pole with a logarithmic gaussian of the same weight. This is conventionally referred to as 'broadening' the spectrum, and makes the spectrum a smooth, continuous function. Further details may be found in Ref. [107].

One additional useful refinement of the NRG was developed by Bulla *et al.* [116]. In this method, the electron self-energy matrix, $\mathbf{\Sigma}_\sigma(z)$, is calculated directly. The initial work by Bulla *et al.* was on the single impurity Anderson model, but the method is readily generalised to the multiple level or multiple impurity case [55]. We begin by using the expression

$$\mathbf{\Sigma}_\sigma(z) = \mathbf{G}_\sigma^{-1}(z)\mathbf{F}_\sigma(z), \tag{3.58}$$

where $z = \omega + i\eta$ with η an infinitesimal, $\mathbf{G}_\sigma$ is the Green function matrix, $\mathbf{\Sigma}_\sigma$ the self-energy matrix, and $\mathbf{F}_\sigma$ is a different correlation function matrix, with elements which may be easily determined from the model Hamiltonian using equation of motion methods [2, 117]:

$$[\mathbf{F}_\sigma]_{ij} = \langle\langle [c_{i\sigma}^\dagger, \hat{H}_I], c_{j\sigma}\rangle\rangle, \tag{3.59}$$

where $c^{\dagger}_{i\sigma}$ ($c_{i\sigma}$) is the creation (destruction) operator for dot i (for the Anderson model $c^{\dagger}_{1\sigma} \equiv c^{\dagger}_{d\sigma}$) and $\hat{H}_I$ is the interacting part of the model Hamiltonian ($\hat{H}_I = Uc^{\dagger}_{d\uparrow}c_{d\uparrow}c^{\dagger}_{d\downarrow}c_{d\downarrow}$ for the single impurity Anderson model). In the case of the single impurity Anderson model $\mathbf{F}_\sigma$ contains only a single element, $F_\sigma = U\langle\langle c_{d\sigma}c^{\dagger}_{d\bar{\sigma}}c_{d\bar{\sigma}}, c^{\dagger}_{d\sigma}\rangle\rangle_\omega$, whilst the elements of $\mathbf{F}_\sigma$ for the triple quantum dot systems studied in this thesis are given in Appendix A. The $\mathbf{\Sigma}_\sigma$ matrix may then be used to recalculate the Green functions;

$$\mathbf{G}_\sigma(z) = [\mathbf{G}^{-1}_{0\sigma}(z) - \mathbf{\Sigma}_\sigma(z)]^{-1}, \tag{3.60}$$

where $\mathbf{G}_{0\sigma}$ is the non-interacting Green function matrix. As Eq. 3.58 involves the *multiplication* rather than the *addition* of two quantities, the error in the calculation of $\mathbf{G}_\sigma$ arising from the broadening process described above is reduced, and so the oscillations in the spectral functions which are an inevitable result of the broadening are much smaller [116] (the oscillations in $\mathbf{G}_\sigma$ and $\mathbf{F}_\sigma$ cancel). However, just as for the FDM-NRG, this improved accuracy comes at a cost — all of the functions in the $\mathbf{G}_\sigma$ and $\mathbf{F}_\sigma$ matrices must be calculated, increasing the computational requirements of the NRG calculation. There is another technique, the so-called interleaved NRG or z-trick of Oliveira and Oliveira [118], which may also be used to reduce the oscillations in the spectra. This technique involves introducing a new parameter, z ($0 \leqslant z \leqslant 1$), which changes the location of the discretisation in the conduction band for a fixed Λ, such that it occurs at Λ^{-n+z}. Averaging over several values of z has been shown to reduce the oscillations within NRG results, and to improve the resolution of the Hubbard satellites in the spectra (discussed below). In this thesis we do not examine the behaviour of Hubbard satellites in any great depth, and typically find that any oscillations in the spectra are removed by use of the directly calculated electron self-energy, and as a result we do not typically use the z-trick in this work.

3.7 NRG Results For The Single Anderson Impurity Model

Having explained how one goes about performing an NRG calculation, static and dynamic results for the simplest general model of a quantum dot — the single Anderson impurity model [6], given by Eq. 2.1 — are now discussed. In addition to providing an illustration of the results of the NRG when applied to a simple quantum dot system, the results presented here are a useful basis for comparison with the more complex coupled quantum dot systems studied in this thesis. Performing a Schrieffer-Wolff transformation [13] (see Section 2.1) upon this Hamiltonian in the region where the dot is singly occupied (i.e. $\epsilon < \epsilon_F < U+\epsilon$) gives an isotropic Kondo model with $J_{\mathrm{K}} > 0$. Poor Man's Scaling results (see Section 2.2) suggest that this low energy effective model has only a single stable fixed point — the strong coupling fixed point — but this lies outside the region where the perturbative analysis of Poor Man's Scaling is valid. The strong coupling fixed point is, however, accessible to the NRG. Results are shown for the simplest case of the Anderson model — the particle-hole symmetric point ($\epsilon = -U/2$), where the potential scattering term in the Schrieffer-Wolff transformation vanishes (see Eq. 2.8) — in the region $\epsilon < \epsilon_F < U+\epsilon$. This corresponds to the model studied in Ref. [7]; Ref. [8] discusses the more general case where $\epsilon \neq -U/2$.

Figure 3.4 shows the impurity contribution to the entropy (S_{imp}) for a single impurity Anderson model with various different values of $\tilde{U} = U/\pi\Gamma$ (we typically quote parameters, temperatures and frequencies in units of $\pi\Gamma$). Figure 3.5 shows $T\chi_{\mathrm{imp}}$ for a single impurity Anderson model with the same parameters. S_{imp} is initially $\ln 4$, characteristic of the so-called free orbital fixed point [7, 8]. $T\chi_{\mathrm{imp}} \approx \frac{1}{8}$ in the same region, again characteristic of the free orbital fixed point. This fixed point corresponds to a region where all four states of the dot are accessible ($|-\rangle$, $|\uparrow\rangle$, $|\downarrow\rangle$ and $|\uparrow\downarrow\rangle$). As the temperature is reduced, the empty and doubly occupied

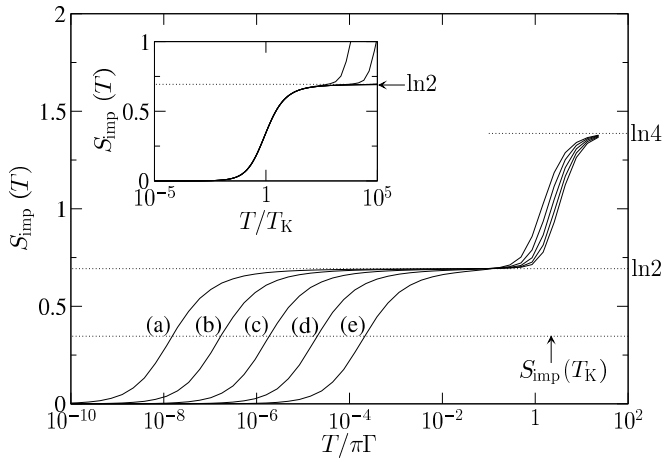


Figure 3.4: The entropy, $S_{\rm imp}$, vs $T/\pi\Gamma$ for a single impurity Anderson model with $\Gamma = 10^{-2}D$, varying $\tilde{U} = U/\pi\Gamma$; (a): $\tilde{U} = 14$, (b): $\tilde{U} = 12$, (c): $\tilde{U} = 10$, (d): $\tilde{U} = 8$, (e): $\tilde{U} = 6$. The inset shows the same data, scaled by the Kondo temperature, $T_{\rm K}$, defined via $S_{\rm imp}(T_{\rm K}) = 0.5\ln 2$.

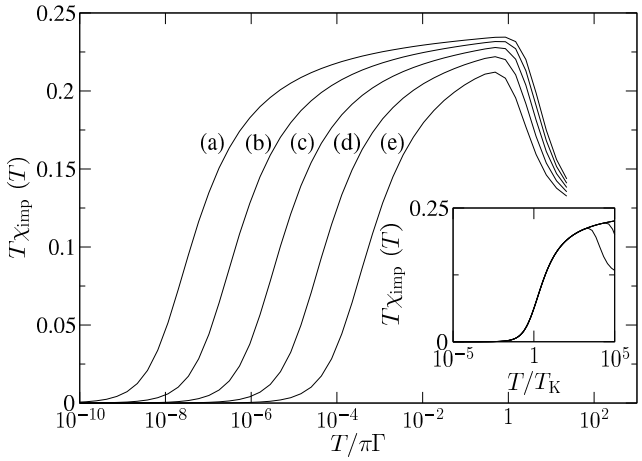


Figure 3.5: $T\chi_{\rm imp}$ for a single impurity Anderson model with $\Gamma = 10^{-2}D$, varying $\tilde{U} = U/\pi\Gamma$; (a): $\tilde{U} = 14$, (b): $\tilde{U} = 12$, (c): $\tilde{U} = 10$, (d): $\tilde{U} = 8$, (e): $\tilde{U} = 6$. The inset shows the same data, scaled by the Kondo temperature, $T_{\rm K}$, defined via $S_{\rm imp}(T_{\rm K}) = 0.5\ln 2$.

states of the dot are projected out (on an energy scale $T \sim U$), and the system flows to the so-called local moment fixed point [7, 8], characterised by $S_{\rm imp} = \ln 2$ and $T\chi_{\rm imp} \approx \frac{1}{4}$. This fixed point corresponds to a free spin-$\frac{1}{2}$. It is below this temperature, when the empty and doubly occupied states of the dot are thermally inaccessible, that the Schrieffer-Wolff transformation is valid, and the low energy effective model derived in Section 2.1 may be used.

When the temperature is reduced further, the system flows away from the local

moment fixed point on an exponentially small energy scale which, for reasons that will shortly become apparent, is labelled $T_{\rm K}$. Below this temperature the system flows to the strong coupling fixed point [7, 8], which is characterised by an entropy and magnetic susceptibility of zero. This corresponds to a quenching of the spin on the quantum dot by coupling to the 0-orbital of the Wilson chain [7,8], and is exactly equivalent to the strong coupling fixed point derived from Poor Man's Scaling (see Section 2.2). It is a very general result that two systems with the same $T_{\rm K}$ will exhibit identical low temperature behaviour [2,4], thus making the Kondo temperature, $T_{\rm K}$, equivalent to the scaling invariant in Poor Man's Scaling (also labelled $T_{\rm K}$). In addition, it is found that in systems with *different* Kondo temperatures, scaling the temperature by $T_{\rm K}$ causes both the entropy and susceptibility curves to collapse onto a *universal* form [4], as shown in the insets to Figures 3.4 and 3.5. To describe the low temperature behaviour of any single impurity Anderson model, one therefore needs only a knowledge of $T_{\rm K}$ and this universal form.

Using the formal description of fixed points introduced in Sec. 3.4 the particle-hole symmetric Anderson model here may be said to have three fixed points [7]. There are two unstable fixed points — the free orbital fixed point and the local moment fixed point (although the latter is the stable fixed point along the line $\Gamma = 0$) — and a single stable fixed point — the strong coupling fixed point — to which the system will ultimately flow at low temperature for all parameters (except $\Gamma = 0$). Away from particle-hole symmetry ($\epsilon \neq -U/2$) the Anderson model has two additional fixed points — the so-called frozen impurity fixed point (shown to be continuously connected to the strong coupling fixed point [8]) and the so-called valence fluctuation fixed point [8].

Moving on to consider dynamic properties of the system, Figure 3.6 shows the single particle spectrum for a single impurity Anderson model with the same parameters as Figures 3.4 and 3.5, calculated with both the full density matrix and the direct calculation of the electron self energy refinements of the basic NRG pro-

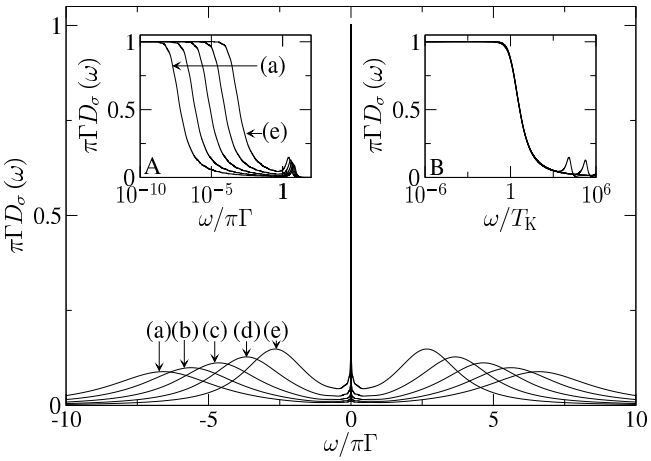


Figure 3.6: The zero-temperature single particle spectrum, $\pi\Gamma D_\sigma(\omega)$, for a single impurity Anderson model with $\Gamma = 10^{-2}D$, varying $\tilde{U} = U/\pi\Gamma$; (a): $\tilde{U} = 14$, (b): $\tilde{U} = 12$, (c): $\tilde{U} = 10$, (d): $\tilde{U} = 8$, (e): $\tilde{U} = 6$ on a linear frequency scale. Inset A shows the same data on a logarithmic scale, whilst inset B shows the data scaled by the Kondo temperature, T_K, defined via $S_{\rm imp}(T_K) = 0.5 \ln 2$.

cedure. The spectrum has the characteristic three peak structure expected for an Anderson impurity model [113]; the two peaks at $\omega \approx \pm U/2$ are known as Hubbard satellites and correspond to atomic limit processes where an electron is added or removed from the dot. The third peak is the so-called Kondo resonance [119], and is by far the most interesting feature in the single particle spectrum. As we can see from inset A to the figure, the frequency at which the Kondo resonance occurs is exponentially small, and varies with U. Inset B shows that the Kondo resonance, like the low temperature behaviour of $S_{\rm imp}$ and $T\chi_{\rm imp}$, scales with T_K. The zero-temperature, zero-frequency value of the single particle spectrum may be related to $n_{{\rm imp},\sigma}|_{T=0}$ using the Friedel Sum Rule [2, 22]

$$\pi\Gamma D_\sigma(T = 0, h, \omega = 0) = \sin^2\left[\pi n_{{\rm imp},\sigma}|_{T=0}\right]. \tag{3.61}$$

Eq. 3.61 is *not* general, but rather specific to the single impurity Anderson model, but we derive an equivalent relationship for our triple quantum dot model in Appendix C. The Luttinger integral, $I_L = {\rm Im\,Tr}\int_{-\infty}^{0} d\omega \frac{\partial\Sigma_\sigma}{\partial\omega} G_\sigma$, is generically found to be zero for the Anderson model, as one would expect, give that the strong coupling

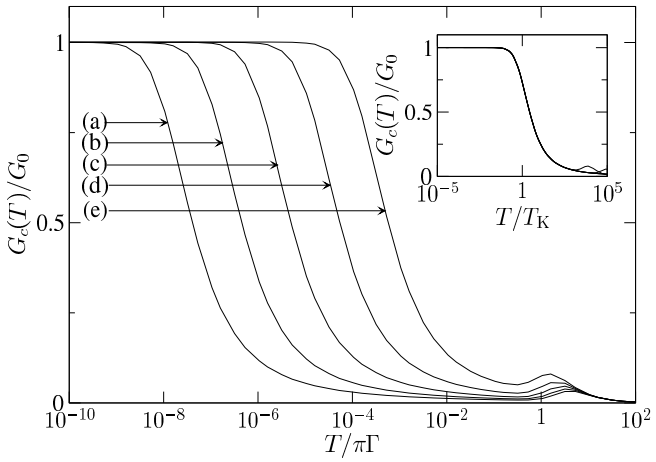


Figure 3.7: The zero-bias conductance, $G_c(T)/G_0$, for a single impurity Anderson model with $\Gamma = 10^{-2}D$, varying $\tilde{U} = U/\pi\Gamma$; (a): $\tilde{U} = 14$, (b): $\tilde{U} = 12$, (c): $\tilde{U} = 10$, (d): $\tilde{U} = 8$, (e): $\tilde{U} = 6$. The inset shows the same data scaled by the Kondo temperature, T_K, defined via $S_{imp}(T_K) = 0.5 \ln 2$.

fixed point is a Fermi liquid [120].

Using Eq. 3.41 the conductance of the single impurity Anderson model at a temperature T may be calculated from the single particle spectrum calculated at the same temperature. Figure 3.7 shows the conductance so calculated, given in units of twice the conductance quantum, $2e^2/h$, which is the maximum value that the conductance through a single channel quantum dot system can take [107]. Hubbard satellites may be identified in the conductance, and it is also clear that upon passing through T_K there is a dramatic enhancement of the conductance, which rises to the unitarity limit. The inset to this figure shows that the the Kondo temperature is a universal scale for the conductance as well as for the single particle spectrum and the various thermodynamic properties of the system.

3.8 Magnetic Fields and the Single Impurity Anderson Model

The NRG has been successfully extended to investigate quantum impurity systems under an applied magnetic field [121–124]. As the effect of a magnetic field upon a

triple quantum dot device is investigated in this thesis, a brief overview of the static and dynamic properties of a single impurity Anderson model under an applied field, as calculated by the NRG, is provided here. In order to study the Anderson model in a magnetic field, the term $\hat{H}_\epsilon = \sum_\sigma \epsilon c^\dagger_{d\sigma} c_{d\sigma}$ in the Anderson Hamiltonian, Eq. 2.1, is replaced with

$$\hat{H}_{\epsilon h} = \sum_\sigma (\epsilon - \sigma h) c^\dagger_{d\sigma} c_{d\sigma}, \tag{3.62}$$

where $\sigma = \uparrow / \downarrow = \pm$ and $h = \frac{1}{2} g \mu_B B$ such that $2h$ is the Zeeman splitting (we refer to h as 'the field'). The introduction of this term obviously lifts the degeneracy of the singly occupied states of the isolated level, and therefore introduces a term $\hat{H}_{Sz} = -2h\hat{S}_z$ into the Kondo model which arises as a result of the Schrieffer-Wolff transformation of the Anderson Hamiltonian. It is conventional within the NRG to assume that the conduction band is unaffected by an applied field [123], an assumption which is entirely valid as long as the applied field is appreciably smaller than the bandwidth, and one which we make throughout this thesis. It is also important to note that it has been shown [122] that the density matrix implementation of the NRG must be used to calculate dynamic properties when a magnetic field is present, as the earlier method for calculating spectral functions incorrectly identifies the ground state at early iterations, and thus can produce results which are quantitatively incorrect.

We assume $h > 0$ throughout, such that as h increases the states of the dot with $S^z > 0$ are stabilised, and those with $S^z < 0$ are destabilised: obviously, a choice of $h < 0$ would have the opposite effect.

Magnetic fields appreciably smaller than the Kondo temperature are found to have no discernible effect upon the physical properties of the system [123], as the impurity is 'singlet locked' (with T_K the energy required to unquench the impurity spin): increasing the magnetic field through T_K suppresses the Kondo effect, and unquenches the singlet, causing the zero-temperature magnetisation, $m = n_{\mathrm{imp},\uparrow}|_{T=0} - n_{\mathrm{imp},\downarrow}|_{T=0}$ to increase from the zero-field value of 0 towards 1 [123]

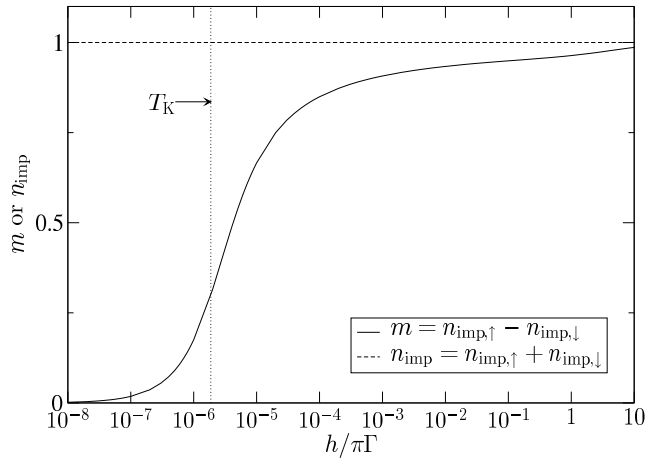


Figure 3.8: The zero temperature magnetisation, $m = n_{\mathrm{imp},\uparrow}|_{T=0} - n_{\mathrm{imp},\downarrow}|_{T=0}$ and dot population, $n_{\mathrm{imp}} = n_{\mathrm{imp},\uparrow}|_{T=0} + n_{\mathrm{imp},\downarrow}|_{T=0}$ for a single impurity Anderson model with $\tilde{U} = 10$ and $\Gamma = 10^{-2}D$.

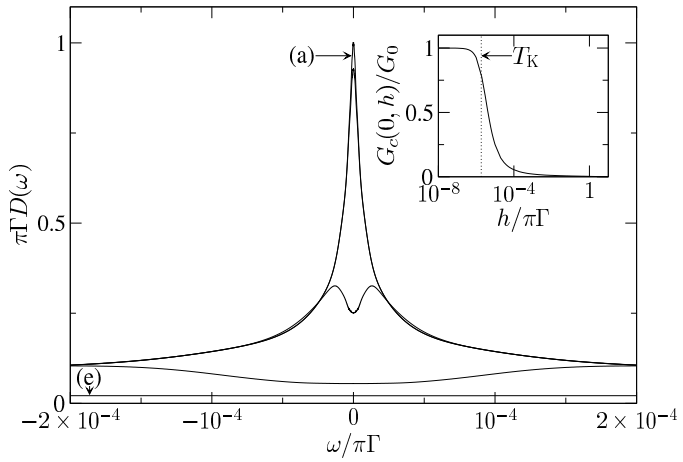


Figure 3.9: The zero-temperature total spectral density, $\pi\Gamma D(\omega) = \frac{1}{2}\pi\Gamma(D_\uparrow(\omega) + D_\downarrow(\omega))$, for a single impurity Anderson model with $\tilde{U} = 10$ and $\Gamma = 10^{-2}D$ for various different field strengths: $\tilde{h} = h/\pi\Gamma = 10^{-7}$ for (a), 10^{-6} for (b), 10^{-5} for (c), 10^{-4} for (d) and 10^{-3} for (e) ($T_K/\pi\Gamma = 1.87 \times 10^{-6}$). The inset shows the zero-temperature conductance, $G_c(0,h)/G_0$, as a function of $h/\pi\Gamma$ for the same system.

(i.e. when $h \gg T_K$ the ground state of the dot is to all intents and purposes the $|\uparrow\rangle$ state, within the singly occupied manifold). This behaviour is shown in Fig. 3.8.

Under an applied field, the spectra $D_\uparrow(\omega)$ and $D_\downarrow(\omega)$ are no longer coincident and so it is typical to discuss the 'total spectral density' — $D(\omega) = \frac{1}{2}(D_\uparrow(\omega) + D_\downarrow(\omega))$ — instead. Suppression of the Kondo effect by an applied field naturally causes the Kondo resonance to vanish from the spectral density. This is a gradual process,

whereby the Kondo resonance is found to first decrease in magnitude, and then ultimately to 'split' into two resonances [123], equidistant from the line $\omega = 0$, as the applied field is increased through T_{K}, before ultimately merging with the Hubbard satellites. This behaviour is shown in Fig. 3.9. Suppression of the Kondo resonance also leads to a dramatic decrease in the zero-temperature conductance through the quantum dot device when the magnetic field is increased through T_{K}, as is shown in the inset to Fig. 3.9.

Chapter 4

The Apex Coupled Trimer Model

Part I: Mirror Symmetry

We now turn our attention to the coupled quantum dot systems which form the main focus of this work: a system of three mutually tunnel-coupled quantum dots, connected to a single conduction channel. The effects of frustration upon the physics of this system are studied, using both analytic methods and the NRG. The first model investigated is shown schematically in Fig. 4.1. It consists of three dots, numbered 1–3, arranged in such a way that only a single dot (dot 2) is tunnel-coupled to the conduction band and so that a plane of mirror symmetry passes through dot 2. We christen this 'the apex coupled trimer model' (ACTM), and

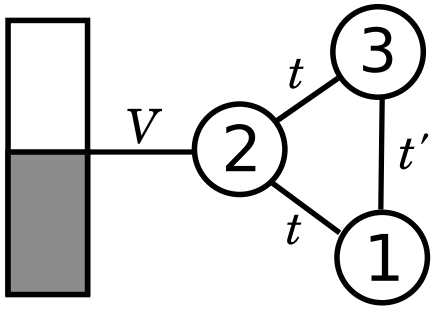


Figure 4.1: A schematic representation of the apex coupled trimer model. The quantum dots (labelled '1', '2' and '3') are linked by tunnel-couplings t and t', with a further tunnel-coupling, V, linking dot 2 to the conduction band.

it is the simplest model studied in this thesis. In subsequent chapters the effects of breaking mirror symmetry upon the triple quantum dot (TQD) device in this geometry (Chapter 5), as well as the effects of coupling the device to conduction bands in parallel (Chapter 6) are investigated. Whilst these models all exhibit different physics, there is, as we shall see, an essential underlying similarity between them: studying the physics of the simpler models will therefore help us to understand the more complex ones discussed later. Some of the results presented in this chapter have been published in Ref. [90].

4.1 The Apex Coupled Trimer Hamiltonian

The apex coupled trimer model is described by the Hamiltonian $\hat{H}_{ACTM} = \hat{H}_L + \hat{H}_{hyb} + \hat{H}_{TQD}$ where $\hat{H}_L = \sum_{\mathbf{k},\sigma} \epsilon_{\mathbf{k}} c^\dagger_{\mathbf{k}\sigma} c_{\mathbf{k}\sigma}$ refers to the non-interacting lead, which couples to dot 2 via $\hat{H}_{hyb} = \sum_{\mathbf{k},\sigma} V(c^\dagger_{2\sigma} c_{\mathbf{k}\sigma} + H.c.)$, with $\hat{H}_{TQD}$, the Hamiltonian for the isolated TQD device, given by

$$\begin{aligned}\hat{H}_{TQD} =& \sum_\sigma (\epsilon - \sigma h)(\hat{n}_{1\sigma} + \hat{n}_{3\sigma}) + \sum_\sigma (\epsilon_2 - \sigma h)\hat{n}_{2\sigma} + \sum_{i=1,2,3} U\hat{n}_{i\uparrow}\hat{n}_{i\downarrow} \\ &+ \sum_\sigma t[(c^\dagger_{1\sigma} + c^\dagger_{3\sigma})c_{2\sigma} + H.c] + \sum_\sigma t'(c^\dagger_{1\sigma} c_{3\sigma} + H.c.)\end{aligned} \tag{4.1}$$

where $c^\dagger_{i\sigma}$ ($c_{i\sigma}$) is the creation (destruction) operator for an electron with spin σ ($=\uparrow$ / $\downarrow$) in dot i, $\hat{n}_{i\sigma} = c^\dagger_{i\sigma} c_{i\sigma}$ the number operator for electrons with spin σ in dot i and $c^\dagger_{\mathbf{k}\sigma}$ ($c_{\mathbf{k}\sigma}$) is the creation (destruction) operator for an electron with spin σ and momentum $\mathbf{k}$ in the conduction band. $H.c.$ denotes a Hermitian conjugate. t, t' and V are hopping parameters, ϵ is the level energy of dots 1 and 3, ϵ_2 is the level energy for dot 2[1] and U is the on-site Coulomb repulsion term. $h = \frac{1}{2} g\mu_B B$ is the magnetic field applied to the dots, where $2h = g\mu_B B$ is the Zeeman splitting. The non-interacting lead is taken to be a wide, flat band of width $2D$, with density

[1]To preserve the mirror symmetry of the system it is only necessary that ϵ for dots 1 and 3 be the same. We have chosen to set ϵ for all three dots to the same value in the results presented here, as we find the results in this case to be entirely representative.

of states per conduction orbital $\rho = 1/(2D)$. D is naturally taken to be the largest energy scale in the problem and we set $D/\Gamma = 100$ (except where otherwise noted) with $\Gamma = \pi\rho NV^2$ the hybridization strength (N is the number of orbitals/$\mathbf{k}$-states in the lead, such that NV^2 is finite in the continuum limit $N \to \infty$). The underlying set of bare model parameters can then be taken as

$$\tilde{U} = \frac{U}{\pi\Gamma}, \quad \tilde{\epsilon} = \frac{\epsilon}{\pi\Gamma}, \quad \tilde{\epsilon}_2 = \frac{\epsilon_2}{\pi\Gamma}, \quad \tilde{t} = \frac{t}{\pi\Gamma}, \quad \tilde{t}' = \frac{t'}{\pi\Gamma}, \tag{4.2}$$

together with $\tilde{h} = h/\pi\Gamma$ for the applied field (the effects of which are considered in Sec. 4.10, 4.11 and 4.12 up to which point $h = 0$ is implicit). In all the systems studied in this chapter we consider the representative case $\epsilon = \epsilon_2 = -U/2$, and therefore specifying $\tilde{U}$, $\tilde{t}$, $\tilde{t}'$ and $\tilde{h}$ is sufficient to identify the system. The NRG discretisation parameter is set to $\Lambda = 3$ throughout, and (except where otherwise noted) a maximum of $N_s = 2000$ states are kept in each iteration.

4.2 Parity and Other Symmetries

A parity operator, $\hat{P}_{1,3}$, which interchanges the labels on dots 1 and 3, may be defined. As shown in Appendix B such an operator is both self-adjoint and involutary ($\hat{P}_{1,3}^2 = 1$), and has eigenvalues ± 1. In addition, we may easily show that $[\hat{H}_{ACTM}, \hat{P}_{1,3}] = 0$, and as such that the model Hamiltonian here conserves parity (as is immediately obvious from the effect of interchanging the labels on dots 1 and 3 in Eq. 4.1). It is also the case that $\hat{P}_{1,3}$ commutes with $\hat{Q}$, $\hat{S}$ and $\hat{S}_z$ — the charge, spin and spin z-component operators, respectively. As a result all the states of $\hat{H}_{ACTM}$ may be classified by their behaviour under $\hat{P}_{1,3}$ as having either odd ('$(-)$'; $\langle\psi|\hat{P}_{1,3}|\psi\rangle = -1$) or even ('$(+)$'; $\langle\psi|\hat{P}_{1,3}|\psi\rangle = +1$) parity.

We also note here that $\hat{H}_{ACTM}$ is, in general, *not* particle-hole symmetric (even when $\epsilon = \epsilon_2 = -\frac{U}{2}$) — that is, it is not possible to define a transformation which changes $c_{i\sigma}^\dagger \to \pm c_{i\sigma}$ (and *vice-versa*) but leaves the Hamiltonian unchanged, al-

though in the limits $t = 0$ or $t' = 0$ it is possible to define a particle-hole transformation for $\hat{H}_{ACTM}$, such that the Hamiltonian is particle-hole symmetric.

4.3 Effective Spin Model

A Schrieffer-Wolff transformation [13] may be used to derive an effective low temperature spin model from Eq. 4.1, which is valid in the limit where all three dots are singly occupied at low temperature (t,t' and $V \ll U$). We split $\hat{H}_{ACTM}$ such that

$$\hat{H}_{ACTM} = \hat{H}_0 + \hat{H}_1, \tag{4.3a}$$

$$\hat{H}_0 = \sum_{i,\sigma} \epsilon \hat{n}_{i\sigma} + \sum_i U \hat{n}_{i\uparrow}\hat{n}_{i\downarrow} + \sum_{\mathbf{k},\sigma} \epsilon_{\mathbf{k}} c^\dagger_{\mathbf{k}\sigma} c_{\mathbf{k}\sigma}, \tag{4.3b}$$

$$\hat{H}_1 = \sum_\sigma t[(c^\dagger_{1\sigma} + c^\dagger_{3\sigma})c_{2\sigma} + H.c] + \sum_\sigma t'(c^\dagger_{1\sigma}c_{3\sigma} + H.c.) + \sum_{\mathbf{k},\sigma} V(c^\dagger_{2\sigma}c_{\mathbf{k}\sigma} + H.c.), \tag{4.3c}$$

and then use Brillouin-Wigner perturbation theory [93] to second order in $\hat{H}_1$, evaluating $\hat{H}_{eff} = \hat{1}[\hat{H}_0 + \hat{H}_1 + \hat{H}_1(E_0 - \hat{H}_0)^{-1}\hat{P}\hat{H}_1]\hat{1}$, where $\hat{1}$ is a unity operator spanning the reduced Hilbert space of the system comprising those states of the trimer where all three dots are singly occupied, and E_0 is the energy of the ground state of the system under $\hat{H}_0$. $\hat{P} = \hat{1}_{full} - \hat{1}$, where $\hat{1}_{full}$ is the unity operator for the complete Hilbert space. After lengthy rearrangement, this gives an effective spin model,

$$\begin{aligned}\hat{H}_{spin} =& J(\hat{\mathbf{S}}_1 + \hat{\mathbf{S}}_3)\cdot\hat{\mathbf{S}}_2 + J'\hat{\mathbf{S}}_1\cdot\hat{\mathbf{S}}_3 + J_{\mathrm{K}}\hat{\mathbf{S}}_2\cdot\hat{\mathbf{S}}(0) \\ &+ \hat{H}_L + K\sum_\sigma f^\dagger_{0\sigma}f_{0\sigma},\end{aligned} \tag{4.4}$$

where $\hat{\mathbf{S}}_i$ is a spin-$\frac{1}{2}$ operator for dot i, and $\hat{\mathbf{S}}(0)$ is the spin density of the conduction band at dot 2, as given in Eq. 2.10. $f^\dagger_{0\sigma}$ ($f_{0\sigma}$) is the creation (destruction) operator for the 0-orbital of the Wilson chain (as given by Eq. 2.11). Retardation effects are neglected here. J, J' and J_{K} are Heisenberg exchange couplings, whilst the final

term in $\hat{H}_{spin}$ represents potential scattering:

$$J = 2t^2 \left(\frac{1}{U + \epsilon - \epsilon_2} + \frac{1}{U + \epsilon_2 - \epsilon} \right), \tag{4.5a}$$

$$J' = \frac{4t'^2}{U}, \tag{4.5b}$$

$$J_{\mathrm{K}} = 2NV^2 \left(\frac{1}{U + \epsilon_2} - \frac{1}{\epsilon_2} \right), \tag{4.5c}$$

$$K = -\frac{NV^2}{2} \left(\frac{1}{\epsilon_2 + U} + \frac{1}{\epsilon_2} \right). \tag{4.5d}$$

It immediately follows that in the limit $\epsilon = \epsilon_2 = -U/2$ (covering all the systems studied in this chapter) the potential scattering term in Eq. 4.4 vanishes. As noted above, the full $\hat{H}_{ACTM}$ is not particle-hole symmetric. However Eq. 4.4 *is* particle-hole symmetric when $\epsilon = \epsilon_2 = -U/2$.

4.4 Conductance and the Friedel-Luttinger Sum Rule

As discussed in Sec. 3.6, the Meir-Wingreen formula (Eq. 3.41) may be used to calculate the zero-bias conductance from the single particle spectrum of the system. In this case $\mathbf{\Gamma}^I$ is a 3×3 matrix, with a single non-zero element, $[\mathbf{\Gamma}^I]_{22} = \Gamma$, and so the relevant form of the Meir-Wingreen formula here is

$$\frac{G_c(T,h)}{G_0} = \int_{-\infty}^{\infty} -\frac{\partial f(\omega)}{\partial \omega} \frac{1}{2} \sum_{\sigma} \pi \Gamma D_{2\sigma}(\omega, T, h) d\omega \tag{4.6}$$

where $G_c(T,h)/G_0$ is the zero-bias conductance through the TQD device, $f(\omega) = [e^{\omega/T} + 1]^{-1}$ the Fermi function (we set $k_B = 1$) and $D_{2\sigma}(\omega)$ the single particle spectrum of dot 2, measured at frequency ω, temperature T and magnetic field h ($\omega = 0$ corresponds to the Fermi level).

In addition, as discussed in Appendix C and Sec. 3.7, a Friedel-Luttinger sum

rule, valid at zero temperature, may be derived for this model,

$$G_c(0,h) = G_0 \tfrac{1}{2} \sum_\sigma \pi\Gamma D_{2\sigma}(\omega=0, T=0, h) \tag{4.7a}$$

$$= G_0 \tfrac{1}{2} \sum_\sigma \sin^2(\delta_\sigma) \tag{4.7b}$$

where $G_c(0,h)$ is the zero-temperature zero-bias conductance through the TQD device, $D_{2\sigma}(\omega=0)$ the zero-frequency (Fermi level) value of the single particle spectrum of dot 2 and δ_σ the static scattering phase shift, given by $\delta_\sigma = \pi n_{\mathrm{imp},\sigma}|_{T=0} + I_{\mathrm{L}}$, with $I_{\mathrm{L}} = \mathrm{Im\,Tr} \int_{-\infty}^{0} d\omega \frac{\partial \mathbf{\Sigma}_\sigma}{\partial \omega} \mathbf{G}_\sigma$ the Luttinger Integral [2,125]. $n_{\mathrm{imp},\sigma}|_{T=0}$ is the zero-temperature value of $n_{\mathrm{imp},\sigma}(T) = \langle \hat{Q} \rangle_{\mathrm{imp}}(T) + \sigma \langle \hat{S}_z \rangle_{\mathrm{imp}}(T)$, effectively indistinguishable from the electronic population of the TQD. As I_{L} is found to be constant within a given phase (see below), we may use Eq. 4.7b to directly relate $n_{\mathrm{imp},\sigma}|_{T=0}$ to the conductance — the dynamic property of the system which is most readily accessible experimentally [5,37].

4.5 The Phase Diagram

Fig. 4.2 shows a phase diagram for the ACTM. We find that in this model there are two stable fixed points — the strong coupling fixed point (SC FP), characterised by $S_{\mathrm{imp}}(T=0) = 0$ and $T\chi_{\mathrm{imp}}|_{T=0} = 0$, and the local moment fixed point (LM FP), characterised by $S_{\mathrm{imp}}(T=0) = \ln 2$ and $T\chi_{\mathrm{imp}}|_{T=0} = 1/4$. These two phases are separated by a line of first order phase transitions. Along this line the system flows to a transition fixed point (TFP) characterised by $S_{\mathrm{imp}}(T=0) = \ln 3$ and $T\chi_{\mathrm{imp}}|_{T=0} = 1/6$ (this is discussed further in Sec. 4.6.2, 4.7.2 and 4.8.2).

The position of the quantum phase transition may be determined using the NRG: fixing $\tilde{U}$ and $\tilde{t}$, we perform NRG calculations for various values of $\tilde{t}'$. We can quickly determine whether a given value of $\tilde{t}'$ gives rise to a system with a strong coupling or local moment ground state. Once we have a value of $\tilde{t}'$ which gives a local moment ground state, and a second value of $\tilde{t}'$ which gives a strong coupling ground state, the

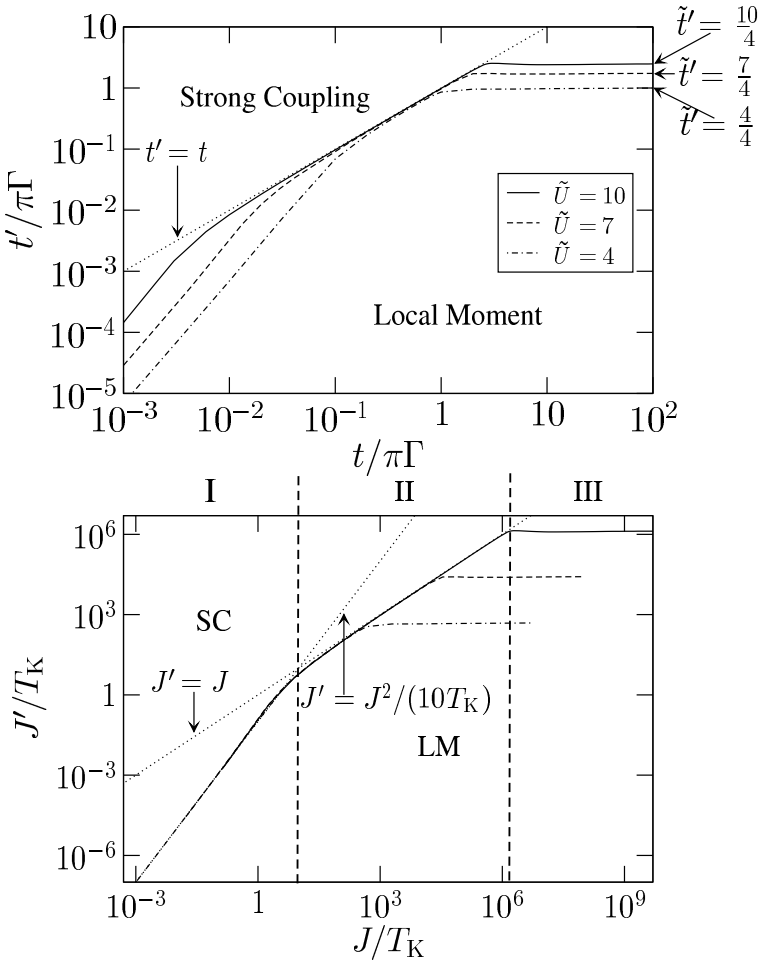


Figure 4.2: The phase diagram for the apex coupled trimer model, for various values of $\tilde{U}$. The top panel shows the phase diagram with axes plotting $\tilde{t}$ against $\tilde{t}'$. The bottom panel shows the same data, but with the axes rescaled as J/T_K and J'/T_K, respectively. The bottom panel also indicates the division of the phase diagram into regimes I, II and III for $\tilde{U} = 10$ (solid black line). The definition of T_K used here is discussed in the main text.

position of the transition can be determined by bisection — as the phase boundary must lie between the highest value of $\tilde{t}'$ we know is within the local moment phase and the smallest value of $\tilde{t}'$ we know is within the strong coupling phase, repeatedly perform NRG calculations for values of $\tilde{t}'$ chosen to be between these two values allows us to determine the position of the phase boundary for a fixed $\tilde{U}$ and $\tilde{t}$ with (effectively) arbitrary precision. Repeating this process for various values of $\tilde{t}$ ultimately gives the lines of quantum phase transitions shown in Fig. 4.2.

It is clear that in all cases the phase boundary may be divided into three regions,

each with a different gradient. We find that in each of these regions, the underlying physics of the system is distinct. These regions are labelled (from left to right) regime I (corresponding to $J \lesssim 10T_{\rm K}$; the phase boundary here follows the line $J' = J^2/10T_{\rm K}$), regime II (corresponding to $J \gtrsim 10T_{\rm K}$ and $t \lesssim U/4$; the phase boundary here follows the line $J = J'$) and regime III (corresponding to $t \gtrsim U/4$; the phase boundary here follows the line $t' = U/4$). In the bottom panel of Fig. 4.2, both regime I and regime II collapse onto a single universal form when the axes are rescaled by $J/T_{\rm K}$ and $J'/T_{\rm K}$. This is indicative of the fact that in both regimes I and II (but *not* regime III) the low temperature behaviour of the system may be described using the effective spin model derived in Sec. 4.3 (we discuss this further in Sec. 4.6 and 4.7). The Kondo temperature, $T_{\rm K}$, is defined here for a given U and Γ via $S_{\rm imp}(T_{\rm K}) = 0.5 \ln 2$ for a single impurity Anderson model with the same U and Γ at particle-hole symmetry ($\epsilon = -\frac{U}{2}$). This is the general definition we shall use for $T_{\rm K}$ and it is chosen so that we have a single universal definition of this low temperature scale, which may be used in all the regimes (and, in later chapters, in all the models) studied[2]. We begin by discussing regime II [90], which is the simplest regime to understand.

4.6 Regime II: $J > 10T_{\rm K}$

4.6.1 Effective Low Energy Model

In regime II the spin model given by Eq. 4.4 describes the system at low temperature. However, in this regime the interdot Heisenberg couplings are relatively large ($J > T_{\rm K}$) and so we must consider initially the states of the bare trimer, described by

$$\hat{H}_{trimer} = J(\hat{\mathbf{S}}_1 + \hat{\mathbf{S}}_3) \cdot \hat{\mathbf{S}}_2 + J' \hat{\mathbf{S}}_1 \cdot \hat{\mathbf{S}}_3 + J_{\rm K} \hat{\mathbf{S}}_2 \cdot \hat{\mathbf{S}}(0), \tag{4.8}$$

[2]This somewhat cumbersome definition corresponds to the Kondo temperature of the ACTM when $t = 0$.

Index	State	Energy
$\lvert\frac{3}{2};-;+\frac{3}{2}\rangle$	$\lvert\uparrow,\uparrow,\uparrow\rangle$	$\frac{J}{2}+\frac{J'}{4}$
$\lvert\frac{3}{2};-;+\frac{1}{2}\rangle$	$\frac{1}{\sqrt{3}}(\lvert\uparrow,\uparrow,\downarrow\rangle+\lvert\uparrow,\downarrow,\uparrow\rangle+\lvert\downarrow,\uparrow,\uparrow\rangle)$	
$\lvert\frac{3}{2};-;-\frac{1}{2}\rangle$	$\frac{1}{\sqrt{3}}(\lvert\downarrow,\downarrow,\uparrow\rangle+\lvert\downarrow,\uparrow,\downarrow\rangle+\lvert\uparrow,\downarrow,\downarrow\rangle)$	
$\lvert\frac{3}{2};-;-\frac{3}{2}\rangle$	$\lvert\downarrow,\downarrow,\downarrow\rangle$	
$\lvert\frac{1}{2};+;+\frac{1}{2}\rangle$	$\frac{1}{\sqrt{2}}(\lvert\uparrow,\uparrow,\downarrow\rangle-\lvert\downarrow,\uparrow,\uparrow\rangle)$	$-\frac{3}{4}J'$
$\lvert\frac{1}{2};+;-\frac{1}{2}\rangle$	$\frac{1}{\sqrt{2}}(\lvert\uparrow,\downarrow,\downarrow\rangle-\lvert\downarrow,\downarrow,\uparrow\rangle)$	
$\lvert\frac{1}{2};-;+\frac{1}{2}\rangle$	$\frac{1}{\sqrt{6}}(\lvert\uparrow,\uparrow,\downarrow\rangle+\lvert\downarrow,\uparrow,\uparrow\rangle-2\lvert\uparrow,\downarrow,\uparrow\rangle)$	$\frac{J'}{4}-J$
$\lvert\frac{1}{2};-;-\frac{1}{2}\rangle$	$\frac{1}{\sqrt{6}}(2\lvert\downarrow,\uparrow,\downarrow\rangle-\lvert\downarrow,\downarrow,\uparrow\rangle-\lvert\uparrow,\downarrow,\downarrow\rangle)$	

Table 4.1: The eigenstates and energies of the bare trimer. Eigenstates are indexed by their quantum numbers; $|S;P;S^z\rangle$, where S is the spin, P the parity, and S^z the z-component of the spin, whilst basis states are labelled $|\sigma_1,\sigma_2,\sigma_3\rangle$, where σ_i is the spin on dot i.

corresponding to Eq. 4.4 when $\hat{H}_L$ and the term coupling the TQD to the conduction band are neglected, before using perturbation theory to determine how they couple to the conduction band. The isolated trimer has three states — a quartet and two doublets — detailed in Table 4.1. Of these states, the quartet is always the highest in energy[3], and it is therefore quickly rendered thermally inaccessible as the temperature of the system is reduced. When the quartet is inaccessible, the unity operator valid in the reduced Hilbert space of the system contains only the two doublet states, one ($|\frac{1}{2};+;S^z\rangle$) with even ($+$) parity and the other ($|\frac{1}{2};-;S^z\rangle$) with odd ($-$) parity[4]:

$$\hat{1} = \hat{1}_+ + \hat{1}_-, \tag{4.9a}$$

$$\hat{1}_+ = \sum_{S^z} |\tfrac{1}{2};+;S^z\rangle\langle\tfrac{1}{2};+;S^z|, \tag{4.9b}$$

$$\hat{1}_- = \sum_{S^z} |\tfrac{1}{2};-;S^z\rangle\langle\tfrac{1}{2};-;S^z|. \tag{4.9c}$$

In the limit $J' \gg J$ only $\hat{1}_+$ need be retained in the low energy manifold on the lowest energy scales, the odd parity doublet being thermally inaccessible. Projecting

[3] As in this model all the Heisenberg exchange couplings are antiferromagnetic.

[4] We label the states of the trimer $|S;P;S^z\rangle$, where S is the spin, S^z the z-component of the spin and P the parity of the state.

into this low energy manifold, we find

$$\hat{H}_{eff} = J_{\rm K}\hat{1}_{+}\hat{\mathbf{S}}_2\hat{1}_{+}\cdot\hat{\mathbf{S}}(0) + \hat{H}_L = J_{\rm K}\hat{\mathbf{S}}\cdot\hat{\mathbf{S}}(0) + \hat{H}_L, \tag{4.10}$$

where $\hat{\mathbf{S}}$ is a spin-$\frac{1}{2}$ operator for the whole TQD. Under these conditions the low energy effective model is merely a classic Kondo model, a spin-$\frac{1}{2}$ with an antiferromagnetic coupling to the conduction band. This model is therefore expected to flow to the strong coupling fixed point on an energy scale $T_{\rm K}$ [4, 14], which should be identical to the Kondo scale of a symmetric single impurity Anderson model with the same U and Γ. By contrast, if $J' \ll J$ only $\hat{1}_{-}$ need be retained in the low energy manifold on the lowest energy scales (as the even parity doublet is thermally inaccessible), and projecting into this low energy manifold we find

$$\hat{H}_{eff} = J_{\rm K}\hat{1}_{-}\hat{\mathbf{S}}_2\hat{1}_{-}\cdot\hat{\mathbf{S}}(0) + \hat{H}_L = -\frac{1}{3}J_{\rm K}\hat{\mathbf{S}}\cdot\hat{\mathbf{S}}(0) + \hat{H}_L, \tag{4.11}$$

is the low energy effective model. This is a most interesting result — a *ferromagnetic* Kondo effect arising solely from antiferromagnetic couplings. A system described by this model should ultimately flow to the local moment fixed point at low temperature [2, 14]. The final case we consider is when the energy separation between the two doublets is small. Under these conditions both doublets are thermally inaccessible even at the lowest temperatures, and so we must retain both states in our low energy manifold and therefore projecting into the low energy manifold we find

$$\begin{aligned}\hat{H}_{eff} =& J_{\rm K}\hat{1}\hat{\mathbf{S}}_2\hat{1}\cdot\hat{\mathbf{S}}(0) + \hat{1}\hat{H}_0\hat{1} + \hat{H}_L \\ =& \frac{J_{\rm K}}{3}(1+4\hat{\mathcal{T}}^z)\hat{\mathbf{S}}\cdot\hat{\mathbf{S}}(0) + E_{\Delta}\hat{\mathcal{T}}^z + \hat{H}_L \ : \text{Regime II},\end{aligned} \tag{4.12}$$

where

$$\hat{\mathcal{T}}^z = \frac{1}{2}(\hat{1}_{+} - \hat{1}_{-}), \tag{4.13}$$

defines a pseudospin operator, such that $\hat{\mathcal{T}}^z|\frac{1}{2};\pm;S^z\rangle = \pm\frac{1}{2}|\frac{1}{2};\pm;S^z\rangle$ and $E_{\Delta} = J -$

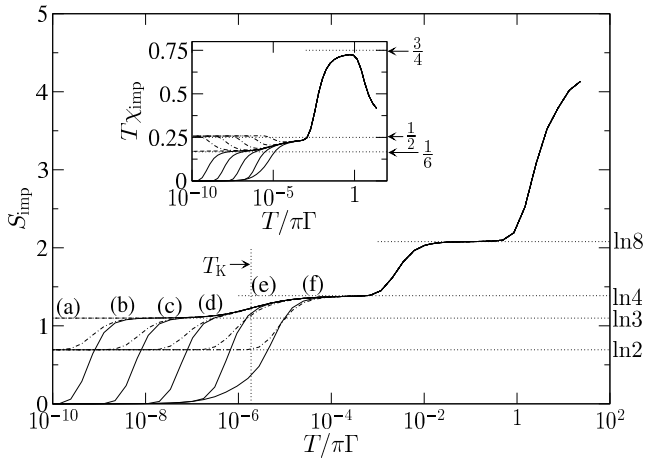


Figure 4.3: Entropy $S_{\rm imp}$ vs $T/\pi\Gamma$ for a system close to the transition in Regime II. $U/\pi\Gamma = 10$, $t/\pi\Gamma = 10^{-1}$ and $t'_c \simeq 9.71824 \times 10^{-2}$. $t'/\pi\Gamma = t'_c \pm \lambda T_{\rm K}$, where $\lambda = 0$ for (a), 10^{-2} for (b), 10^{-1} for (c), 1 for (d), 10 for (e) and 10^2 for (f). The inset shows $T\chi_{\rm imp}$ for the same system.

J' is the energy separation between the two doublets, the constant term $\frac{1}{2}(E_+ + E_-)\hat{1}$ in the equation being neglected. As $[\hat{H}_{spin}, \hat{P}_{1,3}] = 0$, we find that $\hat{1}_\pm \hat{\mathbf{S}}_2 \hat{1}_\mp = 0$: the Hamiltonian here does not mix states with distinct parities. Eq. 4.12 predicts that the system will be described by a classic Kondo model when $E_\Delta < 0$, ultimately flowing to a strong coupling fixed point at zero temperature, and by a ferromagnetic Kondo model when $E_\Delta > 0$, ultimately flowing to a local moment fixed point at zero temperature; E_Δ acts as an effective magnetic field upon the system. This model is therefore predicted to undergo a quantum phase transition when $E_\Delta = 0$, corresponding to the line $J = J'$, which is in agreement with the results shown in Fig. 4.2.

4.6.2 Thermodynamics

We now consider the thermodynamic properties of systems in regime II. Fig. 4.3 shows $S_{\rm imp}$ for systems on either side of the phase transition. The inset shows $T\chi_{\rm imp}$ for the same systems. At high temperatures ($T \sim U$) $S_{\rm imp} = \ln 64 = \ln 4^3$ ($T\chi_{\rm imp} = \frac{3}{8}$), characteristic of the free orbital fixed point [7, 8] when one has three dots. Upon reducing the temperature the empty and doubly occupied states of

each dot are projected out, and $S_{\rm imp}$ falls to $\ln 8$ ($T\chi_{\rm imp} = \frac{3}{4}$) — characteristic of three free spins (this is the energy scale where the spin model, Eq. 4.4, becomes a valid description of the system). Reducing the temperature further projects out the quartet state on an energy scale $T \sim J$, leaving only the two doublets accessible ($S_{\rm imp} = \ln 4$ and $T\chi_{\rm imp} = \frac{1}{2}$). When $J > J'$ (and $|E_\Delta| > T_{\rm K}$), upon further reducing the temperature (such that $T < |E_\Delta|$) the even parity doublet is rendered thermally inaccessible, and so the system flows directly to the local moment fixed point — characterised by $S_{\rm imp} = \ln 2$ ($T\chi_{\rm imp} = \frac{1}{4}$) — which is the ultimate low temperature fixed point of the system in this regime (Eq. 4.11). If, on the other hand, $J' > J$ (and $|E_\Delta| > T_{\rm K}$), upon reducing the temperature such that $|E_\Delta| > T > T_{\rm K}$ the odd parity doublet becomes thermally inaccessible and the system flows close to the local moment fixed point ($S_{\rm imp} = \ln 2$ and $T\chi_{\rm imp} = \frac{1}{4}$) until $T < T_{\rm K}$, at which point the system flows to the strong coupling fixed point ($S_{\rm imp} = 0$ and $T\chi_{\rm imp} = 0$), as one would expect from Eq. 4.10; additionally (and also in agreement with Eq. 4.10) we find that the Kondo temperature here is identical to that of the corresponding single impurity Anderson model.

As we can see from Fig. 4.3, exactly at the phase boundary the system is *frustrated*, and described down to zero temperature by a transition fixed point, characterised by $S_{\rm imp} = \ln 3$ (as the local moment and the strong coupling states are degenerate) and $T\chi_{\rm imp} = \frac{1}{6}$ (being an average of $T\chi_{\rm imp}$ for the local moment and strong coupling states) — the even parity doublet is Kondo quenched on an energy scale $T \sim T_{\rm K}$ even when it is not the ground state. The system flows to the transition fixed point on an energy scale $T \sim T_{\rm K}$, and as such the transition fixed point is accessible only when $|E_\Delta| < T_{\rm K}$. As $|E_\Delta| \to 0$, the system flows close to the transition fixed point over a larger temperature range before eventually flowing away to either the local moment (when $J > J'$) or the strong coupling (when $J' > J$) fixed point on an energy scale $T \sim |E_\Delta|$, the transition fixed point describing the system at zero temperature only when $E_\Delta = 0$ (that is exactly on the phase boundary). We

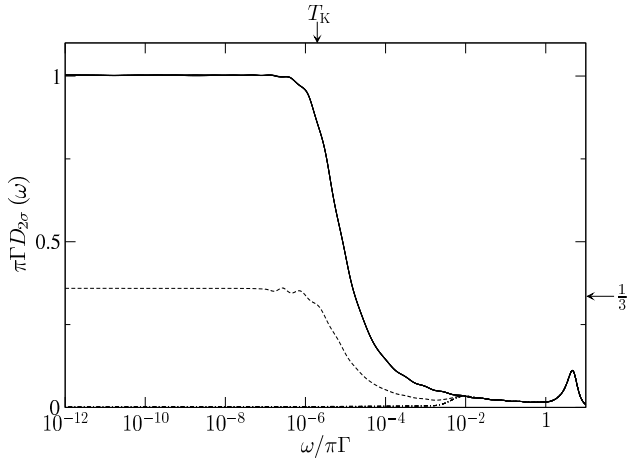


Figure 4.4: The zero-temperature single particle spectrum of dot 2, $\pi\Gamma D_{2\sigma}(\omega)$, for systems approaching the phase transition in Regime II. The same parameters for systems (a)-(f) as in Fig. 4.3 are used; all spectra in the strong coupling phase are coincident, as are all spectra in the local moment phase.

note that our results here are in agreement with the NRG results of Wang [72], and, along the line $t' = 0$, also with the coupled cluster results of Chiappe *et al.* [75].

4.6.3 Dynamics

Turning our attention to the dynamic properties of systems in regime II, Fig. 4.4 shows the zero-temperature single particle spectrum of dot 2, $\pi\Gamma D_{2\sigma}(\omega)$, as a function of frequency, ω, for systems approaching the phase transition. The figure shows that the spectra for all systems in the strong coupling phase which share a common T_K (i.e. a common U and Γ) are identical, flowing to the unitarity limit on an energy scale T_K — we find that they are also identical to that of a single impurity Anderson model with the same U and Γ (as predicted by Eq. 4.12). The spectra for the local moment phase are also coincident, and decay to zero with logarithmic corrections — $\pi\Gamma D_{2\sigma}(\omega) \sim 1/[\ln(\omega/T_0)]^2$ (with T_0 a constant) — exactly as is expected for a system with a local moment ground state [126]. A system lying exactly on the phase boundary has a distinct single particle spectrum, flowing to a zero frequency value of $\frac{1}{3}$, given by a weighted average of the zero frequency values of the single particle spectrum for the local moment and strong coupling phases, as

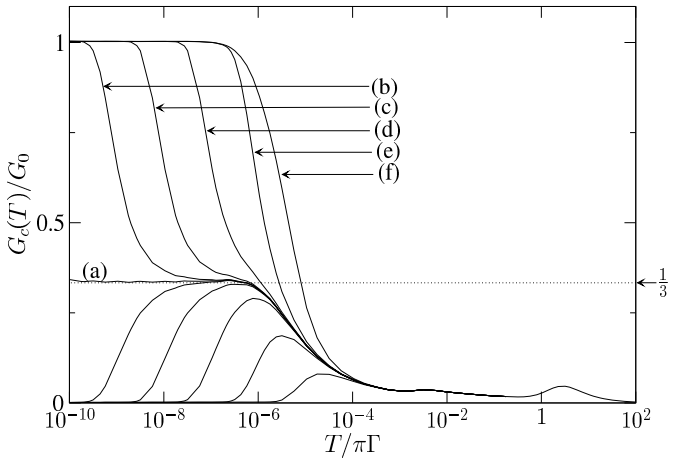


Figure 4.5: The zero-bias conductance for systems approaching the phase transition in Regime II. The same parameters as in Fig. 4.3 are used.

one would expect from the Lehmann representation of the spectra (see Sec. 3.6); $\pi\Gamma D_{2\sigma}(0)|_{TFP} = \frac{1}{3}\pi\Gamma(D_{2\sigma}(0)|_{SC} + 2D_{2\sigma}(0)|_{LM}) = \frac{1}{3}(1+0+0)$. Fig. 4.5 shows the conductance for a range of TQD systems in regime II. The conductance ultimately flows to $G_c(0)/G_0 = 1$ in the strong coupling phase, and $G_c(0)/G_0 = 0$ in the local moment phase — exactly as expected from Eq. 4.7 — with the transition fixed point being characterised by $G_c/G_0 = 1/3$. This means that warming a system in the local moment phase which is close to the phase boundary will revive the antiferromagnetic Kondo effect. As the system approaches the quantum phase transition (i.e. as E_Δ becomes smaller) the conductance flows close to the transition fixed point over a wider temperature range, although, as with the thermodynamic data, the transition fixed point describes the system down to zero-temperature only when $E_\Delta = 0$.

4.6.3.1 Phase Shift and the Friedel-Luttinger Sum Rule

We generically find that the Luttinger integral $I_{\rm L} = \mathrm{Im}\,\mathrm{Tr}\int_{-\infty}^{0} d\omega \frac{\partial \mathbf{\Sigma}_\sigma}{\partial\omega}\mathbf{G}_\sigma = 0$ in the strong coupling phase (as one would expect for a Fermi Liquid phase [120]). It is also found that $|I_{\rm L}| = \frac{\pi}{2}$ throughout the local moment phase, in agreement with the results for a local moment (arising from an underscreened spin-1 phase) reported by Logan *et al.* [55]. As $n_{{\rm imp},\sigma}|_{T=0} = 3/2$ throughout regime II, and $\delta_\sigma =$

$\pi n_{\mathrm{imp},\sigma}|_{T=0} + I_{\mathrm{L}}$, Eq. 4.7 therefore predicts that $G_c/G_0 = 1$ in the strong coupling phase, and 0 in the local moment phase — in precise agreement with the directly calculated values.

4.7 Regime I: $J < 10T_{\mathrm{K}}$

4.7.1 Effective Low Energy Model

We now consider regime I. In this regime, as for regime II, the interdot hoppings, t and t', are small compared to the intradot Coulomb repulsion, U. As a result (just as in regime II ($J > 10T_{\mathrm{K}}$)), Eq. 4.4 describes the low temperature physics of the problem well. As shown in Fig. 4.2 the TQD in regime I has two phases — a local moment phase and a strong coupling phase — separated by a line of first order quantum phase transitions, which is well described by the equation $J' = J^2/10T_{\mathrm{K}}$. Moreover, except when close to the phase boundary with regime II, in regime I it is generically the case that $J \ll T_{\mathrm{K}}$, and in the vicinity of the phase boundary $J, J' \ll T_{\mathrm{K}}$. We therefore anticipate that coupling to the conduction band (occurring on a low energy scale T_{K}) will dominate the low energy physics of the system. It is helpful therefore to consider first a toy model in which the couplings between the orbitals of the Wilson chain for the lead/conduction band are assumed to vanish (as would in fact be the case if the lead bandwidth $D \to 0$). All conduction band orbitals except for the 0-orbital of the Wilson chain — which couples directly to the TQD — can therefore be neglected. The effective spin-model then consists of four spins-$\frac{1}{2}$ as shown schematically in Fig. 4.6: the TQD spins 1-3 and the spin ($\hat{\mathbf{S}}(0)$) associated with the 0-orbital. The effective Hamiltonian is obtained from Eq. 4.4 and given by $\hat{H}_{spin} = \hat{H}^s_{TQD} + \hat{H}_{\mathrm{K}}$, with $\hat{H}^s_{TQD} = J\hat{\mathbf{S}}_2 \cdot (\hat{\mathbf{S}}_1 + \hat{\mathbf{S}}_3) + J'\hat{\mathbf{S}}_1 \cdot \hat{\mathbf{S}}_3$, but with $\hat{H}_{\mathrm{K}}$ now given simply by $\hat{H}_{\mathrm{K}} = J_{\mathrm{K}}\hat{\mathbf{S}}_2 \cdot \hat{\mathbf{S}}(0)$. We consider this model for $(J, J') \ll J_{\mathrm{K}}$.

On an energy scale $T \sim J_{\mathrm{K}}$, spins 2 and 0 quench into a local singlet state,

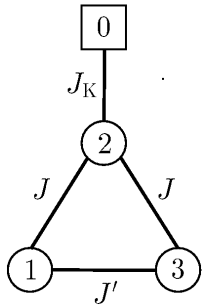


Figure 4.6: Schematic of the toy model discussed in text, consisting of four spins-$\frac{1}{2}$, exchange-coupled as indicated.

which, for the energy scales $\ll J_K$ on which we focus, is thus tightly 'locked', with an excitation energy of $J_K (\gg J, J')$ to the local 2-0 triplet. Spin 2 is then essentially frozen out, with 1 and 3 thus coupled by the remaining antiferromagnetic exchange interaction $\hat{H}_{J'} = J' \hat{\mathbf{S}}_1 \cdot \hat{\mathbf{S}}_3$. This produces a 1-3 singlet state with energy $E_S = -\frac{3}{4}J'$, and a triplet with energy $E_T = +\frac{1}{4}J'$. However an additional, weak RKKY-like ferromagnetic interaction between spins 1 and 3 naturally arises by virtual polarization of the intervening 2-0 singlet; as easily determined (via Brillouin-Wigner perturbation theory [93]) to second order in $\hat{H}_J = J \hat{\mathbf{S}}_2 \cdot (\hat{\mathbf{S}}_1 + \hat{\mathbf{S}}_3)$, with the result that the energy of the 1-3 singlet remains unaffected, but the triplet energy is lowered to $E_T = \frac{1}{4}J' - \frac{J^2}{2J_K}$ (a natural outcome of direct antiferromagnetic coupling between the 2-1 and 2-3 spin-pairs).

The splitting between the 1-3 triplet/singlet states is thus $E_T - E_S = J' - \frac{J^2}{2J_K}$ to leading order in $J/J_K \ll 1$. The underlying calculation requires $J, J' \ll J_K$ but otherwise imposes no constraints on the ratio J'/J. Hence, if $J' > \frac{J^2}{2J_K}$ then the 1-3 ground state is a spin singlet (as in consequence is that of the overall 4-spin system, the 2-0 spin pair being singlet-locked), whilst if $J' < \frac{J^2}{2J_K}$ the ground state is a triplet.

The effective Hamiltonian, $\hat{H}'_{eff}$, for the toy model on energy scales $\ll J_K$ then follows simply. The 1-3 singlet state is $|0;+;0\rangle = \frac{1}{\sqrt{2}}(c^\dagger_{1\uparrow} c^\dagger_{3\downarrow} + c^\dagger_{3\uparrow} c^\dagger_{1\downarrow})|\text{vac}\rangle$, and has $(+)$-parity under $1 \leftrightarrow 3$ exchange; while the 1-3 triplet state has $(-)$-parity, e.g. $|1;-;+1\rangle = c^\dagger_{1\uparrow} c^\dagger_{3\uparrow}|\text{vac}\rangle$. As the unity operator for this local Hilbert space is $\hat{1} =$

$\hat{1}_+ + \hat{1}_-$, with $\hat{1}_+ = |0;+;0\rangle\langle 0;+;0|$ for the singlet and $\hat{1}_- = \sum_{S^z} |1;-;S^z\rangle\langle 1;-;S^z|$ for the triplet, we have $\hat{H}'_{eff} = E_S\hat{1}_+ + E_T\hat{1}_-$. Defining again a pseudospin operator

$$\hat{\mathcal{T}}^z = \tfrac{1}{2}(\hat{1}_+ - \hat{1}_-) \tag{4.14}$$

such that the 1-3 singlet and triplet states are eigenstates of it, $\hat{\mathcal{T}}^z|S;\pm;S^z\rangle = \pm\frac{1}{2}|S;\pm;S^z\rangle$ (reflecting their distinct parities), and using $\hat{1}_\pm = \frac{1}{2}(1 \pm 2\hat{\mathcal{T}}^z)$, gives

$$\hat{H}'_{eff} \;=\; -E_\Delta\hat{\mathcal{T}}^z \tag{4.15}$$

where $E_\Delta = E_T - E_S$ (and we have neglected the common constant $\frac{1}{2}(E_S + E_T)\hat{1}$).

Although this toy model includes only the 0-orbital of the Wilson chain for the lead, we can readily deduce from it the effective low-energy Hamiltonian for the full lead-coupled system in regime I, via two simple considerations. First, as above, J_K in the toy model is the singlet-triplet splitting for the 2-0 spin bond: it is the energy required to unquench the 2-0 singlet. On coupling to the *full* Wilson chain, one naturally expects J_K to be renormalised to the order of T_K — the spin-$\frac{1}{2}$ Kondo scale for coupling spin 2 to the lead, and thus the characteristic scale for unquenching this Kondo singlet — but we also expect the description above to be otherwise robust, and applicable provided the exchange couplings $J, J' \ll T_\mathrm{K}$. The 1-3 singlet/triplet splitting, $E_\Delta = E_T - E_S$, is therefore renormalised to $E'_\Delta = J' - \lambda\frac{J^2}{T_\mathrm{K}}$ (with λ a constant of order 1).

Second, we expect a weak residual antiferromagnetic coupling between the 1-3 spin-triplet and the remainder of the Wilson chain, mediated by virtual polarization of the intervening Kondo singlet (which is itself essentially frozen out on energy scales $\ll T_\mathrm{K}$); that is we expect a contribution to the effective low-energy Hamiltonian ($\hat{H}_{eff}$) in the $\hat{\mathcal{T}}^z = -\frac{1}{2}$ (triplet) sector which is of spin-1 Kondo form, $J^*_\mathrm{K}\hat{\mathbf{S}}\cdot\tilde{\mathbf{S}}(0)$, with $\hat{\mathbf{S}}$ here a spin-1 operator representing the 1-3 triplet, and with the spin-$\frac{1}{2}$ operator $\tilde{\mathbf{S}}(0)$ representing the conduction electron density *excluding* the 0-orbital of

the Wilson chain (which is locked up in the Kondo singlet). We make no attempt to estimate perturbatively the effective exchange coupling $J_{\rm K}^* > 0$, albeit its antiferromagnetic (+) sign is obvious from the fact that the spin-1 is coupled to the remainder of the Wilson chain via the intervening Kondo singlet.

From the above we therefore expect the effective low-energy model describing regime I to be of the form

$$\hat{H}_{eff} = \tfrac{1}{2}(1 - 2\hat{\mathcal{T}}_z) J_{\rm K}^* \hat{\mathbf{S}} \cdot \tilde{\mathbf{S}}(0) - E'_\Delta \hat{\mathcal{T}}_z + \hat{H}_L \ : \text{Regime I} \tag{4.16}$$

where

$$E'_\Delta \ = \ J' - \lambda \frac{J^2}{T_{\rm K}}. \tag{4.17}$$

This effective model should be applicable on energy scales $\ll T_{\rm K}$ (where the Kondo singlet between the 2-spin/orbital and the lead is already frozen out). We note that, as with its counterpart Eq. 4.12 for regime II ($J > 10T_{\rm K}$), $\hat{H}_{eff}$ is separable into distinct ($\hat{\mathcal{T}}^z = \pm\frac{1}{2}$) pseudospin sectors reflecting the strict conservation of $1 \leftrightarrow 3$ parity. The term $-E'_\Delta \hat{\mathcal{T}}^z$ in Eq. 4.16 again acts as an effective field on the pseudospin, picking out the parity sector in which the $T = 0$ ground state lies. For $E'_\Delta > 0$ the $(-)$-parity triplet can be ignored for energy/temperature scales $\lesssim E'_\Delta$. The ground state then lies in the $\hat{\mathcal{T}}^z = +\frac{1}{2}$ sector corresponding to the 1-3 singlet, which state is effectively decoupled from the lead/conduction band (as one expects physically for an 'inert' singlet). This is the strong coupling phase of regime I.

For $E'_\Delta < 0$, by contrast, the ground state clearly lies in the $\hat{\mathcal{T}}^z = -\frac{1}{2}$ sector. Here the 1-3 spin triplet is antiferromagnetically coupled to the lead, and from Eq.(4.16) the effective low-energy model on scales $\lesssim |E'_\Delta|$ is the underscreened spin-1 Kondo model of Nozières and Blandin [21], $\hat{H}_{eff} = J_{\rm K}^* \hat{\mathbf{S}} \cdot \tilde{\mathbf{S}}(0) + \hat{H}_L$.

Hence, on an energy/temperature scale set by the spin-1 Kondo temperature $T_{\rm K}^* \propto e^{-1/\rho J_{\rm K}^*}$ ($\ll T_{\rm K}$), the spin-1 is quenched to a spin-$\frac{1}{2}$ by antiferromagnetic coupling to the lead [21]. The stable ground state fixed point then consists of a

free spin-$\frac{1}{2}$ (leading irrelevant corrections being residual ferromagnetic coupling of the spin-$\frac{1}{2}$ to the lead [21]). This of course describes the local moment phase of regime I, where as $T \to 0$ the spin-$\frac{1}{2}$ becomes asymptotically free. Just as in regime II ($J > 10T_{\rm K}$), the stable fixed point is thus the local moment fixed point with a residual entropy $S_{\rm imp}(0) = \ln 2$. Precisely at the quantum phase transition, $E'_\Delta = 0$, the full Eq.(4.16) is required to describe the system. This again is the transition fixed point which, as in regime II ($J > 10T_{\rm K}$), is characterised by $S_{\rm imp}(0) = \ln 3$ reflecting the degenerate singlet and doublet (underscreened spin-1) states arising at this point, where the system is frustrated. Finally, since the quantum phase transition between the strong coupling and local moment phases occurs for $E'_\Delta = 0$, Eq. 4.17 shows that the phase boundary line for regime I should satisfy $J' \propto J^2/T_{\rm K}$. As discussed above, this is precisely as found from NRG calculations (Fig. 4.2, with the NRG-determined constant $\lambda \simeq 0.1$), for which the above arguments thus provide a natural explanation.

4.7.2 Thermodynamics

We consider first thermodynamic properties, which illustrate the various fixed points determining the physical behaviour of the system. Thermodynamic data for systems which lie within regime I are shown in Figs. 4.7, 4.8 and 4.9.

On the highest temperature scales, $T \gg U$, all four states of each single-level dot in the TQD are energetically accessible. The physics (as in all parameter regimes) is then controlled by the free orbital fixed point [7, 8], with an associated entropy $S_{\rm imp}(T) = \ln(4^3)$ and $T\chi_{\rm imp}(T) = 3 \times \frac{1}{8}$. On decreasing T below $T \sim U$, each dot becomes singly occupied, whence $S_{\rm imp} = \ln 8$ and $T\chi_{\rm imp}(T) = \frac{3}{4}$ naturally arise. On this temperature/energy scale, the effective spin-model Eq. 4.4 now describes the system.

The associated $\ln 8$ entropy plateau then persists down to $T \sim T_{\rm K}$, on which scale (Sec. 4.7) the 2-dot/spin is Kondo quenched by coupling to the lead (and as

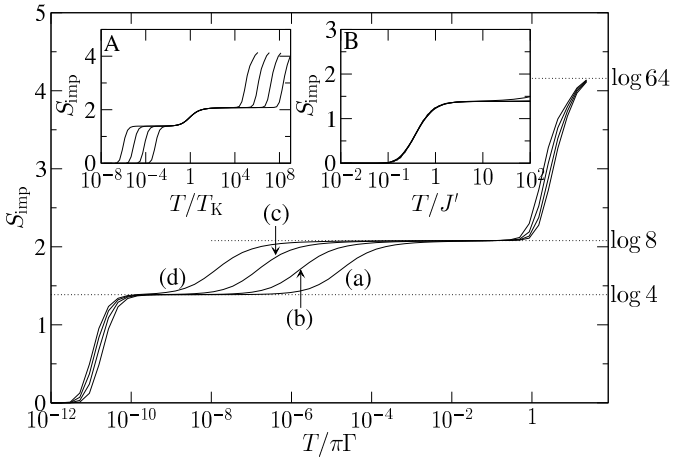


Figure 4.7: Entropy $S_{\rm imp}$ vs $T/\pi\Gamma$ for systems deep in the strong coupling phase of regime I. Here $\tilde{t} = 2 \times 10^{-5}$ and $\tilde{t}' = 10^{-5}$. $\tilde{U}$ varies, with $\tilde{U} = 8$ for line (a), 10 for (b), 12 for (c) and 14 for (d). Inset A shows the data scaled by $T_{\rm K}$, defined as $\mathrm{S}_{\rm imp}(T_{\rm K}) = \frac{1}{2}\ln 2$ for a SIAM with the same $\tilde{U}$, whilst inset B shows the data scaled by J'.

such 'singlet locked' for lower T). The entropy thus drops on the scale $T \sim T_{\rm K}$ to $S_{\rm imp}(T) = \ln 4$ (with $T\chi_{\rm imp}(T) = \frac{1}{2}$), characteristic of the singlet and triplet states associated with spins 1 and 3 (Sec. 4.7).

The behaviour just described is shown in Figs. 4.7-4.9. Inset A to Fig. 4.7 shows same data as the main Fig. 4.7, scaled by the Kondo temperature, $T_{\rm K}$, and shows that the Kondo quenching of dot 2 (corresponding to a flow in $S_{\rm imp}$ from $\ln 8$ to $\ln 4$) is a universal function of $T_{\rm K}$. For temperatures below $T_{\rm K}$ the behavior of the system should be described by the effective low-energy model Eq. 4.16, and the thermal evolution of the system on decreasing T below $T_{\rm K}$ naturally depends on the phase (strong coupling or local moment), and proximity or otherwise to the phase boundary (Fig. 4.2).

Fig. 4.7 illustrates the situation deep in the strong coupling phase ($E'_\Delta \gg 0$), for fixed tunnel couplings $\tilde{t}, \tilde{t}'$ (with exchange couplings $J = 4t^2/U$, $J' = 4t'^2/U$ each $\ll T_{\rm K}$, as appropriate to regime I), and for a range of interactions $\tilde{U}$. Here the $\ln 4$ entropy plateau persists down to $T \sim E'_\Delta$, at which point the triplet combination of spins 1 and 3 is rendered thermally inaccessible and $S_{\rm imp}$ drops to zero ($T\chi_{\rm imp} = 0$). Deep in the strong coupling phase, $E'_\Delta \simeq J'$ (Eq. 4.17); as shown in inset B to Fig. 4.7

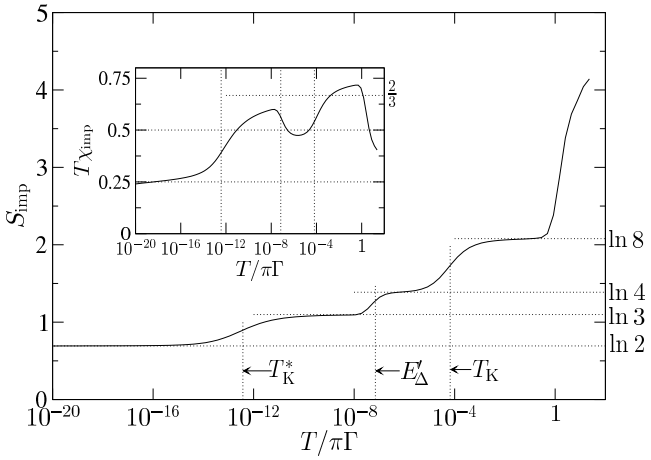


Figure 4.8: Entropy $S_{\rm imp}$ vs $T/\pi\Gamma$ for a system in the local moment phase of regime I. Here $\tilde{U} = 7$, $\tilde{t} = 6 \times 10^{-3}$ and $\tilde{t}' = 10^{-3}$. The scales $T_{\rm K}$, E'_Δ and $T_{\rm K}^*$ (defined by $\mathrm{S}_{\rm imp}(T_{\rm K}^*) = \frac{1}{2}\ln 6$) are also shown on the graph. The inset shows $T\chi_{\rm imp}$ for the same system.

this is the energy scale on which the triplet state becomes thermally inaccessible, and $S_{\rm imp}$ therefore flows from $\ln 4$ to 0 on this scale.

The behaviour of a system deep in the local moment phase ($E'_\Delta \ll 0$) is shown in Fig. 4.8. The $\ln 4$ plateau in the entropy persists until on a scale $T \sim |E'_\Delta|$ the 1–3 singlet is projected out, and $S_{\rm imp}$ falls to $\ln 3$ ($T\chi_{\rm imp}$ to $\frac{2}{3}$), characteristic of a triplet state. Below a scale $T \sim T_{\rm K}^*$ the triplet state is underscreened[5] giving a local moment state with $S_{\rm imp} = \ln 2$ ($T\chi_{\rm imp} = \frac{1}{4}$), the ultimate low-$T$ ground state of the system as predicted by Eq. 4.16.

A system close to the phase boundary ($E'_\Delta \approx 0$), although still in the local moment phase, is exhibited in Fig. 4.9. Here $|E'_\Delta| \ll T_{\rm K}^*$ and so underscreening of the 1–3 triplet state occurs *before* the 1–3 singlet is projected out. The $\ln 4$ entropy plateau is terminated here by a flow to $S_{\rm imp} = \ln 3$ on a scale $T \sim T_{\rm K}^*$, the energy scale on which the triplet state is underscreened. As a result the $\ln 3$ plateau here is indicative *not* of the 1–3 triplet but rather of the transition fixed point, and as such has $T\chi_{\rm imp} = \frac{1}{6}$ (rather than $T\chi_{\rm imp} = \frac{2}{3}$, which is characteristic of the 1–3 triplet). The system flows close to the transition fixed point until $T \sim |E'_\Delta|$ at which point it

[5]We define $T_{\rm K}^*$ via $S_{\rm imp}(T_{\rm K}^*) = 0.5\ln 6$, halfway between $\ln 2$ and $\ln 3$.

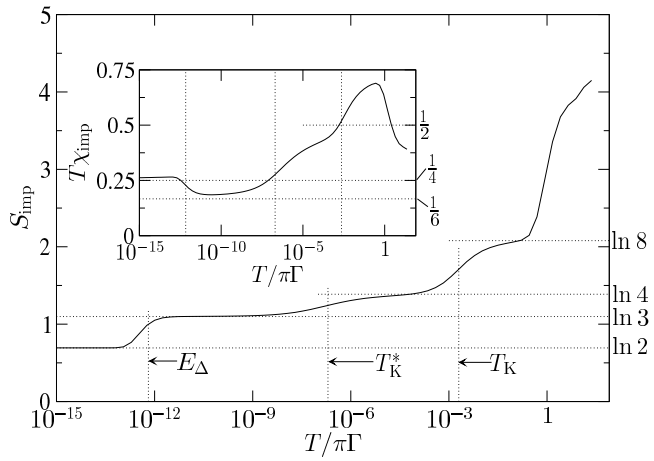


Figure 4.9: Entropy $S_{\rm imp}$ vs $T/\pi\Gamma$ for a system in the local moment regime, very close to the transition, in regime I. Here $\tilde{U} = 4$, $\tilde{t} \approx 3.64 \times 10^{-2}$ and $\tilde{t}' = 10^{-2}$. The inset shows $T\chi_{\rm imp}$ for the same system, and $T_{\rm K}$, E'_Δ and $T_{\rm K}^*$ (defined by $\mathrm{S}_{\rm imp}(T_{\rm K}^*) = \frac{1}{2}\ln 12$, halfway between $\ln 4$ and $\ln 3$) are shown on the graph.

will flow to either the strong coupling or local moment fixed point, depending upon the sign of E'_Δ, the transition fixed point describing the system at $T = 0$ only when $E'_\Delta = 0$. We note that along the line $t' = 0$ our results are in agreement with the coupled cluster results of Chiappe *et al.* [75].

4.7.3 Dynamics

We now consider the dynamic properties of systems in this regime, concentrating on the single particle spectrum of dot 2, $\pi\Gamma D_{2\sigma}(\omega)$, and the zero-bias conductance through the TQD, $G_c(T)$, which may be directly related to the single particle spectrum of the TQD device using Eq. 4.7a.

The single particle spectrum of a system in the strong coupling phase is characterised by the universal scaling form obtained for the SIAM [113][6], as shown in Fig. 4.10. In particular, $\pi\Gamma D_{2\sigma}(0) = 1$, indicating that $G_c(0)/G_0 = 1$ (Eq. 4.7a); we find that $\pi\Gamma D_{2\sigma}(\omega)$ for the strong coupling phase of regime I is coincident with $\pi\Gamma D_\sigma(\omega)$ for a SIAM with the same $\tilde{U}$ and Γ. In the local moment phase, as illustrated in Fig. 4.11, a sharp increase in the single particle spectrum to $\pi\Gamma D_{2\sigma}(\omega) \sim 1$

[6]It is therefore also identical to that of the strong coupling phase of regime II ($J > 10T_{\rm K}$) — see Sec. 4.6.

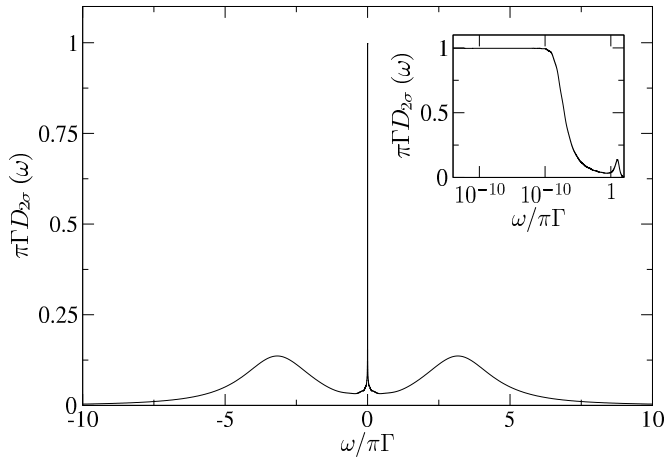


Figure 4.10: The zero-temperature single particle spectrum of dot 2, $\pi\Gamma D_{2\sigma}(\omega)$, for a system deep in the strong coupling phase of regime I. $\tilde{U} = 7$, $\tilde{t} = 4 \times 10^{-3}$ and $\tilde{t}' = 10^{-3}$. The inset shows the same data on a logarithmic scale.

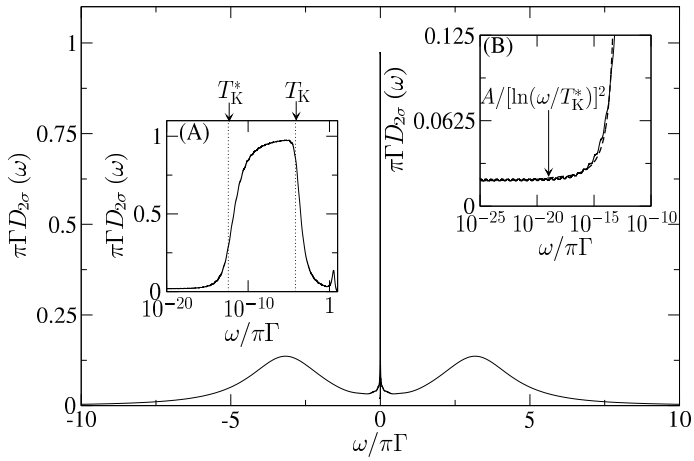


Figure 4.11: The zero-temperature single particle spectrum of dot 2, $\pi\Gamma D_{2\sigma}(\omega)$, for a system deep in the local moment phase of regime I. The parameters here are the same as Fig. 4.8. Inset A shows the single particle spectrum on a logarithmic scale, whilst inset B shows the low frequency behaviour of the spectrum fitted to a line of the form $\pi\Gamma D_{2\sigma}(\omega) = a/\ln^2(\omega/T_K^*)$.

is observed when $\omega \sim T_K$, corresponding to the energy scale on which dot 2 is Kondo quenched. The spectrum then decays to zero on a scale $\omega \sim T_K^*$, as the 1–3 triplet state is underscreened to a local moment. The decay of the spectrum in the local moment phase is described by $\pi\Gamma D_{2\sigma}(\omega) \sim a/\ln^2(|\omega|/T_K^*)$ as expected for a singular Fermi liquid [126], where the slow approach to the fixed point is characterised by marginally irrelevant logarithmic corrections [126, 127].

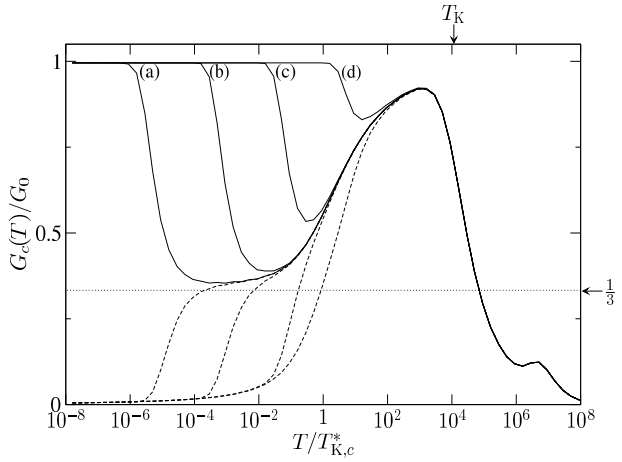


Figure 4.12: Conductance as a function of temperature for systems close to the phase transition in regime I. $\tilde{U} = 4$ and $\tilde{t}' = 10^{-2}$. $\tilde{t} = t_c \pm \lambda T_K$, with $\lambda = 10^{-7}$ for (a), 10^{-5} for (b), 10^{-3} for (c) and 10^{-1} for (d). $\tilde{t}_c \approx 3.64 \times 10^{-2}$ and the temperature is given in terms of $T^*_{K,c}$, the value of T^*_K for a system with $t = t_c$ ($T^*_{K,c} = 2 \times 10^{-7}$).

Fig. 4.12 shows the zero-bias conductance as a function of $T/T^*_{K,c}$ ($T^*_{K,c}$ being the value of T^*_K for a system lying at the transition fixed point) for systems in both strong coupling and local moment phases, approaching the transition fixed point. In all cases there is a sharp increase in $G_c(T)$ when $T \sim T_K$ as dot 2 is Kondo quenched. In the strong coupling phase this is followed by a flow to the strong coupling fixed point (and hence $G_c(T)/G_0 = 1$) on a scale $T \sim |E'_\Delta|$. In the local moment phase having projected out the singlet state on a scale $T \sim |E'_\Delta|$ the conductance falls to zero on a scale $T \sim T^*_K$ when the triplet state is underscreened — giving $G_c(0)/G_0 = 0$ as expected for the local moment fixed point (see Sec. 4.6.3). In this regime (in contrast to regime II ($J > 10T_K$) — see Sec. 4.6) warming a system in the local moment phase will in *all* cases revive the antiferromagnetic Kondo effect as underscreening of the 1–3 triplet state is suppressed.

In the range $|E'_\Delta| < T \ll T^*_K$ the system is described by the transition fixed point and both local moment and strong coupling ground states must be retained in the low energy manifold. From the Lehmann representation of the spectrum it follows that $D_{2\sigma}(\omega, T) = \frac{1}{3}[D^{SC}_{2\sigma}(\omega, T) + 2D^{LM}_{2\sigma}(\omega, T)] = \frac{1}{3}$ under these conditions. Precisely on the phase boundary $E'_\Delta = 0$ and the transition fixed point describes

the system down to $T = 0$, and hence (using Eq. 4.7a) $G_c(0)/G_0 = 1/3$.

4.7.3.1 Phase Shift and the Friedel-Luttinger Sum Rule

Eq. 4.7b relates the zero-temperature zero-bias conductance to the static scattering phase shift, $\delta_\sigma = \pi n_{\mathrm{imp},\sigma} + I_{\mathrm{L}}$. The system being deep in the 3-electron Coulomb blockade valley, $n_{\mathrm{imp},\sigma}|_{T=0} = 3/2$ in the absence of a field. $I_{\mathrm{L}} = \mathrm{Im\,Tr} \int_{-\infty}^{0} d\omega \frac{\partial \mathbf{\Sigma}_\sigma}{\partial \omega} \mathbf{G}_\sigma$, the Luttinger integral [120] is generically found to be zero in the strong coupling phase (as expected for a Fermi liquid [120]), and $|I_{\mathrm{L}}| = \frac{\pi}{2}$ in the local moment phase (as expected for a singular Fermi liquid [55]), just as was the case for regime II ($J > 10T_{\mathrm{K}}$) — see Sec. 4.6.3.1 (an unsurprising result, as the local moment phase of regime I is continuously connected to the corresponding phase of regime II, and the strong coupling phases are similarly connected). Eq. 4.7b then gives $G_c^{SC}(0)/G_0 = 1$ and $G_c^{LM}(0)/G_0 = 0$ — in exact agreement with the directly calculated values (Fig. 4.12).

4.8 Regime III: The Orbital Regime

4.8.1 Effective Low Energy Model

We now consider the third regime of the apex coupled trimer model — a weakly interacting region ($t \sim \mathcal{O}(U)$ or larger) where the effective spin model $\hat{H}_{spin}$ (Eq. 4.4) is no longer valid. As in Sec. 4.7 we focus on the region close to the phase boundary ($t' \lesssim U$) and aim to provide intuitive physical arguments for the low-energy effective model in this regime (Eq. 4.29), and the phase boundary associated with it, which is given by $t' \approx U/4$ when t is large ($t > U$), as shown in Fig. 4.2.

Deep within regime III, $t \gg U$, and so a natural starting point for understanding the physics of this system is provided by the non-interacting TQD, described by the Hamiltonian $\hat{H}_{NIACTM} = \hat{H}_{NITQD} + \hat{H}_L + \hat{H}_{hyb}$, where $\hat{H}_{NITQD}$ is $\hat{H}_{TQD}$ (as given

in Eq. 4.1) with $\tilde{U} = 0$, and we allow arbitrary ϵ;

$$\hat{H}_{NITQD} = \sum_{\sigma,i=1,2,3} \epsilon \hat{n}_{i\sigma} + \sum_{\sigma} t[(c^{\dagger}_{1\sigma} + c^{\dagger}_{3\sigma})c_{2\sigma} + H.c] + \sum_{\sigma} t'(c^{\dagger}_{1\sigma}c_{3\sigma} + H.c.). \quad (4.18)$$

Our approach to the non-interacting TQD here is similar to that taken in Refs [66, 74, 77, 89]. As we are primarily interested in the behaviour of the system close to the phase boundary ($t' \sim U/4$) we further specify that $t \gg t'$. If we take linear combinations of dots 1 and 3, it is clear from Eq. 4.18 that dot 2 couples only to the even (+) parity combination, $c^{\dagger}_{e\sigma}$, whilst the odd (−) parity combination, $c^{\dagger}_{o\sigma}$, is decoupled;

$$c^{\dagger}_{e\sigma} = \frac{1}{\sqrt{2}}(c^{\dagger}_{1\sigma} + c^{\dagger}_{3\sigma}), \quad (4.19a)$$

$$c^{\dagger}_{o\sigma} = \frac{1}{\sqrt{2}}(c^{\dagger}_{1\sigma} - c^{\dagger}_{3\sigma}). \quad (4.19b)$$

Writing Eq. 4.18 in terms of these even and odd parity linear combinations we find

$$\hat{H}_{NITQD} = \sum_{\sigma} \begin{pmatrix} c^{\dagger}_{2\sigma} & c^{\dagger}_{e\sigma} & c^{\dagger}_{o\sigma} \end{pmatrix} \begin{pmatrix} \epsilon & \sqrt{2}t & 0 \\ \sqrt{2}t & (\epsilon + t') & 0 \\ 0 & 0 & (\epsilon - t') \end{pmatrix} \begin{pmatrix} c_{2\sigma} \\ c_{e\sigma} \\ c_{o\sigma} \end{pmatrix}. \quad (4.20)$$

By diagonalising this matrix, we may write $\hat{H}_{NITQD}$ in the form of a simple three level system, viz.

$$\hat{H}_{NITQD} = \sum_{\sigma} (E_u \hat{n}_{u\sigma} + E_o \hat{n}_{o\sigma} + E_l \hat{n}_{l\sigma}), \quad (4.21)$$

where $\hat{n}_{\alpha\sigma} = c^{\dagger}_{\alpha\sigma}c_{\alpha\sigma}$ $(\alpha = u, l, o)$,

$$c^{\dagger}_{u\sigma} = \nu c^{\dagger}_{e\sigma} - \gamma c^{\dagger}_{2\sigma}, \tag{4.22a}$$

$$c^{\dagger}_{l\sigma} = \gamma c^{\dagger}_{e\sigma} + \nu c^{\dagger}_{2\sigma}, \tag{4.22b}$$

$$\tag{4.22c}$$

and

$$\gamma^2 = \frac{1}{2}(1 - y/\sqrt{y^2+8}), \tag{4.23a}$$

$$\nu^2 = 1 - \gamma^2 \tag{4.23b}$$

where $y = t'/t$. The three levels have energies

$$E_u = \epsilon + \frac{1}{2}t' + \frac{1}{2}\sqrt{8t^2 + t'^2}, \tag{4.24a}$$

$$E_o = \epsilon - t', \tag{4.24b}$$

$$E_l = \epsilon + \frac{1}{2}t' - \frac{1}{2}\sqrt{8t^2 + t'^2}, \tag{4.24c}$$

where, as $t \gg t'$ (see above) $E_u > E_o > E_l$. Writing the hybridisation term in the Hamiltonian, $\hat{H}_{hyb}$, in terms of the u, o and l orbitals we find

$$\hat{H}_{hyb} = \sum_{\mathbf{k},\sigma} V[(\nu c^{\dagger}_{l\sigma} - \gamma c^{\dagger}_{u\sigma})c_{\mathbf{k}\sigma} + H.c.], \tag{4.25}$$

and so the o orbital is entirely decoupled from the conduction band.

In the systems we consider, deep within regime III, $t \gg |\epsilon|$ and $\epsilon < 0$, and as such the o orbital lies closest to (but slightly below) the Fermi level at $\epsilon_F = 0$. It follows immediately that the ground state of $\hat{H}_{NITQD}$ is a four electron singlet state, $|0;+;0\rangle = c^{\dagger}_{o\uparrow}c^{\dagger}_{o\downarrow}c^{\dagger}_{l\uparrow}c^{\dagger}_{l\downarrow}|Vac\rangle$, which can be shown to be of even (+) parity (as is immediately obvious from the double occupation of the o orbital; both the l and u orbitals have even parity), and which has energy $E_+ = 2E_l + 2E_o$. The first excited

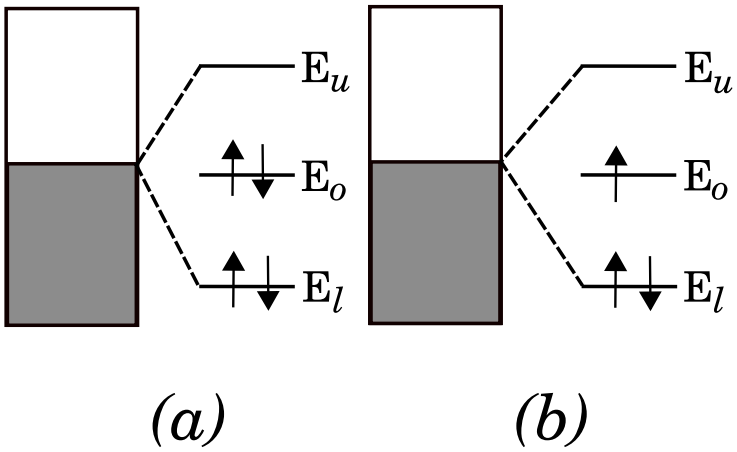


Figure 4.13: A schematic diagram of (a) the $|0;+;0\rangle$ and (b) the $|\frac{1}{2};-;+\frac{1}{2}\rangle$ states of $\hat{H}_{NITQD}$.

state of $\hat{H}_{NITQD}$ is a three electron doublet state, $|\frac{1}{2};-;\sigma\rangle = c^{\dagger}_{o\sigma}c^{\dagger}_{l\uparrow}c^{\dagger}_{l\downarrow}|Vac\rangle$, which has odd $(-)$ parity (a property which follows immediately from the occupation of the o orbital by a single electron), and energy $E_- = 2E_l + E_o$. These states are shown schematically in Fig. 4.13. The energy separation between the two states is given by $E_\Delta = E_+ - E_- = E_o = \epsilon - t'$. Clearly, the non-interacting model does not contain a phase transition, as $E_\Delta < 0$ for all parameters (as $t' > 0$ and $\epsilon < 0$). However, one would naturally expect the Coulomb interaction term in the full Hamiltonian, $\hat{H}_U = \sum_i U\hat{n}_{i\uparrow}\hat{n}_{i\downarrow}$, to lower the energy of the three electron state in relation to that of the four electron state. We therefore consider $\hat{H}_U$ as a first order perturbation to $|0;+;0\rangle$ and $|\frac{1}{2};-;S^z\rangle$. This calculation is somewhat lengthy, although not overly complex, and is discussed in Appendix D. Taking this perturbation into account, we find that the energy separation between the singlet and doublet states is given by

$$E'_\Delta = \epsilon - t' + \frac{U}{2}(1+\gamma^2), \tag{4.26}$$

which reduces to $E'_\Delta = U/4 - t'$ when $\epsilon = -U/2$ and $t \gg t'$ (such that $\gamma^2 \to \frac{1}{2}$). Our work so far therefore predicts that when $E'_\Delta < 0$ (corresponding to $t' > U/4$) the ground state of the TQD will be a four electron singlet state, as shown schematically in (a) of Fig. 4.13; as this state has no spin, it will not exhibit a Kondo coupling

to the conduction band. The singlet state here is fundamentally very similar to the Frozen Impurity fixed point described for the asymmetric Single Impurity Anderson Model by Krishnamurthy *et al.* [8], and just as in that case we find that the four electron singlet is continuously connected to the strong coupling phase.

By contrast, when $E'_\Delta > 0$ (corresponding to $t' < U/4$) the ground state of the TQD is the three electron doublet state, shown schematically in (b) of Fig. 4.13. In this state the TQD spin is localised on the o orbital, which is decoupled from the conduction band. One would therefore anticipate that the ground state would consist of the conduction band and a free spin on the TQD, giving rise to a local moment at low temperature. Another question then arises: as the ground state is a three electron doublet in both regime II ($J > 10T_\mathrm{K}$) and the local moment phase of regime III (see Fig. 4.2), is it possible to describe the evolution of the coupling to the conduction band as one moves from regime II to the local moment phase of regime III?

We find that we can model this coupling by performing a Schrieffer-Wolff transformation [13] upon the system; for all the systems studied in this thesis, the hybridisation, $\Gamma \ll U$. We first determine the ground state of the full $\hat{H}_{TQD}$. This state must lie within the subsector of parameter space in which there are three electrons on the TQD and the total TQD spin is $S = \frac{1}{2}$, although it is not necessarily within the subsector in which each dot is singly occupied; we label this state $|\frac{1}{2}; S^z\rangle$. Projecting into the low energy manifold defined by the unity operator $\hat{1} = \sum_{S^z} |\frac{1}{2}; S^z\rangle\langle\frac{1}{2}; S^z|$, we evaluate

$$\hat{H}_{eff} = \hat{1}\hat{H}_0\hat{1} + \hat{1}\hat{H}_{hyb}(E_0 - \hat{H}_0)^{-1}\hat{P}\hat{H}_{hyb}\hat{1} \tag{4.27}$$

where E_0 is the energy of the ground state under $\hat{H}_0 = \hat{H}_{TQD} + \hat{H}_L$, and we treat $\hat{H}_{hyb}$ as a perturbation (to second order) to the ground state of $\hat{H}_0$; $\hat{P} = \hat{1}_{full} - \hat{1}$, where $\hat{1}_{full}$ is the unity operator for the complete Hilbert space. After detailed calculation,

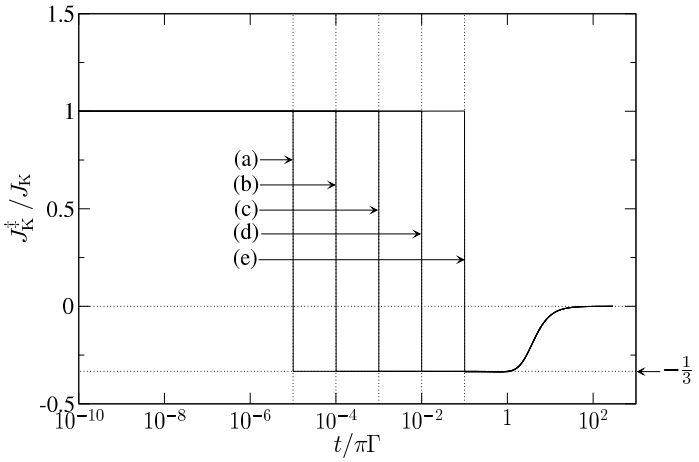


Figure 4.14: The effective exchange coupling $J_{\rm K}^{\ddagger}$ between the ground state doublet and the conduction band, as calculated from perturbation theory for a system with $\tilde{U} = 10$, $\Gamma = 10^{-2}D$ with $\tilde{t'} = 10^{-5}$ for (a), 10^{-4} for (b), 10^{-3} for (c), 10^{-2} for (d) and 10^{-1} for (e).

Eq, 4.27 ultimately gives an effective (isotropic) spin model for the system, viz

$$\hat{H}_{spin}^{II/III} = J_{\rm K}^{\ddagger}\hat{\mathbf{S}} \cdot \hat{\mathbf{S}}(0) + \hat{H}_L, \tag{4.28}$$

where $\hat{\mathbf{S}}$ is a spin-$\frac{1}{2}$ operator for the TQD as a whole, and $\hat{\mathbf{S}}(0)$ is the spin density of the conduction band at dot 2. $J_{\rm K}^{\ddagger}$ is evaluated numerically (neglecting retardation effects), using the method described in Appendix E. In this semi-analytic technique, a computer is used to evaluate the matrix elements arising in Eq. 4.27, from which $J_{\rm K}^{\ddagger}$ may be easily determined. This gives the results shown in Fig. 4.14 and 4.15.

These figures show that our Schrieffer-Wolff transformation accurately reproduces the results of our low energy effective models for both the strong coupling phase of regime II ($J > 10T_{\rm K}$) when $t < t'$ ($J_{\rm K}^{\ddagger} = J_{\rm K}$ — see Eq. 4.10) and the local moment phase of regime II when $t' < t \leq U$ ($J_{\rm K}^{\ddagger} = -\frac{1}{3}J_{\rm K}$ — see Eq. 4.11) and also the results derived above for a system deep within the local moment phase of regime III, when $U \ll t$ ($J_{\rm K}^{\ddagger} = 0$). We find that when $t > t'$ the coupling between the doublet state and the conduction band is always ferromagnetic, approaching zero asymptotically at very large t ($t \gg U$), when the system is deep within regime III. This weak coupling between the doublet state and the conduction band in regime

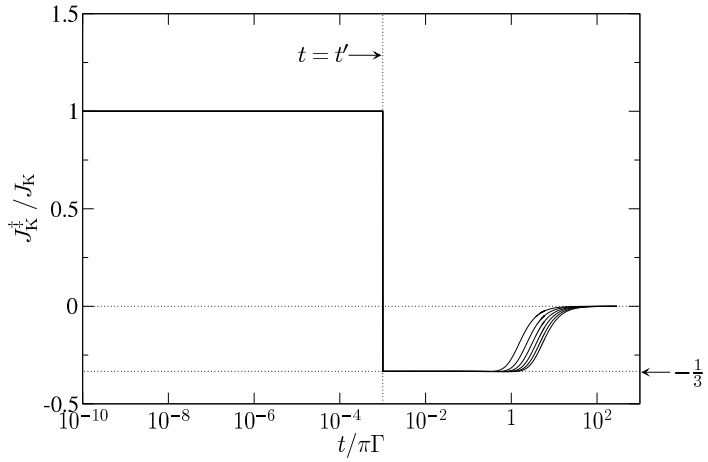


Figure 4.15: The effective exchange coupling $J_{\rm K}^{\ddagger}$ between the ground state doublet and the conduction band, calculated from perturbation theory for a system with $\tilde{t}' = 10^{-3}$ and $\Gamma = 10^{-2}D$, varying $\tilde{U}$ in equal steps between 4 and 14.

III can be readily understood as the result of an indirect coupling between the spin on the o orbital and the conduction band, mediated via the l and u orbitals. As t increases, the energy separation between the o orbital and the l and u orbitals becomes larger (Eq. 4.24), and so this indirect coupling naturally decreases.

The full low energy model for regime III then follows immediately as

$$\hat{H}_{eff} = -\frac{|J_{\rm K}^{\ddagger}|}{2}(1 - 2\hat{\mathcal{T}}^z)\hat{\mathbf{S}} \cdot \hat{\mathbf{s}}(0) + E'_{\Delta}\hat{\mathcal{T}}^z + \hat{H}_L \ : \text{Regime III}, \tag{4.29}$$

where $\hat{\mathcal{T}}^z = \frac{1}{2}(\hat{1}_+ - \hat{1}_-)$ defines a pseudospin operator (with $\hat{1} = |0;+;0\rangle$ and $\hat{1}_- = \sum_{S^z} |\frac{1}{2};-;S^z\rangle\langle\frac{1}{2};-;S^z|$) such that $|0;+;0\rangle$ and $|\frac{1}{2};-;S^z\rangle$ are eigenstates of it, with eigenvalues $\pm\frac{1}{2}$, respectively. This model describes the two phases of the system in regime III; the first, seen when $E'_{\Delta} < 0$, being a four electron singlet state of even parity ($\hat{\mathcal{T}}^z = +\frac{1}{2}$), which is (to this level of description) decoupled from the conduction band. As this phase is continuously connected to the strong coupling phase of regime II ($J > 10T_{\rm K}$), we refer to it as the 'strong coupling phase' of regime III, although, as discussed above, it is more accurately described by a frozen impurity fixed point. The second phase, seen when $E'_{\Delta} > 0$, is a local moment phase ($\hat{\mathcal{T}}^z = -\frac{1}{2}$), of odd parity, with a weak ferromagnetic coupling ($-|J_{\rm K}^{\ddagger}|$) to the

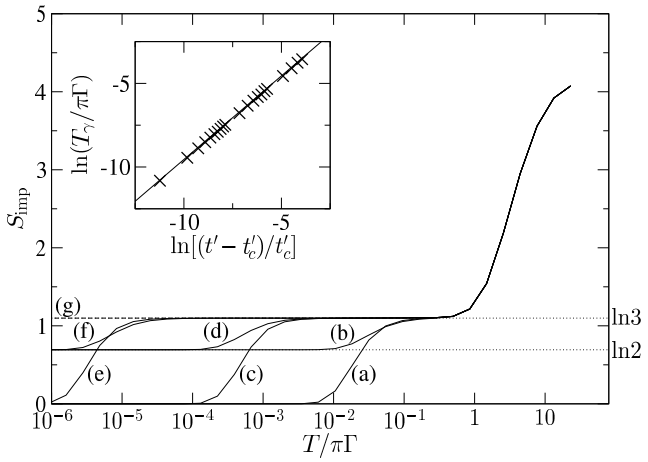


Figure 4.16: Entropy $S_{\rm imp}$ vs $T/\pi\Gamma$ for systems in regime III approaching the phase boundary. $\tilde{U} = 10$ and $\tilde{t} = 5$ here. $\tilde{t'}$ is varied, with $\tilde{t'} = 2.5$ for line (a), 2.4 for (b), 2.459 for (c), 2.457 for (d), 2.45794 for (e) and 2.45792 for (f). $\tilde{t'} = \tilde{t'_c} \simeq 2.45793$ for line (g). The inset shows $\log T_\gamma$ vs $\log[(t'-t'_c)/t'_c]$, where T_γ is defined via $\mathrm{S_{imp}}(T_\gamma) = 0.5 \ln 6$, suitably between $\ln 3$ and $\ln 2$.

conduction band which vanishes when t is extremely large ($t \gg U$), as shown in Fig. 4.14 and 4.15. The $E'_\Delta \hat{T}^z$ term in the effective Hamiltonian acts as an effective magnetic field upon the system, determining the ground state; at temperatures above $|E'_\Delta|$ the system will be described by a transition fixed point, just as was the case for regimes I ($J < 10T_{\rm K}$) and II ($J > 10T_{\rm K}$), which will describe the system at zero temperature only when $E'_\Delta = 0$. The phase boundary should, therefore, be described by $E'_\Delta = 0$, corresponding to the line $t' = U/4$ in the limit of large t — in very good agreement with the results shown in Fig. 4.2. We note that just as in Eq. 4.16 and Eq. 4.12, the corresponding low energy effective models for regimes I and II, Eq. 4.29 is separable into distinct pseudospin sectors, reflecting the strict conservation of $1 \leftrightarrow 3$ parity, with the $E'_\Delta \hat{T}^z$ term acting as an effective magnetic field upon the pseudospin.

4.8.2 Thermodynamics

In regime III we find that retaining a maximum of $N_s = 2000$ states in each iteration is not sufficient to calculate the properties of the system (particularly the dynamic

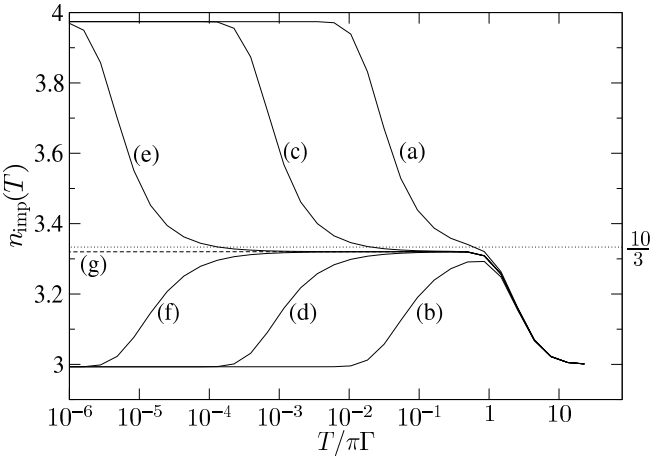


Figure 4.17: Excess impurity charge $n_{\rm imp}(T)$ vs $T/\pi\Gamma$ for systems with the same parameters as Figure 4.16. Note that the transition fixed point has $n_{\rm imp} \approx 10/3$.

properties) accurately within the NRG. We therefore retained a maximum of $N_s = 3000$ states per iteration for the results shown in this subsection, and the one that immediately follows. This is also done in Sec. 4.12, which discusses the effect of an applied magnetic field upon the system in regime III.

Fig. 4.16 and 4.17 illustrate the thermodynamics of the system in this regime. In all cases, at the highest temperature scales ($T \gg t$) the physics is controlled by the free orbital fixed point [7, 8], all four states of each dot being accessible. This fixed point is associated with $S_{\rm imp} = \ln(4^3)$ and $n_{\rm imp}(T) = 3$ (also $T\chi_{\rm imp} = 3 \times \frac{1}{8}$; $T\chi_{\rm imp}$ is not shown). On decreasing T below $T \sim t$, all but the two lowest lying states of the TQD are rendered thermally inaccessible. Retaining only the 4-electron singlet and 3-electron doublet states, the system flows to a transition fixed point characterised by $S_{\rm imp} = \ln 3$ and $n_{\rm imp}(T) = 10/3$ (with $T\chi_{\rm imp} = 1/6$). The $\ln 3$ plateau in the entropy persists here until an energy scale $T \sim |E'_\Delta|$, at which point the system flows to its ultimate low temperature fixed point. If $E'_\Delta > 0$, this is the frozen impurity fixed point, with $S_{\rm imp} = 0$ and $n_{\rm imp}(T) = 4$ ($T\chi_{\rm imp} = 0$), corresponding to the 4-electron singlet state. By contrast, if $E'_\Delta < 0$, the ultimate low-temperature fixed point is the local moment fixed point, characterised by $S_{\rm imp} = \ln 2$ and $n_{\rm imp}(T) = 3$ ($T\chi_{\rm imp} = 1/4$). The value of $n_{\rm imp}(T)$ for the transition fixed point is then naturally

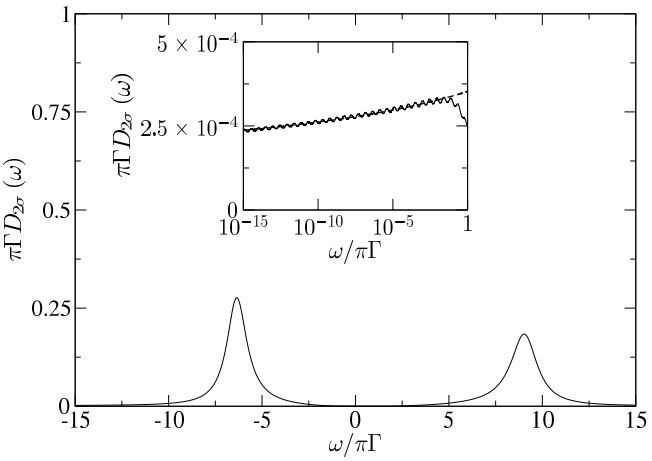


Figure 4.18: The zero-temperature single particle spectrum of dot 2, $\pi\Gamma D_{2\sigma}(\omega)$, for a TQD in the local moment phase of regime III. $\tilde{U} = 10$, $\tilde{t} = 5$ and $\tilde{t}' = 2.4$. The inset shows the low frequency behaviour, fitted to a line of form $\pi\Gamma D_{2\sigma}(\omega) = a/\ln^2(|\omega|/T_0)$.

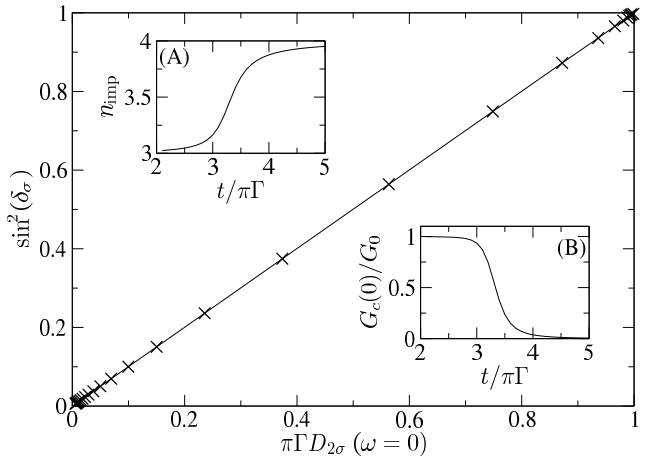


Figure 4.19: The zero-temperature single particle spectrum, $\pi\Gamma D_{2\sigma}(\omega)$, plotted against $\sin^2(\delta_\sigma)$ (with δ_σ the static scattering phase shift) for a TQD crossing from regime II to III in the strong coupling phase. $\tilde{U} = 10$, $\tilde{t}' = 6$ and $2 < \tilde{t} < 5$; inset A shows $n_{\rm imp}|_{T=0}$ as a function of $\tilde{t}$, whilst inset B shows the zero temperature conductance, $G_c(0)/G_0$, as a function of $\tilde{t}$.

given by $n_{\rm imp}^{TFP}(T) = \frac{1}{3}(n_{\rm imp}^{SC}(T) + 2n_{\rm imp}^{LM}(T)) = 10/3$. Exactly at the point $E'_\Delta = 0$ (corresponding to $t' \approx U/4$), the transition fixed point persists down to $T = 0$.

4.8.3 Dynamics and the Friedel-Luttinger Sum Rule

The relationship between the zero-temperature conductance, zero-temperature, zero-frequency single particle spectrum of dot 2, $\pi\Gamma D_{2\sigma}(\omega = 0)$, and the static scattering

phase shift, $\delta_\sigma = \pi n_{\mathrm{imp},\sigma}|_{T=0} + I_{\mathrm{L}}$, is given by Eq. 4.7. We find generically, by direct calculation, that $I_{\mathrm{L}} = \mathrm{Im}\,\mathrm{Tr}\int_{-\infty}^{0} d\omega \frac{\partial \mathbf{\Sigma}_\sigma}{\partial \omega}\mathbf{G}_\sigma = 0$ in the strong coupling phase (as expected for a Fermi liquid [120]), and $|I_{\mathrm{L}}| = \frac{\pi}{2}$ in the local moment phase (in agreement with the results of Logan *et al.* [55] for a singular Fermi liquid). These results were, as for regime I ($J < 10T_{\mathrm{K}}$), anticipated as both strong coupling and local moment phases are continuously connected to their counterparts in regime II ($J > 10T_{\mathrm{K}}$). As $n_{\mathrm{imp},\sigma}|_{T=0} = \frac{1}{2}n_{\mathrm{imp}} = 2$ in the strong coupling phase of regime III ($n_{\mathrm{imp}} = n_{\mathrm{imp}}(T=0)$) and $n_{\mathrm{imp},\sigma}|_{T=0} = \frac{1}{2}n_{\mathrm{imp}} = 3/2$ in the local moment phase it follows immediately that $G_c(0)/G_0 = 0$ in *both* phases here — results that are confirmed via direct calculation of the zero-temperature conductance using the NRG — although the approach to $D_{2\sigma}(\omega = 0)$ and $G_c(0)$ in the local moment phase is characterised by marginally irrelevant logarithmic corrections [127] as expected for a local moment state (Fig. 4.18). These corrections are unsurprisingly absent in the strong coupling phase. It is also found that the zero-temperature conductance at the transition, $G_c^{TFP}(0)/G_0 = 0$, the increase in conductance one might expect to observe when the singly and doubly occupied states of an orbital (in this case the o orbital) are degenerate, the so-called Coulomb blockade peak [128–132], being suppressed by the change in parity occurring across the transition. We also note that the positive and negative frequency Hubbard satellites in Fig. 4.18 are no longer equivalent: this is because the full model Hamiltonian (unlike the spin model) is not particle-hole symmetric, as discussed in Sec. 4.2.

We find that $n_{\mathrm{imp}}^{SC} = 4$ in regime III, but $n_{\mathrm{imp}}^{SC} = 3$ for regime II ($J > 10T_{\mathrm{K}}$) (Sec. 4.5). As $I_{\mathrm{L}} = 0$ throughout the strong coupling phase, this change in n_{imp} must be associated with a change in $G_c(0)/G_0$. The insets to Fig. 4.19 show that as the TQD moves from regime II to III, there is a continuous change in n_{imp} from 3 to 4, associated with a continuous fall in $G_c(0)$, from $G_c(0)/G_0 = 1$ in regime II ($J > 10T_{\mathrm{K}}$) to $G_c(0)/G_0 = 0$ in regime III.

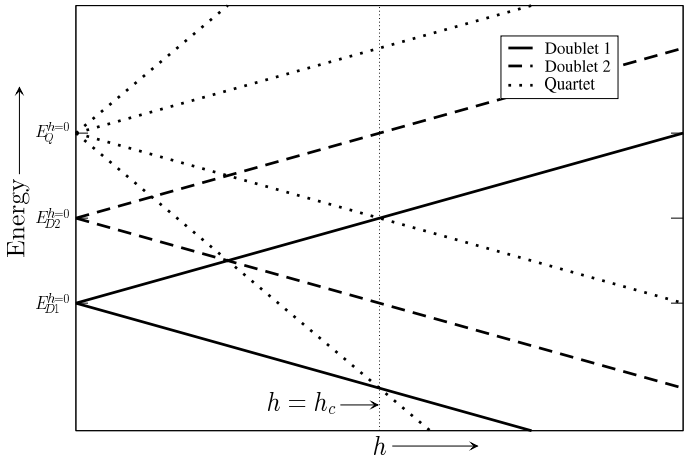


Figure 4.20: A schematic illustration of effect of an applied field, h, upon the energies of the eigenstates of the isolated trimer, given in Table 4.1. The 'critical' field, h_c, at which the lowest lying doublet and quartet states cross is indicated on the figure, as are the energies of the quartet ($E_Q^{h=0}$) and two doublets ($E_{D1}^{h=0}$ and $E_{D2}^{h=0}$) in the absence of a field.

4.9 Magnetic Fields

We consider now the effect of a magnetic field ($h \neq 0$ in Eq. 4.1) upon the TQD, with the aim of providing simple physical arguments and intuitive low energy effective models to accurately explain the behaviour of the system under a field in all regimes. We discuss the regimes in the same order as in the preceding work, considering first regime II, then regime I and finally regime III (see Fig. 4.2).

4.10 Magnetic Fields: Regime II: $J > 10T_{\mathrm{K}}$

4.10.1 Effective Low Energy Models

Under standard transformations [13] an applied field adds an additional term to the effective spin model (Eq. 4.4), which is now $\hat{H}^h_{spin} = \hat{H}_{spin} + \hat{H}_h$ with $\hat{H}_h = -2h\hat{S}^z = -2h(\hat{S}^z_1 + \hat{S}^z_2 + \hat{S}^z_3)$, which stabilises states with $S^z > 0$. In the presence of a field $h \gg T_{\mathrm{K}}$, such that any zero-field Kondo effects are suppressed, the ground state of the trimer is one of three states: $|\frac{1}{2}; -; +\frac{1}{2}\rangle$ ($E_- = -J + \frac{1}{4}J' - h$), $|\frac{1}{2}; +; +\frac{1}{2}\rangle$ ($E_+ = -\frac{3}{4}J' - h$) or $|\frac{3}{2}; -; +\frac{3}{2}\rangle$ ($E_Q = \frac{1}{2}J + \frac{1}{4}J' - 3h$), as illustrated schematically

in Fig. 4.20. The former two are components of the (−)- and (+)- parity doublets which comprise the low energy manifold for the system in the absence of a field (Sec. 4.5), whilst the latter is a component of the quartet state, which is always the highest energy state of the TQD in this regime when there is no field. $|\frac{3}{2};-;+\frac{3}{2}\rangle$ is also the ultimate low-temperature ground state in the limit of large h ($h \gg J, J'$).

All systems within regime II are therefore found to fall into one of two distinct categories. In the first the system lies in the strong coupling phase when $h = 0$ ($J' > J$ — Sec. 4.5). Here, for fields $h \gg T_{\mathrm{K}}$, the ground state of the isolated trimer is either the $|\frac{1}{2};+;+\frac{1}{2}\rangle$ component of the (+)-parity doublet, or the $|\frac{3}{2};-;+\frac{3}{2}\rangle$ component of the (−)-parity quartet. We refer to this as the 'strong coupling case'. In the second the system lies in the local moment phase when $h = 0$ ($J' < J$ — Sec. 4.5), and hence the ground state of the isolated trimer when $h > 0$ is either the $|\frac{1}{2};-;+\frac{1}{2}\rangle$ component of the (−)-parity doublet, or the $|\frac{3}{2};-;+\frac{3}{2}\rangle$ component of the (−)-parity quartet. We refer to this as the 'local moment case'. Distinct physics are observed in these two cases and they are treated separately.

4.10.1.1 The Strong Coupling Case

A weak field ($h \lesssim T_{\mathrm{K}}$) will not affect the low temperature behaviour of a system in the strong coupling case. The system will, therefore, continue to be described down to zero temperature by Eq. 4.10, the low energy effective model for a system in the strong coupling phase of regime II in the absence of a field. Fields $h \geq T_{\mathrm{K}}$ will suppress the (zero-field) Kondo effect, such that for fields $h \gg T_{\mathrm{K}}$ only the $|\frac{1}{2};+;+\frac{1}{2}\rangle$ component of the (+)-parity doublet is thermally accessible at the lowest temperatures. As shown schematically in Fig. 4.20, for a given field, h, the $|\frac{3}{2};-;+\frac{3}{2}\rangle$ state of the isolated trimer is stabilised by $-3h$, whilst the $|\frac{1}{2};+;+\frac{1}{2}\rangle$ state is stabilised by $-h$. Clearly, at some 'critical' field ($h_c = \frac{J'}{2} + \frac{J}{4}$, as is readily calculated from the energies of the isolated states, given above) there will be a crossing between these two states. For fields $h \sim h_c \gg T_{\mathrm{K}}$ the unity operator

spanning the reduced Hilbert space of the low energy manifold is therefore $\hat{1} = \hat{1}_+ + \hat{1}_- = |\frac{1}{2};+;+\frac{1}{2}\rangle\langle\frac{1}{2};+;+\frac{1}{2}| + |\frac{3}{2};-;+\frac{3}{2}\rangle\langle\frac{3}{2};-;+\frac{3}{2}|$ and, projecting into the low energy manifold, the low energy effective model follows immediately as $\hat{H}_{eff} = \hat{1}\hat{H}^h_{spin}\hat{1}$ i.e.

$$\hat{H}_{eff} = J_{\rm K}\hat{1}\hat{\mathbf{S}}_2\hat{1}\cdot\hat{\mathbf{S}}(0) + \frac{1}{2}E_\Delta(\hat{1}_+ - \hat{1}_-) + \hat{H}_L \tag{4.30}$$

where $E_\Delta = E_+ - E_Q = -J' - \frac{1}{2}J + 2h$ is the energy separation between $|\frac{1}{2};+;+\frac{1}{2}\rangle$ and $|\frac{3}{2};-;+\frac{3}{2}\rangle$ and the common constant $\frac{1}{2}(E_Q + E_+)\hat{1}$ is neglected. We define a pseudospin operator,

$$\hat{\mathcal{T}}^z = \frac{1}{2}(\hat{1}_+ - \hat{1}_-), \tag{4.31}$$

such that $|\frac{1}{2};+;+\frac{1}{2}\rangle$ and $|\frac{3}{2};-;+\frac{3}{2}\rangle$ are eigenstates of it; $\hat{\mathcal{T}}^z|S;\pm;S^z\rangle = \pm\frac{1}{2}|S;\pm;S^z\rangle$. Evaluating $\hat{1}\hat{\mathbf{S}}_2\hat{1}$, we find that $\hat{1}\hat{S}^\pm_2\hat{1} = 0$ and $\hat{1}\hat{S}^z_2\hat{1} = +\frac{1}{2}\hat{1}$ (as is immediately obvious from Table 4.1), and so the low energy effective model follows immediately as

$$\hat{H}_{eff} = E_\Delta\hat{\mathcal{T}}^z + \hat{H}_L + \frac{J_{\rm K}}{2}\hat{S}^z(0). \tag{4.32}$$

The model here is a simple uncoupled two level system, with potential scattering. When $E_\Delta < 0$ ($h < \frac{J'}{2}+\frac{J}{4}$) $|\frac{1}{2};+;+\frac{1}{2}\rangle$ is the ground state and when $E_\Delta > 0$ $|\frac{3}{2};-;+\frac{3}{2}\rangle$ is the ground state. The transition between these two phases takes the form of a simple level crossing, just as one would expect given the parity change across the phase boundary, occurring when $E_\Delta = 0$, corresponding to $h = h_c = \frac{J'}{2}+\frac{J}{4}$. Exactly at this point, the system is described down to $T = 0$ by a transition fixed point[7]. As the two states in the low energy manifold have distinct parities Eq. 4.32 is separable into distinct pseudospin sectors, reflecting the strict conservation of $1 \leftrightarrow 3$ parity, with the $E_\Delta\hat{\mathcal{T}}^z$ term acting as an effective magnetic field upon the pseudospin.

[7]This is *not* the transition fixed point which defines the boundary between strong coupling and local moment phases in the absence of a field.

4.10.1.2 The Local Moment Case

In the local moment case, for all fields $h > 0$ only the $|\frac{1}{2};-;+\frac{1}{2}\rangle$ component of the $(-)$-parity doublet is accessible on the lowest energy scales. Just as in the strong coupling case the $|\frac{1}{2};-;+\frac{1}{2}\rangle$ state of the isolated trimer is stabilised less than the $|\frac{3}{2};-;+\frac{3}{2}\rangle$ state by an applied field, and so at some 'critical' field ($h_c = \frac{3}{4}J$, again easily determined from the energies of the isolated states, given above) the two states will cross.

For fields $h \sim h_c$ the unity operator spanning the reduced Hilbert space of the low energy manifold is therefore $\hat{1} = \hat{1}_+ + \hat{1}_- = |\frac{1}{2};-;+\frac{1}{2}\rangle\langle\frac{1}{2};-;+\frac{1}{2}| + |\frac{3}{2};-;+\frac{3}{2}\rangle\langle\frac{3}{2};-;+\frac{3}{2}|$. Projecting into the low energy manifold, the low energy effective model then follows as $\hat{H}_{eff} = \hat{1}\hat{H}^h_{spin}\hat{1}$ i.e. $\hat{H}_{eff} = J_{\rm K}\hat{1}\hat{\mathbf{S}}_2\hat{1}\cdot\hat{\mathbf{S}}(0) + \frac{1}{2}E_\Delta(\hat{1}_+ - \hat{1}_-) + \hat{H}_L$ where $E_\Delta = E_- - E_Q = -\frac{3}{2}J + 2h$ is the energy separation between $|\frac{1}{2};-;+\frac{1}{2}\rangle$ and $|\frac{3}{2};-;+\frac{3}{2}\rangle$. We define a pseudospin operator,

$$\hat{\mathcal{T}}^z = \frac{1}{2}(\hat{1}_+ - \hat{1}_-), \tag{4.33a}$$

$$\hat{\mathcal{T}}^+ = |\tfrac{1}{2};-;+\tfrac{1}{2}\rangle\langle\tfrac{3}{2};-;+\tfrac{3}{2}|, \tag{4.33b}$$

$$\hat{\mathcal{T}}^- = |\tfrac{3}{2};-;+\tfrac{3}{2}\rangle\langle\tfrac{1}{2};-;+\tfrac{1}{2}| \tag{4.33c}$$

such that $|\frac{1}{2};-;+\frac{1}{2}\rangle$ and $|\frac{3}{2};-;+\frac{3}{2}\rangle$ are eigenstates of $\hat{\mathcal{T}}^z$; $\hat{\mathcal{T}}^z|\frac{1}{2};-;+\frac{1}{2}\rangle = +\frac{1}{2}|\frac{1}{2};-;+\frac{1}{2}\rangle$ and $\hat{\mathcal{T}}^z|\frac{3}{2};-;+\frac{3}{2}\rangle = -\frac{1}{2}|\frac{3}{2};-;+\frac{3}{2}\rangle$. Evaluating $\hat{1}\hat{\mathbf{S}}_2\hat{1}$ we find that $\hat{1}_\pm\hat{\mathbf{S}}_2\hat{1}_\mp \neq 0$, unlike the strong coupling case, as both the $|\frac{1}{2};-;+\frac{1}{2}\rangle$ and $|\frac{3}{2};-;+\frac{3}{2}\rangle$ states are of $(-)$-parity. The low energy effective model then follows as

$$\begin{aligned}\hat{H}_{eff} =& \frac{1}{2}J_{\rm K,\perp}\hat{\mathcal{T}}^+\hat{S}^-(0) + \frac{1}{2}J_{\rm K,\perp}\hat{\mathcal{T}}^-\hat{S}^+(0) \\ &+ J_{\rm K,z}\hat{\mathcal{T}}^z\hat{S}^z(0) + E_\Delta\hat{\mathcal{T}}^z + \hat{H}_L: \text{ Regime II},\end{aligned} \tag{4.34}$$

where potential scattering is neglected for clarity. The coupling constants are given

by

$$J_{\mathrm{K},\perp} = -\frac{2J_{\mathrm{K}}}{\sqrt{6}}, \tag{4.35a}$$

$$J_{\mathrm{K},z} = \frac{2}{3}J_{\mathrm{K}}. \tag{4.35b}$$

Eq. 4.34 takes the form of a spin-anisotropic antiferromagnetic Kondo model under an effective magnetic field, E_Δ. When $|E_\Delta| \gg 0$ only one state will be thermally accessible at low T (corresponding to $T < |E_\Delta|$) — $|\frac{1}{2};-;+\frac{1}{2}\rangle$ when $E_\Delta < 0$ and $|\frac{3}{2};-;+\frac{3}{2}\rangle$ when $E_\Delta > 0$. For small E_Δ (in practice $|E_\Delta| < T_{\mathrm{K}}^h$, with T_{K}^h the Kondo temperature for Eq. 4.34) Kondo physics (including an enhanced conductance at low T) should be observed, as the pseudospin is quenched by coupling to the conduction band. This is a most interesting result, as we predict that applying a field to a system which does not exhibit Kondo physics when $h = 0$ will give rise to a finite-field Kondo effect, whilst applying a field to a system which *does* undergo a Kondo effect at zero-field (the strong coupling case) will not. As noted above, the $E_\Delta \hat{\mathcal{T}}^z$ term in Eq. 4.34 acts as an effective magnetic field upon the low energy effective model, and so will suppress the field-induced Kondo physics of the system when $|E_\Delta| \gg T_{\mathrm{K}}^h$, as one would expect from the results of Sec. 3.8.

In this system we may use Anderson's Poor Man's Scaling technique [2, 14] (as described in Sec. 2.2) to estimate the Kondo temperature of the system. The details of this calculation are given in Appendix F. The important result here is that

$$\frac{T_{\mathrm{K}}^h}{D} \propto \exp\left\{-\frac{3}{\sqrt{2}\rho J_{\mathrm{K}}}\left(\frac{\pi}{2} - \arctan\sqrt{2}\right)\right\} \approx \exp\left\{-\frac{1.3056}{\rho J_{\mathrm{K}}}\right\}, \tag{4.36}$$

and so $\ln T_{\mathrm{K}}^h$ is expected to vary linearly with $\frac{1}{\rho J_{\mathrm{K}}}$.

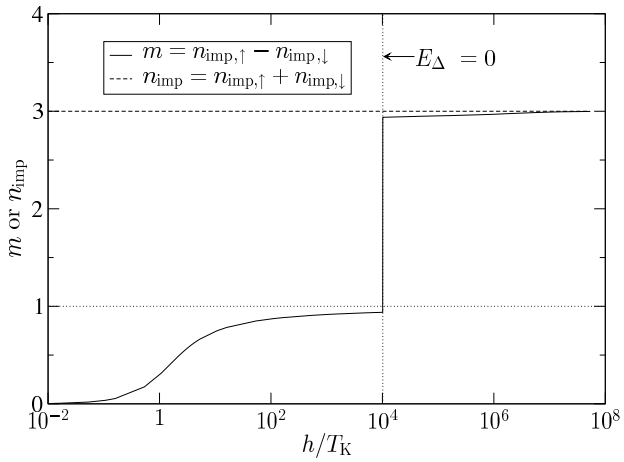


Figure 4.21: Excess impurity charge $n_{\mathrm{imp}} = n_{\mathrm{imp},\uparrow}|_{T=0} + n_{\mathrm{imp}\downarrow}|_{T=0}$ and $m = n_{\mathrm{imp},\uparrow}|_{T=0} - n_{\mathrm{imp}\downarrow}|_{T=0}$ vs applied magnetic field h/T_{K} for a TQD in the strong coupling phase when $h = 0$ with $\tilde{U} = 10$, $\tilde{t} = 10^{-1}$ and $\tilde{t}' = 3 \times 10^{-1}$. The point where $E_\Delta = 0$ ($h = h_c$) is also shown on the figure.

4.10.2 Thermodynamics

4.10.2.1 The Strong Coupling Case

In the strong coupling case ($J' > J$) a small field ($h \ll T_{\mathrm{K}}$) has no discernible effect upon the physics of the system, just as one would expect given the corresponding results for the single impurity Anderson model [122, 123] — see Sec. 3.8. The spin up and spin down electronic populations of the TQD remain equal and so $m = n_{\mathrm{imp},\uparrow}|_{T=0} - n_{\mathrm{imp},\downarrow}|_{T=0} = 0$ ($n_{\mathrm{imp}} = n_{\mathrm{imp},\uparrow}|_{T=0} + n_{\mathrm{imp},\downarrow}|_{T=0} = 3$). As shown in Fig. 4.21, when h is increased through $\sim T_{\mathrm{K}}$ the Kondo effect is suppressed, and $|\frac{1}{2};+;+\frac{1}{2}\rangle$ asymptotically becomes the ground state of the TQD. This leads to an increase in m, which approaches 1 asymptotically ($m = 1$ being characteristic of a free $|\frac{1}{2};\pm;+\frac{1}{2}\rangle$ TQD ground state).

This behaviour changes abruptly at $h \simeq h_c$ ($E_\Delta \simeq 0$ — as accurately predicted by the low energy effective model, Eq. 4.32), where a sharp change in m is seen, with m increasing to ~ 3, characteristic of a $|\frac{3}{2};-;+\frac{3}{2}\rangle$ TQD ground state. As predicted by Eq. 4.32, the change in m here is discontinuous (due to the parity change across the transition). This behaviour is illustrated in Fig. 4.21. We find that for all fields $h > 0$ $S_{\mathrm{imp}}(T = 0) = 0$ and $T\chi_{\mathrm{imp}} = 0$, except when the system lies on the phase

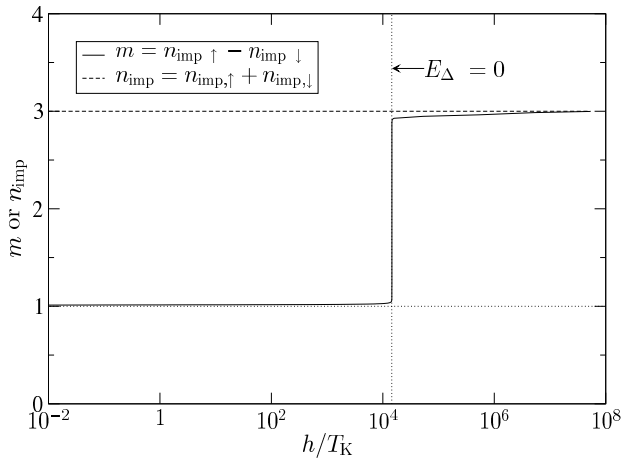


Figure 4.22: Excess impurity charge $n_{\rm imp} = n_{{\rm imp},\uparrow}|_{T=0} + n_{{\rm imp}\downarrow}|_{T=0}$ and $m = n_{{\rm imp},\uparrow}|_{T=0} - n_{{\rm imp}\downarrow}|_{T=0}$ vs applied magnetic field $h/T_{\rm K}$ for a TQD in the local moment phase when $h = 0$ with $\tilde{U} = 10$, $\tilde{t} = 3 \times 10^{-1}$ and $\tilde{t'} = 10^{-1}$. The point where $E_\Delta = 0$ ($h = h_c$) is also shown on the figure.

boundary ($E_\Delta = 0$), where the system is described down to zero temperature by the local moment fixed point ($S_{\rm imp}(T = 0) = \ln 2$ and $T\chi_{\rm imp}|_{T=0} = \frac{1}{4}$), as predicted by Eq. 4.32.

4.10.2.2 The Local Moment Case

Any non-zero h will lift the degeneracy of the $|\frac{1}{2}; -; S^z\rangle$ doublet, and we therefore expect to find that $m = 1$ for all $h > 0$ when $h < h_c$: as shown in Fig. 4.22 this is exactly what is found using the NRG. As in the strong coupling case, for $h \gg h_c$ the TQD ground state is $|\frac{3}{2}; -; +\frac{3}{2}\rangle$, characterised by $m = 3$. When $h \simeq h_c$ there is a sharp but continuous crossover between these two regions (m increases from 1 to 3), as shown in in Fig. 4.22 (Eq. 4.34 predicts the position of this crossover accurately).

In addition, Kondo physics is observed when E_Δ is small ($|E_\Delta| < T_{\rm K}^h$; $T_{\rm K}^h$ is defined via $S_{\rm imp}(T_{\rm K}^h) = 0.5 \ln 2$ for a system with $E_\Delta = 0$, corresponding to $m = 2$), as predicted by the low energy effective model (Eq. 4.34), and now shown.

Fig. 4.23 and its inset show $S_{\rm imp}$ and $T\chi_{\rm imp}$ for a system with $E_\Delta \simeq 0$. The system is initially at the free orbital fixed point, characterised by $S_{\rm imp} = \ln 4^3$ and $T\chi_{\rm imp} = 3 \times \frac{1}{8}$, but flows away from that fixed point on an energy scale $T \sim U$, as

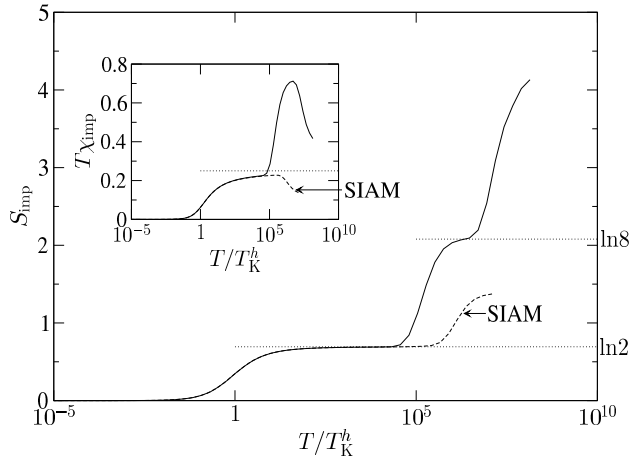


Figure 4.23: Entropy $S_{\rm imp}$ vs $T/T_{\rm K}^h$ for a TQD in the local moment phase when $h = 0$ with $E_\Delta \simeq 0$; $\tilde{U} = 10$, $\tilde{t} = 3 \times 10^{-1}$, $\tilde{t}' = 10^{-1}$ and $h = 2.733441 \times 10^{-2} \simeq h_c$. $T_{\rm K}^h$ is defined via $S_{\rm imp}(T_{\rm K}^h) = 0.5 \ln 2$. The inset shows $T\chi_{\rm imp}$ for the same system. The dashed lines are data for a SIAM with $\tilde{U} = 10$, scaled by $T_{\rm K}$.

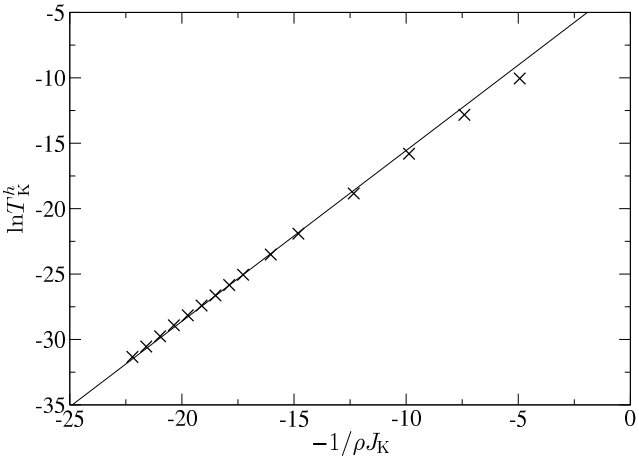


Figure 4.24: $\ln T_{\rm K}^h$ plotted against $-1/\rho J_{\rm K}$ for a range of systems with $E_\Delta = 0$, $\tilde{J} = 1.6 \times 10^{-2}$ and $\tilde{J}' = 4 \times 10^{-3}$. $\tilde{U}$ is varied and $T_{\rm K}^h$ is defined via $S_{\rm imp}(T_{\rm K}^h) = 0.5 \ln 2$. The solid line is $T_{\rm K}^h = A \exp(-1.3056/\rho J_{\rm K})$, the expression for $T_{\rm K}^h$ derived from Poor Man's Scaling.

the empty and doubly occupied states of the TQD are projected out. Below this scale $S_{\rm imp} = \ln 8$ and $T\chi_{\rm imp} = 3 \times \frac{1}{4}$, characteristic of three free spins. Reducing the temperature further, through $T \sim J$, renders all but the two lowest energy states of the trimer, $|\frac{1}{2}; -; +\frac{1}{2}\rangle$ and $|\frac{3}{2}; -; +\frac{3}{2}\rangle$, thermally inaccessible, and so the system flows to the local moment fixed point ($S_{\rm imp} = \ln 2$ and $T\chi_{\rm imp} = \frac{1}{4}$) below this temperature. Finally, the pseudospin is Kondo quenched on an energy scale $T_{\rm K}^h$,

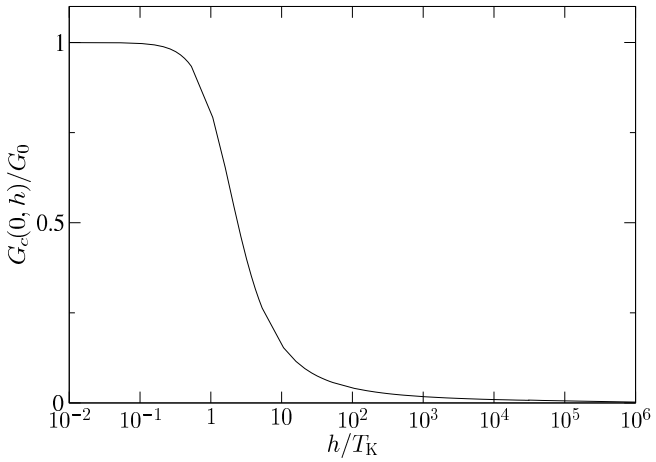


Figure 4.25: $G_c(0,h)/G_0$ as a function of h/T_K for a system deep in the strong coupling phase in the absence of a field; $\tilde{U} = 10$, $\tilde{t} = 3 \times 10^{-1}$ and $\tilde{t}' = 5 \times 10^{-2}$.

and the system flows to the strong coupling fixed point, characterised by $S_{\rm imp} = 0$ and $T\chi_{\rm imp} = 0$. In both the entropy and $T\chi_{\rm imp}$ the flow from the local moment to the strong coupling fixed point can be shown to take the characteristic universal form of the SIAM (dashed lines in Fig. 4.23), this arising quite naturally from the antiferromagnetic spin-$\frac{1}{2}$ Kondo effective low energy model which may be derived in both cases. We predicted in the previous section that $T_{\rm K}^h \propto \exp(-1.3056/\rho J_{\rm K})$; as illustrated in Fig. 4.24 this relationship is confirmed by our NRG results for small $T_{\rm K}^h$. We generically find that $S_{\rm imp}(T=0) = 0$ and $T\chi_{\rm imp}|_{T=0} = 0$ in the local moment case, for all $h \neq 0$.

4.10.3 Dynamics

It is generically found (by direct calculation using the NRG) that the Luttinger integral $I_{\rm L} = {\rm Im\,Tr} \int_{-\infty}^{0} d\omega \frac{\partial \mathbf{\Sigma}_\sigma}{\partial \omega} \mathbf{G}_\sigma = 0$ in *both* the strong coupling and local moment cases, for all $h \neq 0$ — similar results were reported by Wright *et al.* [133] for a two-level system under an applied field. In the strong coupling case the suppression of the Kondo effect by $h \gtrsim T_{\rm K}$ naturally gives rise to a drop off in the $T = 0$ conductance (Fig. 4.25), which falls to zero at $h \gg T_{\rm K}$, where, as discussed above, we define $T_{\rm K}$ as the Kondo temperature for a SIAM with the same U and Γ (this

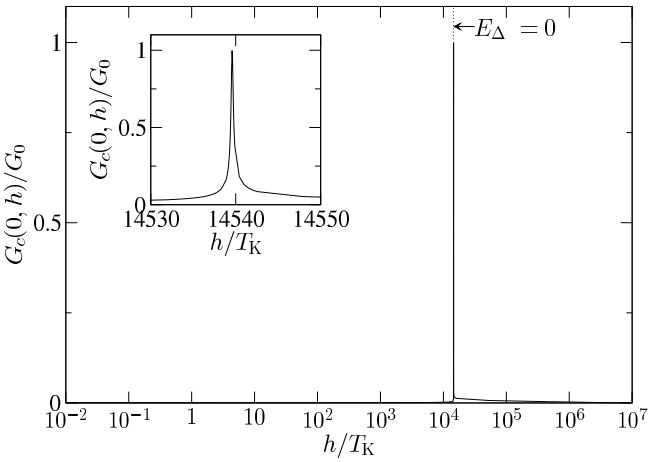


Figure 4.26: $G_c(0,h)/G_0$ as a function of h/T_K for a system deep in the local moment phase in the absence of a field; $\tilde{U} = 10$, $\tilde{t} = 3 \times 10^{-1}$ and $\tilde{t}' = 10^{-1}$. The inset shows the conductance peak on a linear scale.

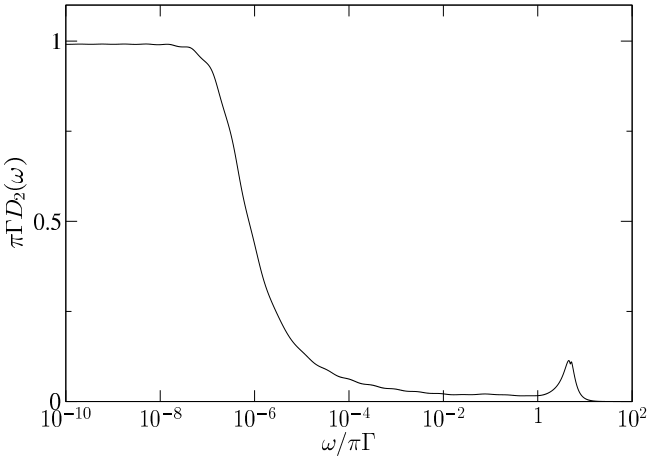


Figure 4.27: The total spectral density of dot 2, $\pi\Gamma D_2(\omega) = \frac{1}{2}\pi\Gamma(D_{2\uparrow}(\omega) + D_{2\downarrow}(\omega))$, for the same parameter set as Fig. 4.23.

behaviour is just that of the SIAM under an applied field — see Sec. 3.8, and in particular compare Fig. 4.25 with the inset to Fig. 3.9).

In the local moment case (see Fig. 4.26) Kondo quenching of the pseudospin leads to an enhanced $T = 0$ conductance in the region $E_\Delta \simeq 0$ ($h \simeq h_c = \frac{3}{4}J$), the conductance rising to the unitarity limit precisely when $E_\Delta = 0$. As shown in Fig. 4.27, the Kondo effect here also naturally gives rise to a Kondo resonance, identical to that of the SIAM, in the total spectral density of dot 2, $\pi\Gamma D_2(\omega)$.

4.11 Magnetic Fields: Regime I: $J < 10T_{\rm K}$

4.11.1 Effective Low Energy Models

We now discuss the effect of magnetic fields upon systems in regime I (see Fig. 4.2). In this section we build upon Eq. 4.16, the low energy effective model derived for the TQD in regime I in the absence of a field in Sec. 4.7. As in that section we concentrate on the region where $T \ll T_{\rm K}$ (where $T_{\rm K}$ is the Kondo temperature of the isolated dot 2), such that dot 2 is Kondo quenched in the absence of a field. The low energy manifold therefore spans the 1-3 singlet and triplet combinations.

The $h = 0$ ground state of a system in the local moment phase of regime I in the absence of a field is a local moment arising as a result of underscreening of the 1–3 triplet (which occurs on an energy scale $T \sim T_{\rm K}^* \ll T_{\rm K}$), as described in Sec. 4.7.1. Any field $h > 0$ will lift the degeneracy of the doublet state which arises as a result of the underscreening, but a field $0 < h < T_{\rm K}^*$ is not expected to have any other effect upon the system. Fields $T_{\rm K}^* \leq h \ll T_{\rm K}$ will suppress underscreening of the 1–3 triplet, such that for fields $T_{\rm K}^* \ll h \ll T_{\rm K}$ only the $S^z = +1$ component of the triplet will be accessible at the lowest temperatures. Increasing the field field further, such that $h \gg T_{\rm K}$, will suppress Kondo quenching of dot 2, and so the ultimate high field ground state of the isolated trimer is $|\frac{3}{2}; -; +\frac{3}{2}\rangle$, just as in regime II (Sec. 4.10.1).

Turning our attention to systems in the strong coupling phase of regime I in the absence of a field, it is clear that the 1–3 singlet state is unaffected by an applied field. However, as the $S^z = +1$ component of the 1–3 triplet is stabilised by the field (when $h > T_{\rm K}^*$), there must exist some 'critical' field ($h_c = \frac{1}{2}(J' - \lambda\frac{J^2}{T_{\rm K}})$, as easily determined from the energies of the states in the absence of a field) at which these states cross. For $h \sim h_c$ the unity operator for the reduced Hilbert space of the low energy manifold is therefore $\hat{1} = \hat{1}_+ + \hat{1}_- = |0; +; 0\rangle\langle 0; +; 0| + |1; -; +1\rangle\langle 1; -; +1|$, and, using identical arguments to Sec. 4.7.1, it immediately follows that the low

energy effective model is

$$\hat{H}_{eff} = -E'_{\Delta}\hat{\mathcal{T}}^{z} + H_{L} : \text{ Regime I} \tag{4.37}$$

where

$$E'_{\Delta} = J' - \lambda\frac{J^2}{T_{\mathrm{K}}} - 2h. \tag{4.38}$$

is the energy separation between the two states ($\lambda \approx 0.1$ is an NRG-derived constant), and we define a pseudospin

$$\hat{\mathcal{T}}^{z} = \tfrac{1}{2}(\hat{1}_{+} - \hat{1}_{-}), \tag{4.39}$$

such that $|0;+;0\rangle$ and $|1;-;+1\rangle$ are eigenstates of $\hat{\mathcal{T}}^{z}$ with eigenvalues $\pm\frac{1}{2}$ respectively.

Eq. 4.37 takes the form of a simple uncoupled two level system, and is separable into distinct pseudospin sectors, this arising naturally from the strict conservation of $1 \leftrightarrow 3$ parity symmetry. For $E'_{\Delta} > 0$ the $(-)$-parity sector can be neglected, as the ground state is the 1-3 singlet state, which lies in the $(+)$-parity subsector. This state is effectively decoupled from the conduction band, as one would expect for an inert singlet. By contrast, if $E'_{\Delta} < 0$ (the local moment case) the ground state is $|1;-;+1\rangle$, and the $(+)$-parity subsector may be neglected at low temperatures. As only a single component of the triplet is retained at low temperature, this state is also effectively decoupled from the conduction band. Precisely at the quantum phase transition the system is described by the full Eq. 4.37 and both $(+)$- and $(-)$-parity states must be retained down to the lowest temperatures. The system here is characterised by a transition fixed point with $S_{\mathrm{imp}} = \ln 2$ and $T\chi_{\mathrm{imp}} = \frac{1}{4}$ (the local moment fixed point), which will describe the system down to zero temperature only when $E'_{\Delta} = 0$. As the quantum phase transition occurs when $E'_{\Delta} = 0$, Eq. 4.38 shows that the phase boundary should satisfy $h = \frac{1}{2}(J' - \lambda\frac{J^2}{T_{\mathrm{K}}})$.

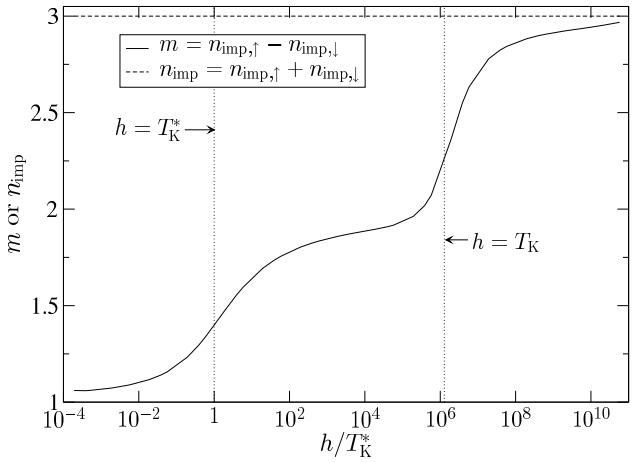


Figure 4.28: $m = n_{\mathrm{imp}\uparrow}|_{T=0} - n_{\mathrm{imp}\downarrow}|_{T=0}$ and $n_{\mathrm{imp}} = n_{\mathrm{imp}\uparrow}|_{T=0} - n_{\mathrm{imp}\downarrow}|_{T=0}$ vs h/T_{K} for a TQD device in the local moment phase of regime I when $h = 0$ with $\tilde{U} = 7$, $\tilde{t} = 7 \times 10^{-3}$ and $\tilde{t}' = 10^{-3}$.

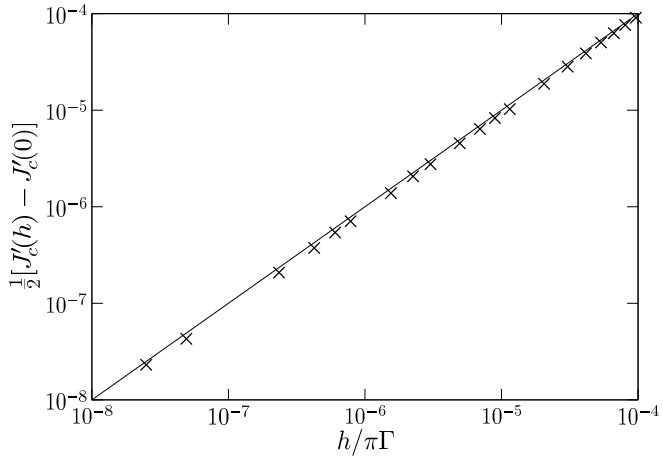


Figure 4.29: The change in J_c', the value of J' at the transition, as a function of $\tilde{h}$ for systems in regime I. $\tilde{U} = 4$ and $\tilde{t} = 3 \times 10^{-2}$ here.

4.11.2 Thermodynamics

As shown in Fig. 4.28, for systems in the local moment phase of regime I in the absence of a field, we find that any $h \neq 0$ lifts the degeneracy of the underscreened triplet, giving rise (for $h < T_{\mathrm{K}}^*$) to a ground state with $S_z = +\frac{1}{2}$, such that $m \to 1$ as $h/T_{\mathrm{K}}^* \to 0^+$, as shown in Fig. 4.28. When $h \sim T_{\mathrm{K}}^*$, the underscreening of the 1-3 triplet is suppressed, and m increases smoothly towards 2 (characteristic of an $S_z = +1$ ground state). Further increasing h through T_{K} suppresses Kondo quenching of spin 2, causing m to rise towards $m = 3$, characteristic of the $|\frac{3}{2}; -; +\frac{3}{2}\rangle$

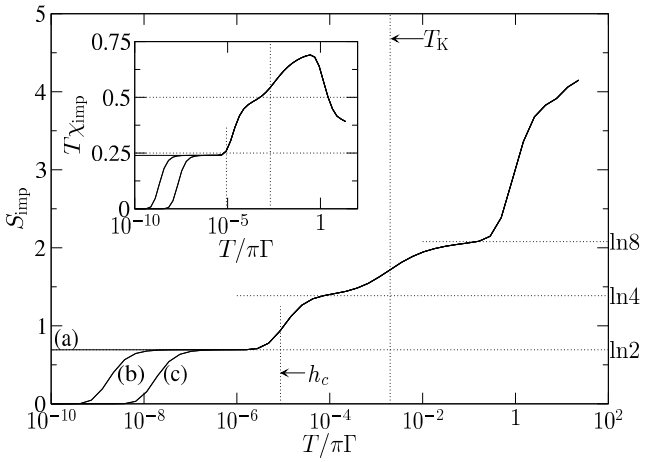


Figure 4.30: Entropy $S_{\rm imp}$ vs $T/\pi\Gamma$ for systems approaching the quantum phase transition in regime I. $\tilde{U} = 4$, $\tilde{t} = 2 \times 10^{-2}$ and $\tilde{t}' = 7 \times 10^{-3}$. $\tilde{h}$ is varied; $h = h_c \pm \lambda T_{\rm K}$ with $\lambda = 0$ for (a), 10^{-6} for (b) and 10^{-5} for (c) with $\tilde{h}_c \simeq 8.68559 \times 10^{-6}$. The inset shows $T\chi_{\rm imp}$ for the same systems.

state which is the ultimate large-h ground state for all TQD described at low energies by $\hat{H}^h_{spin}$.

A system in the strong coupling phase in the absence of a field is unaffected by an applied field $h < h_c \simeq \frac{1}{2}(J' - \lambda\frac{J^2}{T_{\rm K}})$, but, as shown in Fig. 4.29, the value of E'_Δ is found to vary linearly with h, in agreement with Eq. 4.38.

Fig. 4.30 shows the entropy, $S_{\rm imp}$, and $T\chi_{\rm imp}$ for systems close to the phase boundary here. Line (a) in Fig. 4.30 shows the behaviour of a system exactly at the phase boundary (i.e. where $h = h_c$ and so $E'_\Delta = 0$). At high temperature, the system is initially described by the free orbital fixed point ($S_{\rm imp} = \ln 64$ and $T\chi_{\rm imp} = \frac{3}{8}$), but on an energy scale $T \sim U$ the empty and doubly occupied states of the dots become thermally inaccessible, and the entropy falls to $\ln 8$, characteristic of three free spins ($T\chi_{\rm imp} = \frac{3}{4}$). On an energy scale $T \sim T_{\rm K}$ dot 2 is then Kondo quenched, leaving free spins on dots 1 and 3: $S_{\rm imp} = \ln 4$ and $T\chi_{\rm imp} = \frac{1}{2}$. Upon reducing the temperature further, through $T \sim h$, the $S^z = 0$ and $S^z = -1$ components of the triplet become thermally inaccessible, and the system flows to the local moment fixed point ($S_{\rm imp} = \ln 2$ and $T\chi_{\rm imp} = \frac{1}{4}$), which is the ultimate low temperature fixed point of the system at the phase boundary. The system is described by the

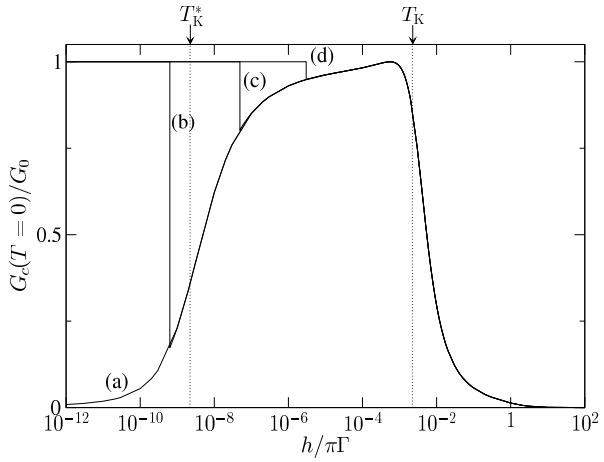


Figure 4.31: $G_c(0,h)/G_0$ vs $h/\pi\Gamma$ for systems in regime I in both the local moment (line (a)) and strong coupling (lines (b)-(d)) phases in the absence of a field. $U/\pi\Gamma = 4$, $t/\pi\Gamma = 3 \times 10^{-2}$ and $\Gamma = 10^{-2}D$. $t'/\pi\Gamma$ is varied: $t'/\pi\Gamma = 6 \times 10^{-3}$ for (a), 6.594×10^{-3} for (b), 6.6×10^{-3} for (c) and 7×10^{-3} for (d).

transition fixed point down to zero temperature only when $E'_\Delta = 0$: when $h \neq h_c$ the system ultimately flows away from the local moment fixed point on an energy scale $T \sim |E'_\Delta|$. In this case the ultimate low temperature fixed point of the system is characterised by $S_{\rm imp} = 0$ and $T\chi_{\rm imp} = 0$, as shown in lines (b) and (c) of Fig. 4.30.

4.11.3 Dynamics

As expected from the corresponding results for regime II ($J > 10T_{\rm K}$), it is generically found that in the presence of a field the Luttinger integral $I_{\rm L} = {\rm Im\,Tr} \int_{-\infty}^{0} d\omega \frac{\partial \mathbf{\Sigma}_\sigma}{\partial \omega} \mathbf{G}_\sigma = 0$ in *both* the strong coupling *and* the local moment phases of regime I. Fig. 4.31 shows the zero-temperature conductance through the TQD for various systems in regime I under an applied field. Line (a) shows the behaviour of a system in the local moment phase when $h = 0$ (i.e. $E'_\Delta < 0$ in Eq. 4.37 for all h). Here we find that the $T = 0$ conductance is negligible for $h < T_{\rm K}^*$, but $G_c(0,h)$ increases rapidly at $h \sim T_{\rm K}^*$, as underscreening of the 1-3 triplet is suppressed. Further increasing h through $T_{\rm K}$ causes the $T = 0$ conductance to fall to zero — a perfectly natural result of suppression of the Kondo quenching of dot 2.

The conductance of systems where the ground state of the isolated trimer is the

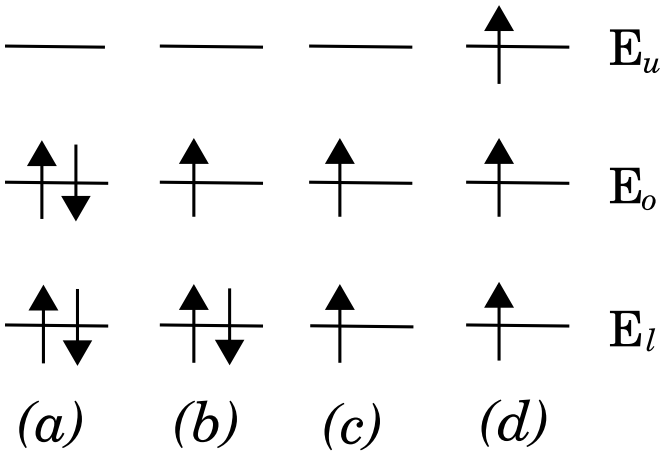


Figure 4.32: A schematic diagram showing (a) the $|0;+;0\rangle$ state, (b) the $|\frac{1}{2};-;+\frac{1}{2}\rangle$ state, (c) the $|1;-;+1\rangle$ state and (d) the $|\frac{3}{2};-;+\frac{3}{2}\rangle$ state.

1–3 singlet is not changed by an applied field, and therefore $G_c(0,h)/G_0 = 1$ for all systems with $E'_\Delta > 0$. However, for all systems in the strong coupling phase of regime I in the absence of a field there exists some $h_c \simeq \frac{1}{2}(J' - \lambda\frac{J^2}{T_K})$, such that for $h > h_c$, $E'_\Delta < 0$, as discussed in Sec. 4.11.1. As shown in lines (b)-(d) of Fig. 4.31, when $E'_\Delta = 0$ there is a discontinuous change in the conductance, from the 1–3 singlet ground state value of $G_c/G_0 = 1$ to the 1–3 triplet ground state value, which varies according to the relative sizes of h, T_K^* and T_K, as discussed previously.

4.12 Magnetic Fields: Regime III: The Orbital Regime

4.12.1 Effective Low Energy Models

As discussed in Sec. 4.8 we may understand the physics of the system in regime III (where $t \geq U$; see Fig. 4.2) by considering the non-interacting TQD Hamiltonian, treating the Coulomb interaction term as a perturbation to the states of $\hat{H}_{NITQD}$. As shown in Sec. 4.8.1, $\hat{H}_{NITQD}$ may be written as a three level system, which allows a simple and physically intuitive description of the behaviour of the TQD in regime III. We continue to use that description when considering the effect of an applied

field upon the TQD. As discussed above, an applied field stabilises states with high S^z more than those with low S^z. As such, it is physically intuitive to expect the ground state of the trimer to be one of the four states illustrated schematically in Fig. 4.32:

$$|0;+;0\rangle = c^\dagger_{o\uparrow}c^\dagger_{o\downarrow}c^\dagger_{l\uparrow}c^\dagger_{l\downarrow}|Vac\rangle, \tag{4.40a}$$

$$|\tfrac{1}{2};-;+\tfrac{1}{2}\rangle = c^\dagger_{o\uparrow}c^\dagger_{l\uparrow}c^\dagger_{l\downarrow}|Vac\rangle, \tag{4.40b}$$

$$|1;-;+1\rangle = c^\dagger_{o\uparrow}c^\dagger_{l\uparrow}|Vac\rangle, \tag{4.40c}$$

$$|\tfrac{3}{2};-;+\tfrac{3}{2}\rangle = c^\dagger_{u\uparrow}c^\dagger_{o\uparrow}c^\dagger_{l\uparrow}|Vac\rangle \equiv c^\dagger_{1\uparrow}c^\dagger_{2\uparrow}c^\dagger_{3\uparrow}|Vac\rangle. \tag{4.40d}$$

The former state has $(+)$-parity, and the latter three states $(-)$-parity (results which follow immediately from the occupation number of the o orbital in these states). $|0;+;0\rangle$ is, of course, the four electron singlet state which is the ground state of the TQD in regime III in the absence of a field when $t' > U/4$, and $|\frac{1}{2};-;+\frac{1}{2}\rangle$ is the $S^z = +\frac{1}{2}$ component of the three electron doublet state which is the ground state of the TQD in regime III in the absence of a field when $t' < U/4$. $|1;-;+1\rangle$ and $|\frac{3}{2};-;+\frac{3}{2}\rangle$ are higher spin states which become accessible only at large fields ($h \sim t$). A given field, h, will stabilise $|+\frac{1}{2};-;+\frac{1}{2}\rangle$ by h, $|1;-;+1\rangle$ by $2h$ and $|+\frac{3}{2};-;+\frac{3}{2}\rangle$ by $3h$, respectively, whilst leaving the energy of the $|0;+;0\rangle$ state unchanged.

Under a weak magnetic field ($h < t$), therefore, the ground state of the isolated trimer is either $|0;+;0\rangle$ or $|\frac{1}{2};-;S^z\rangle$. For a system in the local moment phase in the absence of a field, the ground state of the isolated trimer is $|\frac{1}{2};-;+\frac{1}{2}\rangle$, the $S^z = -\frac{1}{2}$ component of the $(-)$-parity doublet state being destabilised by the applied field. For a system in the strong coupling phase in the absence of a field, the ground state of the isolated trimer is $|0;+;0\rangle$ for weak fields, but at some 'critical' field $h_{c,1} = t' - \epsilon - \frac{U}{2}(1+\gamma^2)$ (which follows immediately from the energies of the states in the absence of a field — see Eq. 4.26 and 4.23) the $|\frac{1}{2};-;+\frac{1}{2}\rangle$ state becomes the ground state of the isolated trimer. For $h \sim h_{c,1}$ the unity operator spanning

the reduced Hilbert space of the low energy manifold is therefore $\hat{1} = \hat{1}_+ + \hat{1}_-$ with $\hat{1}_+ = |0;+;0\rangle\langle 0;+;0|$ and $\hat{1}_- = |\frac{1}{2};-;+\frac{1}{2}\rangle\langle\frac{1}{2};-;+\frac{1}{2}|$, and it immediately follows that the effective Hamiltonian for the model is $\hat{H}'_{eff} = \frac{1}{2}E'_\Delta(\hat{1}_+ - \hat{1}_-)$ (where the common constant $\frac{1}{2}(E_+ + E_-)\hat{1}$ is neglected). We define a pseudospin operator,

$$\hat{\mathcal{T}}^z = \frac{1}{2}(\hat{1}_+ - \hat{1}_-) \tag{4.41}$$

such that $|0;+;0\rangle$ and $|\frac{1}{2};-;+\frac{1}{2}\rangle$ are eigenstates of the operator, with eigenvalues $\pm\frac{1}{2}$, respectively. This gives

$$\hat{H}'_{eff} = E'_\Delta \hat{\mathcal{T}}^z. \tag{4.42}$$

Both the (+)- and (−)-parity states are effectively decoupled from the conduction band here, and it naturally follows that the full low energy effective model here is

$$\hat{H}_{eff} = E'_\Delta \hat{\mathcal{T}}^z + \hat{H}_L. \tag{4.43}$$

This model takes the form of a simple level crossing, with no associated Kondo physics (and hence no enhancement in conductance) predicted due to the change in parity across the phase boundary; when $E'_\Delta < 0$ the ground state is the $|0;+;0\rangle$ state, whilst when $E'_\Delta > 0$ the ground state is the $|\frac{1}{2};-;+\frac{1}{2}\rangle$ state. Close to the transition ($T > |E'_\Delta|$) the system is frustrated, and described by a transition fixed point (the local moment fixed point), which persists to zero temperature only when $E'_\Delta = 0$. E'_Δ is expected to vary linearly with h.

Increasing h further, such that $E'_\Delta \gg 0$, will stabilise the $S^z = +\frac{3}{2}$ state of the TQD, $|\frac{3}{2};-;+\frac{3}{2}\rangle$, and also the $S^z = +1$ component of a triplet state, $|1;-;+1\rangle$. The behaviour of the system then depends upon the relative positions of the crossings between these states. We may determine the energies of these states by using similar perturbative arguments to those leading to Eq. 4.43 and described in Appendix D — first determining the energies of the states in the non-interacting limit, and then treating $\hat{H}_U = \sum_i U\hat{n}_{i\uparrow}\hat{n}_{i\downarrow}$ as a first order perturbation to the states of $\hat{H}_{NITQD}$.

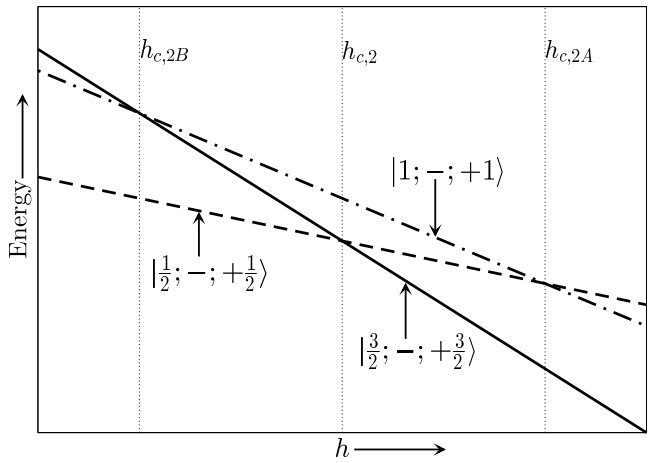


Figure 4.33: A schematic illustration of the relative positions of the energies of low-lying states of the TQD in regime III when $h_{c,2B} < h_{c,2A}$. Clearly in this case the ground state is either the $|\frac{1}{2};-;+\frac{1}{2}\rangle$ state (when $h < h_{c,2}$) or the $|+\frac{3}{2};-;+\frac{3}{2}\rangle$ state (when $h > h_{c,2}$).

As illustrated schematically in Fig. 4.33, if $h_{c,2B} = \epsilon + \frac{1}{2}t' + \frac{1}{2}\sqrt{8t^2 + t'^2}$, the field at which the $|\frac{3}{2};-;+\frac{3}{2}\rangle$ and $|1;-;+1\rangle$ states are degenerate, is smaller than $h_{c,2A} = \frac{1}{2}\sqrt{8t^2 + t'^2} - \epsilon - \frac{t'}{2} - U - \frac{3U}{2}(\gamma^4 - \gamma^2)$, the field at which the $|1;-;+1\rangle$ and $|\frac{1}{2};-;+\frac{1}{2}\rangle$ states are degenerate, then the ground state of the isolated trimer is either $|\frac{1}{2};-;+\frac{1}{2}\rangle$ or $|\frac{3}{2};-;+\frac{3}{2}\rangle$, with the crossover between the two states occurring at a 'critical' field $h_{c,2} = \frac{1}{2}(\sqrt{8t^2 + t'^2} - U - \frac{3U}{2}(\gamma^4 - \gamma^2))$.

When $h \sim h_{c,2}$ the unity operator for the reduced Hilbert space of the low energy manifold is $\hat{1} = \hat{1}_+ + \hat{1}_- = |\frac{3}{2};-;+\frac{3}{2}\rangle\langle\frac{3}{2};-;+\frac{3}{2}| + |\frac{1}{2};-;+\frac{1}{2}\rangle\langle\frac{1}{2};-;+\frac{1}{2}|$. As these states have the same parity, when they are degenerate (i.e. $h \approx h_{c,2}$) a finite-field Kondo effect is naturally expected to arise. The TQD here is an effective two level system (the o-orbital being decoupled from the conduction band), such as that studied in Ref. [134]. The low energy effective model for such a system is generically a spin-anisotropic Kondo model [134], and so the low energy effective model may be written

$$\hat{H}_{eff} = \tfrac{1}{2}J_{\mathrm{K},\perp}\hat{\mathcal{T}}^+\hat{S}^-(0) + \tfrac{1}{2}J_{\mathrm{K},\perp}\hat{\mathcal{T}}^-\hat{S}^+(0) + J_{\mathrm{K},z}\hat{\mathcal{T}}^z\hat{S}^z(0) + E_\Delta\hat{\mathcal{T}}^z + \hat{H}_L, \qquad (4.44)$$

where potential scattering is neglected for clarity, and we define the components of

the pseudospin $\hat{\mathcal{T}}$,

$$\hat{\mathcal{T}}^{+} = |\tfrac{3}{2};-;+\tfrac{3}{2}\rangle\langle\tfrac{1}{2};-;+\tfrac{1}{2}|, \tag{4.45a}$$

$$\hat{\mathcal{T}}^{-} = |\tfrac{1}{2};-;+\tfrac{1}{2}\rangle\langle\tfrac{3}{2};-;+\tfrac{3}{2}|, \tag{4.45b}$$

$$\hat{\mathcal{T}}^{z} = \frac{1}{2}(\hat{1}_{+} - \hat{1}_{-}), \tag{4.45c}$$

such that $|\frac{3}{2};-;+\frac{3}{2}\rangle$ and $|\frac{1}{2};-;+\frac{1}{2}\rangle$ are eigenvectors of the operator $\hat{\mathcal{T}}^{z}$ with eigenvalues $\pm\frac{1}{2}$, respectively. $E_{\Delta} = \sqrt{8t^2 + t'^2} - U - \frac{3U}{2}(\gamma^4 - \gamma^2) - 2h$ is the energy separation between $|\frac{3}{2};-;+\frac{3}{2}\rangle$ and $|\frac{1}{2};-;+\frac{1}{2}\rangle$. This model takes the form of a spin-anisotropic Kondo model under an effective magnetic field, E_{Δ}, and is therefore very similar in form to Eq. 4.34, the low energy effective model for the local moment case of regime II ($J > 10T_{\mathrm{K}}$) under a magnetic field. Just as in that case, we expect to observe a field-induced Kondo effect (arising as a result of a quenching of the pseudospin by coupling to the conduction band) when $|E_{\Delta}| < T_{\mathrm{K}}^{h}$, where T_{K}^{h} is the Kondo temperature of Eq. 4.44. When $|E_{\Delta}| \gg T_{\mathrm{K}}^{h}$ the field-induced Kondo effect will be suppressed, and the ground state will be characterised by $m = 1$ (when $E_{\Delta} > 0$) or $m = 3$ (when $E_{\Delta} < 0$). We may numerically evaluate $J_{\mathrm{K},\perp}$ and $J_{\mathrm{K},z}$ here, using the procedure outlined in Appendix E (just as was done in Sec. 4.8.1). The hybridisation term in $\hat{H}_{ACTM}$ may be expressed as $\hat{H}_{hyb} = \sum_{\mathbf{k},\sigma} V[(\nu c_{l\sigma}^{\dagger} - \gamma c_{u\sigma}^{\dagger})c_{\mathbf{k}\sigma} + H.c.]$ and it is therefore not surprising that we find that in the limit $t \gg t'$ ($\gamma^2 = \nu^2$) Eq. 4.44 reduces to an isotropic Kondo model ($J_{\mathrm{K}z} = |J_{\mathrm{K}\perp}|$), in agreement with the results of Pustilnik *et. al.* [134].

If, on the other hand, $h_{c,2A} < h_{c,2B}$, as illustrated schematically in Fig. 4.34, the transition between a $|\frac{3}{2};-;+\frac{3}{2}\rangle$ and a $|\frac{1}{2};-;+\frac{1}{2}\rangle$ isolated trimer ground state is not direct, but occurs via the triplet state, $|1;-;+1\rangle$. As h is increased, we will therefore see a transition from $|\frac{1}{2};-;+\frac{1}{2}\rangle$ to $|1;-;+1\rangle$, followed by a second transition from $|1;-;+1\rangle$ to $|\frac{3}{2};-;+\frac{3}{2}\rangle$. In this region, the field induced Kondo effect will be suppressed, being replaced by a two stage transition, the first, occurring at $h_{c,2A} = \frac{1}{2}\sqrt{8t^2 + t'^2} - \epsilon - \frac{t'}{2} - U - \frac{3U}{2}(\gamma^4 - \gamma^2)$ taking the system from a $|\frac{1}{2};-;+\frac{1}{2}\rangle$

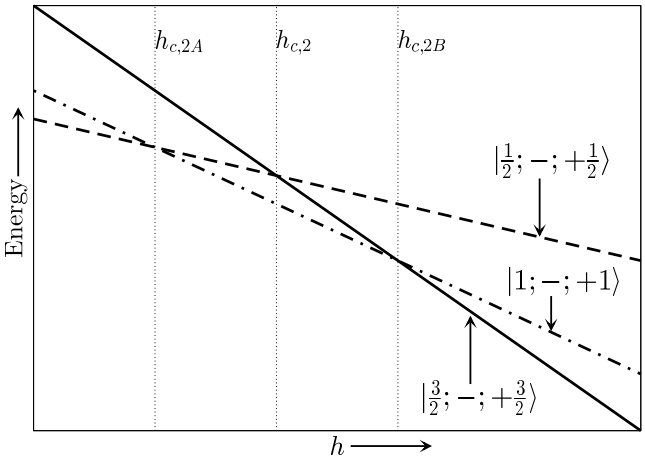


Figure 4.34: A schematic illustration of the relative positions of the energies of low-lying states of the TQD in regime III when $h_{c,2A} < h_{c,2B}$. Clearly in this case the ground state is the $|\frac{1}{2};-;+\frac{1}{2}\rangle$ state when $h < h_{c,2A}$, the $|1;-;+1\rangle$ state when $h_{c,2A} < h < h_{c,2B}$, and the $|+\frac{3}{2};-;+\frac{3}{2}\rangle$ state when $h > h_{c,2B}$.

ground state to a $|1;-;+1\rangle$ ground state, and the second, occurring at $h_{c,2B} = \epsilon + \frac{1}{2}t' + \frac{1}{2}\sqrt{8t^2 + t'^2}$, taking the system to a $|\frac{3}{2};-;+\frac{3}{2}\rangle$ ground state. All three states ($|\frac{1}{2};-;+\frac{1}{2}\rangle$, $|1;-;+1\rangle$ and $|\frac{3}{2};-;+\frac{3}{2}\rangle$) here have the same (odd) parity, and so both transitions should be associated with a continuous change in both $n_{\rm imp}$ and m.

It may easily be shown that the field at which $h_{c,2A} = h_{c,2B}$, where we expect to see a change from a direct transition between the $|\frac{1}{2};-;+\frac{1}{2}\rangle$ ground state and the $|\frac{3}{2};-;+\frac{3}{2}\rangle$ ground state to one mediated via a $|1;-;+1\rangle$ ground state, corresponds to $t' = \frac{3U}{2}(\gamma^2 - \gamma^4)$, reducing to $t' = \frac{3U}{8}$ in the limit of large t. Therefore for $t' < \frac{3U}{2}(\gamma^2 - \gamma^4)$ (corresponding to the $h = 0$ local moment phase, and the region of the $h = 0$ strong coupling phase close to the phase boundary) we expect to see a finite field Kondo effect, whilst for $t' > \frac{3U}{2}(\gamma^2 - \gamma^4)$ (corresponding to the $h = 0$ strong coupling phase away from the phase boundary) the finite field Kondo effect should be suppressed.

4.12.2 Thermodynamics

When studying regime III, we find it necessary to retain more states at each iteration of our NRG calculation (a maximum of $N_s = 3000$ states per iteration, rather than

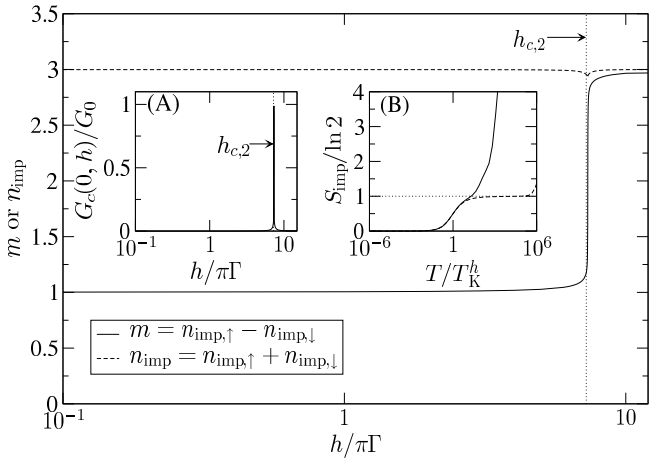


Figure 4.35: m and $n_{\rm imp}$ vs $h/\pi\Gamma$ for a system in the local moment phase of regime III when $h = 0$. $\tilde{U} = 4$, $\tilde{t} = 6$ and $\tilde{t}' = 5 \times 10^{-1}$. Inset A shows $G_c(0,h)/G_0$ for the same system, whilst inset B shows $S_{\rm imp}/\ln 2$ vs $T/T_{\rm K}$ for a system with $E_\Delta \simeq 0$ ($\tilde{h} = 7.3277 \simeq \tilde{h}_{c,2}$); $T_{\rm K}^h$ is defined via $S_{\rm imp}(T_{\rm K}^h) = 0.5 \ln 2$. The dashed line here is a SIAM with the same values of Γ and U.

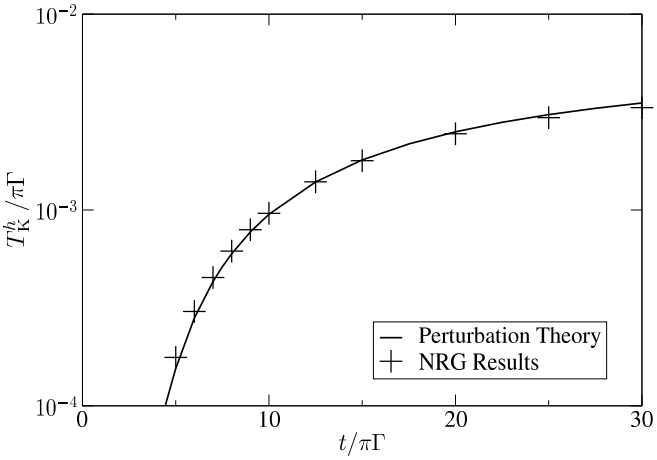


Figure 4.36: The Kondo temperature, $T_{\rm K}^h$ (defined via $S_{\rm imp}(T_{\rm K}^h) = 0.5 \ln 2$) as a function of $\tilde{t}$ for a range of systems with $\tilde{U} = 10$ and $\tilde{t}' = 3$, under magnetic fields tuned such that $h \simeq h_{c,2}$. The solid line shows $T_{\rm K}^{PT} = A \exp(-1/\rho J_{{\rm K},z})$, with $J_{{\rm K},z}$ given by perturbation theory, as discussed in Sec. 4.12.1.

the maximum of $N_s = 2000$ we typically use), as discussed in Sec. 4.8.2.

Fig. 4.35 shows the behaviour of a system which lies in the local moment phase of regime III in the absence of a field, as a function of h. There is only a single 'critical' field here (as in the schematic diagram Fig. 4.33), $h_{c,2} \approx \frac{1}{2}(\sqrt{8t^2 + t'^2} - U - \frac{3U}{2}(\gamma^4 - \gamma^2))$, which corresponds to the field at which the states $|\frac{3}{2}; -; +\frac{3}{2}\rangle$ and $|\frac{1}{2}; -; +\frac{1}{2}\rangle$ are degenerate ($E_\Delta = 0$ in Eq. 4.44). As there is no parity change associated with

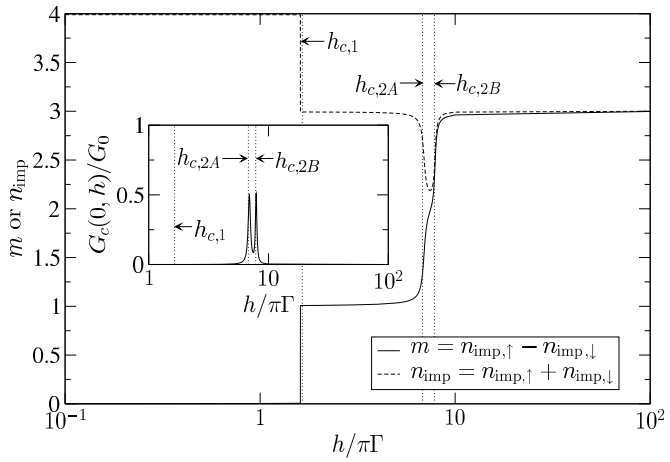


Figure 4.37: m and $n_{\rm imp}$ vs $h/\pi\Gamma$ for a system in the strong coupling phase of regime III when $h = 0$. $\tilde{U} = 4$, $\tilde{t} = 6$ and $\tilde{t}' = 2.5$. The inset shows $G_c(0,h)/G_0$ for the same system.

the transition here, the change in m (from 1 to 3) is sharp but continuous. When $|E_\Delta| > T_{\rm K}^h$, $S_{\rm imp}(T=0) = 0$ and $T\chi_{\rm imp}|_{T=0} = 0$ ($T\chi_{\rm imp}$ not shown) in both phases: the thermodynamics of the system are characterised by a rapid drop from the initial (free orbital fixed point) values of $S_{\rm imp} = \ln 4^3$ and $T\chi_{\rm imp} = 3 \times \frac{1}{8}$ to zero on an energy scale $T \sim t$. Close to the transition ($h \sim h_{c,2}$, such that $|E_\Delta| < T_{\rm K}^h$) however the system approaches the local moment fixed point ($S_{\rm imp} = \ln 2$ and $T\chi_{\rm imp} = \frac{1}{4}$), before ultimately flowing to the strong coupling fixed point, as a result of the field-induced Kondo effect predicted by the low energy effective model, Eq. 4.44. The flow away from the local moment fixed point, which occurs on an energy scale $T \sim T_{\rm K}^h$, is characterised by the universal scaling form obtained for the SIAM [7,8], as shown in inset B to Fig. 4.35; we define $T_{\rm K}^h$ via $S_{\rm imp}(T_{\rm K}^h) = 0.5 \ln 2$ for a system with $m = 2$ (and therefore $E_\Delta = 0$). The change in $T_{\rm K}^h$ as a function of t and t' may be estimated from the value of $J_{{\rm K},z}$ derived from the Schrieffer-Wolff transformation (Eq. 4.44), as shown in Fig. 4.36.

Fig. 4.37 shows a system which lies in deep the strong coupling phase of Regime III in the absence of a field. A small ($h < h_{c,1} = t' - \epsilon - \frac{U}{2}(1+\gamma^2)$) field has no discernible impact upon the system, but at the point $h = h_{c,1}$, corresponding to the field at which the singlet state $|0;+;0\rangle$ and doublet state $|\frac{1}{2};-;+\frac{1}{2}\rangle$ are

degenerate, there is a discontinuous change in both $n_{\rm imp}$, which decreases from 4 to 3, and in m which increases from 0 to 1; this change does not affect the zero-temperature conductance. In this case we also find that $t' > \frac{3U}{2}(\gamma^2 - \gamma^4)$ ($h_{c,2B} < h_{c,2A}$), and so the field-induced Kondo effect is suppressed, and instead two distinct transitions are observed, the first (at $h = h_{c,2A}$, as predicted in Sec. 4.12.1) between a $|\frac{1}{2}; -; +\frac{1}{2}\rangle$ ground state and a $|1; -; +1\rangle$ ground state. At this critical field m increases continuously from 1 to 2, and $n_{\rm imp}$ falls continuously from 3 to 2. The second transition, occurring at $h = h_{c,2B}$ (again, as predicted in Sec. 4.12.1) occurs when the $|1; -; +1\rangle$ and $|\frac{3}{2}; -; +\frac{3}{2}\rangle$ states are degenerate, and is characterised by a smooth increase in both m and $n_{\rm imp}$ from 2 to 3.

4.12.3 Dynamics

We find (via direct calculation using the NRG) that, just as in regimes I ($J < 10T_{\rm K}$) and II ($J > 10T_{\rm K}$) (Sec. 4.11 and 4.10) the Luttinger integral $I_{\rm L} = {\rm Im\,Tr}\int_{-\infty}^{0} d\omega \frac{\partial \mathbf{\Sigma}_\sigma}{\partial \omega}\mathbf{G}_\sigma =$ 0 in all cases here. Inset A to Fig. 4.35 illustrates the behaviour of $G_c(0,h)/G_0$ for a system in the local moment phase of regime III in the absence of a field as a function of h. When $h \simeq h_{c,2}$ the $|\frac{1}{2}; -; +\frac{1}{2}\rangle$ and $|\frac{3}{2}; -; +\frac{3}{2}\rangle$ trimer ground states are near degenerate, and a field-induced Kondo effect is observed, which gives rise to an enhanced conductance (Kondo resonance), with $G_c(0,h)/G_0$ rising to the unitarity limit when $E_\Delta = 0$ ($h = h_{c,2}$).

In inset A to Fig. 4.37, which shows the conductance for a system deep within the strong coupling phase in the absence of a field, we see that the presence of an $m = 2$ plateau suppresses the Kondo peak in the conductance, although enhanced conductance is seen on either side of the $m = 2$ plateau (at $h \approx h_{c,2A}$ and $h \approx h_{c,2B}$) — Coulomb blockade peaks arising as a natural consequence of the change in the electronic population of the TQD (unlike in the transition from the 4-electron singlet state, seen at $h = h_{c,1}$, all states here have the same (odd) parity, and so the Coulomb blockade peaks are not suppressed).

4.13 Summary

In this chapter we investigate a mirror symmetric model ('the apex coupled trimer model') in which only one of the dots is connected to the conduction band. The Hamiltonian for this model is examined in Sec. 4.1, and we then discuss the symmetry properties of the model in Sec. 4.2. We find that in the case where all three dots are singly occupied at low temperature an effective spin model may be derived, which describes the system at low temperatures: we discuss the derivation of this model in Sec. 4.3. In the following section, Sec. 4.4, we explain how the electronic population of the dot may be related to the zero-temperature conductance using a Friedel-Luttinger sum rule.

In Sec. 4.5 we discuss the phase diagram of the apex coupled trimer model. We find that the system contains two phases — a local moment phase and a strong coupling phase — and that these are separated by a line of first order quantum phase transitions. Three distinct regimes, each with a different functional form for the phase boundary, may be identified. We refer to these as regimes I, II and III. Regimes I and II lie within the parameter space where the effective spin model derived in Sec. 4.3 is valid, whilst regime III lies outside that parameter space.

We first discuss the physics observed in regime II (Sec. 4.6), before investigating the physics of regimes I (Sec. 4.7) and III (Sec. 4.8). In all cases we find that low energy effective models which accurately describe the physics of the system at low temperature may be derived. These models give an accurate prediction of the position of the phase boundary in all three regimes, and the phase diagram for any ACTM device may be accurately described by the three lines $J' = J^2/10T_{\mathrm{K}}$, $J' = J$ and $t' = U/4$.

We find that although the strong coupling and local moment phases of each regime are continuously connected to those of the neighbouring regimes, the underlying physics is distinct in each case: the local moment phase of regime I arises as a result of an underscreened triplet state, whilst the local moment phase of regime

II is a doublet state coupling ferromagnetically to the conduction band, and the local moment phase deep in regime III is a free spin, entirely decoupled from the conduction band. The strong coupling phases in both regimes I and II are the result of similar physics (singlet locking of spins 1 and 3, followed by or preceding Kondo quenching of dot 2), but the 'strong coupling' phase of regime III is, in fact, best described by a frozen impurity fixed point.

The chapter concludes with an examination of the effect of an applied field upon the TQD device. We again consider initially systems in regime II (Sec. 4.10), before investigating the physics of regimes I (Sec. 4.11) and III (Sec. 4.12). Low energy effective models which describe the physics of the system well at low temperature may be derived in all three regimes. In regimes II and III, we find that for certain parameter regimes field-induced Kondo effects may be observed, giving rise to an enhanced conductance at some 'critical' field, which we may predict using our low energy effective models.

In all regimes we find that the parity symmetry of the Hamiltonian has an important effect upon the physics of the system: first order quantum phase transitions are seen when there is a change in the parity of the ground state of the system. In the next chapter we therefore investigate the effect of breaking the mirror symmetry of the TQD device.

Chapter 5

The Apex Coupled Trimer Model Part II: Breaking Mirror Symmetry

We now consider a more complex variant of the model discussed in Chapter 4. Here the condition that the tunnel-coupling between the 1-2 and 2-3 dot pairs must be identical is no longer imposed and as a result breaking of the mirror symmetry of the system is permitted. The model investigated is shown schematically in Fig. 5.1, and we will refer to it as 'the asymmetric apex coupled trimer model' (AACTM). The most important theoretical consequence of breaking mirror symmetry is that

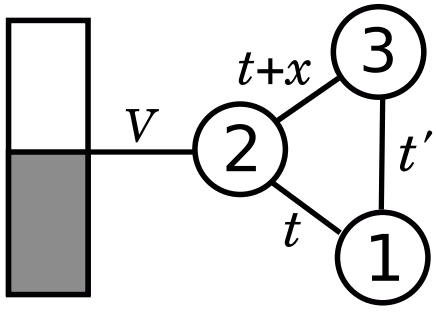


Figure 5.1: A schematic representation of the asymmetric version of the apex coupled trimer model. The quantum dots (labelled '1', '2' and '3') are linked by tunnel-couplings t, t' and x, with a further tunnel-coupling, V, linking dot 2 to the conduction band.

the parity under $1 \leftrightarrow 3$ interchange (see Sec. 4.2 and Appendix B) is no longer a good quantum number and, as we shall see, this means that phase transitions are not expected to take the form of level crossings. We generally find that the physical behaviour of the mirror symmetric and asymmetric systems is very similar when the TQD does not lie close to a phase boundary, and as a result we concentrate in this chapter upon the behaviour of an asymmetric TQD device when close to the phase boundaries of the system.

5.1 The Asymmetric Apex Coupled Trimer Hamiltonian

The Hamiltonian here is given by $\hat{H}_{AACTM} = \hat{H}_L + \hat{H}_{hyb} + \hat{H}_{TQD}$ where $\hat{H}_L = \sum_{\mathbf{k},\sigma} \epsilon_{\mathbf{k}} c^\dagger_{\mathbf{k}\sigma} c_{\mathbf{k}\sigma}$ refers to the non-interacting lead, which couples to dot 2 via $\hat{H}_{hyb} = \sum_{\mathbf{k},\sigma} V(c^\dagger_{2\sigma} c_{\mathbf{k}\sigma} + H.c.)$, with $\hat{H}_{TQD}$, the Hamiltonian for the isolated TQD device, given by

$$\begin{aligned}\hat{H}_{TQD} = &\sum_{\sigma,i=1,2,3} (\epsilon_i - \sigma h)\hat{n}_{i\sigma} + \sum_{i=1,2,3} U\hat{n}_{i\uparrow}\hat{n}_{i\downarrow} + \sum_{\sigma} t[(c^\dagger_{1\sigma} + c^\dagger_{3\sigma})c_{2\sigma} + H.c] \\ &+ \sum_{\sigma} t'(c^\dagger_{1\sigma} c_{3\sigma} + H.c.) + \sum_{\sigma} x(c^\dagger_{2\sigma} c_{3\sigma} + H.c.).\end{aligned} \tag{5.1}$$

This Hamiltonian is, of course, almost identical to Eq. 4.1, with the crucial addition of $\hat{H}_{AS} = \sum_\sigma x(c^\dagger_{2\sigma} c_{3\sigma} + H.c.)$, which breaks the mirror symmetry of the system (formally, $[\hat{P}_{1,3}, \hat{H}_{AS}] \neq 0$). x is the difference in the strength of the tunnel-coupling between the 1-2 and 2-3 dot pairs, and as such parameterises the asymmetry of the system. In addition, as we no longer impose mirror symmetry upon the Hamiltonian, we no longer need specify that $\epsilon_1 = \epsilon_3 = \epsilon$. We discuss the effect of setting $\epsilon_1 \neq \epsilon_3$ in Sec. 5.12; until that point $\epsilon_1 = \epsilon_3$ is implicit, and we consider only the representative case $\epsilon_i = \epsilon = -U/2$. Likewise, the effect of an applied field is discussed in Sec. 5.9, 5.10 and 5.11, until which point $h = 0$ is also implicit. The

non-interacting lead is taken to be a wide, flat band of width $2D$, with density of states per conduction orbital $\rho = 1/(2D)$. D is naturally taken to be the largest energy scale in the problem and we set $D/\Gamma = 100$ (except where otherwise noted) with $\Gamma = \pi\rho NV^2$ the hybridization strength (N is the number of orbitals/$\mathbf{k}$-states in the lead, such that NV^2 is finite in the continuum limit $N \to \infty$). The underlying set of bare model parameters may therefore be taken as

$$\tilde{U} = \frac{U}{\pi\Gamma}, \quad \tilde{t} = \frac{t}{\pi\Gamma}, \quad \tilde{t}' = \frac{t'}{\pi\Gamma}, \quad \tilde{x} = \frac{x}{\pi\Gamma}, \tag{5.2}$$

together with $\tilde{h} = h/\pi\Gamma$, the applied field, in Sec. 5.9, 5.10 and 5.11. As in Chapter 4 we set the NRG discretisation parameter $\Lambda = 3$ throughout, and keep a maximum of $N_s = 2000$ states per iteration, except in the sections on regime III (the orbital regime) (Sec. 5.7 and 5.11), where a maximum of $N_s = 3000$ states are kept in each iteration.

5.2 The Spin Model

We may use a Schrieffer-Wolff transformation [13] to derive an effective low temperature spin model from Eq. 5.1, valid in the region where all three dots are singly occupied at low temperature (corresponding to $x, t, t', V \ll U$). The transformation is described in Sec. 4.3, and the final result is a spin model of the form

$$\begin{aligned} \hat{H}_{spin} =& J(\hat{\mathbf{S}}_1 + \hat{\mathbf{S}}_3) \cdot \hat{\mathbf{S}}_2 + J'\hat{\mathbf{S}}_1 \cdot \hat{\mathbf{S}}_3 + \delta\hat{\mathbf{S}}_2 \cdot \hat{\mathbf{S}}_3 + J_{\mathrm{K}}\hat{\mathbf{S}}_2 \cdot \hat{\mathbf{S}}(0) \\ &+ \hat{H}_L + K\sum_\sigma f^\dagger_{0\sigma} f_{0\sigma}, \end{aligned} \tag{5.3}$$

where $\hat{\mathbf{S}}_i$ is a spin-$\frac{1}{2}$ operator for dot i, $\hat{\mathbf{S}}(0)$ is the spin density of the conduction band at the dot, and $f^\dagger_{0\sigma}$ ($f_{0\sigma}$) is the creation (destruction) operator for the 0-orbital of the Wilson chain (as described in Sec. 4.3); retardation effects are neglected. The Heisenberg exchange couplings, J, J', J_{K} and the potential scattering coefficient,

K, are identical to those for the mirror symmetric apex coupled trimer model, and are given by Eq. 4.5. δ is also a Heisenberg exchange coupling,

$$\delta = 4\frac{(2tx + x^2)}{U}, \tag{5.4}$$

which parameterises the asymmetry of the system in the regime where the spin model is valid. As δ does not have a simple linear dependence upon x and is, moreover, a function of t, we will find it convenient to specify a fixed δ, rather than x, when we consider systems described by Eq. 5.3 at low temperatures. We also note at this juncture that although Eq. 5.1 is *not*, in general, particle-hole symmetric, Eq. 5.3 *does* conserve particle-hole symmetry when $\epsilon_i = \epsilon = -U/2$.

5.3 Conductance and the Friedel-Luttinger Sum Rule

Just as in Chapter 4 (Sec. 4.4) the Meir-Wingreen formula (Eq. 3.41) may be used to relate the conductance through the TQD device, $G_c(T, h)$, to the single particle spectrum of dot 2, $D_{2\sigma}(\omega, T, h)$:

$$\frac{G_c(T,h)}{G_0} = \int_{\infty}^{\infty} -\frac{\partial f(\omega)}{\partial \omega}\frac{1}{2}\sum_{\sigma}\pi\Gamma D_{2\sigma}(\omega, T, h)d\omega. \tag{5.5}$$

In addition, as discussed in Appendix C and Sec. 3.7, a Friedel-Luttinger sum rule may be derived for the AACTM, just as for the ACTM,

$$G_c(0,h) = G_0\ \tfrac{1}{2}\sum_{\sigma}\pi\Gamma D_{2\sigma}(\omega = 0, T = 0, h) \tag{5.6a}$$

$$= G_0\ \tfrac{1}{2}\sum_{\sigma}\sin^2(\delta_\sigma), \tag{5.6b}$$

where $G_c(0, h)$ is the zero-temperature zero-bias conductance through the TQD device, $D_{2\sigma}(\omega = 0, T = 0, h)$ the zero-temperature, zero-frequency value of the

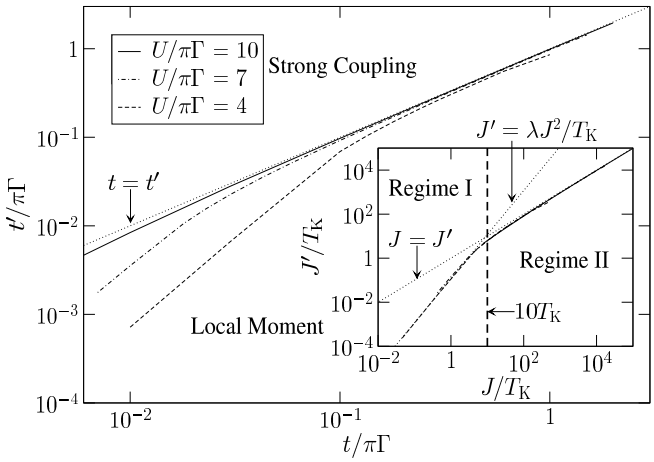


Figure 5.2: The phase diagram for the asymmetric model, for various values of $\tilde{U}$. $\tilde{\delta} = 10^{-5}$ is fixed. The main diagram shows the phase diagram with axes plotting $\tilde{t}$ against $\tilde{t}'$. The inset shows the same data, but with the axes rescaled as J/T_K and J'/T_K, respectively, and also shows the division of the phase diagram into regimes I ($J < 10T_K$) and II ($J > 10T_K$).

single particle spectrum of dot 2 and δ_σ the static scattering phase shift, given by $\delta_\sigma = \pi n_{\mathrm{imp},\sigma}|_{T=0} + I_L$, with $I_L = \mathrm{Im}\,\mathrm{Tr}\int_{-\infty}^{0} d\omega \frac{\partial \mathbf{\Sigma}_\sigma}{\partial \omega}\mathbf{G}_\sigma$ the Luttinger Integral [125] and $n_{\mathrm{imp},\sigma}|_{T=0}$ the zero-temperature value of $n_{\mathrm{imp},\sigma}(T) = \langle \hat{Q}\rangle_{\mathrm{imp}}(T) + \sigma\langle \hat{S}_z\rangle_{\mathrm{imp}}(T)$. As I_L is found to be constant within a given phase (see below), we may use Eq. 5.6b to relate the thermodynamic properties of the system to the conductance — the dynamic property of the system which is most readily accessible experimentally [5, 37].

5.4 The Phase Diagrams

We find that the phase diagram of the AACTM contains two stable fixed points, the first, characterised by $S_{\mathrm{imp}}(T = 0) = 0$ and $T\chi_{\mathrm{imp}}|_{T=0} = 0$, corresponding to a strong coupling fixed point (within this phase we generically find that the Luttinger integral, $I_L = \mathrm{Im}\,\mathrm{Tr}\int_{-\infty}^{0} d\omega \frac{\partial \mathbf{\Sigma}_\sigma}{\partial \omega}\mathbf{G}_\sigma = 0$, as expected for a Fermi Liquid [120]), and the second, characterised by $S_{\mathrm{imp}}(T = 0) = \ln 2$ and $T\chi_{\mathrm{imp}}|_{T=0} = 1/4$, corresponding to a local moment fixed point (within this phase it is generically found that $|I_L| = \frac{\pi}{2}$, in agreement with the results of Logan *et al.* [55] for a singular Fermi Liquid). These

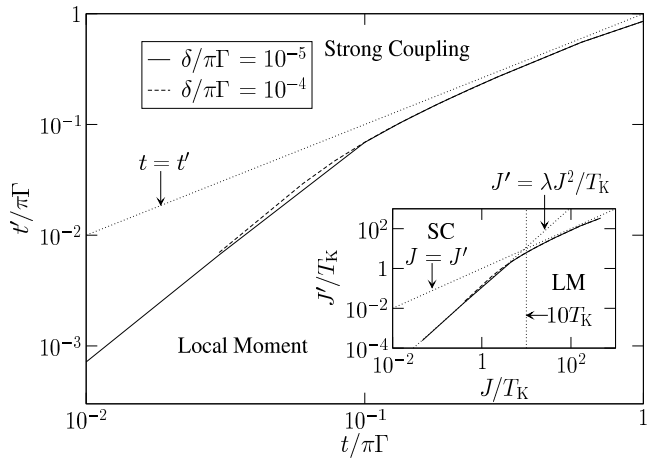


Figure 5.3: The phase diagram for the asymmetric model with $\tilde{U} = 4$, for various values of δ. The main diagram shows the phase diagram with axes plotting $\tilde{t}$ against $\tilde{t}'$, whilst the inset shows the same data, but with the axes rescaled as J/T_K and J'/T_K, respectively.

phases are separated by a line of Kosterlitz-Thouless transitions [135], characterised by an exponentially vanishing Kondo temperature as the phase boundary is approached, and we see no evidence of a transition fixed point which persists to zero temperature at the transition[1]. Just as in Sec. 4.5 we use the NRG to determine the position of the phase boundary by fixing $\tilde{U}$, $\tilde{t}$ and $\tilde{x}/\tilde{\delta}$ (see below), and then varying $\tilde{t}'$. However, as Kosterlitz-Thouless transitions are observed here (rather than first order quantum phase transitions, as seen in the previous chapter), we cannot use a simple bisection technique to determine the position of the phase boundary, but rather have to extrapolate to determine the value of $\tilde{t}'$ for which the Kondo temperature is zero; this process is described in some detail in Sec. 5.4.1.

As with the mirror symmetric model (Chapter 4) we find that the parameter space of the model may be divided into three distinct sections, labelled regimes I (corresponding to $J \lesssim 10T_K$), II (corresponding to $J \gtrsim 10T_K$ and $t \lesssim U/4$) and III (corresponding to $t \gtrsim U/4$), which exhibit distinct physics. Regimes I and II span the parameter space where the spin model, Eq. 5.3, describes the system at low temperature, whilst regime III lies outside this region. Therefore, unlike the mirror

[1] Although, as discussed below, the system may flow close to a 'transition fixed point' at non-zero temperatures.

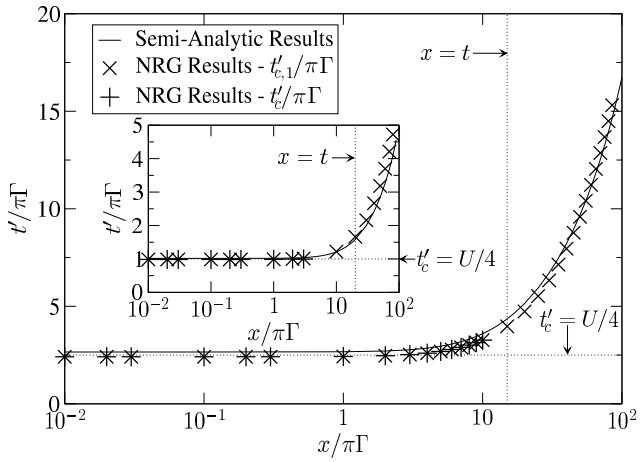


Figure 5.4: $\tilde{t}'_{c,1}$ and $\tilde{t}'_c$ as a function of $\tilde{x}$ for a system in regime III with $\tilde{U} = 10$ and $\tilde{t} = 15$. Both the results of our NRG calculations and the semi-analytic model (solid black line) are shown. We define $t'_{c,1}$ via $n_{\rm imp}(t'_c)|_{T=0} = 3.5$ (as discussed in the text). The inset plots $\tilde{t}'_c$ and $\tilde{t}'_{c,1}$ against $\tilde{x}$ for a system with $\tilde{U} = 4$ and $\tilde{t} = 20$.

symmetric case (Fig. 4.2), we cannot present a phase diagram spanning the entire parameter space, as the variable which parameterises the asymmetry of the system at low temperature in regime III (x) differs from that in regimes I and II (δ).

Fig. 5.2 shows the phase boundary (defined as the point as which the Kondo temperature is zero — see Sec. 5.4.1) in regimes I and II for a fixed $\tilde{\delta} = \delta/\pi\Gamma$, for various different values of $\tilde{U}$. Fig. 5.3 shows the regime I and II phase diagram for a fixed $\tilde{U}$, but various values of $\tilde{\delta}$. The insets to both figures show that upon rescaling the axes as $J/T_{\rm K}$ and $J'/T_{\rm K}$ the phase boundary in both regimes I and II collapses onto a universal scaling form[2] — $J = J'$ for regime II and $J' = \lambda J^2/T_{\rm K}$ for regime I, with $\lambda \approx 0.1$ (just as in the mirror symmetric case — see Sec. 4.5). These numerical results would therefore appear to indicate that the phase boundary in both regimes I and II is effectively independent of δ when δ is small.

In regime III we again see a local moment phase and a strong coupling phase separated by a line of Kosterlitz-Thouless transitions. In the mirror symmetric case, the phase boundary between the strong coupling and local moment phases was found to be coincident with a discontinuous change in $n_{\rm imp}$ from 3 to 4 (Sec. 4.8.1), but

[2] As in the previous chapter, we define $T_{\rm K}$ for a TQD with a given $\tilde{U}$ and Γ via $S_{\rm imp}(T_{\rm K}) = 0.5 \ln 2$ for a SIAM at particle-hole symmetry ($\epsilon = -U/2$) with the same $\tilde{U}$ and Γ.

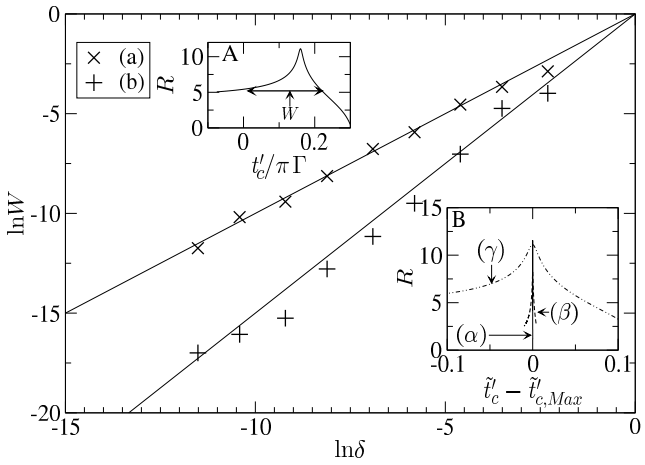


Figure 5.5: The logarithm of the width at half maximum of the $R = -\log(1-\chi^2)$ peak, W, plotted against $\ln\delta$ for two systems, one (a) with $\tilde{U} = 10$ and $\tilde{t} = 10^{-1}$, and the other (b) with $\tilde{U} = 4$ and $\tilde{t} = 5 \times 10^{-2}$. Inset A to the figure shows how W is defined, whilst inset B shows R as a function of $\tilde{t}'_c - \tilde{t}'_{c,Max}$ (where $\tilde{t}'_{c,Max}$ is the value of $\tilde{t}'_c$ at the maximum in R) for system (a) with $\tilde{\delta} = 10^{-5}$ for (α), 10^{-3} for (β) and 10^{-1} for (γ).

this is not the case when the mirror symmetry is broken. The change in $n_{\rm imp}$ is now continuous, and no longer coincident with the phase boundary and we may therefore define two 'critical' values of t'. The first, t'_c, corresponds to the value of t' exactly at the phase boundary between the strong coupling and local moment phases (i.e. the value of t' when the Kondo scale is zero), whilst the second, $t'_{c,1}$, corresponding to $n_{\rm imp}|_{T=0} = 3.5$, may be used to define the crossover from a three-electron to a four-electron state (i.e. from a strong coupling fixed point to a frozen impurity fixed point). We find that in the region where t'_c may be accurately determined (generally, $x < t$) the phase boundary follows the line $t' \approx U/4$, just as in the mirror symmetric case. This is also the case for $t'_{c,1}$ when $x < t$, but for $x > t$ we find that $t'_{c,1}$ depends linearly upon x, as shown in Fig. 5.4.

We therefore find that in *all* regimes when the asymmetry is small the phase boundary is identical to that of the mirror symmetric case. As discussed in the next section, we cannot determine t'_c accurately when x is large (i.e. $x > t$).

5.4.1 Uncertainty in the Position of the Phase Boundary

As discussed above, the quantum phase transition in all cases of the asymmetric model is of Kosterlitz-Thouless form [135], and so the Kondo scale of the problem, T_{K}^{AS} (defined via $S_{\mathrm{imp}}(T_{\mathrm{K}}^{AS}) = 0.5 \ln 2$, suitably between $\ln 2$ and 0), vanishes as the transition is approached, obeying the relationship

$$\ln T_{\mathrm{K}}^{AS} \propto \frac{1}{t' - t'_c}, \tag{5.7}$$

where t'_c is the value of t' exactly at the transition (i.e. where $T_{\mathrm{K}}^{AS} = 0$). This result is unsurprising — it has been shown that other methods for breaking the mirror symmetry of a TQD device (as seen in Wang's investigation of Aharonov-Bohm effects in triple quantum dots [72]) give rise to Kosterlitz-Thouless transitions. The NRG cannot be used down to zero-temperature (as discussed in Chapter 3, this would require an infinite number of iterations) and so we must determine t'_c indirectly. In practice, this is done by determining the value of t'_c for which a plot of $\ln T_{\mathrm{K}}^{AS}$ against $(t' - t'_c)^{-1}$ (for fixed $\tilde{U}$, $\tilde{t}$ and $\tilde{\delta}$) most closely approximates a straight line. We do this by calculating the maximum value of R, where R is given by

$$R = -\log(1 - \chi^2) \tag{5.8}$$

with χ^2 the Pearson correlation number [136]. For a perfectly correlated system [in our case, $\ln T_{\mathrm{K}}^{AS} = A(t' - t'_c)^{-1}$], $\chi^2 = 1$, corresponding to a singularity in R. Obviously this point is never actually reached, and so we content ourselves with choosing the largest possible value of R (typically $R \approx 10$, corresponding to $\chi^2 \approx 1 - 10^{-10}$). However, as shown in the insets to Fig. 5.5, we typically find that rather than there being a single value of t'_c corresponding to a uniquely large value of R, instead a broad peak in R is seen — with a width, W, (defined at half maximum) which is a function of δ. Allowing for the inevitable (although low level) noise present in the NRG results, we are therefore presented with a range

within which the phase boundary must fall (see Fig. 5.5). There is, therefore, an uncertainty in the position of the phase boundary which increases with δ and so we typically restrict ourselves to small values of δ (compared to the other relevant low energy scales of the problem — J, J' and/or $T_{\rm K}$) in the sections on regime I ($J < 10T_{\rm K}$) and II ($J > 10T_{\rm K}$) which follow. Similar restrictions are placed upon the accurate determination of t_c' when investigating regime III (the orbital regime), but in this case the operative scale is of course x, rather than δ.

5.5 Regime II: $J > 10T_{\rm K}$

We initially consider the physics of regime II (see Fig. 5.2), as this is the simplest and least subtle of the three regimes. This section builds on the discussion of the physics of regime II in the mirror symmetric limit, given in Sec. 4.6.

5.5.1 Effective Low Energy Model

We approach the derivation of the low energy effective model here much as we did in the mirror symmetric case — initially considering the states of the isolated trimer, described by

$$\hat{H}_{trimer} = J(\hat{\mathbf{S}}_1 + \hat{\mathbf{S}}_3) \cdot \hat{\mathbf{S}}_2 + J'\hat{\mathbf{S}}_1 \cdot \hat{\mathbf{S}}_3 + \delta\hat{\mathbf{S}}_2 \cdot \hat{\mathbf{S}}_3, \tag{5.9}$$

and then considering the effects of coupling to the conduction band as a perturbation to those states. The states of the isolated trimer are a quartet and two doublets (just as in the mirror symmetric case — see Table 4.1), the quartet, $|\frac{3}{2}; S^z\rangle$, with energy $E_Q = \frac{J}{2} + \frac{J'}{4} + \frac{\delta}{4}$, always being the highest energy state in the absence of a field.

Our low energy manifold therefore contains only the two doublet states. As Eq. 5.9 does not conserve parity, we can no longer classify the eigenstates of $\hat{H}_{trimer}$ according to their parity under $1 \leftrightarrow 3$ interchange. However, we may write the unity operator spanning the reduced Hilbert space of the low energy manifold here

in terms of the odd and even parity doublets of the ACTM in regime II, $\hat{1} = \sum_{S^z} |\frac{1}{2};+;S^z\rangle\langle\frac{1}{2};+;S^z| + \sum_{S^z} |\frac{1}{2};-;S^z\rangle\langle\frac{1}{2};-;S^z|$ (see Table 4.1). These two doublets are, of course, eigenstates of the Hamiltonian $\hat{H}^{sym}_{trimer} = J(\hat{\mathbf{S}}_1+\hat{\mathbf{S}}_3)\cdot\hat{\mathbf{S}}_2+J'\hat{\mathbf{S}}_1\cdot\hat{\mathbf{S}}_3$. We find that

$$\hat{1}\hat{H}_{trimer}\hat{1} = \begin{pmatrix} |\frac{1}{2};+;S^z\rangle & |\frac{1}{2};-;S^z\rangle \end{pmatrix} \begin{pmatrix} -\frac{3}{4}J' & \frac{\sqrt{3}}{4}\delta \\ \frac{\sqrt{3}}{4}\delta & \frac{J'}{4} - J - \frac{1}{2}\delta \end{pmatrix} \begin{pmatrix} \langle\frac{1}{2};+;S^z| \\ \langle\frac{1}{2};-;S^z| \end{pmatrix}, \tag{5.10}$$

and it naturally follows that we may write the doublet eigenstates of $\hat{H}_{trimer}$ in terms of linear combinations of the odd and even parity doublets, $|\frac{1}{2};\pm;S^z\rangle$:

$$|\tfrac{1}{2};A;S^z\rangle = \alpha|\tfrac{1}{2};-;S^z\rangle + \beta|\tfrac{1}{2};+;S^z\rangle, \tag{5.11a}$$

$$|\tfrac{1}{2};B;S^z\rangle = \alpha|\tfrac{1}{2};+;S^z\rangle - \beta|\tfrac{1}{2};-;S^z\rangle, \tag{5.11b}$$

where

$$\alpha^2 = \frac{1}{2}\left(1 + \frac{J - J' + \frac{1}{2}\delta}{\sqrt{(J - J' + \frac{1}{2}\delta)^2 + \frac{3}{4}\delta^2}}\right), \tag{5.12a}$$

$$\beta^2 = \frac{1}{2}\left(1 - \frac{J - J' + \frac{1}{2}\delta}{\sqrt{(J - J' + \frac{1}{2}\delta)^2 + \frac{3}{4}\delta^2}}\right), \tag{5.12b}$$

such that $\alpha^2 = 1 - \beta^2$. These states have energies

$$E_A = \frac{1}{2}\left(-J - \tfrac{1}{2}J' - \tfrac{1}{2}\delta\right) - \frac{1}{2}\sqrt{(J - J' + \tfrac{1}{2}\delta)^2 + \tfrac{3}{4}\delta^2}, \tag{5.13a}$$

$$E_B = \frac{1}{2}\left(-J - \tfrac{1}{2}J' - \tfrac{1}{2}\delta\right) + \frac{1}{2}\sqrt{(J - J' + \tfrac{1}{2}\delta)^2 + \tfrac{3}{4}\delta^2}, \tag{5.13b}$$

such that $E_A < E_B$ for all values of J, J' and δ. Unlike the mirror symmetric case, there is therefore no change in the identity of the ground state doublet as J, J' and δ are varied here. Indeed, if the transition in the $\delta = 0$ case is considered a level crossing, the behaviour of the system in the asymmetric case may be considered an

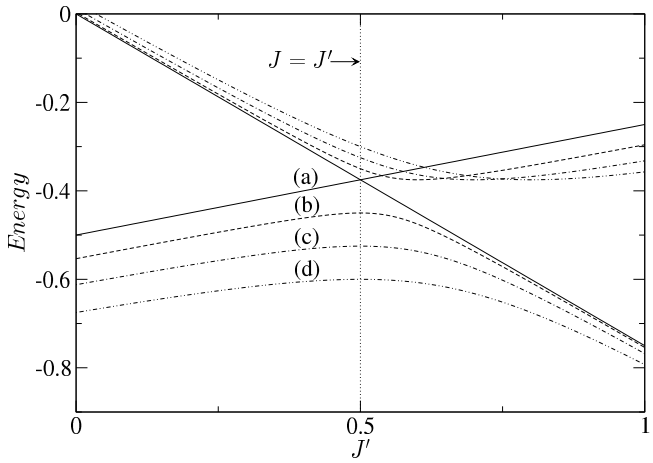


Figure 5.6: The energy of the two low-lying doublet states of the isolated asymmetric TQD with $J = 5 \times 10^{-1}$, varying δ, with $\delta = 0$ for (a), 10^{-1} for (b), 2×10^{-1} for (c) and 3×10^{-1} for (d).

avoided crossing, the mixing of the two doublet states leading to a 'bending' of the energy levels, such that the energy of the ground state in the vicinity of the $\delta = 0$ transition is reduced — this is shown in Fig. 5.6. Increasing δ both increases the size of the minimum energy separation of the doublets, and changes the position of the minimum. It can easily be shown that the closest approach of the two doublet energies is $E_{\Delta}^{Min} = \frac{\sqrt{3}}{2}\delta$, occurring when $J' = J + \frac{1}{2}\delta$. This, of course, reduces (as it must) to the mirror symmetric result of $E_{\Delta}^{Min} = 0$ when $J' = J$ in the limit $\delta = 0$.

The unity operator for the reduced Hilbert space of the problem expressed in terms of the $|\frac{1}{2}; A; S^z\rangle$ and $|\frac{1}{2}; B; S^z\rangle$ states is therefore

$$\hat{1} = \hat{1}_+ + \hat{1}_-, \tag{5.14a}$$

$$\hat{1}_+ = \sum_{S^z} |\tfrac{1}{2}; B; S^z\rangle\langle\tfrac{1}{2}; B; S^z|, \tag{5.14b}$$

$$\hat{1}_- = \sum_{S^z} |\tfrac{1}{2}; A; S^z\rangle\langle\tfrac{1}{2}; A; S^z|. \tag{5.14c}$$

We may define a pseudospin operator,

$$\hat{\mathcal{T}}^z = \frac{1}{2}(\hat{1}_+ - \hat{1}_-), \tag{5.15a}$$

$$\hat{\mathcal{T}}^+ = \sum_{S^z} |\tfrac{1}{2}; B; S^z\rangle\langle\tfrac{1}{2}; A; S^z|, \tag{5.15b}$$

$$\hat{\mathcal{T}}^- = \sum_{S^z} |\tfrac{1}{2}; A; S^z\rangle\langle\tfrac{1}{2}; B; S^z|, \tag{5.15c}$$

such that $|\frac{1}{2}; B; S^z\rangle$ and $|\frac{1}{2}; A; S^z\rangle$ are eigenstates of $\hat{\mathcal{T}}^z$ with eigenvalues $\pm\frac{1}{2}$, respectively. We also define

$$\hat{\mathcal{T}}^+ = \hat{\mathcal{T}}^x + i\hat{\mathcal{T}}^y, \tag{5.16a}$$

$$\hat{\mathcal{T}}^- = \hat{\mathcal{T}}^x - i\hat{\mathcal{T}}^y, \tag{5.16b}$$

by analogy with the corresponding spin operator expressions[3]. It then follows immediately (using the same arguments as in Sec. 4.6) that the low energy effective model may be written

$$\hat{H}_{eff} = J_{\rm K}\hat{1}\hat{\mathbf{S}}_2\hat{1}\cdot\hat{\mathbf{S}}(0) + E_\Delta\hat{\mathcal{T}}^z + \hat{H}_L, \tag{5.17}$$

where $E_\Delta = E_B - E_A = \sqrt{(J - J' + \frac{1}{2}\delta)^2 + \frac{3}{4}\delta^2} > 0$ is the energy separation between the two doublet states. When $T \ll \delta$ only the lowest energy doublet ($|\frac{1}{2}; A; S^z\rangle$) need be retained in the low energy manifold, as the $|\frac{1}{2}; B; S^z\rangle$ doublet is thermally inaccessible. The unity operator spanning the reduced Hilbert space of the low energy manifold here is simply $\hat{1}_-$, and so Eq. 5.17 reduces to

$$\hat{H}_{eff} = J_{\rm K}\left(1 - \frac{4}{3}\alpha^2\right)\hat{\mathbf{S}}\cdot\hat{\mathbf{S}}(0) + \hat{H}_L: \text{ Regime II (A)}, \tag{5.18}$$

an effective spin-$\frac{1}{2}$ Kondo model with $J_{{\rm K},eff} = (1 - \frac{4}{3}\alpha^2)J_{\rm K}$. As $J_{\rm K}$ is positive,

[3]It may be shown that the pseudospin operators $\hat{\mathcal{T}}^\alpha$ ($\alpha = x, y, z$) satisfy the relevant commutation relation; $[\hat{\mathcal{T}}^\alpha, \hat{\mathcal{T}}^\beta] = i\epsilon_{\alpha\beta\gamma}\hat{\mathcal{T}}^\gamma$.

this corresponds to an antiferromagnetic Kondo model when $(1 - \frac{4}{3}\alpha^2) > 0$, and a ferromagnetic Kondo model when $(1 - \frac{4}{3}\alpha^2) < 0$. In this model $J_{\mathrm{K},eff}$ varies continuously — vanishing completely when $\alpha^2 = \frac{3}{4}$, corresponding to $J = J'$ — behaviour which we know from perturbative scaling arguments (see Sec. 2.2 and Refs [2, 14]) should naturally give rise to a Kosterlitz-Thouless transition between the strong coupling and local moment phases of the system. We therefore predict that the phase boundary should follow the line $J = J'$, *independent* of the value of δ — in agreement with the results shown in Fig. 5.2 and 5.3. In addition, for $J \gg (J', \delta)$, we find that $J_{\mathrm{K},eff} \to -\frac{1}{3}J_{\mathrm{K}}$, and when $J' \gg (J, \delta)$, we find $J_{\mathrm{K},eff} \to J_{\mathrm{K}}$ — recovering the mirror symmetric results when the system is far from the transition.

In the region $T \gg \delta$, on the other hand, both doublets are thermally accessible, and so must be retained in the low energy manifold: the unity operator is in this case $\hat{1} = \hat{1}_+ + \hat{1}_-$. Evaluating $\hat{1}\hat{\mathbf{S}}_2\hat{1}$, and noting that (due to the breaking of the parity symmetry of the system) it is no longer the case that $\hat{1}_\pm\hat{\mathbf{S}}_2\hat{1}_\mp = 0$, Eq. 5.17 may equivalently be written

$$\hat{H}_{eff} = \frac{J_{\mathrm{K}}}{3}\left(1 + 4([\alpha^2 - \beta^2]\hat{\mathcal{T}}^z + \alpha\beta[\hat{\mathcal{T}}^+ + \hat{\mathcal{T}}^-])\right)\hat{\mathbf{S}} \cdot \hat{\mathbf{S}}(0) + E_\Delta\hat{\mathcal{T}}^z + \hat{H}_L, \quad (5.19)$$

where $\hat{\mathbf{S}}$ is a spin-$\frac{1}{2}$ operator for the TQD as a whole. Using Eq. 5.16, Eq. 5.19 may be written in the form

$$\hat{H}_{eff} = \frac{J_{\mathrm{K}}}{3}\left(1 + 4([\alpha^2 - \beta^2]\hat{\mathcal{T}}^z + 2\alpha\beta\hat{\mathcal{T}}^x)\right)\hat{\mathbf{S}} \cdot \hat{\mathbf{S}}(0) + E_\Delta\hat{\mathcal{T}}^z + \hat{H}_L. \quad (5.20)$$

We next define a new set of pseudospin operators, $\hat{\mathcal{T}}^{x'}$, $\hat{\mathcal{T}}^{y'}$ and $\hat{\mathcal{T}}^{z'}$, corresponding to a rotation of the pseudospin in the x-z plane, such that

$$\begin{pmatrix} \hat{\mathcal{T}}^{x'} \\ \hat{\mathcal{T}}^{y'} \\ \hat{\mathcal{T}}^{z'} \end{pmatrix} = \begin{pmatrix} \cos\theta & 0 & -\sin\theta \\ 0 & 1 & 0 \\ \sin\theta & 0 & \cos\theta \end{pmatrix} \begin{pmatrix} \hat{\mathcal{T}}^{x} \\ \hat{\mathcal{T}}^{y} \\ \hat{\mathcal{T}}^{z} \end{pmatrix}, \quad (5.21)$$

where

$$\cos\theta = \alpha^2 - \beta^2, \tag{5.22a}$$

$$\sin\theta = 2\alpha\beta. \tag{5.22b}$$

Using Eq. 5.21, Eq. 5.20 may be written

$$\hat{H}_{eff} = \frac{J_{\mathrm{K}}}{3}(1 + 4\hat{\mathcal{T}}^{z'})\hat{\mathbf{S}} \cdot \hat{\mathbf{S}}(0) + E_{\Delta}(\cos\theta\hat{\mathcal{T}}^{z'} - \sin\theta\hat{\mathcal{T}}^{x'}) + \hat{H}_L \tag{5.23a}$$

$$= \frac{J_{\mathrm{K}}}{3}(1 + 4\hat{\mathcal{T}}^{z'})\hat{\mathbf{S}} \cdot \hat{\mathbf{S}}(0) + E_{\Delta}(\alpha^2 - \beta^2)\hat{\mathcal{T}}^{z'} - 2\alpha\beta E_{\Delta}\hat{\mathcal{T}}^{x'} + \hat{H}_L \tag{5.23b}$$

$$= \frac{J_{\mathrm{K}}}{3}(1 + 4\hat{\mathcal{T}}^{z'})\hat{\mathbf{S}} \cdot \hat{\mathbf{S}}(0) + (J - J' + \tfrac{1}{2}\delta)\hat{\mathcal{T}}^{z'} + \frac{\sqrt{3}}{2}\delta\hat{\mathcal{T}}^{x'} + \hat{H}_L : \text{ Regime II (B)}, \tag{5.23c}$$

where Eq. 5.23c is the final form of the low energy effective model. In this model the $(J - J' + \frac{1}{2}\delta)\hat{\mathcal{T}}^{z'}$ term acts as an effective longitudinal magnetic field upon the pseudospin, whilst the $\frac{\sqrt{3}}{2}\delta\hat{\mathcal{T}}^{x'}$ term acts as an effective transverse magnetic field upon the pseudospin. An applied field, h, will only affect the behaviour of a system on energy scales $T \leq h$, and therefore in the region where δ is small compared to the temperature, the penultimate term in Eq. 5.23c may be neglected. The model is then effectively equivalent to the low energy effective model for the mirror symmetric case of this regime (Eq. 4.12). The asymmetric system should therefore exhibit similar behaviour to the mirror symmetric model at temperatures much large than δ, and in the limit $\delta \to 0$, the mirror symmetric results are recovered exactly (which is indeed what is found, as discussed in the next section).

5.5.2 Thermodynamics

The position of the phase boundary in regime II is found to be independent of δ, as shown in Fig. 5.2 and 5.3, and discussed in Sec. 5.4. We consider initially the behaviour of a system which lies exactly upon the phase boundary, before discussing the behaviour of the system as the phase boundary is approached. Fig. 5.7 shows

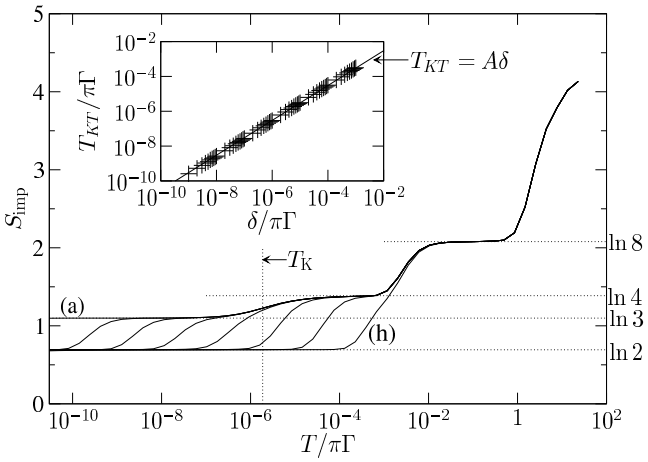


Figure 5.7: The entropy $S_{\rm imp}$ vs $T/\pi\Gamma$ for systems in regime II at the phase boundary: $\tilde{U} = 10$, $\tilde{t} = 10^{-1}$ and $\tilde{t}' = \tilde{t}'_c \simeq 9.69325 \times 10^{-2}$. $\tilde{\delta}$ is varied, with $\tilde{\delta} = 0$ for line (a), 10^{-9} for (b), 10^{-8} for (c), 10^{-7} for (d), 10^{-6} for (e), 10^{-5} for (f), 10^{-4} for (g) and 10^{-3} for (h). The inset shows T_{KT} (defined via $S_{\rm imp}(T_{KT}) = 0.5 \ln 6$, suitably between $\ln 3$ and $\ln 2$) as a function of δ (A is a constant).

how the impurity contribution to the entropy varies for a system at the transition ($t' = t'_c$), for various values of δ. At high temperature, the entropy is initially $S_{\rm imp} = \ln 64$ ($T\chi_{\rm imp} = \frac{3}{8}$, not shown), characteristic of the free orbital fixed point [7,8]. On an energy scale $T \sim U$ the empty and doubly occupied states of the dots become thermally inaccessible, and the entropy falls to $\ln 8$ ($T\chi_{\rm imp} = \frac{3}{4}$), characteristic of three free spins. Below this temperature the effective spin model, Eq. 5.3, describes the system well. The quartet state, always being higher in energy than the doublet states of $\hat{H}_{trimer}$, is then projected out on an energy scale $T \sim J$, at which point the entropy falls to $\ln 4$ ($T\chi_{\rm imp} = \frac{1}{4}$), as the low energy manifold spans only the two doublet states.

The behaviour of the system below this temperature depends upon the relative sizes of two energy scales, $T_{\rm K}$, the Kondo temperature of the mirror symmetric system ($\delta = 0$), and T_{KT}, the energy scale on which the higher energy doublet state ($|\frac{1}{2}; B; S^z\rangle$) becomes thermally inaccessible. When $T_{KT} > T_{\rm K}$, on an energy scale T_{KT} the higher energy doublet state is projected out, and the system flows to the local moment fixed point ($S_{\rm imp} = \ln 2$ and $T\chi_{\rm imp} = \frac{1}{4}$), which is effectively

the ultimate low temperature fixed point of the system[4]. When $T_{KT} < T_{\rm K}$, by contrast, the higher energy doublet state is Kondo quenched on an energy scale $T_{\rm K}$, and the system flows to the 'transition fixed point' described in Sec. 4.6.2, which is characterised by $S_{\rm imp} = \ln 3$ ($T\chi_{\rm imp} = \frac{1}{6}$). The system flows away from this fixed point on an energy scale T_{KT}, flowing to the local moment fixed point ($S_{\rm imp} = \ln 2$ and $T\chi_{\rm imp} = \frac{1}{4}$), which is, just as in the $T_{\rm K} < T_{KT}$ case, effectively the ultimate low temperature fixed point of the system.

The behaviour of the system is fundamentally different from that observed in the mirror symmetric case because the 'transition fixed point' does not describe the system at zero temperature *even at the phase boundary* when $\delta \neq 0$. This is easily understood: as discussed in Sec. 5.5.1 there is a minimum energy separation between the doublet states here, and therefore (unlike the mirror symmetric case) there is always a low energy scale below which the $|\frac{1}{2}; B; S^z\rangle$ doublet state becomes inaccessible. Eq. 5.18 therefore describes all systems in regime II at sufficiently low temperatures ($T < T_{KT}$). From Eq. 5.19, we naturally expect that the low energy scale on which the higher energy doublet becomes thermally inaccessible, $T_{KT} \sim E_\Delta$. At the phase boundary $J = J'$ (as discussed above) and therefore $E_\Delta = \delta$. It is therefore expected that $T_{KT} \propto \delta$ when at the phase boundary, which is exactly what is found in the NRG, as shown in the inset to Fig. 5.7.

Fig. 5.8 and 5.9 show the behaviour of systems approaching the phase boundary. On energy scales $T > T_{KT}$ the behaviour of both these systems is identical to that shown in Fig. 5.7 and discussed above. Below T_{KT} the systems flow to the local moment fixed point ($S_{\rm imp} = \ln 2$ and $T\chi_{\rm imp} = \frac{1}{4}$), before ultimately flowing to the strong coupling fixed point on an energy scale $T_{\rm K}^{AS}$, which vanishes exponentially as the phase boundary is approached, as expected for a Kosterlitz-Thouless transition (as shown in insets (B) of Fig. 5.8 and 5.9). On energy scales below T_{KT}, the low energy effective model, Eq. 5.18, should describe the system well. This is a Kondo

[4]As the system lies exactly on the phase boundary here, the low energy scale upon which the local moment is Kondo quenched, $T_{\rm K}^{AS} = 0$, by definition.

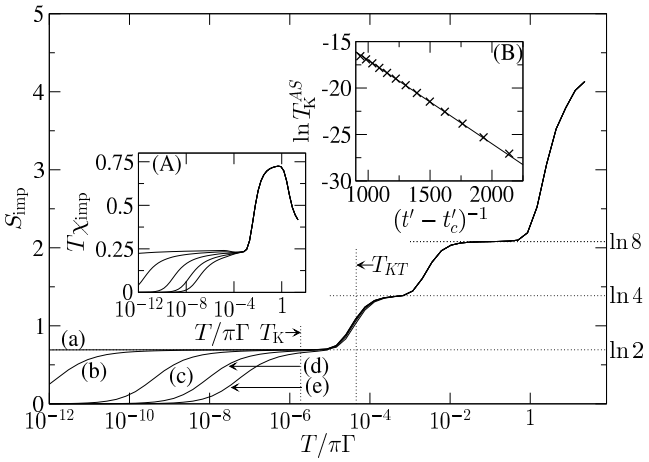


Figure 5.8: The entropy $S_{\rm imp}$ vs $T/\pi\Gamma$, for systems in regime II approaching the phase boundary when $T_{\rm K} < T_{KT}$. $\tilde{U} = 10$ and $\tilde{t} = 10^{-1}$ with $\tilde{\delta} = 10^{-4}$. $\tilde{t'}$ is varied with $\tilde{t'} = 9.72 \times 10^{-2}$ for (a), 9.74×10^{-2} for (b), 9.76×10^{-2} for (c), 9.78×10^{-2} for (d) and 9.8×10^{-2} for (e). Inset A shows $T\chi_{\rm imp}$ for the same data, whilst inset B shows that $\ln T_{\rm K}^{AS} \propto (t' - t'_c)^{-1}$, with $t'_c \simeq 9.69325 \times 10^{-2}$ and $T_{\rm K}^{AS}$ defined via $S_{\rm imp}(T_{\rm K}^{AS}) = 0.5 \ln 2$.

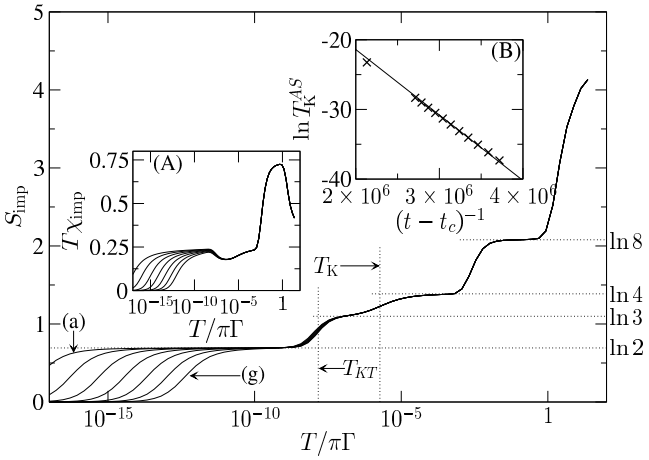


Figure 5.9: The entropy $S_{\rm imp}$ vs $T/\pi\Gamma$, for systems in regime II approaching the phase boundary when $T_{\rm K} > T_{KT}$. $\tilde{U} = 10$ and $\tilde{t} = 10^{-1}$ with $\tilde{\delta} = 10^{-7}$. $\tilde{t'}$ is varied with $\tilde{t'} = 9.718268 \times 10^{-2}$ for (a), 9.71827×10^{-2} for (b), 9.718272×10^{-2} for (c), 9.718274×10^{-2} for (d), 9.718276×10^{-2} for (e), 9.718278×10^{-2} for (f), and 9.71828×10^{-2} for (g). Inset A shows $T\chi_{\rm imp}$ for the same data, whilst inset B shows that $\ln T_{\rm K}^{AS} \propto (t' - t'_c)^{-1}$, with $t'_c \simeq 9.71824 \times 10^{-2}$ and $T_{\rm K}^{AS}$ defined via $S_{\rm imp}(T_{\rm K}^{AS}) = 0.5 \ln 2$.

model with an effective coupling $J_{{\rm K},eff}$ which vanishes as the phase boundary at $J' = J$ is approached. As shown in Fig. 5.10 we find a very good agreement between $J_{{\rm K},eff}$ as calculated from Eq. 5.18, and the $J_{{\rm K},eff}$ which we may determine from the NRG. As one might expect, both from the form of Eq. 5.23c and the limiting values of $J_{{\rm K},eff}$ for large J and J' (as discussed in Sec. 5.5.1) we find that when $J - J'$

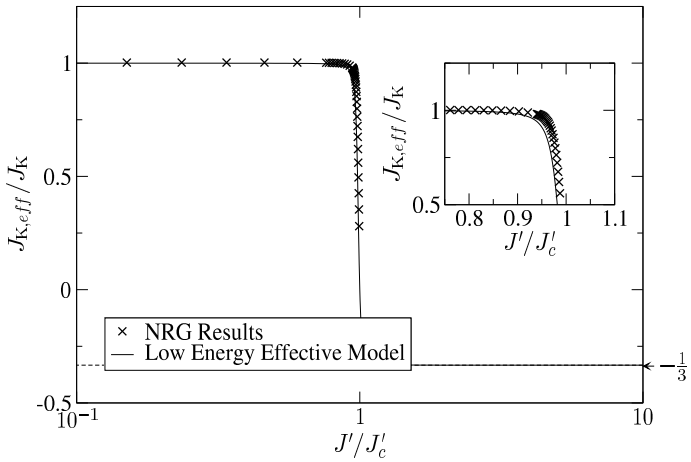


Figure 5.10: $J_{\mathrm{K},eff}$ plotted against J'/J'_c for a system with $\tilde{U} = 10$, $\tilde{t} = 10^{-1}$ and $\tilde{\delta} = 10^{-4}$, comparing the results of the NRG (crosses) to Eq. 5.18 (solid line), using $T_{\mathrm{K}}^{AS} = A\exp(-1/\rho J_{\mathrm{K},eff})$ to determine $J_{\mathrm{K},eff}$ from the NRG results. The inset shows detail on the same data, plotted on a linear scale.

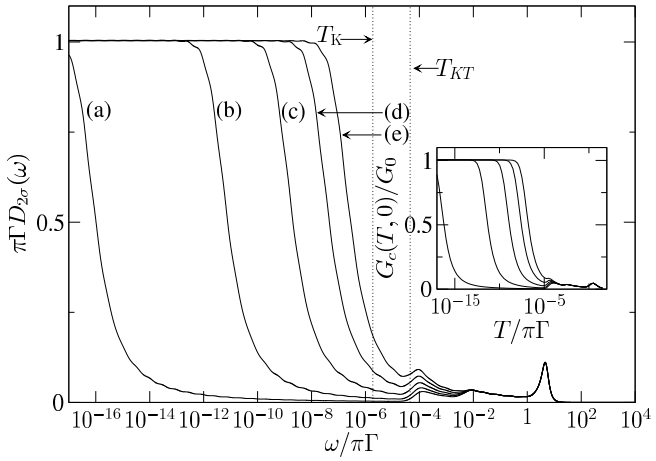


Figure 5.11: The $T = 0$ single particle spectrum of dot 2, $\pi\Gamma D_{2\sigma}(\omega)$, for a TQD in regime II approaching the phase boundary with $T_{KT} \gg T_{\mathrm{K}}$. $\tilde{U} = 10$, $\tilde{t} = 10^{-1}$ and $\tilde{\delta} = 10^{-4}$; $\tilde{t}'$ is varied, with $\tilde{t}' = 9.72 \times 10^{-2}$ for (a), 9.74×10^{-2} for (b), 9.76×10^{-2} for (c), 9.78×10^{-2} for (d) and 9.8×10^{-2} for (e) ($\tilde{t}'_c \simeq 9.71824 \times 10^{-2}$). The inset shows the conductance for the same data.

is large compared to δ the behaviour of the system is essentially indistinguishable from that of the corresponding mirror symmetric case, described in Sec. 4.6.

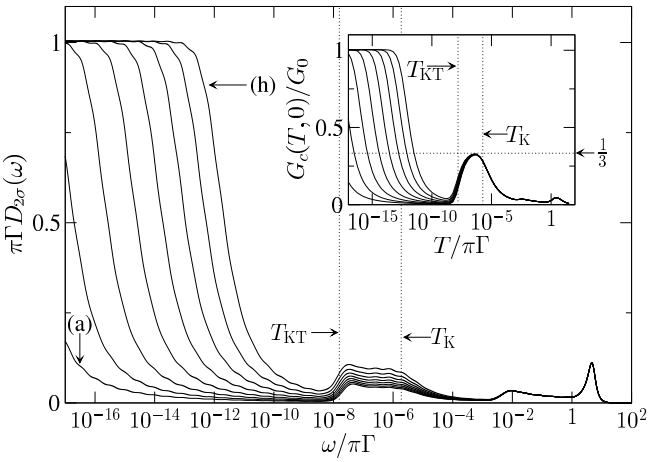


Figure 5.12: The $T = 0$ single particle spectrum of dot 2, $\pi\Gamma D_{2\sigma}(\omega)$, for a TQD in regime II approaching the phase boundary with $T_{KT} \ll T_{\rm K}$. $\tilde{U} = 10$, $\tilde{t} = 10^{-1}$ and $\tilde{\delta} = 10^{-7}$; $\tilde{t}'$ is varied, with $\tilde{t}' = 9.718266 \times 10^{-2}$ for (a), 9.718268×10^{-2} for (b), 9.71827×10^{-2} for (c), 9.718272×10^{-2} for (d), 9.718274×10^{-2} for (e), 9.718276×10^{-2} for (f), 9.718278×10^{-2} for (g) and 9.71828×10^{-2} for (h) ($t'_c \simeq 9.71824 \times 10^{-2}$). The inset shows the conductance for the same data.

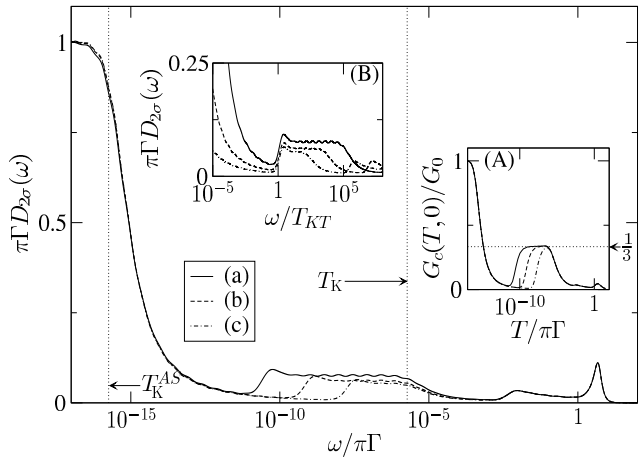


Figure 5.13: The $T = 0$ single particle spectrum of dot 2, $\pi\Gamma D_{2\sigma}(\omega)$, for TQD systems with varying δ, tuned such that $T_{\rm K}^{AS}$ is the same in all cases. $\tilde{U} = 10$ and $\tilde{t} = 10^{-1}$, with $\tilde{\delta} = 10^{-9}$ and $\tilde{t}' \simeq 9.71824 \times 10^{-2}$ for (a), $\tilde{\delta} = 10^{-8}$ and $\tilde{t}' \simeq 9.71824 \times 10^{-2}$ for (b) and $\tilde{\delta} = 10^{-7}$ and $\tilde{t}' \simeq 9.71827 \times 10^{-2}$ for (c). Inset A to the figure shows the conductance for the same data, which inset B shows the spectra scaled by T_{KT}.

5.5.3 Dynamics

We next consider the dynamic properties exhibited by the model when in regime II, concentrating upon the zero-temperature single particle spectrum of dot 2, $\pi\Gamma D_{2\sigma}(\omega)$, and the zero-bias conductance. As expected, we generally find that far from the

transition both the zero-temperature single particle spectrum, $\pi\Gamma D_{2\sigma}(\omega)$, and the conductance are indistinguishable from the corresponding mirror symmetric case (whether strong coupling or local moment), rising to the unitarity limit on a scale $T_{\rm K}$ in the strong coupling phase, and decaying to zero in the local moment phase (with logarithmic corrections — as discussed in Sec. 4.6.3) as $\omega \to 0$ ($T \to 0$). As the transition is approached, the Kondo scale, $T_{\rm K}^{AS}$, vanishes exponentially, and this leads to the disappearance of the Kondo resonance; this is shown clearly in Fig. 5.11. The Kondo resonance does however still have a functional form identical to that of the SIAM and exhibits scaling by $T_{\rm K}^{AS}$. In addition, it is generically found that the Luttinger integral $I_{\rm L} = \mathrm{Im}\,\mathrm{Tr}\int_{-\infty}^{0} d\omega \frac{\partial \mathbf{\Sigma}_\sigma}{\partial \omega}\mathbf{G}_\sigma = 0$ in the strong coupling phase (as expected for a Fermi Liquid phase [120]). We also generically find that $|I_{\rm L}| = \frac{\pi}{2}$ in the local moment phase (in agreement with the results of Logan *et al.* for a singular Fermi liquid [55], just as for the ACTM). As $n_{{\rm imp},\sigma}|_{T=0} = 3/2$ in both the local moment and strong coupling phases here, it therefore follows immediately from Eq. 5.6 that there is a discontinuous change in the zero-temperature conductance through the TQD at the phase boundary.

Fig. 5.11 shows data for a system in the region $T_{KT} \gg T_{\rm K}$, whilst Fig. 5.12 shows the conductance and zero-temperature single particle spectrum of dot 2, $\pi\Gamma D_{2\sigma}(\omega)$, for systems in the region $T_{KT} \ll T_{\rm K}$. Although the overall behaviour of the system is similar, and in both cases the Kondo resonance vanishes as the transition is approached, in the case where $T_{KT} \ll T_{\rm K}$ (Fig. 5.12) an additional feature is observed in the spectrum. This peak is found to lie between $\omega \sim T_{KT}$ and $\omega \sim T_{\rm K}$ in the zero-temperature single particle spectrum and between $T \sim T_{KT}$ and $T \sim T_{\rm K}$ in the conductance (see Fig. 5.13). The peak lies in the temperature (frequency) window where the system flows close to the 'transition fixed point' (which is why it is not observed when $T_{KT} \gg T_{\rm K}$), and the maximum height of this feature in the conductance is found to be $G_c(T)/G_0 = \frac{1}{3}$, corresponding to the conductance at the transition fixed point, G_c^{TFP}/G_0, for the ACTM, as described in Sec. 4.6.1.

5.6 Regime I: $J < 10T_{\mathrm{K}}$

We now consider regime I (see Fig. 5.2). As in regime II ($J > 10T_{\mathrm{K}}$), in this regime t and t' are small compared to the intradot Coulomb repulsion, U, and so the effective spin model, Eq. 5.3, describes the system well at low temperatures. Just as in the corresponding case of the ACTM (Sec. 4.7) we find that the system has two phases here — a strong coupling phase and a local moment phase — separated by a phase boundary which is well described by $J' = \lambda J^2/T_{\mathrm{K}}$, although here the phase boundary is a line of Kosterlitz-Thouless transitions, rather than the first order quantum phase transitions seen in mirror symmetric systems. Just as for the ACTM, (except when close to the phase boundary with regime II) it is generically the case in this regime that $J \ll T_{\mathrm{K}}$, and in the vicinity of the phase boundary $J, J' \ll T_{\mathrm{K}}$. To minimise the effects of uncertainty upon the phase boundary (see Sec. 5.4.1) an additional restriction of $\delta < J$ (and therefore implicitly $\delta \ll T_{\mathrm{K}}$) is imposed. As a result, we anticipate that coupling to the conduction band (occurring on an energy scale T_{K}) will dominate the low temperature physics of the system, just as in regime I of the ACTM. We therefore initially approach the problem in much the same way as the corresponding case of the ACTM (Sec. 4.7.1), first considering a toy model in which the couplings between the orbitals of the conduction band are assumed to vanish.

This model comprises four spins — the three dots and the 0-orbital of the Wilson chain. The effective Hamiltonian for this model is then $\hat{H}_{spin} = \hat{H}^s_{TQD} + \hat{H}_K$, with $\hat{H}^s_{TQD} = J\hat{\mathbf{S}}_2 \cdot (\hat{\mathbf{S}}_1 + \hat{\mathbf{S}}_3) + J'\hat{\mathbf{S}}_1 \cdot \hat{\mathbf{S}}_3 + \delta\hat{\mathbf{S}}_2 \cdot \hat{\mathbf{S}}_3$ and $\hat{H}_K = J_{\mathrm{K}}\hat{\mathbf{S}}_2 \cdot \hat{\mathbf{S}}(0)$. Spins 2 and 0 quench to form a singlet state on an energy scale $T \sim J_{\mathrm{K}}$. On energy scales $\ll J_{\mathrm{K}}$ spin 2 is therefore essentially frozen out, and spins 1 and 3 are coupled by the remaining antiferromagnetic exchange interaction, $\hat{H}_{J'} = J'\hat{\mathbf{S}}_1 \cdot \hat{\mathbf{S}}_3$. This gives a 1–3 singlet state with energy $E_s = -\frac{3}{4}J'$, and a 1–3 triplet with energy $E_T = +\frac{1}{4}J'$, just as for the corresponding case of the ACTM. Just as in that case there is an additional (ferromagnetic) RKKY-like interaction between spins 1 and 3, mediated via the 2–0 singlet state. This coupling can be easily determined via Brillouin-

Wigner perturbation theory (to second order) in $\hat{H}_{J\delta} = J\hat{\mathbf{S}}_2 \cdot (\hat{\mathbf{S}}_1 + \hat{\mathbf{S}}_3) + \delta\hat{\mathbf{S}}_2 \cdot \hat{\mathbf{S}}_3$. As one might expect from the results for the mirror symmetric case, this interaction stabilises the 1–3 triplet state, which has energy $E_T = \frac{1}{4}J' - \frac{J}{2J_\mathrm{K}}(J+\delta)$ (the energy of the singlet state is unaffected by the RKKY interaction).

The low energy manifold here spans the singlet ($|S\rangle$) and triplet ($|T;S^z\rangle$) states of the 1–3 pair, and the unity operator for the reduced Hilbert space of this problem is therefore given by

$$\hat{1} = \hat{1}_+ + \hat{1}_-, \tag{5.24a}$$

$$\hat{1}_+ = |S\rangle\langle S|, \tag{5.24b}$$

$$\hat{1}_- = \sum_{S^z} |T;S^z\rangle\langle T;S^z|. \tag{5.24c}$$

Defining a pseudospin operator, $\hat{\mathcal{T}}^z = \frac{1}{2}(\hat{1}_+ - \hat{1}_-)$, such that $|S\rangle$ and $|T;S^z\rangle$ are eigenstates of it, with eigenvalues $\pm\frac{1}{2}$, respectively, the effective Hamiltonian for this toy model may then be written

$$\hat{H}_{eff} = -E_\Delta \hat{\mathcal{T}}^z, \tag{5.25}$$

where $E_\Delta = E_T - E_S$. This equation is, of course, extremely similar to Eq. 4.15, the corresponding $\hat{H}_{eff}$ for the toy model used to derive the effective low energy model for the mirror symmetric case. Just as in that case, upon moving from the toy model to the full system, we would expect Eq. 5.25 to undergo two major changes. First, the energy scale J_K in the denominator of E_Δ, quantifying as it does the energy separation between the 2-0 singlet and triplet combinations, will naturally be renormalised to a value $\mathcal{O}(T_K)$. Second, spins 1 and 3 will couple to the wider conduction band. In the mirror symmetric system, this simply led to underscreening of the 1–3 triplet state, but in the asymmetric case the coupling has a more subtle effect.

We can understand the effect of this coupling to the conduction band by ex-

tending our toy model to include the 1-orbital of the Wilson chain, as well as the 0-orbital (we initially neglect the remaining orbitals of the chain). As the 2–0 singlet is tightly locked on all energy scales $\ll J_{\mathrm{K}}$, we may consider this as a simple trimer model;

$$\begin{aligned}\hat{H}^{*}_{trimer} =& J^{*}\tilde{\mathbf{S}}(0)\cdot(\hat{\mathbf{S}}_1+\hat{\mathbf{S}}_3)+\delta^{*}\tilde{\mathbf{S}}(0)\cdot\hat{\mathbf{S}}_3+\left(J'-\frac{J}{2J_{\mathrm{K}}}(J+\delta)\right)\hat{\mathbf{S}}_1\cdot\hat{\mathbf{S}}_3 \\ =& J^{*}\tilde{\mathbf{S}}(0)\cdot(\hat{\mathbf{S}}_1+\hat{\mathbf{S}}_3)+\delta^{*}\tilde{\mathbf{S}}(0)\cdot\hat{\mathbf{S}}_3+J'^{*}\hat{\mathbf{S}}_1\cdot\hat{\mathbf{S}}_3\end{aligned} \tag{5.26}$$

where $\tilde{\mathbf{S}}(0)$ is the the conduction electron density *excluding* the 0-orbital of the Wilson chain (which is locked up in the Kondo singlet) and J^{*} and δ^{*} are the couplings linking spins 1 and 3 to the 1-orbital of the Wilson chain (we make no attempt to quantify these couplings, albeit their antiferromagnetic (+) sign is obvious from the fact that the spins 1 and 3 are coupled to the remainder of the Wilson chain via the intervening Kondo singlet). $J'^{*}=J'-J(J+\delta)/2J_{\mathrm{K}}$ is the effective exchange coupling linking spins 1 and 3. Eq. 5.26 is, of course, identical in form to Eq. 5.9, and will have the same eigenstates.

When $\delta=0$ the eigenstates of Eq. 5.26 are given by Table 4.1: the $|\frac{1}{2};+;S^z\rangle$ doublet corresponds to the 1–3 singlet state, decoupled from the 1-orbital of the Wilson chain, which acts as a free spin. The $|\frac{1}{2};-;S^z\rangle$ doublet on the other hand corresponds to the 1–3 triplet state, underscreened by coupling to the 1-orbital of the Wilson chain. A first order quantum phase transition occurs when $E_{\Delta}=J'^{*}-J^{*}=0$. Now $J^{*}\ll J,J',\delta$, and so $J'^{*}-J^{*}=0$ implies $J'^{*}\approx 0$, corresponding to $J'-J^2/2J_{\mathrm{K}}=0$, which is renormalised to $J'-\lambda J^2/T_{\mathrm{K}}=0$ when coupling to the full conduction band is taken into account.

When $\delta^{*}\neq 0$ (i.e. when $\delta\neq 0$) mixing between the even and odd parity doublet states occurs, giving rise to an avoided crossing, as described in Sec. 5.5.1. The ground state, $|\frac{1}{2};A;S^z\rangle$, is now a linear combination of the $|\frac{1}{2};+;S^z\rangle$ ($|S\rangle$) and $|\frac{1}{2};-;S^z\rangle$ (underscreened $|T;S^z\rangle$) doublets, and the minimum energy separation between the $|\frac{1}{2};A;S^z\rangle$ doublet and the first excited state, the $|\frac{1}{2};B;S^z\rangle$ doublet, is

$\frac{\sqrt{3}}{2}\delta^*$. As a result of this mixing, we no longer expect to see a first order quantum phase transition here, although as $\delta^* \ll J, J', \delta$ the mixing will have a minimal effect upon the system except when J'^* is very small (as discussed in Sec. 5.5.1, when $E_\Delta \gg \delta$ it was found that the mirror symmetric results were recovered, essentially exactly) — in practice, when $|J'^*| \ll \delta^*$.

When $J'^* = E'_\Delta \gg 0$ then $|\frac{1}{2}; A; S^z\rangle \simeq |\frac{1}{2}; +; S^z\rangle$, and the system will ultimately flow to the strong coupling fixed point at low temperature (corresponding to a 1–3 singlet ground state). By contrast, when $E'_\Delta \ll 0$ $|\frac{1}{2}; A; S^z\rangle \simeq |\frac{1}{2}; -; S^z\rangle$ and the system will ultimately flow to the local moment fixed point at low temperature (corresponding to an underscreened 1–3 triplet ground state). We therefore expect the phase boundary to be found when $J^* = E'_\Delta \approx 0$, corresponding to $J' = J(J+\delta)/2J_\mathrm{K}$ (which is naturally renormalised to $J' = \lambda J(J+\delta)/T_\mathrm{K}$ when we take account of coupling to the full conduction band). In the limit $\delta/J \ll 1$ (describing all the systems investigated in this thesis), the phase boundary should therefore be described by $J' \simeq \lambda J^2/T_\mathrm{K}$, which is indeed what is found using the NRG, as described in Sec. 5.4.

5.6.1 Thermodynamics

We find that away from the phase boundary the behaviour of a system in regime I is identical to that of the corresponding regime for the mirror symmetric model, as one would expect from the discussion above. This behaviour is described in detail in Sec. 4.7. We therefore concentrate on the physics of the system close to the phase boundary in this section and the one that follows.

Fig. 5.15 shows S_imp as a function of temperature for systems at the phase boundary with varying δ (as discussed above and in Sec. 5.3, the phase boundary in regime I is independent of δ when $\delta/J \ll 1$). At high temperature, the system is initially at the free orbital fixed point [7,8] ($S_\mathrm{imp} = \ln 64$ and $T\chi_\mathrm{imp} = \frac{3}{8}$, not shown). The empty and doubly occupied states of the dots become thermally inaccessible on

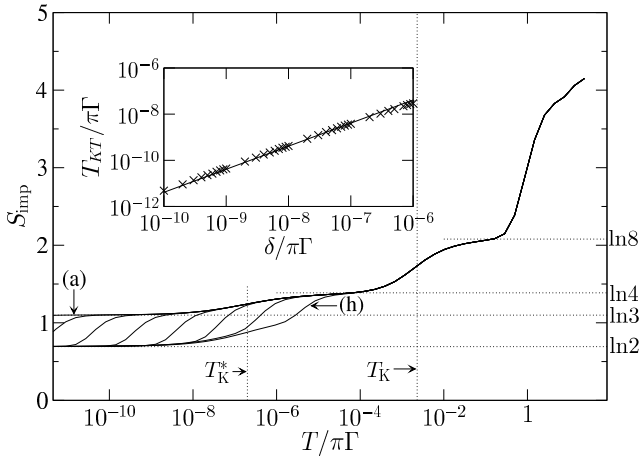


Figure 5.14: The entropy $S_{\rm imp}$ vs $T/\pi\Gamma$ for systems in regime I at the phase boundary. $\tilde{U} = 4$, $\tilde{t} \approx 3.640 \times 10^{-2}$ and $\tilde{t}' = \tilde{t}'_c = 10^{-2}$. $\tilde{\delta} = 0$ for line (a), 10^{-10} for (b), 10^{-9} for (c), 10^{-8} for (d), 10^{-7} for (e), 10^{-6} for (f), 10^{-5} for (g) and 10^{-4} for (h). The inset shows that T_{KT} (defined via $S_{\rm imp}(T_{KT}) = 0.5 \ln 6$) varies linearly with $\tilde{\delta}$.

an energy scale $T \sim U$, at which point $S_{\rm imp}$ falls to $\ln 8$ ($T\chi_{\rm imp} = \frac{3}{4}$), characteristic of three free spins. As the temperature is further reduced, the spin on dot 2 is Kondo quenched on an energy scale $T \sim T_{\rm K}$, leaving free spins on dots 1 and 3 ($S_{\rm imp} = \ln 4$ and $T\chi_{\rm imp} = \frac{1}{4}$). On a further low energy scale $T_{\rm K}^*$ the 1–3 triplet state is then underscreened, and the system flows to the 'transition fixed point' ($S_{\rm imp} = \ln 3$ and $T\chi_{\rm imp} = \frac{1}{6}$). The system remains at the 'transition fixed point' until an energy scale T_{KT} is reached, at which point the system flows to the local moment fixed point ($S_{\rm imp} = \ln 2$ and $T\chi_{\rm imp} = \frac{1}{4}$), which is effectively the ultimate low temperature fixed point of the system[5]. As shown in the inset to Fig. 5.15 the scale T_{KT} (which we define via $S_{\rm imp}(T_{KT}) = 0.5 \ln 6$, suitably between $\ln 3$ and $\ln 2$) is found to be $\propto \delta$, and as such the 'transition fixed point' describes the system at the phase boundary down to zero temperature *only* when $\delta = 0$. This behaviour is (as one would expect) fundamentally very similar to that observed in regime II: compare Fig. 5.7 with Fig. 5.14. Just as in Sec. 5.5, T_{KT} here is the energy scale upon which the first excited state (a linear combination of the 1–3 singlet and the underscreened 1–3 triplet states of the TQD) becomes thermally inaccessible. At

[5]Just as in regime II ($J > 10T_{\rm K}$) — see Sec. 5.5.2.

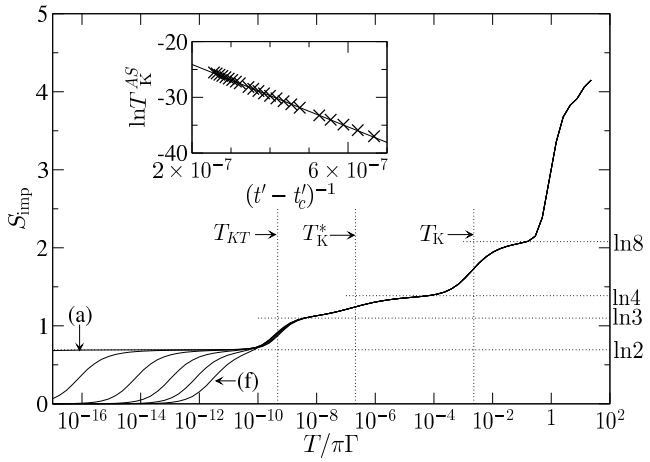


Figure 5.15: The entropy $S_{\rm imp}$ vs $T/\pi\Gamma$ for systems closely approaching the phase boundary. $\tilde{U} = 4$, $\tilde{t} \approx 3.640 \times 10^{-2}$ and $\tilde{\delta} = 10^{-5}$, with $\tilde{t}' = 1.004107 \times 10^{-2}$ for (a), 1.0041075×10^{-2} for (b), 1.004108×10^{-2} for (c), 1.0041085×10^{-2} for (d) and 1.004109×10^{-2} for (e). $\tilde{t}'_c = 1.004106 \times 10^{-2}$, and the inset shows $\ln T_{\rm K}^{AS}$ as a function of $(t' - t'_c)^{-1}$. (We define $T_{\rm K}^{AS}$ via $S_{\rm imp}(T_{\rm K}^{AS}) = 0.5 \ln 2$).

the phase boundary $T_{KT} \sim \delta^*$: from the discussion above one would expect both that $\delta^* = \delta^*(\delta)$ and that $\delta^* \ll \delta$, results which are both confirmed by the NRG, as shown in the inset to Fig. 5.14.

Having discussed the behaviour of a system at the phase boundary, we now consider the behaviour of the TQD as the phase boundary is approached: Fig. 5.15 shows the behaviour of such a system. The system here exhibits an identical physics to that described above until the energy scale T_{KT}, below which the system flows to the local moment fixed point (as the lowest lying excited state becomes thermally inaccessible). The system is found to flow away from the local moment fixed point on an energy scale $T_{\rm K}^{AS}$ (defined via $S_{\rm imp}(T_{\rm K}^{AS}) = 0.5 \ln 2$, suitably between $\ln 2$ and 0), which vanishes exponentially as the phase boundary is approached, giving rise to a Kosterlitz-Thouless transition, as shown in the inset to Fig. 5.15. As discussed above, the asymmetry in the system leads to mixing between the 1–3 singlet and (underscreened) triplet states, and the avoided crossing which results naturally means that a first order quantum phase transition is not seen.

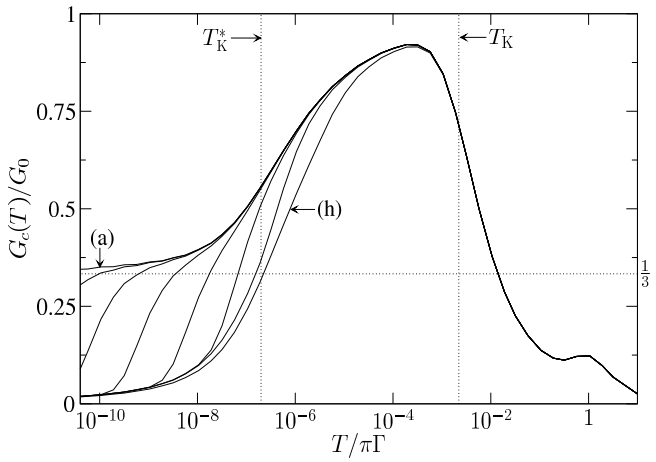


Figure 5.16: The zero-bias conductance for systems in regime I at the phase boundary, with the same parameters as Fig. 5.14.

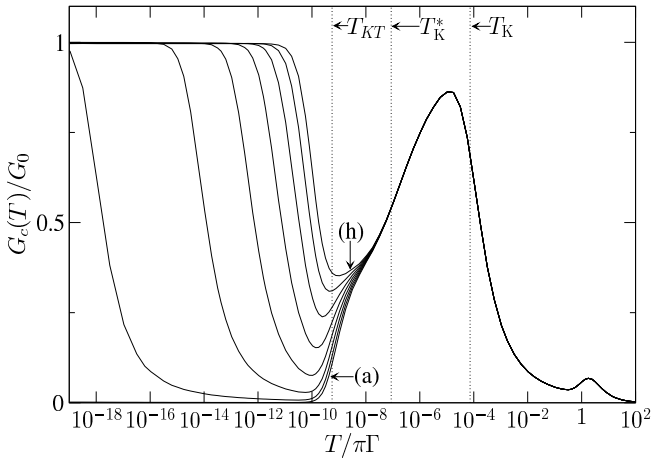


Figure 5.17: The zero-bias conductance for systems in regime I close to the phase boundary. $\tilde{U} = 7$, $\tilde{t} = 10^{-2}$ and $\tilde{\delta} = 10^{-6}$. $\tilde{t}' = 3.285 \times 10^{-3}$ for (a), 3.28504×10^{-3} for (b), 3.28508×10^{-3} for (c), 3.28512×10^{-3} for (d), 3.28516×10^{-3} for (e), 3.2852×10^{-3} for (f), 3.28524×10^{-3} for (g) and 3.28528×10^{-3} for (h), with $\tilde{t}'_c = 3.28497 \times 10^{-3}$.

5.6.2 Dynamics

We now consider the dynamical properties of the asymmetric TQD in regime I. When far removed from the transition it is generically found that the zero-temperature single particle spectrum of dot 2, $\pi\Gamma D_{2\sigma}(\omega)$, and conductance are indistinguishable from those of regime I of the ACTM, discussed in Sec. 4.7.3 and 4.7.3.1, rising to the unitarity limit on a scale $\omega \sim T_{\rm K}$ ($T \sim T_{\rm K}$ for the conductance) in the strong coupling phase. In the local moment phase, the spectra (conductance) initially

increases to near the unitarity limit on a scale $\omega \sim T_{\rm K}$ ($T \sim T_{\rm K}$), and then decays to zero with logarithmic corrections when $\omega < T_{\rm K}^{*}$ ($T < T_{\rm K}^{*}$), as one would expect for a singular Fermi Liquid [126, 127].

Fig. 5.16 shows the zero-bias conductance for a system at the phase boundary, for various values of δ. The conductance is very similar to that found in the corresponding case of the ACTM (see Fig. 4.12), except that the system ultimately flows away from the 'transition fixed point' (where $G_c/G_0 = 1/3$) on an energy scale T_{KT}, which varies linearly with δ. As discussed above, T_{KT} corresponds to the energy scale upon which the lowest lying excited state becomes thermally inaccessible.

Fig. 5.17 shows the behaviour of systems approaching the phase boundary. Here an initial increase in G_c/G_0 to $G_c/G_0 \sim 1$ is observed at an energy scale $T \sim T_{\rm K}$, corresponding to the scale on which the 2 site is Kondo quenched. The conductance decays on an energy scale $T \sim T_{\rm K}^{*}$, when the triplet is underscreened by coupling to the wider conduction band, to $G_c/G_0 \sim \frac{1}{3}$, characteristic of the 'transition fixed point'. On a further low energy scale $T \sim T_{KT}$ (defined via $S_{\rm imp}(T_{KT}) = 0.5 \ln 6$), the lowest excited state is projected out and the conductance falls towards zero (characteristic of the local moment fixed point), before finally rising to $G_c/G_0 = 1$ on an energy scale $T_{\rm K}^{AS}$, which vanishes exponentially as the phase boundary is approached. The final value, $G_c/G_0 = 1$, is characteristic of the strong coupling fixed point, which is (as discussed above) the ultimate low temperature fixed point of the system in the strong coupling phase. It is generically found that the Luttinger integral, $I_{\rm L} = {\rm Im\,Tr} \int_{-\infty}^{0} d\omega \frac{\partial \mathbf{\Sigma}_\sigma}{\partial \omega} \mathbf{G}_\sigma = 0$ in the strong coupling phase (as expected for a Fermi Liquid [120]) and $|I_{\rm L}| = \frac{\pi}{2}$ in the local moment phase (as expected for a singular Fermi Liquid [55]), and so we expect there to be a discontinuous change in the zero-temperature zero-bias conductance of the system exactly at the phase boundary.

5.7 Regime III: The Orbital Regime

We consider next regime III (see Sec. 5.4 and Fig. 5.4), which is, just as in the ACTM, a weakly interacting regime ($t \sim \mathcal{O}(U)$ or larger), where the effective spin model $\hat{H}_{spin}$ is no longer a valid description of the system at low temperature. We find that the phase boundary follows the line $t' \approx U/4$ when x is small ($x \ll t$), independent of the value of t and x. However when $x \geq t$ this line no longer describes the phase boundary well, as shown in Fig. 5.4. In this section we attempt to provide a theoretical justification for the position of the phase boundary, and the behaviour of the system in both the local moment and strong coupling phases. Just as in the mirror symmetric case (Sec. 4.8.1) a natural starting point for a theoretical examination of the system in regime III is provided by the non-interacting TQD Hamiltonian, $\hat{H}_{NIAACTM} = \hat{H}_{NITQD} + \hat{H}_{hyb} + \hat{H}_L$, with

$$\hat{H}_{NITQD} = \sum_{i,\sigma} \epsilon \hat{n}_{i\sigma} + \sum_{\sigma} t[(c^{\dagger}_{1\sigma} + c^{\dagger}_{3\sigma})c_{2\sigma} + H.c.] + \sum_{\sigma} t'[c^{\dagger}_{1\sigma}c_{3\sigma} + H.c.] + \sum_{\sigma} x[c^{\dagger}_{2\sigma}c_{3\sigma} + H.c.]. \tag{5.27}$$

where we remove the restriction that $\epsilon = -U/2$, but we do specify that $t \gg |\epsilon|, t'$ and $\epsilon < 0$ (just as was the case for regime III of the ACTM). At this stage we make no assumptions about the relative size of x. Taking even and odd parity combinations of the 1 and 3 orbitals, $c^{\dagger}_{e\sigma} = \frac{1}{\sqrt{2}}(c^{\dagger}_{1\sigma} + c^{\dagger}_{3\sigma})$ and $c^{\dagger}_{o\sigma} = \frac{1}{\sqrt{2}}(c^{\dagger}_{1\sigma} - c^{\dagger}_{3\sigma})$, $\hat{H}_{NITQD}$ may be written

$$\hat{H}_{NITQD} = \sum_{\sigma} \begin{pmatrix} c^{\dagger}_{2\sigma} & c^{\dagger}_{e\sigma} & c^{\dagger}_{o\sigma} \end{pmatrix} \begin{pmatrix} \epsilon & \sqrt{2}(t + \frac{x}{2}) & -\frac{x}{\sqrt{2}} \\ \sqrt{2}(t + \frac{x}{2}) & (\epsilon + t') & 0 \\ -\frac{x}{\sqrt{2}} & 0 & (\epsilon - t') \end{pmatrix} \begin{pmatrix} c_{2\sigma} \\ c_{e\sigma} \\ c_{o\sigma} \end{pmatrix}. \tag{5.28}$$

From Eq. 5.28 it is clear that $\hat{H}_{NITQD}$ can formulated as a very simple three level system (just as was done in the mirror symmetric case — see Eq. 4.21),

$$\hat{H}_{NITQD} = \sum_{\sigma} E_{\alpha} c^{\dagger}_{\alpha\sigma} c_{\alpha\sigma} + \sum_{\sigma} E_{\beta} c^{\dagger}_{\beta\sigma} c_{\beta\sigma} + \sum_{\sigma} E_{\gamma} c^{\dagger}_{\gamma\sigma} c_{\gamma\sigma} \tag{5.29}$$

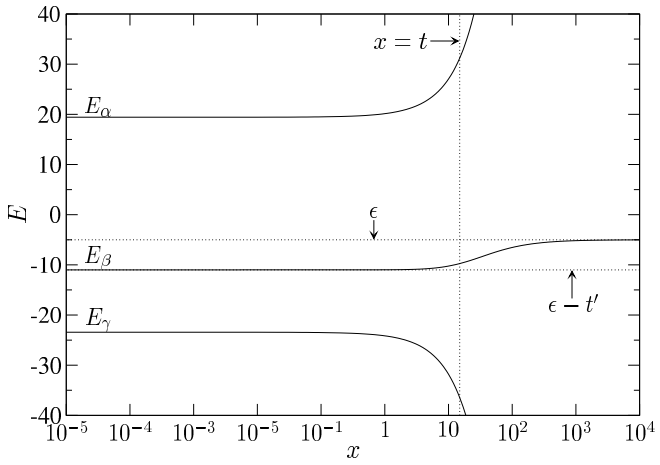


Figure 5.18: Energies of the α, β and γ orbitals of the isolated, non-interacting TQD as a function of x. $\epsilon = -5$, $t = 15$ and $t' = 6$ in arbitrary units.

where E_α, E_β and E_γ are the eigenvalues of the matrix

$$\mathbf{M} = \begin{pmatrix} \epsilon & \sqrt{2}(t + \frac{x}{2}) & -\frac{x}{\sqrt{2}} \\ \sqrt{2}(t + \frac{x}{2}) & (\epsilon + t') & 0 \\ -\frac{x}{\sqrt{2}} & 0 & (\epsilon - t') \end{pmatrix} \tag{5.30}$$

(which we diagonalise numerically), and

$$c^\dagger_{\alpha\sigma} = \alpha_1 c^\dagger_{e\sigma} + \alpha_2 c^\dagger_{o\sigma} + \alpha_3 c^\dagger_{2\sigma}, \tag{5.31a}$$

$$c^\dagger_{\beta\sigma} = \beta_1 c^\dagger_{e\sigma} + \beta_2 c^\dagger_{o\sigma} + \beta_3 c^\dagger_{2\sigma}, \tag{5.31b}$$

$$c^\dagger_{\gamma\sigma} = \gamma_1 c^\dagger_{e\sigma} + \gamma_2 c^\dagger_{o\sigma} + \gamma_3 c^\dagger_{2\sigma}. \tag{5.31c}$$

We define $E_\alpha > E_\beta > E_\gamma$, and find that the β orbital is closest to the Fermi level — indeed, we generally find that for $x \ll t$ $E_\beta = \epsilon - t'$, just as for the mirror symmetric case, and for $x \gg t$ $E_\beta = \epsilon$, as shown in Fig. 5.18. The ground state of Eq. 5.29 is therefore naturally a four electron singlet state ($|0;0\rangle$), and the first excited state is a three electron doublet state ($|\frac{1}{2};S^z\rangle$) (again, very similar to the results derived in

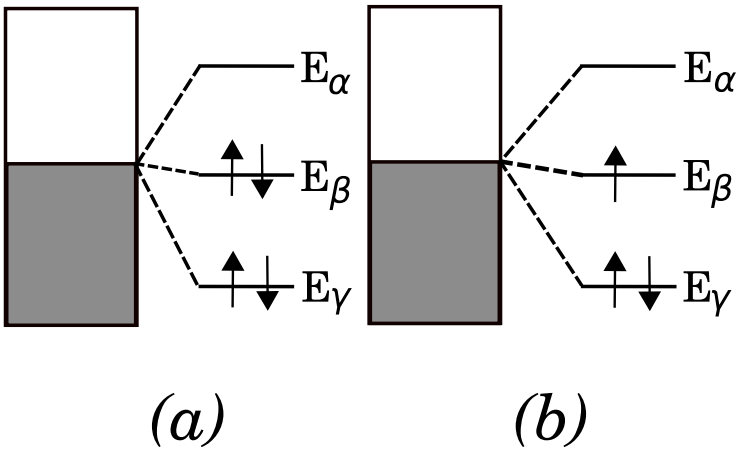


Figure 5.19: A schematic illustration of the (a) $|0;0\rangle$ and (b) $|\frac{1}{2};S^z\rangle$ states of the AACTM in regime III.

the mirror symmetric case):

$$|0;0\rangle = c^\dagger_{\beta\uparrow}c^\dagger_{\beta\downarrow}c^\dagger_{\gamma\uparrow}c^\dagger_{\gamma\downarrow}|Vac\rangle, \tag{5.32a}$$

$$|\tfrac{1}{2};\sigma\rangle = c^\dagger_{\beta\sigma}c^\dagger_{\gamma\uparrow}c^\dagger_{\gamma\downarrow}|Vac\rangle, \tag{5.32b}$$

as illustrated schematically in Fig. 5.19. The energy difference between these two states is evidently

$$\langle 0;0|\hat{H}_{NITQD}|0;0\rangle - \langle \tfrac{1}{2};S^z|\hat{H}_{NITQD}|\tfrac{1}{2};S^z\rangle = E_\beta. \tag{5.33}$$

However, we must also take account of electron-electron correlations, which we do by treating $\hat{H}_U = \sum_i U\hat{n}_{i\uparrow}\hat{n}_{i\downarrow}$ as a perturbation (to first order) to $|0;0\rangle$ and $|\frac{1}{2};S^z\rangle$, as described in Appendix D. The energy difference between these two states, *including*

electron-electron correlations is then determined to be

$$E'_\Delta = \langle 0;0|\hat{H}_{NITQD}|0;0\rangle + \langle 0;0|\hat{H}_U|0;0\rangle - \langle \tfrac{1}{2};S^z|\hat{H}_{NITQD}|\tfrac{1}{2};S^z\rangle - \langle \tfrac{1}{2};S^z|\hat{H}_U|\tfrac{1}{2};S^z\rangle, \tag{5.34a}$$

$$\begin{aligned} =& E_\beta + \frac{U}{4}(\beta_1+\beta_2)^2[(\beta_1+\beta_2)^2+(\gamma_1+\gamma_2)^2] + U\beta_3^2(\beta_3^2+\gamma_3^2) \\ &+ \frac{U}{4}(\beta_1-\beta_2)^2[(\beta_1-\beta_2)^2+(\gamma_1-\gamma_2)^2]. \end{aligned} \tag{5.34b}$$

We note that in the mirror symmetric case,

$$\begin{aligned} &\alpha_1 = \nu, \quad \alpha_2 = 0, \quad \alpha_3 = -\gamma, \\ &\beta_1 = 0, \quad \beta_2 = 1, \quad \beta_3 = 0, \\ &\gamma_1 = \gamma, \quad \gamma_2 = 0, \quad \gamma_3 = \nu, \end{aligned} \tag{5.35}$$

where γ and ν are defined in Eq. 4.23. In the limit $x = 0$ E'_Δ reduces to

$$E'_\Delta(x=0) = \epsilon - t' + \frac{U}{2}(1+\gamma^2), \tag{5.36}$$

thereby recovering the mirror symmetric results. We therefore predict that the ground state of the system will be either a four-electron singlet state (when $E'_\Delta < 0$) or a three-electron doublet state (when $E'_\Delta > 0$), with a phase transition at $E'_\Delta = 0$. As there is no longer a parity change associated with the phase transition, close to the transition there will be mixing between the singlet and doublet states, leading to charge fluctuations on the TQD, and so there will not be a first order quantum phase transition: we would expect to see a smooth crossover from $n_{\rm imp}^{LM} = 3$ to $n_{\rm imp}^{SC} = 4$ when $E'_\Delta \approx 0$, rather than the discontinuous change in $n_{\rm imp}$ seen in the ACTM (Sec. 4.8.2). As discussed in Sec. 5.4 this is indeed what we find, with the line $E'_\Delta = 0$ describing the position of the crossover well for all x (this line is labelled "semi-analytic results" in Fig. 5.4).

When $|E'_\Delta| \gg 0$ (in practice $|E'_\Delta| \gg T_{KT}$, as discussed below in Sec. 5.7.1) there

is negligible mixing between the singlet and doublet states (as is easily confirmed by calculating $n_{\rm imp}$ for the local moment and strong coupling phases), and so the states of the trimer may be treated as entirely singlet or entirely doublet in character. This allows us to estimate the coupling of these states to the conduction band; deep in the strong coupling phase ($E'_\Delta \ll 0$), where the ground state of the TQD is $|0;0\rangle$, this presents no difficulties: the system will ultimately flow to a frozen impurity fixed point, just as was the case for the corresponding mirror symmetric case.

Similarly, deep in the local moment phase ($E'_\Delta \gg 0$), the ground state of the TQD is the $|\frac{1}{2};S^z\rangle$ doublet. The coupling of this doublet state to the conduction band is more complex to determine, as, unlike the corresponding case of the ACTM (Sec. 4.8.1), the β orbital here is not necessarily decoupled from the conduction band. However, our approach is not fundamentally different from that taken in Sec. 4.8.1: after determining the ground state of the full $\hat{H}_{TQD}$, which is a doublet in the three-electron subsector, we project into the low energy manifold containing only that doublet state, and perform a Schrieffer-Wolff transformation [13] (just as was done in Sec. 4.8.1), evaluating

$$\hat{H}_{eff} = \hat{1}\hat{H}_0\hat{1} + \hat{1}\hat{H}_{hyb}(E_0 - \hat{H}_0)^{-1}\hat{P}\hat{H}_{hyb}\hat{1} \tag{5.37}$$

where $\hat{H}_0 = \hat{H}_{TQD} + \hat{H}_L$, $\hat{P} = \hat{1}_{full} - \hat{1}$, with $\hat{1}_{full}$ the complete Hilbert space, and E_0 is the energy of the ground state under $\hat{H}_0$. Eq. 5.37 gives rise to an effective (isotropic) Kondo model for the system in this regime,

$$\hat{H}_{eff} = J_{{\rm K},eff}\hat{\mathbf{S}}\cdot\hat{\mathbf{S}}(0) + \hat{H}_L, \tag{5.38}$$

where $\hat{\mathbf{S}}$ is a spin-$\frac{1}{2}$ operator for the TQD as a whole and $\hat{\mathbf{S}}(0)$ is the electron spin density at dot 2. Neglecting retardation effects, we can evaluated $J_{{\rm K},eff}$ numerically here, as described in Appendix E. We find that the coupling of the doublet state to the conduction band is ferromagnetic for all x, approaching zero when $x \geq t$,

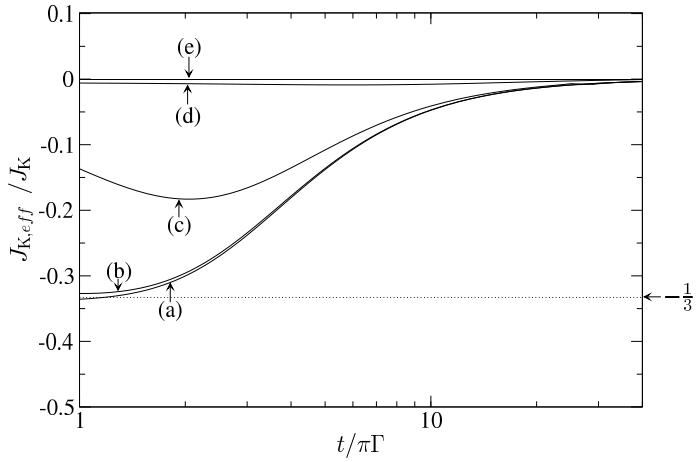


Figure 5.20: The effective Kondo coupling, $J_{\mathrm{K},eff}$, between the three electron doublet state and the conduction band as a function of $\tilde{t}$ for a system with $\tilde{U} = 10$ and $\tilde{t}' = 10^{-1}$ for varying $\tilde{x}$, with $\tilde{x} = 10^{-2}$ for line (a), 10^{-1} for (b), 1 for (c), 10 for (d) and 10^2 for (e).

as shown in Fig. 5.20. This behaviour is easily understood as the result of dots 2 and 3 locking up in a singlet state when x is large ($x > t$), leaving the spin of the doublet state localised on dot 1, which is naturally decoupled from the conduction band; further support for this argument is provided by the limiting value of E_β at large x, ϵ, as shown in Fig. 5.18. When $E'_\Delta \gg 0$ we therefore expect the system to ultimately flow to the local moment fixed point, for all x.

However, the arguments given above are valid *only* in the case where charge fluctuations are negligible — i.e. when the system is far from the transition. Close to the transition ($|E'_\Delta| < T_{KT}$, where we define T_{KT} below) mixing between the singlet and doublet states occurs, and significant charge fluctuations on the TQD are seen. As a result, although our semi-analytic results accurately predict the shape and position of the crossover in n_{imp}, we are unable to derive a low energy effective model which accurately describes the system close to the phase boundary.

5.7.1 Thermodynamics

We find that in order to obtain accurate results, it is necessary to retain a maximum of $N_s = 3000$ states in each iteration here, just as in Sec. 4.8. Just as in regimes I ($J < 10T_{\mathrm{K}}$) and II ($J > 10T_{\mathrm{K}}$), we find that when the behaviour of the system is

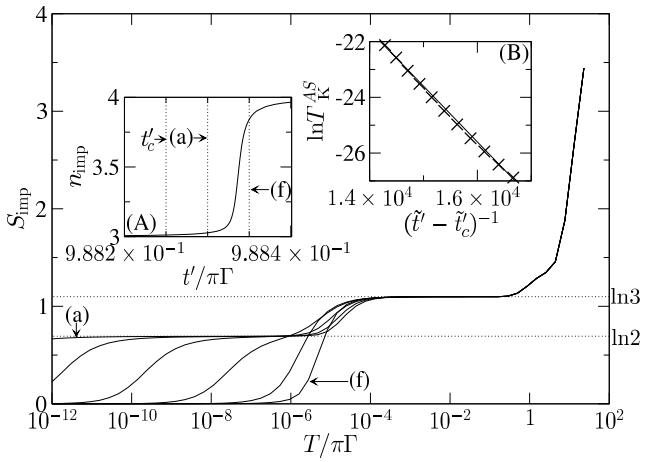


Figure 5.21: Entropy $S_{\rm imp}$ vs $T/\pi\Gamma$ for a system in regime III approaching the phase boundary; $\tilde{U} = 4$, $\tilde{t} = 2 \times 10^1$ and $\tilde{x} = 1$. $\tilde{t}'$ is varied, with $\tilde{t}' = 9.883 \times 10^{-1}$ for (a), 9.8831×10^{-1} for (b), 9.8832×10^{-1} for (c), 9.8833×10^{-1} for (d), 9.8834×10^{-1} for (e) and 9.8835×10^{-1} for (f). Inset A shows $n_{\rm imp}$ as a function of $\tilde{t}'$ for the same system, and the positions of lines (a) and (f) from the main graph are shown. Inset B plots $(\tilde{t}' - \tilde{t}'_c)^{-1}$ against $\ln T_{\rm K}^{AS}$, with $T_{\rm K}^{AS}$ defined via $S_{\rm imp}(T_{\rm K}^{AS}) = 0.5 \ln 2$ and $\tilde{t}'_c = 9.8825 \times 10^{-1}$.

identical to that of the corresponding mirror symmetric case (described in Sec. 4.8) when it is not close to the phase boundary. In this section we therefore confine our discussion to systems close to the phase boundary.

The impurity contribution to the entropy for a system approaching the phase boundary is shown in Fig. 5.21. We find that the system is initially described at high temperature by the free orbital fixed point [7,8], giving rise to an initial entropy of $\ln 64$ and a $T\chi_{\rm imp}$ of $3 \times \frac{1}{8}$ (not shown); $n_{\rm imp} = 3$ here. At $T \sim t$ the system then flows to the 'transition fixed point', characterised by $S_{\rm imp} = \ln 3$ and $T\chi_{\rm imp} = \frac{1}{6}$. In this region only the two lowest energy states, comprising linear combinations of the four electron singlet and three electron doublet states, are accessible. The system flows close to the 'transition fixed point' until an energy scale $T \sim T_{KT}$ is reached. The system flows to the local moment fixed point ($S_{\rm imp} = \ln 2$ and $T\chi_{\rm imp} = 1/4$) on this scale, which corresponds to the temperature below which the lowest lying excited state of the system becomes thermally inaccessible. We find from the NRG that $T_{KT} \propto x^2$ (for fixed $\tilde{U}$ and $T_{\rm K}^{AS}$), and so, just as in regime I ($J < 10T_{\rm K}$) and II ($J > 10T_{\rm K}$), the system at the phase boundary is described by the 'transition fixed

point' down to zero temperature *only* when $x = 0$.

If the system is in the strong coupling phase (corresponding to $t' \gtrsim U/4$ when $x < t$) , it will then flow to the strong coupling fixed point ($S_{\rm imp} = 0$ and $T\chi_{\rm imp} = 0$) on an energy scale $T_{\rm K}^{AS}$ (defined via $S_{\rm imp}(T_{\rm K}^{AS}) = 0.5 \ln 2$, suitably between $\ln 2$ and 0) which vanishes exponentially as the phase transition is approached — as shown in inset B to Fig. 5.21 — giving rise to a Kosterlitz-Thouless transition. If the system lies within the local moment phase, then the local moment fixed point is obviously the ultimate low temperature fixed point, and the system will not flow away from it.

As shown in inset B to Fig. 5.21, and very much unlike corresponding case of the ACTM, the change in $n_{\rm imp}$ from 3 to 4 that is observed here is *continuous*, and is *not* coincident with the phase transition: we can understand this as the ultimate low temperature fixed point of the system changing from the local moment fixed point to the strong coupling fixed point when $t' = t'_c$, and then from the strong coupling fixed point to the frozen impurity fixed point when $t' = t'_{c,1}$. As is shown in Fig. 5.4, when $x < t$ the change in $n_{\rm imp}$ and the phase transition are found to occur at very similar values of t'. Unfortunately, these two scales appear to diverge when $x > t$, but as we are unable to determine t'_c in this region with any degree of accuracy (see Sec. 5.4.1), this is something of a moot point. A good agreement of our semi-analytic results, as described in the previous section, with the position of the crossover in $n_{\rm imp}$ is found for all parameters.

5.7.2 Dynamics

In the mirror symmetric case we found that $G_c(0)/G_0 = 0$ (and therefore $\pi\Gamma D_{2\sigma}(\omega) = 0$) in both the strong coupling and local moment phases of regime III, as although the Luttinger integral, $I_{\rm L} = {\rm Im\,Tr} \int_{-\infty}^{0} d\omega \frac{\partial \mathbf{\Sigma}_\sigma}{\partial \omega} \mathbf{G}_\sigma$, changed discontinuously across the phase boundary (being generically found to be 0 in the strong coupling phase, and $\pm\frac{\pi}{2}$ in the local moment phase), $n_{\rm imp}$ also changed discontinuously from 3 to

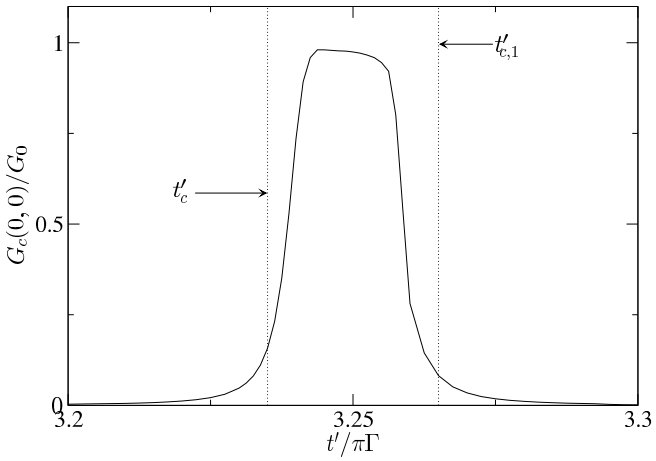


Figure 5.22: The zero-temperature, zero-bias conductance for a system with $\tilde{U} = 10$, $\tilde{t} = 15$ and $\tilde{x} = 10$, as a function of $\tilde{t}'$. The scales $t'_{c,1}$ and t'_c are shown on the figure, where t'_c is the value of t' for which the Kondo temperature $T_{\rm K}^{AS} = 0$.

4 across the phase boundary (see Sec. 4.8.3). In the asymmetric case, we also find generically (via direct calculation using the NRG) that $I_{\rm L} = 0$ in the strong coupling phase and $|I_{\rm L}| = \frac{\pi}{2}$ in the local moment phase. However, as noted in the previous section, the change in $n_{\rm imp}$ is *not* coincident with the phase boundary in the mirror symmetric case. This leads to the behaviour shown in Fig. 5.22, where an enhanced conductance is observed in the region between t'_c and $t'_{c,1}$ (corresponding to the region where the ultimate low temperature fixed point of the system is the strong coupling fixed point), which, if the two scales are sufficiently well separated, may rise to the unitarity limit. Deep in the strong coupling and local moment phases, $G_c(0)/G_0$ is found to be zero, just as in the mirror symmetric case, although, as expected, logarithmic corrections are observed in the local moment phase, but absent in the strong coupling phase.

5.8 Magnetic Fields

We now consider the effect of an applied field ($h \neq 0$) upon the system, with the aim of providing simple physical arguments and intuitive low energy effective models to accurately explain the behaviour of the system under a field in all regimes. We

discuss the regimes in the same order as in the preceding work, considering first regime II, then regime I and finally regime III (see Sec. 5.4).

5.9 Magnetic Fields: Regime II: $J > 10T_{\mathrm{K}}$

We now consider the effect of an applied field upon the system in regime II (see Fig. 5.2). Introducing a magnetic field generates a term of the form $\hat{H}_h = -2h\hat{S}_z = -2h(\hat{S}_1 + \hat{S}_2 + \hat{S}_3)$ in the effective spin model for this system (Eq. 5.3), which is now $\hat{H}^h_{spin} = \hat{H}_{spin} + \hat{H}_h$, just as in the mirror symmetric case.

5.9.1 Effective Low Energy Model

A weak field ($h \ll T_{\mathrm{K}}^{AS}$) will have no effect upon the physical properties of a system in the strong coupling phase of regime II[6], which will continue to be described by the low energy effective model Eq. 5.18 on the lowest temperature scales. At larger fields ($h \gtrsim T_{\mathrm{K}}^{AS}$) the zero-field Kondo effect will be suppressed, such that when $h \gg T_{\mathrm{K}}^{AS}$ only the $|\frac{1}{2}; A; +\frac{1}{2}\rangle$ component of the ground state doublet of the isolated trimer will be accessible at the lowest temperatures (this is the case for any $h > 0$ for systems in the local moment phase in the absence of a field). An applied field stabilises states with $S^z > 0$, and stabilises states with high S^z more than states with low S^z. As such, it is clear that the ground state of the trimer for fields $h \gg T_{\mathrm{K}}^{AS}$ (such that any zero-field Kondo effects are suppressed) will be either the $|\frac{1}{2}; A; +\frac{1}{2}\rangle$ state or the $|\frac{3}{2}; +\frac{3}{2}\rangle$ component of the quartet state (as discussed in Sec. 5.5.1 the $|\frac{1}{2}; B; S^z\rangle$ doublet is always higher in energy than the $|\frac{1}{2}; A; S^z\rangle$ doublet). At some 'critical' field ($h_c = \frac{1}{2}(J + \frac{J'}{2} + \frac{\delta}{2} + \frac{1}{2}\sqrt{(J - J' + \frac{1}{2}\delta)^2 + \frac{3}{4}\delta^2})$, as easily determined from the energies of the isolated states) the two states, $|\frac{1}{2}; A; +\frac{1}{2}\rangle$ and $|\frac{3}{2}; +\frac{3}{2}\rangle$ will cross, and we would expect (based on our results for the apex coupled trimer model, described in Sec. 4.10.1) to observe a field-induced Kondo effect.

[6] Any non-zero field will, of course, lift the degeneracy of the ground state of a system in the local moment phase in the absence of a field.

For fields $h \sim h_c$ the unity operator spanning the reduced Hilbert space of the low energy manifold is $\hat{1} = \hat{1}_+ + \hat{1}_- = |\frac{3}{2};+\frac{3}{2}\rangle\langle\frac{3}{2};+\frac{3}{2}| + |\frac{1}{2};A;+\frac{1}{2}\rangle\langle\frac{1}{2};A;+\frac{1}{2}|$. Projecting into this manifold, the low energy effective model follows immediately as $\hat{H}_{eff} = \hat{1}\hat{H}^h_{spin}\hat{1}$ i.e. $\hat{H}_{eff} = J_{\rm K}\hat{1}\hat{\mathbf{S}}_2\hat{1}\cdot\hat{\mathbf{S}}(0) + \frac{1}{2}E_\Delta(\hat{1}_+ - \hat{1}_-) + \hat{H}_L$ where $E_\Delta = J + \frac{J'}{2} + \frac{\delta}{2} + \frac{1}{2}\sqrt{(J - J' + \frac{1}{2}\delta)^2 + \frac{3}{4}\delta^2} - 2h$ is the energy separation between the quartet and doublet states. Defining a pseudospin

$$\hat{\mathcal{T}}^z = \frac{1}{2}(\hat{1}_+ - \hat{1}_-), \tag{5.39a}$$

$$\hat{\mathcal{T}}^+ = |\tfrac{3}{2};+\tfrac{3}{2}\rangle\langle\tfrac{1}{2};A;+\tfrac{1}{2}|, \tag{5.39b}$$

$$\hat{\mathcal{T}}^- = |\tfrac{1}{2};A;+\tfrac{1}{2}\rangle\langle\tfrac{3}{2};+\tfrac{3}{2}|, \tag{5.39c}$$

such that $|\frac{3}{2};+\frac{3}{2}\rangle$ and $|\frac{1}{2};A;+\frac{1}{2}\rangle$ are eigenstates of $\hat{\mathcal{T}}^z$ with eigenvalues $\pm\frac{1}{2}$, respectively, and evaluating $\hat{1}\hat{\mathbf{S}}_2\hat{1}$, we find that the low energy effective model may be written

$$\begin{aligned}\hat{H}_{eff} =& \frac{2}{3}J_{\rm K}\alpha^2\hat{\mathcal{T}}^z\hat{S}^z(0) - \frac{2}{\sqrt{6}}J_{\rm K}\alpha\frac{1}{2}\hat{\mathcal{T}}^+\hat{S}^-(0) - \frac{2}{\sqrt{6}}J_{\rm K}\alpha\frac{1}{2}\hat{\mathcal{T}}^-\hat{S}^+(0) + E_\Delta\hat{\mathcal{T}}^z \qquad (5.40a)\\ &+ \hat{H}_L,\\ =& J_{{\rm K},z}\hat{\mathcal{T}}^z\hat{S}^z(0) + \frac{1}{2}J_{{\rm K},\perp}\hat{\mathcal{T}}^+\hat{S}^-(0) + \frac{1}{2}J_{{\rm K},\perp}\hat{\mathcal{T}}^-\hat{S}^+(0) + E_\Delta\hat{\mathcal{T}}^z + \hat{H}_L, \qquad (5.40b)\end{aligned}$$

where potential scattering is neglected for clarity. Eq. 5.40 takes the form of a spin-anisotropic Kondo model under a longitudinal magnetic field, E_Δ, with $J_{{\rm K},\perp} = -\frac{2}{\sqrt{6}}\alpha J_{\rm K}$ and $J_{{\rm K},z} = \frac{2}{3}\alpha^2 J_{\rm K}$ — just as in the ACTM. From Sec. 5.5.1 we know that $-1 < \alpha < 1$ and therefore $0 < \alpha^2 < 1$, with the ACTM being described by $\alpha^2 = 0$ (for the strong coupling case) and $\alpha^2 = 1$ (for the local moment case). Let us therefore examine these limits; in the limit $\alpha \to 0$, Eq. 5.40 reduces to

$$\hat{H}_{eff} = E_\Delta\hat{\mathcal{T}}^z + \hat{H}_L, \tag{5.41}$$

recovering the results of the strong coupling case (Eq. 4.32 with potential scattering

neglected), where mixing between the quartet and doublet states is forbidden by symmetry. Likewise, taking the limit $\alpha \to 1$ recovers the results of the local moment case (Eq. 4.34) exactly — an anisotropic Kondo model with $J_{\mathrm{K},\perp} = -\frac{2}{\sqrt{6}}J_{\mathrm{K}}$ and $J_{\mathrm{K},z} = \frac{2}{3}J_{\mathrm{K}}$.

As discussed in Sec. 4.10 and Appendix F we may use the Poor Man's Scaling technique of Anderson [2,14] to derive an expression for T_{K}^h, the Kondo temperature of the effective model Eq. 5.40:

$$\frac{T_{\mathrm{K}}^h}{D} \propto \exp\left\{-\frac{1}{\rho\left|2\alpha J_{\mathrm{K}}\sqrt{\frac{1}{6}-\frac{\alpha^2}{9}}\right|}\left(\frac{\pi}{2} - \arctan\left[\frac{|\alpha|}{3\sqrt{\frac{1}{6}-\frac{\alpha^2}{9}}}\right]\right)\right\}. \tag{5.42}$$

As the sign of $J_{\mathrm{K},\perp}$ does not affect the scaling properties of the system [2, 14], we predict from Eq. 5.40 that for all non-zero α, Kondo physics may be observed when E_Δ is small (in practice, for $|E_\Delta| < T_{\mathrm{K}}^h$): the $E_\Delta \hat{\mathcal{T}}^z$ term in Eq. 5.40 acts as an effective magnetic field upon the pseudospin, and so will suppress the Kondo effect when $|E_\Delta| > T_{\mathrm{K}}^h$. However, we also note that the Kondo coupling may be extremely weak here, and may not therefore be observable on any reasonable temperature scale.

5.9.2 Thermodynamics

Fig. 5.23 shows m as a function of $\tilde{h}$ for a system which lies in the strong coupling phase of regime II in the absence of a field. Magnetic fields smaller than the Kondo temperature ($h \ll T_{\mathrm{K}}^{AS}$) have no discernible impact upon the thermodynamic properties of the system. As h is increased through T_{K}^{AS}, the Kondo quenching of the doublet is suppressed, and m increases smoothly from 0 towards 1 (asymptotically). A system initially in the local moment phase has no Kondo scale, and so any non-zero field gives an m of 1 in that case. m then remains ~ 1, until a field of $h \simeq h_c = \frac{J}{2} + \frac{J'}{4} + \frac{\delta}{4} + \frac{1}{4}\sqrt{(J - J' + \frac{1}{2}\delta)^2 + \frac{3}{4}\delta^2}$, corresponding to the point where

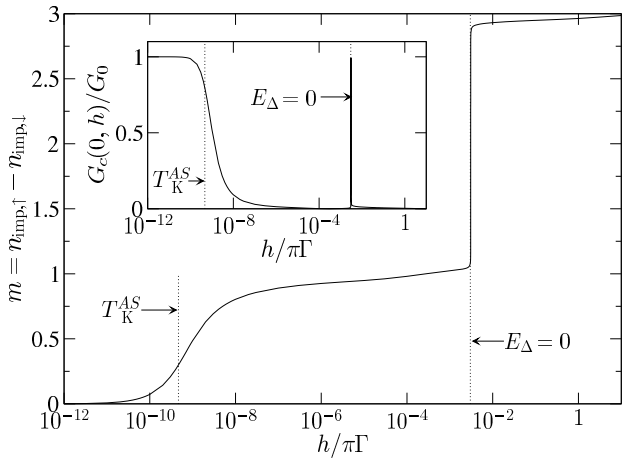


Figure 5.23: $m = n_{\mathrm{imp},\uparrow} - n_{\mathrm{imp},\downarrow}$ as a function of $\tilde{h}$ for a system in the strong coupling phase of regime II when $h = 0$ with $\tilde{U} = 10$, $\tilde{t} = 10^{-1}$, $\tilde{t}' = 9.76 \times 10^{-2}$ and $\tilde{\delta} = 10^{-4}$. The inset shows the zero-temperature, zero-bias conductance, $G_c(0,h)/G_0$, as a function of $\tilde{h}$, for the same system.

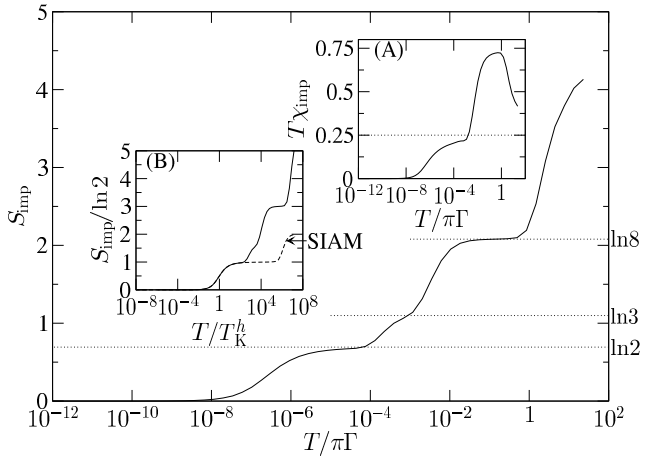


Figure 5.24: Entropy S_{imp} vs $T/\pi\Gamma$ for a system in regime II with $E_\Delta \simeq 0$. $\tilde{U} = 10$, $\tilde{t} = 10^{-1}$, $\tilde{t}' = 9.76 \times 10^{-2}$, $\tilde{\delta} = 10^{-4}$ and $\tilde{h} = 3.067 \times 10^{-3} \simeq \tilde{h}_c$. Inset A shows $T\chi_{\mathrm{imp}}$ for the same system, whilst inset B shows $S_{\mathrm{imp}}/\ln 2$ as a function of T/T_{K}^h (with T_{K}^h defined via $S_{\mathrm{imp}}(T_{\mathrm{K}}^h) = 0.5 \ln 2$). The dashed line in inset B is $S_{\mathrm{imp}}/\ln 2$ for a SIAM with $\tilde{U} = 10$, scaled by T_{K}.

$E_\Delta = J + \frac{J'}{2} + \frac{\delta}{2} + \frac{1}{2}\sqrt{(J - J' + \frac{1}{2}\delta)^2 + \frac{3}{4}\delta^2} - 2h \simeq 0$, is reached. At this point there is a sharp but continuous change in m, which increases towards 3. In all cases, and for all fields $S_{\mathrm{imp}}(T = 0) = 0$ and $T\chi_{\mathrm{imp}}|_{T=0} = 0$.

The thermodynamic properties of a system where $E_\Delta \simeq 0$ are shown in Fig. 5.24. At high temperature, the system is initially at the free orbital fixed point, characterised by $S_{\mathrm{imp}} = \ln 4^3$ and $T\chi_{\mathrm{imp}} = 3 \times \frac{1}{8}$. As the temperature is reduced through

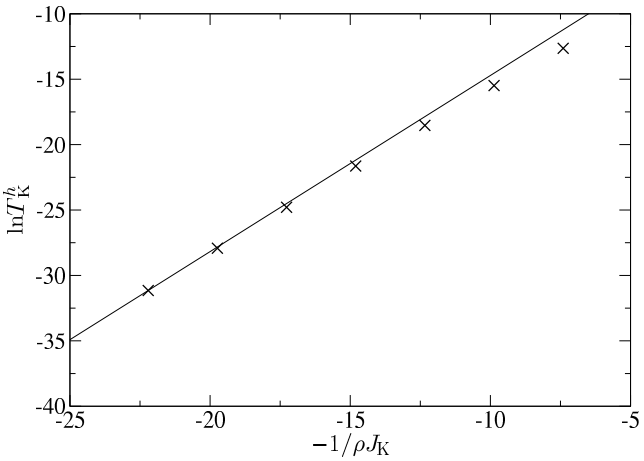


Figure 5.25: $\ln T_{\rm K}^h$ plotted against $-1/\rho J_{\rm K}$ for a range of systems with $E_\Delta \simeq 0$, $\tilde{\delta} = 10^{-4}$, $\tilde{J} = 4 \times 10^{-3}$ and $J' = 3.81 \times 10^{-3}$. $\tilde{U}$ is varied and $T_{\rm K}^h$ is defined via $S_{\rm imp}(T_{\rm K}^h) = 0.5 \ln 2$. The solid line is the expression for $T_{\rm K}^h$ derived from Poor Man's Scaling, given by Eq. 5.42.

$T \sim U$, the empty and doubly occupied states of each dot are projected out, and $S_{\rm imp}$ falls to $\ln 8$ ($T\chi_{\rm imp} = 3 \times \frac{1}{4}$), characteristic of three free spins. All but the three lowest lying states ($|\frac{1}{2}; A; +\frac{1}{2}\rangle$, $|\frac{1}{2}; B; +\frac{1}{2}\rangle$ and $|\frac{3}{2}; +\frac{3}{2}\rangle$) are then projected out on an energy scale $T \sim J$, at which point we find $S_{\rm imp} = \ln 3$. The $|\frac{1}{2}; B; +\frac{1}{2}\rangle$ state is rendered thermally inaccessible shortly thereafter, on an energy scale $T \sim \delta$. The system then flows to the local moment fixed point, characterised by $S_{\rm imp} = \ln 2$ and $T\chi_{\rm imp} = \frac{1}{4}$. Finally, on an energy scale $T_{\rm K}^h$, which we define by $S_{\rm imp}(T_{\rm K}^h) = 0.5 \ln 2$, the pseudospin is Kondo quenched, and the system flows to the strong coupling fixed point ($S_{\rm imp} = 0$ and $T\chi_{\rm imp} = 0$), which is the ultimate low temperature fixed point of the system. The flow to the strong coupling fixed point has the same functional form as the corresponding flow in the single impurity Anderson model — as is shown in inset B to Fig. 5.24.

As shown in Fig. 5.25 we find, just as in the ACTM, a very good agreement between the predicted behaviour of the Kondo temperature, $T_{\rm K}^h$, as given by Eq. 5.42, and the NRG when $T_{\rm K}^h$ is small (corresponding to $\tilde{U} \geq 6$).

5.9.3 Dynamics

The Luttinger integral, $I_{\rm L} = {\rm Im\,Tr}\int_{-\infty}^{0} d\omega \frac{\partial \mathbf{\Sigma}_\sigma}{\partial \omega}\mathbf{G}_\sigma$, is generically found (via direct calculation using the NRG) to be zero for all non-zero h for systems in both the local moment and strong coupling phases in the absence of a field, just as in the corresponding regime for the ACTM (see Sec. 4.10.3), and so $G_c(0,h)/G_c$ may be readily determined using Eq. 5.6b. Fields smaller than $T_{\rm K}^{AS}$ have no observable effect upon the system, and so the conductance remains at the unitarity limit. Increasing the field through $T_{\rm K}^{AS}$ causes the conductance to fall to zero, as the Kondo effect is suppressed. When $E_\Delta \simeq 0$ the pseudospin is quenched and a field-induced Kondo effect is observed, giving rise to a peak in the conductance which rises to the unitarity limit when $E_\Delta = 0$. This is shown in the inset to Fig. 5.23.

5.10 Magnetic Fields: Regime I: $J < 10T_{\rm K}$

We now consider the effect of an applied field upon a system in regime I (see Fig. 5.2), and build heavily upon the discussion of the low energy physics of regime I in the absence of a field, given in Sec. 5.6. As in that section we concentrate on the region where $T \ll T_{\rm K}$, such that dot 2 is Kondo quenched in the absence of a field. The low energy manifold therefore spans the 1-3 singlet and triplet combinations.

The $h = 0$ ground state of a system in the local moment phase of regime I in the absence of a field is a local moment arising as a result of underscreening of the 1–3 triplet, as described in Sec. 4.7. Any field ($h \neq 0$) will lift the degeneracy of the doublet state which arises as a result of the underscreening, but a field $0 < h \ll T_{\rm K}^*$ is not expected to have any other effect upon the system. Fields $T_{\rm K}^* \leq h \ll T_{\rm K}$ will suppress underscreening of the 1–3 triplet, such that for fields $T_{\rm K}^* \ll h \ll T_{\rm K}$ only the $S^z = +1$ component of the triplet will be accessible at the lowest temperatures. Increasing the field field further, such that $h \gg T_{\rm K}$, will suppress Kondo quenching of dot 2, and so the ultimate high field ground state of the isolated trimer is $|\frac{3}{2};-;+\frac{3}{2}\rangle$,

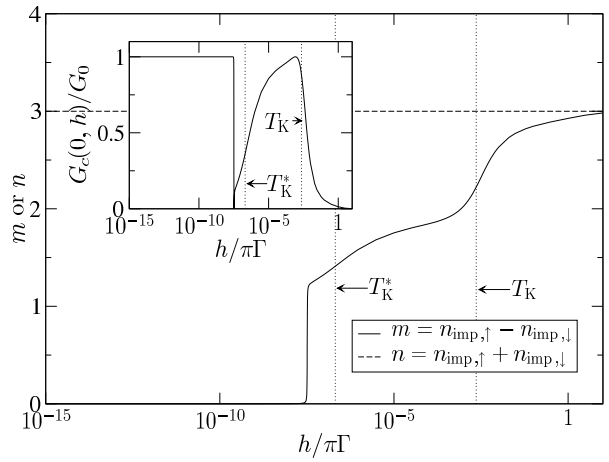


Figure 5.26: m and $n_{\rm imp}$ plotted against the applied field, $\tilde{h}$, for a system in the strong coupling phase of regime I when $h = 0$, with $\tilde{U} = 4$, $\tilde{t} \simeq 3.640 \times 10^{-2}$, $\tilde{t}' = 1.0043 \times 10^{-2}$ and $\tilde{\delta} = 10^{-5}$. Both $T_{\rm K}$ and $T_{\rm K}^*$ are shown on the diagram. The inset shows the zero-temperature, zero-bias conductance, $G_c(0,h)/G_0$ as a function of $\tilde{h}$ for the same system.

just as in regime II (Sec. 5.9.1).

Turning our attention to systems in the strong coupling phase of regime I in the absence of a field, it is clear that the 1–3 singlet state is unaffected by an applied field. As the $S^z = +1$ component of the triplet is stabilised by the field, there must exist some 'critical' field ($h_c = \frac{1}{2}(J' - \lambda\frac{J}{T_{\rm K}}(J+\delta))$, as easily determined from the energies of the states in the absence of a field) at which these states cross. Unlike the mirror symmetric case (Sec. 4.11) the singlet and triplet states do *not* have distinct parities here, and we would therefore expect to see a continuous change in m at $h \simeq h_c$.

5.10.1 Thermodynamics

An applied field is expected to stabilise states with $S_z > 0$, and so (as discussed above) one would expect the 1-3 triplet state (and the doublet which arises when the triplet is underscreened) to be stabilised at the expense of the 1-3 singlet state. This is indeed the case; Fig. 5.26 shows $m = n_{\rm imp,\uparrow}|_{T=0} - n_{\rm imp,\downarrow}|_{T=0}$ for a system in the strong coupling phase of regime I in the absence of a field. We find that above some 'critical' field, h_c, the 1-3 triplet state is stabilised sufficiently that it becomes

the ground state. At this point a sharp but continuous change in m from 0 to ~ 1 is observed. The change in m is continuous here as mixing between the singlet and triplet states is not forbidden (unlike the ACTM — see Sec. 4.11 and 5.6). As h is increased further m also increases, rising to ~ 2 when $h \gg T_{\rm K}^*$, as underscreening of the 1-3 triplet is suppressed, and then ultimately to ~ 3 when $h \gg T_{\rm K}$ as the Kondo quenching of the 2 dot is suppressed. We therefore find that the $S_z = +\frac{3}{2}$ component of the quartet state is the ultimate ground state in the limit of large h. We note that the behaviour of the system here is, with the sole exception of the crossover from $m = 0$ to $m \sim 1$, identical to that observed in the mirror symmetric case, and discussed in Sec. 4.11.

5.10.2 Dynamics

The inset to Fig. 5.26 shows the zero-temperature, zero-bias conductance for a system in regime I under an applied field. As one would expect, in *all* cases in this regime under a magnetic field the Luttinger Integral, $I_{\rm L} = \mathrm{Im}\,\mathrm{Tr}\int_{-\infty}^{0} d\omega \frac{\partial \mathbf{\Sigma}_\sigma}{\partial \omega}\mathbf{G}_\sigma = 0$, and so the conductance may be related directly to $n_{{\rm imp},\sigma}|_{T=0}$ using Eq. 5.6b. Just as in the preceding section the conductance of regime I of the AACTM resembles that of regime I of the ACTM very closely. When the 1-3 singlet state is the gound state, the conductance is at the unitarity limit. Conversely, if the 1-3 triplet is the ground state, for fields below $T_{\rm K}^*$ the conductance is negligible, but as underscreening of the triplet is suppressed when $h \sim T_{\rm K}^*$, on this scale the conductance rises to around 1. A further increase in h through $h \sim T_{\rm K}$ suppresses Kondo screening of dot 2, and causes the conductance to flow back to zero.

The only difference in behaviour from the mirror symmetric case that is observed is the crossover between $m = 0$ and $m \sim 1$ is now sharp but continuous, which gives rise to a sharp drop in G_c/G_0, which falls to zero during the crossover, only to recover immediately thereafter. This is shown clearly in the inset to Fig. 5.26.

This is an interesting contrast with the effect of breaking mirror symmetry upon

a system in regime II ($J > 10T_{\mathrm{K}}$); there an asymmetry allows a field-induced Kondo effect to occur even in the strong coupling case, and therefore an enhanced conductance is observed at the point of the crossover, which is absent in the mirror symmetric case. In regime I, by contrast, the presence of an asymmetry causes a dramatic fall in the conductance at the crossover — something which is forbidden by symmetry in the ACTM.

5.11 Magnetic Fields: Regime III: The Orbital Regime

5.11.1 Effective Low Energy Model

We now consider the effect of an applied field upon a system in regime III (where $t \sim \mathcal{O}(U)$ or larger — see Sec. 5.4 and Fig. 5.4). As discussed in Sec. 5.7, we can understand the physics of the system in this regime by considering the non-interacting TQD Hamiltonian, $\hat{H}_{NITQD}$, and treating the Coulomb interaction term in the full model Hamiltonian, $\hat{H}_U = \sum_i U\hat{n}_{i\uparrow}\hat{n}_{i\downarrow}$, as a perturbation to the states of $\hat{H}_{NITQD}$, in order to more accurately determine the energies of the states of the TQD. As shown in Sec. 5.7, $\hat{H}_{NITQD}$ may be written as a simple three level system, and we continue to use that physically intuitive description here. As in the mirror symmetric case (Sec. 4.12), we find that the ground state of the isolated trimer is one of four states,

$$|0;0\rangle = c^\dagger_{\beta\uparrow}c^\dagger_{\beta\downarrow}c^\dagger_{\gamma\uparrow}c^\dagger_{\gamma\downarrow}|Vac\rangle, \tag{5.43a}$$

$$|\tfrac{1}{2};+\tfrac{1}{2}\rangle = c^\dagger_{\beta\uparrow}c^\dagger_{\gamma\uparrow}c^\dagger_{\gamma\downarrow}|Vac\rangle, \tag{5.43b}$$

$$|1;+1\rangle = c^\dagger_{\beta\uparrow}c^\dagger_{\gamma\uparrow}|Vac\rangle, \tag{5.43c}$$

$$|\tfrac{3}{2};+\tfrac{3}{2}\rangle = c^\dagger_{\alpha\uparrow}c^\dagger_{\beta\uparrow}c^\dagger_{\gamma\uparrow}|Vac\rangle = c^\dagger_{1\uparrow}c^\dagger_{2\uparrow}c^\dagger_{3\uparrow}|Vac\rangle, \tag{5.43d}$$

where $|0;0\rangle$ is the four electron singlet state, which describes the TQD deep in the strong coupling phase in the absence of a field, and $|\frac{1}{2};+\frac{1}{2}\rangle$ is the $S^z = +\frac{1}{2}$ component of the doublet state which describes the TQD deep in the local moment phase in the absence of a field. $|1;+1\rangle$ and $|\frac{3}{2};+\frac{3}{2}\rangle$ are high spin states which are accessible only at large fields ($h \sim t$ or larger): $|\frac{3}{2};+\frac{3}{2}\rangle$, the $S^z = +\frac{3}{2}$ component of the three-electron quartet state, is the ultimate high-field ground state of the TQD. Just as in the mirror symmetric case, a magnetic field has no effect upon the energy of the four electron singlet state, but stabilises the other three states. A system in the strong coupling phase in the absence of a field will undergo a crossover to a $|\frac{1}{2};+\frac{1}{2}\rangle$ TQD ground state at a 'critical' field

$$\begin{aligned} h_{c,1} = &- E_\beta - \frac{U}{4}(\beta_1+\beta_2)^2[(\beta_1+\beta_2)^2+(\gamma_1+\gamma_2)^2] - U\beta_3^2(\beta_3^2+\gamma_3^2) \\ &- \frac{U}{4}(\beta_1-\beta_2)^2[(\beta_1-\beta_2)^2+(\gamma_1-\gamma_2)^2]. \end{aligned} \tag{5.44}$$

As the mirror symmetry of the system is broken here, we anticipate that this crossover should be continuous, rather than a level crossing; as a result, a continuous change in $n_{\rm imp}$ and m should be seen when $h \simeq h_{c,1}$.

Increasing the field further stabilises both the $|1;+1\rangle$ and $|\frac{3}{2};+\frac{3}{2}\rangle$ states, but the behaviour of the system depends upon the relative sizes of the fields at which these states cross, in much the same way as in the ACTM (and as illustrated schematically in Fig. 4.33 and 4.34). We must consider two distinct cases: in both the ultimate high-field ground state of the trimer is $|\frac{3}{2};+\frac{3}{2}\rangle$, but in the first case a direct crossover between $|\frac{1}{2};+\frac{1}{2}\rangle$ and $|\frac{3}{2};+\frac{3}{2}\rangle$ is observed, whilst in the second case a two stage crossover is seen, with an initial crossover from $|\frac{1}{2};+\frac{1}{2}\rangle$ to $|1;+1\rangle$ followed by a second crossover between $|1;+1\rangle$ and $|\frac{3}{2};+\frac{3}{2}\rangle$. The former case is seen when $h_{c,2B} < h_{c,2A}$,

$$\begin{aligned} h_{c,2A} = &- E_\gamma - \frac{U}{4}(\gamma_1+\gamma_2)^2[(\beta_1+\beta_2)^2+(\gamma_1+\gamma_2)^2] - U\gamma_3^2(\beta_3^2+\gamma_3^2) \\ &- \frac{U}{4}(\gamma_1-\gamma_2)^2[(\beta_1-\beta_2)^2+(\gamma_1-\gamma_2)^2] \end{aligned} \tag{5.45}$$

being the field at which the $|\frac{1}{2};+\frac{1}{2}\rangle$ and $|1;+1\rangle$ states cross and $h_{c,2B} = E_\alpha$ being the field at which the $|1;+1\rangle$ and $|\frac{3}{2};+\frac{3}{2}\rangle$ states cross.

Just as in the corresponding mirror symmetric case, the degeneracy of the $|\frac{1}{2};+\frac{1}{2}\rangle$ and $|\frac{3}{2};+\frac{3}{2}\rangle$ states gives rise to a finite field Kondo effect, with the TQD here being an effective two level system (see Sec. 4.12). When $h \sim h_{c,2}$ (with

$$\begin{aligned} h_{c,2} =& \frac{1}{2}\Bigg(E_\alpha - E_\gamma - \frac{U}{4}(\gamma_1+\gamma_2)^2[(\beta_1+\beta_2)^2 + (\gamma_1+\gamma_2)^2] - U\gamma_3^2(\beta_3^2+\gamma_3^2) \\ & - \frac{U}{4}(\gamma_1-\gamma_2)^2[(\beta_1-\beta_2)^2 + (\gamma_1-\gamma_2)^2]\Bigg). \end{aligned} \tag{5.46}$$

being the 'critical' field at which the $|\frac{1}{2};+\frac{1}{2}\rangle$ and $|\frac{3}{2};+\frac{3}{2}\rangle$ states cross, as easily determined from the energies of the isolated states), the unity operator spanning the reduced Hilbert space of the low energy manifold is $\hat{1} = \hat{1}_+ + \hat{1}_- = |\frac{3}{2};+\frac{3}{2}\rangle\langle\frac{3}{2};+\frac{3}{2}| + |\frac{1}{2};+\frac{1}{2}\rangle\langle\frac{1}{2};+\frac{1}{2}|$. Performing a Schrieffer-Wolff transformation [13] (as described in Sec. 4.12.1) we may write the low energy effective model here as

$$\hat{H}_{eff} = \tfrac{1}{2}J_{\mathrm{K},\perp}\hat{\mathcal{T}}^+\hat{\mathbf{S}}^-(0) + \tfrac{1}{2}J_{\mathrm{K},\perp}\hat{\mathcal{T}}^-\hat{\mathbf{S}}^+(0) + J_{\mathrm{K},z}\hat{\mathcal{T}}^z\hat{\mathbf{S}}^z(0) + E_\Delta\hat{\mathcal{T}}^z, \tag{5.47}$$

where

$$E_\Delta = E_Q - E_D \tag{5.48a}$$

$$\begin{aligned} =& E_\alpha - E_\gamma - \frac{U}{4}(\gamma_1+\gamma_2)^2[(\beta_1+\beta_2)^2 + (\gamma_1+\gamma_2)^2] - U\gamma_3^2(\beta_3^2+\gamma_3^2) \\ & - \frac{U}{4}(\gamma_1-\gamma_2)^2[(\beta_1-\beta_2)^2 + (\gamma_1-\gamma_2)^2] - 2h \end{aligned} \tag{5.48b}$$

is the energy separation between the quartet and doublet states, and we define the components of the pseudospin $\hat{\mathcal{T}}$,

$$\hat{\mathcal{T}}^+ = |\tfrac{3}{2};+\tfrac{3}{2}\rangle\langle\tfrac{1}{2};+\tfrac{1}{2}|, \tag{5.49a}$$

$$\hat{\mathcal{T}}^- = |\tfrac{1}{2};+\tfrac{1}{2}\rangle\langle\tfrac{3}{2};+\tfrac{3}{2}|, \tag{5.49b}$$

$$\hat{\mathcal{T}}^z = \frac{1}{2}(\hat{1}_+ - \hat{1}_-), \tag{5.49c}$$

such that $|\frac{3}{2};+\frac{3}{2}\rangle$ and $|\frac{1}{2};+\frac{1}{2}\rangle$ are eigenvectors of the operator $\hat{\mathcal{T}}^z$ with eigenvalues $\pm\frac{1}{2}$, respectively. This model takes the form of a spin-anisotropic Kondo model under an effective magnetic field, E_Δ. As the system here is effectively equivalent to a two level system, we anticipate that the low energy effective model will reduce to an isotropic Kondo model in the limit $t \gg t', x$, just as in the mirror symmetric case, and in agreement with the results of Pustilnik *et al* [134] — and this is indeed what is found when we evaluate $J_{\mathrm{K},\perp}$ and $J_{\mathrm{K},z}$ numerically, using the technique described in Appendix E. We therefore expect to observe a finite field Kondo effect, with a Kondo temperature $T_{\mathrm{K}}^h \propto \exp(-1/\rho J_{\mathrm{K},z})$, when $E_\Delta \simeq 0$, corresponding to a critical field of $h \simeq h_{c,2}$. This finite field Kondo effect will be suppressed when the effective field $|E_\Delta| > T_{\mathrm{K}}^h$.

The second case we consider (occurring when $h_{c,2A} < h_{c,2B}$) has a two-stage crossover, with the initial crossover between states $|\frac{1}{2};+\frac{1}{2}\rangle$ and $|1;+1\rangle$ occurring at a critical field $h = h_{c,2A}$, followed by a second crossover between states $|1;+1\rangle$ and $|\frac{3}{2};+\frac{3}{2}\rangle$ at a critical field $h = h_{c,2B}$. This two stage process leads to suppression of the finite field Kondo effect, just as in the mirror symmetric case, and in all cases here we recover the mirror symmetric results (see Sec. 4.12) in the limit $x \to 0$.

5.11.2 Thermodynamics

We find that in order to obtain accurate results, it is necessary to retain a maximum of $N_s = 3000$ states in each iteration here. Fig. 5.27 and 5.28 show m and n_{imp} for asymmetric systems within regime III. In Fig. 5.27 we see a system initially in the strong coupling phase, which undergoes a transition to a $|\frac{1}{2};+\frac{1}{2}\rangle$ TQD ground state at a 'critical' field $h \sim h_{c,1}$ (as predicted in Sec. 5.11.1), at which point m increases sharply but continuously from 0 to 1, and n_{imp} falls sharply but continuously from 4 to 3. As the field is further increased, the system undergoes a two stage crossover to the ultimate high field TQD ground state, $|\frac{3}{2};+\frac{3}{2}\rangle$. The first crossover, occurring at $h \simeq h_{c,2A}$ (as accurately predicted in Sec. 5.11.1), corresponds to a transition

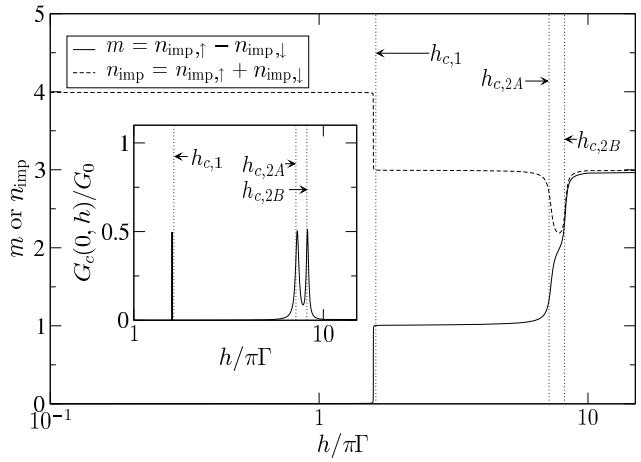


Figure 5.27: m and n_{imp} vs $h/\pi\Gamma$ for a system in the strong coupling phase of regime III when $h = 0$, with $\tilde{U} = 4$, $\tilde{t} = 6$, $\tilde{t}' = 2.5$ and $\tilde{x} = 5 \times 10^{-1}$. The inset shows the zero-temperature, zero-bias conductance for the same system. In both cases the scales $h_{c,1}$, $h_{c,2A}$ and $h_{c,2B}$ are shown on the figure.

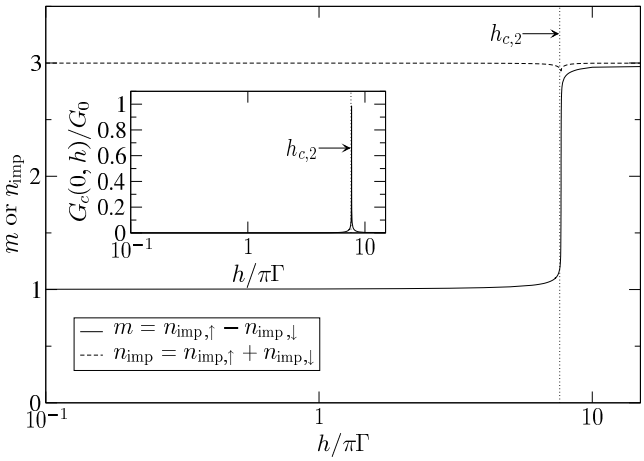


Figure 5.28: m and n_{imp} vs $h/\pi\Gamma$ for a system in the local moment phase of regime III when $h = 0$, with $\tilde{U} = 4$, $\tilde{t} = 6$, $\tilde{t}' = 5 \times 10^{-1}$ and $\tilde{x} = 5 \times 10^{-1}$. The inset shows the zero-temperature, zero-bias conductance for the same system. In both cases the scale $h_{c,2}$ is shown on the figure.

between $|\frac{1}{2};+\frac{1}{2}\rangle$ and $|1;+1\rangle$ TQD ground states, characterised by a smooth increase in m from 1 to 2. The second stage, corresponding to a transition between $|1;+1\rangle$ and $|\frac{3}{2};+\frac{3}{2}\rangle$ TQD ground states, occurs at a field $h \simeq h_{c,2B}$ (also accurately predicted in Sec. 5.11.1) and is characterised by a smooth increase in m from 2 to 3. As a result of this two stage process the finite field Kondo effect is suppressed here.

Fig. 5.28, on the other hand, shows a system which undergoes a direct crossover

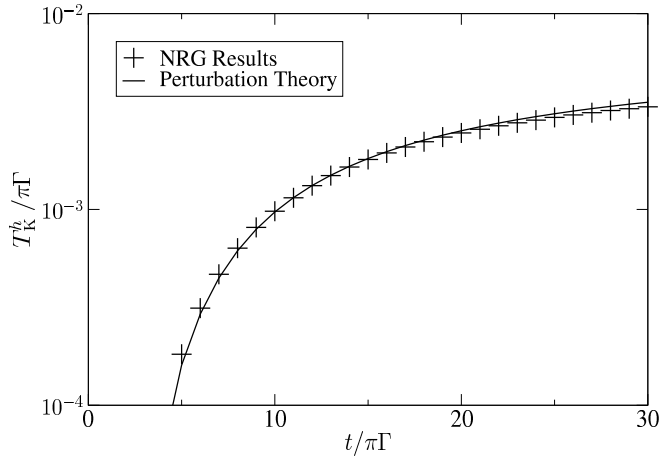


Figure 5.29: The Kondo temperature, $T_{\rm K}^h$ (defined via $S_{\rm imp}(T_{\rm K}^h) = 0.5\ln 2$) as a function of $\tilde{t}$ for a range of systems with $\tilde{U} = 10$, $\tilde{x} = 5 \times 10^{-1}$ and $\tilde{t}' = 3$, under magnetic fields tuned such that $h = h_{c,2}$. The solid line shows $T_{\rm K}^{PT} = A\exp(-1/\rho J_{{\rm K},z})$, with $J_{{\rm K},z}$ given by perturbation theory.

between $|\frac{1}{2};+\frac{1}{2}\rangle$ and $|\frac{3}{2};+\frac{3}{2}\rangle$ (i.e. $h_{c,2B} < h_{c,2A}$). As the system lies in the local moment phase in the absence of a field, there is no $h_{c,1}$ scale; any non-zero field splits the doublet state and gives rise to $m = 1$. The first change observed in the system at $h > 0$ is the crossover between the doublet and quartet states which is observed at $h \simeq h_{c,2}$ (as accurately predicted in Sec. 5.11.1), and is characterised by an increase in m from 1 to 3, $n_{\rm imp}$ being unchanged. We expect to observe a finite field Kondo effect under these conditions, and this is indeed what we find. Perturbation theory may be used to estimate the Kondo temperature here, as discussed in Sec. 5.11.1: as shown in Fig. 5.29 we find good agreement between the NRG results and perturbation theory, just as for the mirror symmetric case. For all systems in regime III under an applied field we find that $S_{\rm imp}(T = 0) = 0$ and $T\chi_{\rm imp}|_{T=0} = 0$.

5.11.3 Dynamics

We now consider the dynamic properties of systems in regime III under an applied field. The insets to Fig. 5.27 and 5.28 show the zero-temperature, zero-bias conductance for systems in regime III. In Fig. 5.27 there are three conductance peaks: these occur at $h \sim h_{c,1}$, $h \sim h_{c,2A}$ and $h \sim h_{c,2B}$, rise to a maximum height of

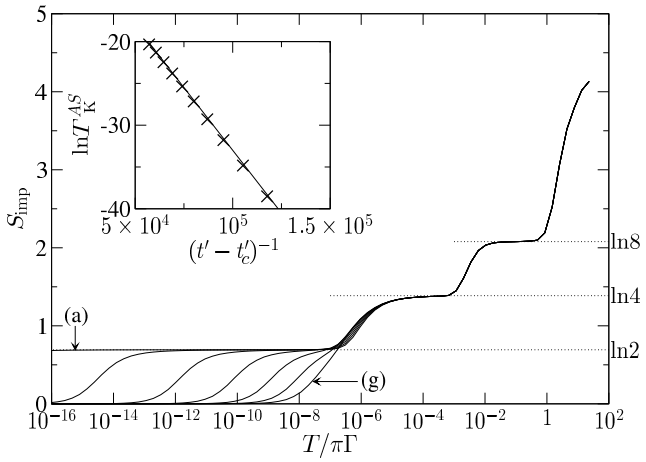


Figure 5.30: The entropy $S_{\rm imp}$ vs $T/\pi\Gamma$ for a system with $\tilde{U} = 10$, $\tilde{t} = 10^{-1}$ and $\tilde{x} = 0$ with $\tilde{\epsilon}_2 = \tilde{\epsilon_3} = -5 = -U/2$ and $\tilde{\epsilon}_1 = -4.9$. $\tilde{t'}$ is varied, with $\tilde{t'} = 9.7215 \times 10^{-2}$ for (a), 9.72175×10^{-2} for (b), 9.722×10^{-2} for (c), 9.72225×10^{-2} for (d), $9,7225 \times 10^{-2}$ for (e), 9.2275×19^{-2} for (f) and 9.23×10^{-2} for (g). The inset plots $T_{\rm K}^{AS}$ (defined via $S_{\rm imp}(T_{\rm K}^{AS}) = 0.5 \ln 2$) against $(t' - t'_c)^{-1}$, with $\tilde{t'}_c = 9.72075 \times 10^{-2}$.

$G_c/G_0 = \frac{1}{2}$ and are coincident with the (continuous) changes in m and $n_{\rm imp}$ that are observed. These are essentially Coulomb blockade peaks, arising when two states of the TQD with different occupancy levels are degenerate. The finite field Kondo effect is suppressed here.

In Fig. 5.28 on the other hand, the finite field Kondo effect is *not* suppressed, and so we observe a single peak in the conductance, corresponding to the Kondo resonance, and occurring at $h \sim h_{c,2}$. This peak rises to the unitarity limit, $G_c/G_0 = 1$. We generically find (via direct calculation using the NRG) that the Luttinger integral $I_{\rm L} = {\rm Im\,Tr} \int_{-\infty}^{0} d\omega \frac{\partial \mathbf{\Sigma}_\sigma}{\partial \omega} \mathbf{G}_\sigma = 0$ for all $h \neq 0$, as expected.

5.12 Inducing Asymmetry By Other Means

Until this point, we have concentrated exclusively upon an asymmetry induced by setting $x \neq 0$ in Eq. 5.1. However, as shown in Appendix B, the parity operator $\hat{P}_{1,3}$ commutes with the TQD Hamiltonian *only* when *both* $x = 0$ *and* $\epsilon_1 = \epsilon_3$. We therefore anticipate that a system with $\epsilon_1 \neq \epsilon_3$ will exhibit the much same physics as a system with $x \neq 0$ — and, most importantly, the phase boundary between

the local moment and strong coupling phases is expected to be described by a line of Kosterlitz-Thouless transitions, rather than a line of first order quantum phase transitions. As shown by Fig. 5.30, this is indeed the case: the system shown in this figure lies deep within regime II ($J > 10T_{\mathrm{K}}$ — see Fig. 5.2), and comparing the results presented here with those in Sec. 5.5.2 it is clear that the low temperature physics is described by the same low energy effective model in both cases. This can be easily understood in the case of regimes I ($J < 10T_{\mathrm{K}}$) and II ($J > 10T_{\mathrm{K}}$). We may write the TQD part of the AACTM Hamiltonian, Eq. 5.1, in the following form

$$\hat{H}_{\mathrm{TQD}} = \sum_{\sigma,i=1,2,3} (\epsilon_i - \sigma h)\hat{n}_{i\sigma} + \sum_{i=1,2,3} U\hat{n}_{i\uparrow}\hat{n}_{i\downarrow} + \sum_{\sigma,i,j\neq i} t_{ij}c^{\dagger}_{i\sigma}c_{j\sigma}, \tag{5.50}$$

where t_{ij} is the hopping parameter linking dots i and j (i.e. $t_{12} = t$, $t_{13} = t'$ and $t_{23} - t_{12} = x$). Performing a Schrieffer-Wolff transformation upon the Hamiltonian $\hat{H}_{AACTM} = \hat{H}_L + \hat{H}_{hyb} + \hat{H}_{TQD}$, as described in Sec. 5.2, leads to the result

$$\hat{H}_{eff} = J_{12}\hat{\mathbf{S}}_1 \cdot \hat{\mathbf{S}}_2 + J_{23}\hat{\mathbf{S}}_2 \cdot \hat{\mathbf{S}}_3 + J_{13}\hat{\mathbf{S}}_1 \cdot \hat{\mathbf{S}}_3 + J_{\mathrm{K}}\hat{\mathbf{S}}_2 \cdot \hat{\mathbf{S}}(0) + K\sum_{\sigma} f^{\dagger}_{0\sigma}f_{0\sigma}, \tag{5.51}$$

where J_{ij} is a Heisenberg exchange coupling given by

$$J_{ij} = 2t_{ij}^2\left[\frac{1}{U + \epsilon_i - \epsilon_j} + \frac{1}{U + \epsilon_j - \epsilon_i}\right]. \tag{5.52}$$

K and J_{K} are defined in Eq. 4.5. It is clear from this formula that setting $\epsilon_1 \neq \epsilon_2 = \epsilon_3$ *must* result in $\delta = J_{23} - J_{12} \neq 0$, assuming that $t_{12} = t_{23}$[7]. However, varying ϵ_1 alters the value of both J_{12} and J_{13}, whilst setting $x \neq 0$ changes only J_{23}. As we generally aim to vary only one parameter at a time, using $x \neq 0$ to generate asymmetry is

[7]In fact the form of the commutator $[\hat{P}_{1,3}, \hat{H}]$ given in Appendix B means that the overall Hamiltonian only has a parity symmetry if both $x = 0$ and $\epsilon_1 = \epsilon_3$. For example, one might naively expect from Eq. 5.52 that if $2\epsilon_2 = \epsilon_1 + \epsilon_3$ and $\epsilon_1 \neq \epsilon_3$, as $J_{12} = J_{23}$ when $x = 0$, that the system would contain a first order quantum phase transition between the strong coupling and local moment phases. However a Kosterlitz-Thouless transition is observed under these conditions as the parity symmetry of the system is still broken, even if this is not apparent from the second order perturbation theory results of Eq. 5.51.

generally a more useful method. We also note that other effects, such as a magnetic flux affecting the interdot hoppings, may also be used to break the mirror symmetry of the system [72]. Similar arguments apply in regime III (the orbital regime).

5.13 Summary

In this chapter we investigate a model in which only one of the dots is coupled to the conduction band, but which does not possess a plane of mirror symmetry ('the asymmetric apex coupled trimer model'). In Sec. 5.1 we discuss the Hamiltonian for this model, and in Sec. 5.2 we derive an effective spin model which describes the system in the parameter space where all three dots are singly occupied at low temperature. We find that the asymmetry of the system in the spin regime may be parameterised by a variable, δ. Sec. 5.3 describes the relevant Friedel-Luttinger sum rule for this model.

In Sec. 5.4 we discuss the phase diagrams for this model. We find that the system has two phases — a local moment phase and a strong coupling phase — which are separated by a line of Kosterlitz-Thouless transitions. Just as in Chapter 4 we identify three different regimes — regimes I, II and III — which each have a distinct functional form for the phase boundary. Regimes I ($J < 10T_{\mathrm{K}}$) and II ($J > 10T_{\mathrm{K}}$) lie within the region where the system may be described using the effective spin model at low temperature, whilst regime III (the orbital regime) lies outside this region. The position of the phase boundary is found to be independent of the asymmetry of the system when the asymmetry is small, being described by $J' = \lambda J^2/T_{\mathrm{K}}$ in regime I, $J = J'$ in regime II and $t' = U/4$ in regime III — identical to the results of the mirror symmetric case. We find that there is an inherent uncertainty, which increases with δ, in our determination of the phase boundary in regimes I and II and we discuss this in Sec. 5.4.1.

We then investigate the physics of each of the regimes in turn, beginning with regime II (Sec. 5.5), which is the simplest regime to understand, before moving on to

consider regimes I (Sec. 5.6) and III (Sec. 5.7). We find that in all three regimes we may identify a low temperature scale, T_{KT}, below which the system will flow away from the 'transition fixed point' *even at the phase boundary*. As such, we find that the 'transition fixed point' will describe a system at the phase boundary down to zero temperature *only* when the TQD possesses a plane of mirror symmetry. This behaviour is the result of mixing between the low-lying states of the TQD, which is permitted as the parity symmetry of the system is broken. The mixing gives rise to an 'avoided crossing', and as a result of this avoided crossing the first order quantum phase transitions observed in the mirror symmetric case become Kosterlitz-Thouless transitions when the mirror symmetry of the system is broken. In effect, the avoided crossing ensures that the system cannot be frustrated at zero temperature.

In Sec. 5.9, 5.10 and 5.11 the effect of an applied magnetic field upon the system in regimes II, I and III (respectively) are discussed. Low energy effective models which describe the physics of the system well at low temperature are derived for regimes II and III. In regimes II and III, we find that for certain parameter regimes field-induced Kondo effects may be observed, giving rise to an enhanced conductance at some 'critical' field, which we may predict using our low energy effective models.

We conclude this chapter in Sec. 5.12 by examining the effect of using a change in the level energies of the dots, ϵ_i, to induce an asymmetry. We find that this also gives rise to a Kosterlitz-Thouless transition between a local moment and a strong coupling state, and that the low temperature physics is described by the same low energy effective models as in the case where mirror symmetry is broken by asymmetry in the interdot hoppings.

Chapter 6

The Trimer in Parallel

We now consider the third model investigated in this thesis — a triple quantum dot attached to a single conduction band in parallel (i.e. all three dots are connected to the same conduction band). As we shall see, this model exhibits a physics in many ways very distinct from that seen in the previous two chapters, the most notable difference being the presence of a ferromagnetic Ruderman-Kittel-Kasuya-Yosida (RKKY) interaction between the dots in the spin regime, as we discuss in Sec. 6.2. We will refer to this model, which is shown schematically in Fig. 6.1, as 'the trimer in parallel model' (TiP). We confine ourselves to the mirror symmetric case of the trimer in parallel. As discussed in Chapter 1 there has been more theoretical interest in parallel TQD devices than in devices such as those described by the apex coupled

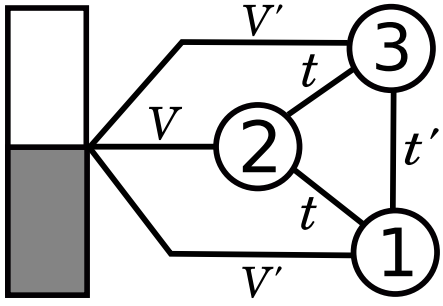


Figure 6.1: A schematic representation of the trimer in parallel. The quantum dots (labelled '1', '2' and '3') are linked by tunnel-couplings t and t', with further tunnel couplings V and V' linking the dots to the conduction band.

trimer Hamiltonian, but we do not believe there has previously been a study of the TQD in parallel covering the whole parameter space of t, t', V and V': in particular, there has been very little study of the effect of setting $V \neq V'$.

6.1 The Trimer in Parallel Hamiltonian

The trimer in parallel is described by the Hamiltonian $\hat{H}_{TiP} = \hat{H}_L + \hat{H}_{hyb} + \hat{H}_{TQD}$ where $\hat{H}_L = \sum_{\mathbf{k},\sigma} \epsilon_{\mathbf{k}} c^\dagger_{\mathbf{k}\sigma} c_{\mathbf{k}\sigma}$ refers to the non-interacting lead, which couples to the TQD device via

$$\hat{H}_{hyb} = \sum_{\mathbf{k},\sigma} V(c^\dagger_{2\sigma} c_{\mathbf{k}\sigma} + H.c.) + \sum_{\mathbf{k},\sigma} V'[(c^\dagger_{1\sigma} + c^\dagger_{3\sigma}) c_{\mathbf{k}\sigma} + H.c.] \tag{6.1}$$

with $\hat{H}_{TQD}$, the Hamiltonian for the isolated TQD device, given by

$$\begin{aligned} \hat{H}_{TQD} = &\sum_\sigma (\epsilon - \sigma h)(\hat{n}_{1\sigma} + \hat{n}_{3\sigma}) + \sum_\sigma (\epsilon_2 - \sigma h)\hat{n}_{2\sigma} + \sum_i U \hat{n}_{i\uparrow}\hat{n}_{i\downarrow} \\ &+ \sum_\sigma t[(c^\dagger_{1\sigma} + c^\dagger_{3\sigma})c_{2\sigma} + H.c] + \sum_\sigma t'(c^\dagger_{1\sigma} c_{3\sigma} + H.c.), \end{aligned} \tag{6.2}$$

the Hamiltonian $\hat{H}_{TiP}$ being almost identical to Eq. 4.1 with the addition of $\hat{H}_{hyb,2} = \sum_{\mathbf{k},\sigma} V'[(c^\dagger_{1\sigma} + c^\dagger_{3\sigma}) c_{\mathbf{k}\sigma} + H.c.]$, connecting dots 1 and 3 directly to the conduction band, with V' a hopping parameter. Unlike the preceding two chapters we will vary $\Gamma = \pi\rho N V^2$, which is the hybridisation strength between dot 2 and the conduction band; N is the number of orbitals in the conduction band and $\rho = 1/2D$ the density of states per conduction band orbital, such that NV^2 is finite in the continuum limit $N \to \infty$. D is the bandwidth, which is naturally taken to be the largest energy scale of the problem. We also permit Γ' to vary between 0 and Γ, with $\Gamma' = \pi\rho N V'^2$ the hybridisation strength between dots 1 and 3 and the conduction band. To maintain the mirror symmetry of the system, it is only necessary that we specify that the level energies of dots 1 and 3 be equal, but, just as in Chapter 4, we consider only the representative case $\epsilon = \epsilon_2 = -U/2$ in this chapter. The underlying set of bare

model parameters here may therefore be taken to be

$$\tilde{U} = \frac{U}{\pi\Gamma}; \quad \tilde{t} = \frac{t}{\pi\Gamma}; \quad \tilde{t'} = \frac{t'}{\pi\Gamma}; \quad \tilde{\Gamma} = \frac{\Gamma}{D}; \quad \tilde{\Gamma'} = \frac{\Gamma'}{D}, \tag{6.3}$$

along with $\tilde{h} = h/\pi\Gamma$, the magnetic field strength. We consider the effect of an applied field in Sec. 6.10 and 6.11, up to which point $\tilde{h} = 0$ is implicit. We set the NRG discretisation parameter $\Lambda = 3$, and retain a maximum of $N_s = 2000$ states per iteration, except in Sec. 6.7 and 6.11, where a maximum of $N_s = 3000$ states is retained in each iteration.

6.2 The Effective Spin Model and the Absence of Regime I

A Schrieffer-Wolff transformation [13] may be used to derive an effective low temperature spin model from Eq. 6.2, valid in the limit where all three dots are singly occupied at low temperature ($t, t', V, V' \ll U, \epsilon$). We split $\hat{H}_{TiP}$ such that

$$\hat{H}_{TiP} = \hat{H}_0 + \hat{H}_1, \tag{6.4a}$$

$$\hat{H}_0 = \sum_{i,\sigma} \epsilon \hat{n}_{i\sigma} + \sum_i U \hat{n}_{i\uparrow}\hat{n}_{i\downarrow} + \sum_{\mathbf{k},\sigma} \epsilon_{\mathbf{k}} c^\dagger_{\mathbf{k}\sigma} c_{\mathbf{k}\sigma}, \tag{6.4b}$$

$$\hat{H}_1 = \sum_\sigma t[(c^\dagger_{1\sigma} + c^\dagger_{3\sigma})c_{2\sigma} + H.c] + \sum_\sigma t'(c^\dagger_{1\sigma}c_{3\sigma} + H.c.) + \sum_{\mathbf{k},\sigma} V(c^\dagger_{2\sigma}c_{\mathbf{k}\sigma} + H.c.) \tag{6.4c}$$

$$+ \sum_{\mathbf{k},\sigma} V'[(c^\dagger_{1\sigma} + c^\dagger_{3\sigma})c_{\mathbf{k}\sigma} + H.c.],$$

and then use Brillouin-Wigner perturbation theory [93] up to fourth order in $\hat{H}_1$. We find that the only significant contributions to the low energy effective Hamiltonian come from terms $\mathcal{O}(t^2)$, $\mathcal{O}(t'^2)$, $\mathcal{O}(V^2)$, $\mathcal{O}(V'^2)$, $\mathcal{O}(V^2V'^2)$ and $\mathcal{O}(V'^4)$. Most of the remaining terms vanish, as they cannot connect states within the low energy

manifold (for example, terms $\mathcal{O}(V)$ change the electronic population of the TQD, and as all states within the low energy manifold have three electrons on the TQD are necessarily zero). The only other non-zero terms arising in the perturbation theory expansion up to fourth order are $\mathcal{O}(t^3)$, $\mathcal{O}(t^4)$, $\mathcal{O}(V^2t)$ and $\mathcal{O}(V^2t^2)$ (where we conflate the interdot hoppings t and t' and the hopping terms to the leads V and V' for brevity). From our work in Chapters 4 and 5, and the work by Wang on Aharonov-Bohm effects in triple quantum dots [72] it is clear that the terms $\mathcal{O}(t^3)$ and $\mathcal{O}(t^4)$ will be very small compared to terms $\mathcal{O}(t^2)$, and may be safely neglected. The term $\mathcal{O}(V^2t)$ is found to vanish in the particular case where $\epsilon_i = \epsilon = -U/2$ which we consider in this thesis, and in their work on the corresponding parallel double quantum dot system, Žitko and Bonča found that perturbation theory terms which mixed t and V could be neglected [53]; the effect of terms $\mathcal{O}(V^2t)$ and $\mathcal{O}(V^2t^2)$ will therefore be neglected. We may then write an effective low temperature spin model for the system,

$$\begin{aligned}\hat{H}_{spin} =&(J - J_{\mathrm{RKKY}})(\hat{\mathbf{S}}_1 + \hat{\mathbf{S}}_3)\cdot\hat{\mathbf{S}}_2 + (J' - J'_{\mathrm{RKKY}})\hat{\mathbf{S}}_1\cdot\hat{\mathbf{S}}_3 \\ &+ J_{\mathrm{K}}\hat{\mathbf{S}}_2\cdot\hat{\mathbf{S}}(0) + J'_{\mathrm{K}}(\hat{\mathbf{S}}_1 + \hat{\mathbf{S}}_3)\cdot\hat{\mathbf{S}}(0) + \hat{H}_L + K\sum_\sigma f^\dagger_{0\sigma}f_{0\sigma}\end{aligned} \tag{6.5}$$

where $\hat{\mathbf{S}}_i$ is a spin-$\frac{1}{2}$ operator for dot i, $\hat{\mathbf{S}}(0)$ is the spin density of the conduction band at the TQD, as given by Eq. 2.10, and $f^\dagger_{0\sigma}$ ($f_{0\sigma}$) is the creation (destruction) operator for the 0-orbital of the Wilson chain (as given by Eq. 2.11), and the final term represents potential scattering, with

$$K = -\frac{NV^2}{2}\left(\frac{1}{\epsilon_2 + U} + \frac{1}{\epsilon_2}\right) + NV'^2\left(\frac{1}{\epsilon + U} + \frac{1}{\epsilon}\right), \tag{6.6}$$

vanishing when $\epsilon = \epsilon_2 = -U/2$ (which is the case for all the systems investigated here). The other parameters in Eq. 6.5 are Heisenberg exchange couplings, given in

the case where $\epsilon = \epsilon_2 = -U/2$ by

$$J = \frac{4t^2}{U}, \tag{6.7a}$$

$$J' = \frac{4t'^2}{U}, \tag{6.7b}$$

$$J_{\mathrm{RKKY}} = 0.62\frac{64}{\pi^2}\frac{\Gamma\Gamma'}{U} \approx 4\frac{\Gamma\Gamma'}{U}, \tag{6.7c}$$

$$J'_{\mathrm{RKKY}} = 0.62\frac{64}{\pi^2}\frac{\Gamma'^2}{U} \approx 4\frac{\Gamma'^2}{U}, \tag{6.7d}$$

$$J_{\mathrm{K}} = \frac{8NV^2}{U} = \frac{8\Gamma}{\pi\rho U}, \tag{6.7e}$$

$$J'_{\mathrm{K}} = \frac{8NV'^2}{U} = \frac{8\Gamma'}{\pi\rho U}, \tag{6.7f}$$

where we use Žitko and Bonča's expressions for J_{RKKY} and J'_{RKKY} [53]. As discussed in Section 6.6 we find that in the region where all three dots are singly occupied at low temperature this model describes the low temperature behaviour of the trimer in parallel very well.

In the apex coupled trimer model in the region where the interdot exchange couplings (J and J') were smaller than T_{K}, the Kondo temperature of the isolated dot 2, a distinct physics which we referred to as 'regime I' was observed (see Sec. 4.7 and 5.6). Due to the presence of RKKY interactions between the dots in the trimer in parallel spin model, Eq. 6.5, one would not expect to see a corresponding regime here when J and J' are small (compared to T_{K}), although one might expect to see a physics analogous to regime I when both $|J - J_{RKKY}| < T_{\mathrm{K}}$ *and* $|J' - J'_{RKKY}| < T_{\mathrm{K}}$. However (as we can see from the phase diagrams in Sec. 6.5) this corresponds to a very small region of the parameter space of the problem, and so to all intents and purposes no analogue of regime I is seen in the trimer in parallel model. We also note however that in the limit $V' = 0$ we recover the effective spin Hamiltonian for the apex coupled trimer model — Eq. 4.4.

6.3 Symmetries of the Bare and Effective Hamiltonians

We may define a parity operator, $\hat{P}_{1,3}$, which interchanges the labels on dots 1 and 3. As shown in Appendix B such an operator is both self-adjoint and involutary ($\hat{P}_{1,3}^2 = 1$), and has eigenvalues ± 1. In addition, we may easily show that $[\hat{H}_{TiP}, \hat{P}_{1,3}] = 0$, and as such that the model Hamiltonian conserves parity, in the same way as $\hat{H}_{ACTM}$. It is also the case that $\hat{P}_{1,3}$ commutes with $\hat{Q}$, $\hat{S}^2$ and $\hat{S}_z$ — the charge, spin and spin z-component operators, respectively. As a result we may classify all the states of $\hat{H}_{TiP}$ by their behaviour under $\hat{P}_{1,3}$ as having either odd ('$(-)$'; $\langle\psi|\hat{P}_{1,3}|\psi\rangle = -1$) or even ('$(+)$'; $\langle\psi|\hat{P}_{1,3}|\psi\rangle = +1$) parity.

We also note here that $\hat{H}_{TiP}$ is, in general, *not* particle-hole symmetric (except in the limits $t = 0$ or $t' = 0$). However $\hat{H}_{spin}$ *is* particle-hole symmetric when $\epsilon = \epsilon_2 = -U/2$.

In the limit $V = V'$ (corresponding to $J_{\mathrm{K}} = J'_{\mathrm{K}}$), the effective spin model, Eq. 6.5, is found to conserve the total spin on the TQD device: formally $[\hat{H}_{spin}, \hat{\mathbf{S}}^2] = 0$, where $\hat{\mathbf{S}}^2 = (\hat{\mathbf{S}}_1 + \hat{\mathbf{S}}_2 + \hat{\mathbf{S}}_3) \cdot (\hat{\mathbf{S}}_1 + \hat{\mathbf{S}}_2 + \hat{\mathbf{S}}_3)$ is a spin operator for the TQD device as a whole. In this particular limit we may therefore classify all the states of the system by *both* parity *and* TQD spin. We note that $\hat{H}_{TiP}$ does not conserve the electronic population of the TQD, and as such total TQD spin is therefore *not* a good quantum number for the whole system (TQD and conduction band) outside the region where $\hat{H}_{spin}$ is valid.

6.4 Conductance and the Friedel-Luttinger Sum Rule

As discussed in Sec. 3.6 we may use the Meir-Wingreen formula to calculate the zero-bias conductance through the TQD device from the single particle spectra of

the system. The relevant form of the Meir-Wingreen formula here is

$$\frac{G_c(T,h)}{G_0} = \int_{-\infty}^{\infty} -\frac{\partial f(\omega)}{\partial \omega} \frac{1}{2} \sum_{\sigma} \pi \Gamma_s D_{s\sigma}(\omega, T, h) d\omega, \tag{6.8}$$

where $G_c(T,h)$ is the zero-bias conductance through the TQD device, $f(\omega) = [e^{\omega/T} + 1]^{-1}$ the Fermi function and where we define $\Gamma_s = \Gamma + 2\Gamma'$. $D_{s\sigma}(\omega, T, h) = \frac{1}{\pi}\mathrm{Im}G_{s\sigma}(\omega)$ is the single particle spectrum of the orbital which couples directly to the conduction band, $c^\dagger_{s\sigma}$:

$$c^\dagger_{s\sigma} = \frac{1}{\sqrt{V^2 + 2V'^2}}[V c^\dagger_{2\sigma} + V'(c^\dagger_{1\sigma} + c^\dagger_{3\sigma})], \tag{6.9}$$

and so $G_{s\sigma}$ is given by

$$G_{s\sigma}(\omega) = \frac{1}{\Gamma_s} \sum_{i,j} \Gamma_{ij} G_{ij\sigma}(\omega) \tag{6.10}$$

where $\Gamma_{ij} = \pi N \rho V_i V_j = \Gamma_{ji}$ with $V_1 = V_3 = V'$ and $V_2 = V$, and $G_{ij\sigma}(\omega)$ is the Green function for dots i and j with spin σ. We note that in the limit $V' = 0$ we recover Eq. 4.6, the result for the apex coupled trimer model. In addition, as discussed in Appendix C and Sec. 3.7, we may derive a Friedel-Luttinger sum rule for this model,

$$G_c(0,h) = G_0 \tfrac{1}{2} \sum_{\sigma} \pi \Gamma_s D_{s\sigma}(\omega = 0, h) \tag{6.11a}$$

$$= G_0 \tfrac{1}{2} \sum_{\sigma} \sin^2(\delta_\sigma), \tag{6.11b}$$

where $G_c(0,h)$ is the zero-temperature zero-bias conductance through the TQD device, $D_{s\sigma}(\omega = 0, h)$ the zero-temperature, zero-frequency value of $D_{s\sigma}(\omega)$ and δ_σ the static scattering phase shift, given by $\delta_\sigma = \pi n_{\mathrm{imp},\sigma}|_{T=0} + I_{\mathrm{L}}$ with $I_{\mathrm{L}} = \mathrm{Im}\,\mathrm{Tr} \int_{-\infty}^{0} d\omega \frac{\partial \mathbf{\Sigma}_\sigma}{\partial \omega} \mathbf{G}_\sigma$ the Luttinger integral. As I_{L} is found to be constant within a given phase (see below) we may use Eq. 6.11b to directly relate $n_{\mathrm{imp},\sigma}$ to the zero-temperature conductance, just as we did for the ACTM and AACTM (Sec. 4.4 and 5.3, respectively).

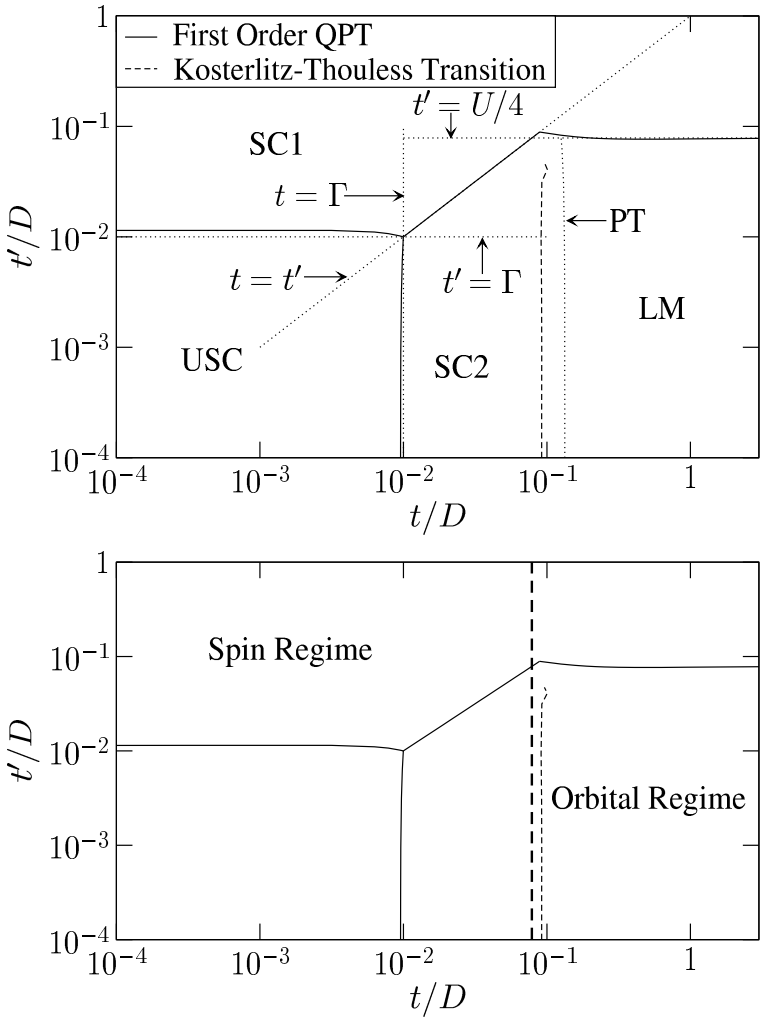


Figure 6.2: The phase diagram for a TQD with $\tilde{U} = 10$ and $\Gamma = \Gamma' = 10^{-2}D$ as a function of t/D and t'/D. First order quantum phase transitions are indicated by solid lines, and Kosterlitz-Thouless transitions by dashed lines. In the top panel dotted lines indicate useful analytic results; the bottom panel shows the division between the spin and orbital regimes (thick dashed line).

6.5 The Phase Diagram

We now consider the phase diagram of the trimer in parallel model. Just as in Sec. 4.5 and Sec. 5.4 the phase diagram is constructed by fixing all but one of the variables of the system (we typically fix U, t, Γ and Γ', and vary t') and then using the NRG to determine the ultimate low temperature fixed point of the system for various values of the remaining, unfixed parameter. Repeating this process for various values of t then allows the construction of a $2D$ phase diagram — Fig. 6.2, 6.3 and 6.4.

The system has, we find, three distinct stable fixed points. The first, characterised by $S_{\rm imp}(T=0)=0$ and $T\chi_{\rm imp}|_{T=0}=0$, is a strong coupling fixed point (SC FP), which is generically found to have a Luttinger integral, $I_{\rm L}={\rm Im\,Tr}\int_{-\infty}^{0}d\omega\frac{\partial\mathbf{\Sigma}_\sigma}{\partial\omega}\mathbf{G}_\sigma=0$, as expected for a Fermi Liquid [120], and the second is a local moment fixed point (LM FP), characterised by $S_{\rm imp}(T=0)=\ln 2$ and $T\chi_{\rm imp}|_{T=0}=1/4$, which is generically found to have $|I_{\rm L}|=\frac{\pi}{2}$, as expected for a singular Fermi Liquid [55]. These are both exactly equivalent to the corresponding fixed points in the apex coupled trimer model. The third fixed point, an underscreened fixed point (USC FP), is characterised by $S_{\rm imp}(T=0)=\ln 3$ and $T\chi_{\rm imp}|_{T=0}=1$ and has no analogue in the apex coupled trimer case. This phase is generically found to have $I_{\rm L}=0$.

We find that, as shown in the bottom panel of Fig. 6.2, the phase diagram may be divided into two regions: in the first (corresponding to the region where $t<U/4$) the system is described at low temperature by the effective spin model, Eq. 6.5. This region is analogous to regime II for the apex coupled trimer model (see Fig. 4.2: as discussed above, no analogue of regime I is observed due to the presence of RKKY interactions between the dots), and we will refer to it as the 'spin regime'. The second region ($t>U/4$) is, as we shall see, exactly equivalent to regime III for the apex coupled trimer model. We refer to this as the 'orbital regime'.

The system (in both regimes) contains a number of phase boundaries. As discussed below, some are found to be lines of first order quantum phase transitions, and others are lines of Kosterlitz-Thouless transitions. The position of a first order quantum phase transition may be fixed using the simple bisection method described in Sec. 4.5, whilst to determine the position of the phase boundary when the system undergoes a Kosterlitz-Thouless transition we use the extrapolation method described in Sec. 5.4.1.

We consider initially the special case where $V=V'$ (shown in Fig. 6.2) before examining the more general case where $V\neq V'$ (Fig. 6.3 and 6.4). In the $V=V'$ case, the system lies in the underscreened phase when $t\ll\Gamma$ and $t'\ll\Gamma$. A first

order quantum phase transition to a strong coupling phase is seen when $t \sim \Gamma$ and when $t' \sim \Gamma$. The phase boundary in both cases here is a line of transition fixed points with $S_{\text{imp}} = \ln 4$ and $T\chi_{\text{imp}} = \frac{1}{2}$.

When $t' > t$ the strong coupling phase is found to have (+)-parity (we refer to this as SC1) and when $t > t'$ the strong coupling phase has (−)-parity (we refer to this as SC2). Exactly at the point $t = t'$ there is a first order quantum phase transition between the SC1 and SC2 phases, characterised by a line of transition fixed points with $S_{\text{imp}} = \ln 2$ and $T\chi_{\text{imp}} = 0$.

When $t = t' \approx U/4$ the gradient of the phase boundary between the even and odd parity states changes to $t' \approx U/4$ as the system enters the orbital regime, just as seen in the apex coupled trimer model. When $t' > U/4$, the system still lies within the strong coupling phase, but n_{imp} increases from 3 to 4 (again, just as for the apex coupled trimer model). When $t' < U/4$, on the other hand, the system flows to the local moment fixed point (again, similar to the behaviour seen in the apex coupled trimer model), and a Kosterlitz-Thouless transition between the local moment and SC2 phases is seen when $t \sim U/4$.

As discussed above, to determine the position of the Kosterlitz-Thouless transition we use the extrapolation method described in Sec. 5.4.1; to use this method successfully we must be able to measure how the scale vanishes as the transition is approached. When the SC1/SC2 phase boundary is close to the SC2/LM phase boundary we cannot determine how the Kondo temperature of the SC2 phase vanishes as the transition is approached, and as such we cannot determine the position of the phase boundary between the SC2 and LM phases in this case; this is why the line indicating the boundary between the two phases derived from the NRG vanishes so abruptly in Fig. 6.2.

We may use perturbation theory to estimate the position and form of this phase boundary, as discussed in Sec. 6.8 (this is shown on the phase diagram as the line labelled 'PT'), and these results indicate that the phase boundary between the SC2

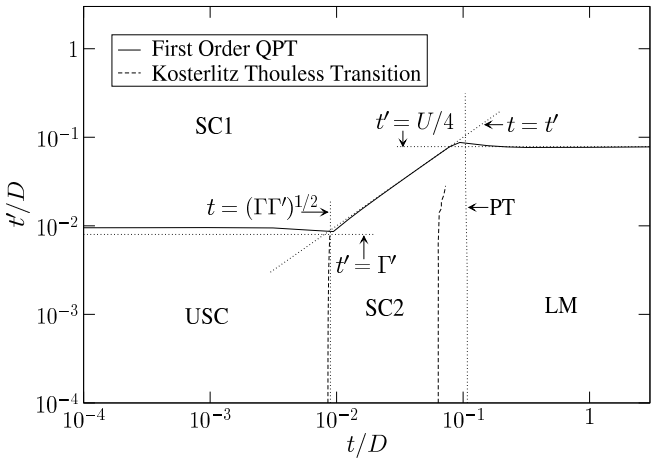


Figure 6.3: The phase diagram for a TQD with $\tilde{U} = 10$, $\Gamma = 10^{-2}D$ and $\Gamma' = 8 \times 10^{-3}D$ as a function of t/D and t'/D. First order quantum phase transitions are indicated by solid lines, and Kosterlitz-Thouless transitions by dashed lines. Dotted lines indicate useful analytic results.

and LM phases ultimately terminates at the phase boundary between the odd and even parity states (i.e. at the SC1/SC2 phase boundary), giving rise to a second 'triple point' in the phase diagram (the first being where $t = t' = \Gamma$).

The phase boundary between the local moment and strong coupling phases in the orbital regime is a line of transition fixed points, characterised by $S_{\text{imp}} = \ln 3$, $T\chi_{\text{imp}} = \frac{1}{6}$ and $n_{\text{imp}} = 10/3$. Our results here along the line $t = t'$ are in agreement with both those of Wang [66] and of Žitko and Bonča [52, 53] (these papers consider the special case of the trimer in parallel model where $t = t'$ and $V = V'$).

We now consider the more general case where $V \neq V'$. The relevant phase diagrams are given in Fig. 6.3 and 6.4. These phase diagrams are generally very similar to those of the $V = V'$ case, and we therefore concentrate upon the differences. The boundaries of the underscreened phase now follow the lines $t \sim (\Gamma\Gamma')^{1/2}$ and $t' \sim \Gamma'$, and when $\Gamma' \sim \Gamma$ (as is the case in Fig. 6.3) we find that the phase boundary between the underscreened and SC2 phase is now a line of Kosterlitz-Thouless transitions, rather than a line of first order quantum phase transitions. When Γ' is smaller (as is the case in Fig. 6.4) the SC2 phase is not observed, and a Kosterlitz-Thouless transition between the underscreened and local moment phases is seen when $t \sim (\Gamma\Gamma')^{1/2}$.

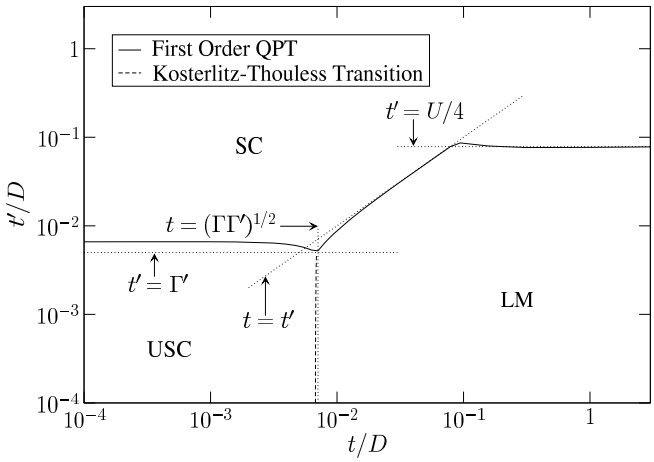


Figure 6.4: The phase diagram for a TQD with $\tilde{U} = 10$, $\Gamma = 10^{-2}D$ and $\Gamma' = 5 \times 10^{-3}D$ as a function of t/D and t'/D. First order quantum phase transitions are indicated by solid lines, and Kosterlitz-Thouless transitions by dashed lines. Dotted lines indicate useful analytic results.

As we shall see (Sec 6.6.1.3), the SC2 phase formally disappears when $\Gamma' = \frac{1}{4}\Gamma$, but as the Kondo temperature vanishes exponentially as this point is approached, we may observe this physics for larger values of Γ' (as is the case in Fig. 6.4), because our calculations necessarily terminate at a finite (although very low) temperature. In addition, whilst we find that in the $V \neq V'$ case that the line of first order quantum phase transitions between the SC1 and SC2/LM phases still follows the line $t \simeq t'$, the phase boundary is no longer found to lie exactly at the point $t = t'$.

6.6 The Spin Regime

We consider first the spin regime, wherein the TQD device is described at low temperatures by the effective spin model, Eq. 6.5 (see Fig. 6.2).

6.6.1 Effective Low Energy Models

We approach the derivation of low energy effective models here in much the same way as we did the derivation of the low energy effective model for regime II of the apex coupled trimer model (Sec. 4.6.1). We initially consider the states of the bare

Index	State	Energy
$\|\frac{3}{2};-;+\frac{3}{2}\rangle$	$\|\uparrow,\uparrow,\uparrow\rangle$	$\frac{J}{2}-\frac{1}{2}J_{\mathrm{RKKY}}+\frac{J'}{4}-\frac{1}{4}J'_{\mathrm{RKKY}}$
$\|\frac{3}{2};-;+\frac{1}{2}\rangle$	$\frac{1}{\sqrt{3}}(\|\uparrow,\uparrow,\downarrow\rangle+\|\uparrow,\downarrow,\uparrow\rangle+\|\downarrow,\uparrow,\uparrow\rangle)$	
$\|\frac{3}{2};-;-\frac{1}{2}\rangle$	$\frac{1}{\sqrt{3}}(\|\downarrow,\downarrow,\uparrow\rangle+\|\downarrow,\uparrow,\downarrow\rangle+\|\uparrow,\downarrow,\downarrow\rangle)$	
$\|\frac{3}{2};-;-\frac{3}{2}\rangle$	$\|\downarrow,\downarrow,\downarrow\rangle$	
$\|\frac{1}{2};+;+\frac{1}{2}\rangle$	$\frac{1}{\sqrt{2}}(\|\uparrow,\uparrow,\downarrow\rangle-\|\downarrow,\uparrow,\uparrow\rangle)$	$-\frac{3}{4}J'+\frac{3}{4}J'_{\mathrm{RKKY}}$
$\|\frac{1}{2};+;-\frac{1}{2}\rangle$	$\frac{1}{\sqrt{2}}(\|\uparrow,\downarrow,\downarrow\rangle-\|\downarrow,\downarrow,\uparrow\rangle)$	
$\|\frac{1}{2};-;+\frac{1}{2}\rangle$	$\frac{1}{\sqrt{6}}(\|\uparrow,\uparrow,\downarrow\rangle+\|\downarrow,\uparrow,\uparrow\rangle-2\|\uparrow,\downarrow,\uparrow\rangle)$	$\frac{J'}{4}-\frac{1}{4}J'_{\mathrm{RKKY}}-J+J_{\mathrm{RKKY}}$
$\|\frac{1}{2};-;-\frac{1}{2}\rangle$	$\frac{1}{\sqrt{6}}(2\|\downarrow,\uparrow,\downarrow\rangle-\|\downarrow,\downarrow,\uparrow\rangle-\|\uparrow,\downarrow,\downarrow\rangle)$	

Table 6.1: The eigenstates and energies of the bare trimer. Eigenstates are indexed by their quantum numbers; $|S;P;S^z\rangle$, where S is the spin, P the parity, and S^z the z-component of the spin, whilst basis states are labelled $|\sigma_1,\sigma_2,\sigma_3\rangle$, where σ_i is the spin on dot i.

trimer and then treat the J_{K} and J'_{K} terms in Eq. 6.5 as perturbations to these states. The states of the TQD, described by

$$\hat{H}_s = (J - J_{\mathrm{RKKY}})(\hat{\mathbf{S}}_1 + \hat{\mathbf{S}}_3)\cdot\hat{\mathbf{S}}_2 + (J' - J'_{\mathrm{RKKY}})\hat{\mathbf{S}}_1\cdot\hat{\mathbf{S}}_3 \tag{6.12}$$

are a quartet and two doublets (just as for the apex coupled trimer model), as detailed in Table 6.1. The quartet has $(-)$-parity, as does one of the doublet states; the other has $(+)$-parity. The crucial difference between the parallel TQD and the apex coupled trimer model is that the presence of the ferromagnetic RKKY interactions between neighbouring dots stabilises the quartet state, even in the absence of a field.

6.6.1.1 The Underscreened Phase

In the region where $(J, J') \ll (J_{\mathrm{RKKY}}, J'_{\mathrm{RKKY}})$ the ground state of the trimer is the quartet, with both the doublet states lying much higher in energy. The unity operator spanning the reduced Hilbert space of the low energy manifold is therefore $\hat{1} = \sum_{S^z} |\frac{3}{2};-;S^z\rangle\langle\frac{3}{2};-;S^z|$. Projecting into this low energy manifold, it immediately follows that the effective Hamiltonian for the system is described by

$\hat{H}_{eff} = \hat{1}\hat{H}_{spin}\hat{1}$;

$$\hat{H}_{eff} = J_{\rm K}\hat{1}\hat{\mathbf{S}}_2\hat{1}\cdot\hat{\mathbf{S}}(0) + J'_{\rm K}\hat{1}(\hat{\mathbf{S}}_1+\hat{\mathbf{S}}_3)\hat{1}\cdot\hat{\mathbf{S}}(0) + \hat{H}_L, \tag{6.13}$$

where the constant term $(\frac{J}{2} - \frac{1}{2}J_{RKKY} + \frac{J'}{4} - \frac{1}{4}J'_{RKKY})\hat{1}$ is neglected. Evaluating $\hat{1}\hat{\mathbf{S}}_2\hat{1}$ and $\hat{1}(\hat{\mathbf{S}}_1+\hat{\mathbf{S}}_3)\hat{1}$, the low energy effective model here may be written

$$\hat{H}_{eff} = \frac{1}{3}(J_{\rm K}+2J'_{\rm K})\hat{\mathbf{S}}\cdot\hat{\mathbf{S}}(0) + \hat{H}_L, \tag{6.14}$$

where $\hat{\mathbf{S}}$ is a spin-$\frac{3}{2}$ operator for the TQD as a whole. This is an antiferromagnetic spin-$\frac{3}{2}$ Kondo model with an effective coupling $J_{{\rm K},eff} = \frac{1}{3}(J_{\rm K}+2J'_{\rm K})$ which reduces to $J_{\rm K}$ in the limit $V = V'$. In this model the quartet state is underscreened to give a free triplet ($S_{\rm imp} = \ln 3$ and $T\chi_{\rm imp} = 1$) on an energy scale $T_{\rm K}^{USC} \propto e^{-1/\rho J_{{\rm K},eff}}$, which should be identical to $T_{\rm K}$ in the limit $V = V'$ (As in Chapters 4 and 5, $T_{\rm K}$ here is the Kondo temperature of the isolated dot 2).

6.6.1.2 The SC1 Phase

We next consider the region where $J' \gg J, J_{\rm RKKY}, J'_{\rm RKKY}$. Here the ground state of the trimer is the even parity doublet, $|\frac{1}{2};+;S^z\rangle$, with the odd parity doublet and the quartet lying much higher in energy. The unity operator spanning the reduced Hilbert space of the low energy manifold here is therefore $\hat{1} = \sum_{S^z}|\frac{1}{2};+;S^z\rangle\langle\frac{1}{2};+;S^z|$. Projecting into this manifold, just as in the preceding section, $\hat{H}_{eff} = \hat{1}\hat{H}_{spin}\hat{1}$, leading to Eq. 6.13. Evaluating $\hat{1}\hat{\mathbf{S}}_2\hat{1}$ and $\hat{1}(\hat{\mathbf{S}}_1+\hat{\mathbf{S}}_3)\hat{1}$ gives the low energy effective model

$$\hat{H}_{eff} = J_{\rm K}\hat{\mathbf{S}}\cdot\hat{\mathbf{S}}(0) + \hat{H}_L, \tag{6.15}$$

where $\hat{\mathbf{S}}$ is a spin-$\frac{1}{2}$ operator for the TQD as a whole. This is then an antiferromagnetic spin-$\frac{1}{2}$ Kondo model, which we expect to flow to a strong coupling fixed point on an energy scale $T_{\rm K} \propto e^{-1/\rho J_{\rm K}}$, entirely independent of the value of $J'_{\rm K}$. In the limit $J'_{\rm K} = 0$ this equation (trivially) recovers the result for the apex coupled trimer

model, Eq. 4.10.

6.6.1.3 The SC2 and Local Moment Phases

When $J \gg J', J_{\mathrm{RKKY}}, J'_{\mathrm{RKKY}}$ the ground state is the odd parity doublet, with the even parity doublet and quartet being much higher in energy. The unity operator spanning the reduced Hilbert space of the low energy manifold is therefore $\hat{1} = \sum_{S^z} |\frac{1}{2}; -; S^z\rangle\langle\frac{1}{2}; -; S^z|$. Projecting into this manifold, just as in the preceding sections, $\hat{H}_{eff} = \hat{1}\hat{H}_{spin}\hat{1}$, leading to Eq. 6.13. Evaluating $\hat{1}\hat{\mathbf{S}}_2\hat{1}$ and $\hat{1}(\hat{\mathbf{S}}_1 + \hat{\mathbf{S}}_3)\hat{1}$, we find that the low energy effective model may be written

$$\hat{H}_{eff} = \frac{1}{3}(4J'_{\mathrm{K}} - J_{\mathrm{K}})\hat{\mathbf{S}} \cdot \hat{\mathbf{S}}(0) + \hat{H}_L, \tag{6.16}$$

where $\hat{\mathbf{S}}$ is a spin-$\frac{1}{2}$ operator for the TQD as a whole. This is a spin-$\frac{1}{2}$ Kondo model with $J_{\mathrm{K},eff} = \frac{1}{3}(4J'_{\mathrm{K}} - J_{\mathrm{K}})$, being antiferromagnetic when $J'_{\mathrm{K}} > J_{\mathrm{K}}/4$ ($\Gamma' > \frac{1}{4}\Gamma$) and ferromagnetic when $J'_{\mathrm{K}} < J_{\mathrm{K}}/4$ ($\Gamma' < \frac{1}{4}\Gamma$), with $J_{\mathrm{K},eff}$ vanishing smoothly as the point $J'_{\mathrm{K}} = J_{\mathrm{K}}/4$ is reached. As (from perturbative scaling arguments [2, 14]) $T_{\mathrm{K}}^{SC2} \propto e^{-1/\rho J_{\mathrm{K},eff}}$, this is behaviour which we naturally expect to give rise to a Kosterlitz-Thouless transition. We note that in the limit $J'_{\mathrm{K}} = 0$ Eq. 6.16 reduces to $H_{eff} = -\frac{1}{3}J_{\mathrm{K}}\hat{\mathbf{S}} \cdot \hat{\mathbf{S}}(0) + \hat{H}_L$, recovering the result for the apex coupled trimer model (Eq. 4.11), whilst in the limit $J_{\mathrm{K}} = J'_{\mathrm{K}}$ Eq. 6.16 reduces to $H_{eff} = J_{\mathrm{K}}\hat{\mathbf{S}} \cdot \hat{\mathbf{S}}(0) + \hat{H}_L$, which is identical to Eq. 6.15, suggesting that under these conditions the Kondo temperature in both the SC1 and SC2 phases should be the same (and identical to T_{K}).

6.6.1.4 The SC1, SC2 and Local Moment Phases and Phase Boundary

We next consider the region in which the ground state of the trimer is one of the two doublet states. This is defined as the region where either $\frac{1}{2}J + J' > \frac{1}{2}J_{\mathrm{RKKY}} + J'_{\mathrm{RKKY}}$ or $J > J_{\mathrm{RKKY}}$. Using Table 6.1 we may easily determine that the two doublet states are degenerate when $J' = J'_c = J + J_{RKKY} - J'_{RKKY}$. When $J' \approx J'_c$ the

unity operator for the reduced Hilbert space of the low energy manifold is therefore $\hat{1} = \hat{1}_+ + \hat{1}_- = \sum_{S^z} |\frac{1}{2};+;S^z\rangle\langle\frac{1}{2};+;S^z| + \sum_{S^z} |\frac{1}{2};-;S^z\rangle\langle\frac{1}{2};-;S^z|$, and using this unity operator in Eq. 6.18 gives the low energy effective model

$$\hat{H}_{eff} = \frac{1}{3}[(J_{\rm K} + 2J'_{\rm K}) + 4(J_{\rm K} - J'_{\rm K})\hat{\mathcal{T}}^z]\hat{\mathbf{S}} \cdot \hat{\mathbf{S}}(0) + E_\Delta \hat{\mathcal{T}}^z + \hat{H}_L \tag{6.17}$$

where $\hat{\mathbf{S}}$ is a spin-$\frac{1}{2}$ operator for the TQD as a whole, $E_\Delta = E_+ - E_- = J + J'_{\rm RKKY} - J' - J_{\rm RKKY}$ is the energy separation between the two doublet states and we define a pseudospin operator, $\hat{\mathcal{T}}^z = \frac{1}{2}(\hat{1}_+ - \hat{1}_-)$, such that $\hat{\mathcal{T}}^z|\frac{1}{2};\pm;S^z\rangle = \pm\frac{1}{2}|\frac{1}{2};\pm;S^z\rangle$. We neglect the common constant $\frac{1}{2}(E_+ + E_-)\hat{1}$.

This model reduces to Eq. 6.15 when $E_\Delta < 0$ and $T < |E_\Delta|$, Eq. 6.16 when $E_\Delta > 0$ and $T < |E_\Delta|$ and Eq. 4.12, the corresponding low energy effective Hamiltonian for the apex coupled trimer model, when $J'_{\rm K} = 0$. In all cases when E_Δ is small the full Eq. 6.17 must be used. This describes a transition fixed point, characterised by $S_{\rm imp} = \ln 2$ and $T\chi_{\rm imp} = 0$ when $J'_{\rm K} > \frac{1}{4}J_{\rm K}$ (when the phase boundary is between SC1 and SC2) and $S_{\rm imp} = \ln 3$ and $T\chi_{\rm imp} = \frac{1}{6}$ when $J'_{\rm K} < \frac{1}{4}J_{\rm K}$ (when the phase boundary is between SC1 and the local moment phase). On an energy scale $T \sim |E_\Delta|$ the system flows away from the transition fixed point to the SC1 fixed point (when $E_\Delta < 0$) or the SC2/LM fixed point (when $E_\Delta > 0$). The transition fixed point persists to zero temperature only when $E_\Delta = 0$. Just as in Eq. 6.19, the two states in the low energy manifold here have distinct parities, and as a result there is no mixing between them; the low energy effective model being separable into distinct pseudospin sectors, with the $E_\Delta\hat{\mathcal{T}}^z$ term acting as an effective magnetic field upon the system, determining which pseudospin sector the ground state is found in, just as in Sec. 6.6.1.5.

Eq. 6.17 predicts that the phase boundary between the even and odd parity doublet states (i.e. between the SC1 and SC2 phases, or between the SC1 and LM phases) should follow the line $J' = J + J_{\rm RKKY} - J'_{\rm RKKY}$ ($E_\Delta = 0$). As shown in Fig. 6.15 (discussed below), the phase boundary is well described by this equation,

which reduces to $J' \simeq J$ when $(J, J') \gg (J_{RKKY}, J'_{RKKY})$: as discussed in Sec. 6.5 this is in good agreement with our phase diagrams (in the special case where $\Gamma = \Gamma'$ the phase boundary should follow the line $J' = J$ exactly, which is exactly what we find).

6.6.1.5 The Underscreened and SC1 Phases and Phase Boundary

Having considered the regions in which only one state need be retained in the low energy manifold, we next derive low energy models for the TQD when close to phase boundaries, where two states must be retained in the low energy manifold. When $J' > J$, the ground state of the trimer is either the quartet state or the (+)-parity doublet state. Clearly, there must exist some critical J' ($J'_c = J'_{RKKY} - \frac{1}{2}(J - J_{RKKY})$, as easily determined from Table 6.1) at which the quartet and doublet are degenerate. Close to this phase boundary (when $J' \sim J'_c$), the unity operator spanning the reduced Hilbert space of the low energy manifold is therefore $\hat{1} = \hat{1}_+ + \hat{1}_- = \sum_{S^z} |\frac{3}{2}; -; S^z\rangle\langle\frac{3}{2}; -; S^z| + \sum_{S^z} |\frac{1}{2}; +; S^z\rangle\langle\frac{1}{2}; +; S^z|$. Projecting into this manifold, the low energy effective model here is given by $\hat{H}_{eff} = \hat{1}\hat{H}_{spin}\hat{1}$, which can be equivalently written

$$\hat{H}_{eff} = J_{\mathrm{K}}\hat{1}\hat{\mathbf{S}}_2\hat{1}\cdot\hat{\mathbf{S}}(0) + J'_{\mathrm{K}}\hat{1}(\hat{\mathbf{S}}_1 + \hat{\mathbf{S}}_3)\hat{1}\cdot\hat{\mathbf{S}}(0) + \hat{1}\hat{H}_s\hat{1} + \hat{H}_L. \tag{6.18}$$

Evaluating $\hat{1}\hat{H}_s\hat{1}$, $\hat{1}\hat{\mathbf{S}}_2\hat{1}$ and $\hat{1}(\hat{\mathbf{S}}_1 + \hat{\mathbf{S}}_3)\hat{1}$ gives

$$\hat{H}_{eff} = \frac{1}{2}J_{\mathrm{K}}(1-2\hat{\mathcal{T}}^z)\tilde{\mathbf{S}}_{\frac{1}{2}}\cdot\hat{\mathbf{S}}(0) + \frac{1}{6}(J_{\mathrm{K}}+2J'_{\mathrm{K}})(1+2\hat{\mathcal{T}}^z)\tilde{\mathbf{S}}_{\frac{3}{2}}\cdot\hat{\mathbf{S}}(0) + E_\Delta\hat{\mathcal{T}}^z + \hat{H}_L \tag{6.19}$$

where $E_\Delta = E_Q - E_+ = \frac{1}{2}(J - J_{\mathrm{RKKY}}) + J' - J'_{\mathrm{RKKY}}$ is the energy difference between the quartet and doublet states, $\tilde{\mathbf{S}}_i$ is a spin-i operator for the TQD as a whole, and we define a pseudospin operator, $\hat{\mathcal{T}}^z = \frac{1}{2}(\hat{1}_+ - \hat{1}_-)$, such that $|\frac{3}{2}; -; S^z\rangle$ and $|\frac{1}{2}; +; \frac{1}{2}\rangle$ are eigenstates of it, with eigenvalues $\pm\frac{1}{2}$, respectively (we neglect the constant term $\frac{1}{2}(E_Q + E_+)\hat{1}$). When $E_\Delta < 0$, for $T < |E_\Delta|$ Eq. 6.19 reduces to Eq. 6.14, whilst

when $E_\Delta > 0$, for $T < |E_\Delta|$ it reduces to Eq. 6.15. When $|E_\Delta|$ is small, the full Eq. 6.19 must be retained down to the lowest temperatures: Eq. 6.19 describes a transition fixed point, characterised by $S_{\rm imp} = \ln 4$ and $T\chi_{\rm imp} = \frac{1}{2}$, which persists down to an energy scale $T \sim |E_\Delta|$, below which temperature the system flows to the SC1 or USC fixed points (depending upon whether $E_\Delta > 0$ or $E_\Delta < 0$). This transition fixed point persists down to zero temperature only when $E_\Delta = 0$. No mixing between the quartet and doublet states is seen, because they have distinct parities, and so the effective model is separable into distinct pseudospin sectors, with the $E_\Delta \hat{\mathcal{T}}^z$ term in the Hamiltonian acting as an effective magnetic field upon the system, determining which pseudospin sector the ground state is found in.

Eq. 6.19 predicts that the phase boundary between the USC and SC2 phase should be defined by the line $J' = J'_{RKKY} - \frac{1}{2}(J - J_{RKKY})$ (corresponding to $E_\Delta = 0$). This agrees well with the results of our phase diagrams, Fig. 6.2, 6.3 and 6.4, as we discuss in Sec. 6.6.2.5.

6.6.1.6 The Underscreened (USC), SC2 and Local Moment (LM) Phases and Phase Boundary

The final case we must consider is when the low energy manifold spans the odd parity doublet and quartet states. This corresponds to the region where $J \approx J_c = J_{RKKY}$, as easily determined from Table 6.1. The unity operator spanning the reduced Hilbert space of the low energy manifold here is $\hat{1} = \hat{1}_+ + \hat{1}_- = \sum_{S^z} |\frac{3}{2}; -; S^z\rangle\langle\frac{3}{2}; -; S^z| + \sum_{S^z} |\frac{1}{2}; -; S^z\rangle\langle\frac{1}{2}; -; S^z|$. Projecting into the low energy

manifold, and using Eq. 6.18, the low energy effective model here is then given by

$$\begin{aligned}\hat{H}_{eff} =&\frac{1}{6}(4J'_{\rm K}-J_{\rm K})(1-2\hat{\mathcal{T}}^z)\tilde{\mathbf{S}}_{\frac{1}{2}}\cdot\hat{\mathbf{S}}(0)+\frac{1}{6}(J_{\rm K}+2J'_{\rm K})(1+2\hat{\mathcal{T}}^z)\tilde{\mathbf{S}}_{\frac{3}{2}}\cdot\hat{\mathbf{S}}(0)+E_\Delta\hat{\mathcal{T}}^z\\
&+\frac{2}{\sqrt{6}}(J_{\rm K}-J'_{\rm K})[-|\tfrac{3}{2};-;+\tfrac{3}{2}\rangle\langle\tfrac{1}{2};-;+\tfrac{1}{2}|\\
&+|\tfrac{1}{2};-;-\tfrac{1}{2}\rangle\langle\tfrac{3}{2};-;-\tfrac{3}{2}|+|\tfrac{3}{2};-;-\tfrac{3}{2}\rangle|\tfrac{1}{2};-;-\tfrac{1}{2}\rangle\\
&-|\tfrac{1}{2};-;+\tfrac{1}{2}\rangle\langle\tfrac{3}{2};-;+\tfrac{3}{2}|+\tfrac{1}{\sqrt{3}}(-|\tfrac{3}{2};-;+\tfrac{1}{2}\rangle\langle\tfrac{1}{2};-;-\tfrac{1}{2}|\\
&+|\tfrac{1}{2};-;+\tfrac{1}{2}\rangle\langle\tfrac{3}{2};-;-\tfrac{1}{2}|+|\tfrac{3}{2};-;-\tfrac{1}{2}\rangle\langle\tfrac{1}{2};-;+\tfrac{1}{2}|\\
&-|\tfrac{1}{2};-;-\tfrac{1}{2}\rangle\langle\tfrac{3}{2};-;+\tfrac{1}{2}|+|\tfrac{3}{2};-;+\tfrac{1}{2}\rangle\langle\tfrac{1}{2};-;+\tfrac{1}{2}|\\
&+|\tfrac{3}{2};-;-\tfrac{1}{2}\rangle\langle\tfrac{1}{2};-;-\tfrac{1}{2}|+|\tfrac{1}{2};-;+\tfrac{1}{2}\rangle\langle\tfrac{3}{2};-;+\tfrac{1}{2}|\\
&+|\tfrac{1}{2};-;-\tfrac{1}{2}\rangle\langle\tfrac{3}{2};-;-\tfrac{1}{2}|)]\cdot\hat{\mathbf{S}}(0)+\hat{H}_L,\end{aligned}\tag{6.20}$$

where $\tilde{\mathbf{S}}_i$ is a spin-i operator for the TQD as a whole and $E_\Delta = E_Q - E_- = \frac{3}{2}(J - J_{\rm RKKY})$ is the energy separation between the quartet and the doublet, the common constant $\frac{1}{2}(E_Q + E_-)\hat{1}$ being neglected. We define a pseudospin operator, $\hat{\mathcal{T}}^z = \frac{1}{2}(\hat{1}_+ - \hat{1}_-)$, such that $|\frac{3}{2};-;S^z\rangle$ and $|\frac{1}{2};-;\frac{1}{2}\rangle$ are eigenstates of it with eigenvalues $\pm\frac{1}{2}$, respectively. Unfortunately, due to the mixing which occurs between the doublet and quartet states (as they are both of the same parity) we are unable to derive much useful information from this low energy effective model, although it is clear that a first order quantum phase transition will *not*, in general, be observed. However in the limit $J_{\rm K} = J'_{\rm K}$ Eq. 6.20 reduces to

$$\hat{H}_{eff} = \frac{1}{2}J_{\rm K}(1-2\hat{\mathcal{T}}^z)\tilde{\mathbf{S}}_{\frac{1}{2}}\cdot\hat{\mathbf{S}}(0)+\frac{1}{2}J_{\rm K}(1+2\hat{\mathcal{T}}^z)\tilde{\mathbf{S}}_{\frac{3}{2}}\cdot\hat{\mathbf{S}}(0)+E_\Delta\hat{\mathcal{T}}^z+\hat{H}_L. \tag{6.21}$$

Mixing between the quartet and doublet states is prohibited here by the spin symmetry which the full spin Hamiltonian, Eq. 6.5, conserves in this limit (as discussed in Sec. 6.3), and as a result the low energy effective model is simplified, describing a simple level crossing transition, which will occur when $E_\Delta = 0$, the system being described by a transition fixed point with $S_{\rm imp} = \ln 4$ and $T\chi_{\rm imp} = \frac{1}{2}$ until an energy

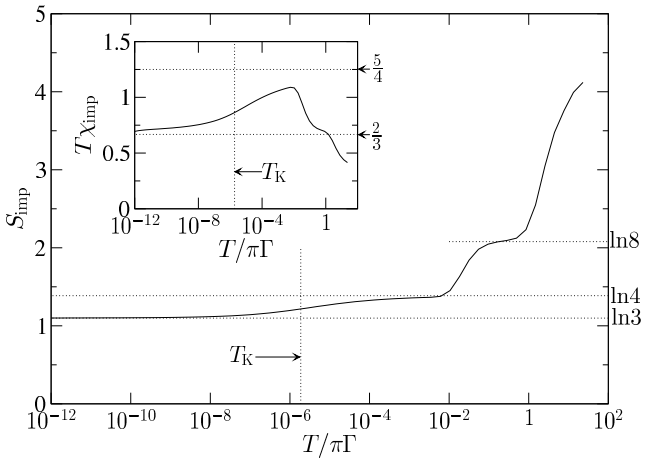


Figure 6.5: Entropy $S_{\rm imp}$ vs $T/\pi\Gamma$ for a system deep inside the USC phase, with $\tilde{U} = 10$, $\tilde{t} = \tilde{t}' = 10^{-1}$ and $\tilde{\Gamma} = \tilde{\Gamma}' = 10^{-2}D$. The inset shows $T\chi_{\rm imp}$ vs $T/\pi\Gamma$ for the same system.

scale $T \sim |E_\Delta|$ is reached, below which the system will flow to the USC (when $E_\Delta < 0$) or SC2 (when $E_\Delta > 0$) fixed point, the transition fixed point describing the system down to zero temperature only when $E_\Delta = 0$. Eq. 6.21 is separable into distinct spin sectors, with the $E_\Delta \hat{\mathcal{T}}^z$ term acting as an effective magnetic field upon the system, with the sign of E_Δ determining the spin of the ground state.

It is clear that Eq. 6.21 predicts that the phase boundary should follow the line $J = J_{\rm RKKY}$, corresponding to $t \simeq \Gamma$. However, we also find, as discussed in Sec. 6.5, that the phase boundary in the case where $\Gamma \neq \Gamma'$ is well described by the line $J = J_{\rm RKKY}$ ($t \simeq \sqrt{\Gamma\Gamma'}$), indicating that the mixing between the quartet and doublet states present in Eq. 6.20 is only significant when the energy separation between the quartet and doublet states is small.

6.6.2 Thermodynamics

We first describe the behaviour of systems deep within each of the four phases of the trimer in parallel — USC, SC1, SC2 and LM — before considering the behaviour of the TQD when close to the phase boundaries.

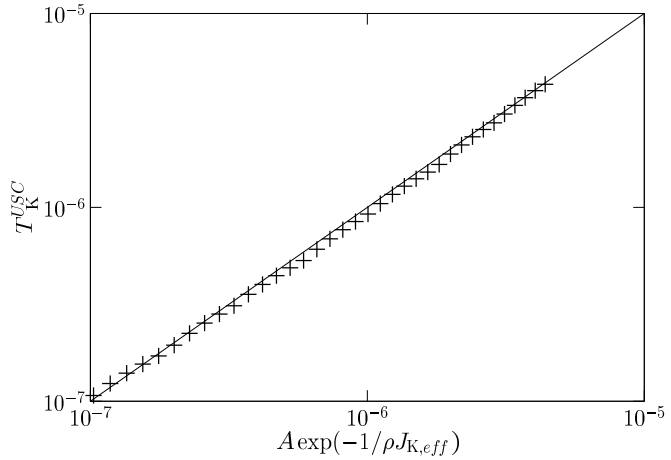


Figure 6.6: The variation of $T_{\rm K}^{USC}$ (defined via $S_{\rm imp}(T_{\rm K}^{USC}) = 0.5 \ln 12$, suitably between $\ln 4$ and $\ln 3$) with $A\exp(-1/\rho J_{{\rm K},eff})$, with $J_{{\rm K},eff}$ as given by Eq. 6.14, for a system with $\tilde{U} = 10$, $\tilde{t} = \tilde{t}' = 10^{-1}$ and $\Gamma = 10^{-2}D$, varying Γ' between $6 \times 10^{-3}D$ and Γ (A is a constant).

6.6.2.1 The Underscreened (USC) Phase

Fig. 6.5 and the inset to that figure show thermodynamic properties of a system deep within the USC phase. At high temperature, the system initially lies close to the free orbital fixed point [7, 8], characterised by $S_{\rm imp} = \ln 4^3$ and $T\chi_{\rm imp} = 3 \times \frac{1}{8}$. On an energy scale $T \sim U$ the doubly occupied and empty states of each dot become thermally inaccessible; the entropy flows to $\ln 8$, and $T\chi_{\rm imp}$ to $\frac{3}{4}$ at this point, characteristic of three free spins. As the temperature is reduced further the two doublet states are projected out when $T \sim J_{\rm RKKY}$, at which point the entropy flows to $\ln 4$ and $T\chi_{\rm imp} = \frac{5}{4}$, characteristic of a quartet state. This quartet is underscreened on an energy scale $T_{\rm K}^{USC}$, which we find to be identical to $T_{\rm K}$ in the special case $\Gamma = \Gamma'$ (in agreement with Eq. 6.14), as illustrated in Fig. 6.5[1]. The underscreened fixed point which is the ultimate low temperature fixed point of the system is characterised by $S_{\rm imp} = \ln 3$ and $T\chi_{\rm imp} = \frac{2}{3}$, as expected for a triplet state, corresponding to the underscreened spin-$\frac{3}{2}$ state of Nozieres and Blandin [21]. We find that $T_{\rm K}^{USC} \sim A\exp(-1/\rho J_{{\rm K},eff})$, with $J_{{\rm K},eff} = \frac{1}{3}(J_{\rm K} + 2J'_{\rm K})$ as predicted by Eq. 6.14 — this is shown in Fig. 6.6.

[1] As discussed above, $T_{\rm K}$ is the Kondo temperature of the isolated dot 2.

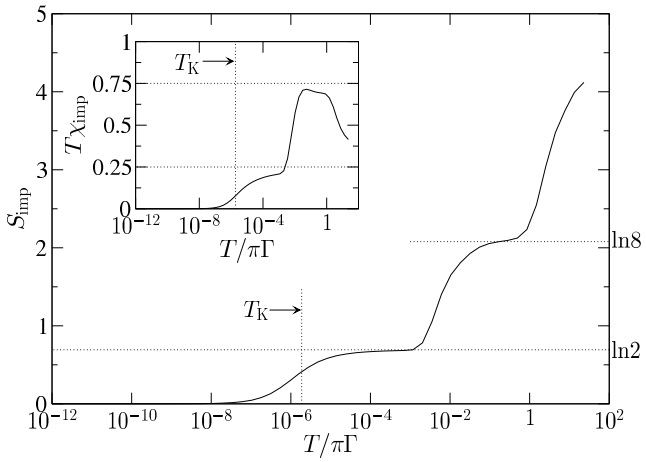


Figure 6.7: Entropy $S_{\rm imp}$ vs $T/\pi\Gamma$ for a system deep inside the SC1 phase, with $\tilde{U} = 10$, $\tilde{t} = 10^{-1}$, $\tilde{t}' = 4 \times 10^{-1}$ and $\tilde{\Gamma} = \tilde{\Gamma}' = 10^{-2}D$. The inset shows $T\chi_{\rm imp}$ vs $T/\pi\Gamma$ for the same system.

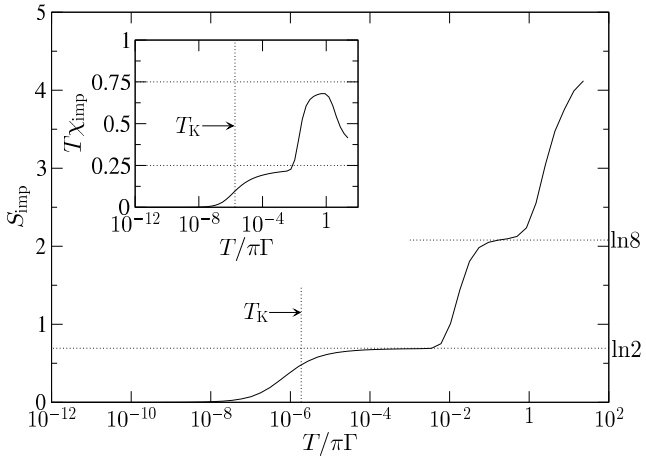


Figure 6.8: Entropy $S_{\rm imp}$ vs $T/\pi\Gamma$ for a system deep inside the SC2 phase, with $\tilde{U} = 10$, $\tilde{t} = 4 \times 10^{-1}$, $\tilde{t}' = 10^{-1}$ and $\tilde{\Gamma} = \tilde{\Gamma}' = 10^{-2}D$. The inset shows $T\chi_{\rm imp}$ vs $T/\pi\Gamma$ for the same system.

6.6.2.2 The SC1 and SC2 Phases

We now consider the two strong coupling phases, SC1 ((+)-parity) and SC2 ((−)-parity), the thermodynamic properties of which are shown in Fig. 6.7 and 6.8, respectively. The low temperature physics is the same in both cases. At high temperature, the system is initially at the free orbital fixed point ($S_{\rm imp} = \ln 4^3$ and $T\chi_{\rm imp} = 3 \times \frac{1}{8}$), but on an energy scale $T \sim U$ the empty and doubly occupied states of each dot are projected out, and so the entropy flows to $\ln 8$ and $T\chi_{\rm imp} = \frac{3}{4}$, indicative of

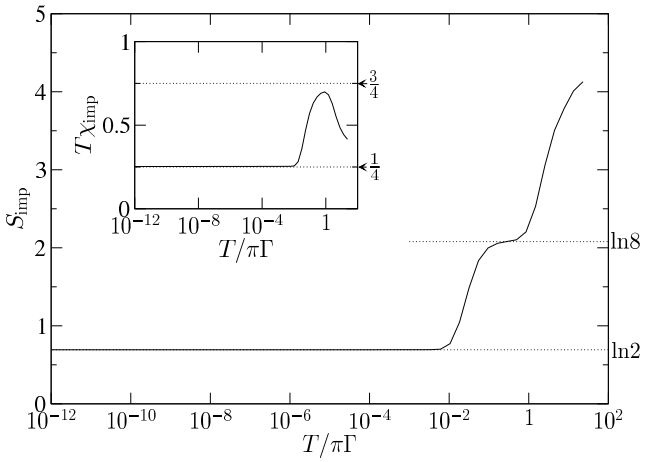


Figure 6.9: Entropy $S_{\rm imp}$ vs $T/\pi\Gamma$ for a system deep within the LM phase, with $\tilde{U} = 10$, $\tilde{t} = 4 \times 10^{-1}$, $\tilde{t}' = 10^{-1}$, $\tilde{\Gamma} = 10^{-2}D$ and $\tilde{\Gamma}' = 2 \times 10^{-3}D$. The inset shows $T\chi_{\rm imp}$ vs $T/\pi\Gamma$ for the same system.

three free spins. Reducing the temperature through $T \sim J$ projects out the quartet and higher energy doublet states, and so the system flows to the local moment fixed point, characterised by $S_{\rm imp} = \ln 2$ and $T\chi_{\rm imp} = \frac{1}{4}$. Finally, on an energy scale $T_{\rm K}^{SCi}$ ($i = 1, 2$) the local moment is screened, and the system flows to the strong coupling fixed point ($S_{\rm imp} = 0$ and $T\chi_{\rm imp} = 0$) which is the ultimate low temperature fixed point of the system ($T_{\rm K}^{SCi}$ is defined via $S_{\rm imp}(T_{\rm K}^{SCi}) = 0.5 \ln 2$, suitably between $\ln 2$ and 0). In the special case $\Gamma = \Gamma'$ (shown in Fig. 6.7 and 6.8) our low energy models (Eq. 6.15 and 6.16) predict from perturbative scaling arguments [2, 14] that $T_{\rm K}^{SC1} = T_{\rm K}^{SC2} = T_{\rm K}$. Eq. 6.15 also predicts, quite generally, that $T_{\rm K}^{SC1} = T_{\rm K}$, independent of the value of Γ'. We find that both these relationships hold when the system is deep within the spin regime, but (as one would expect) as the system approaches the orbital regime (see Fig. 6.2) this description breaks down, as discussed in Sec. 6.8.

6.6.2.3 The Local Moment and SC2 Phases

The physics observed deep within the local moment phase is illustrated in Fig. 6.9. At high temperature the system is initially at the free orbital fixed point ($S_{\rm imp} = \ln 4^3$ and $T\chi_{\rm imp} = 3 \times \frac{1}{8}$) but enters the spin regime ($S_{\rm imp} = \ln 8$ and $T\chi_{\rm imp} = 3 \times \frac{1}{4}$)

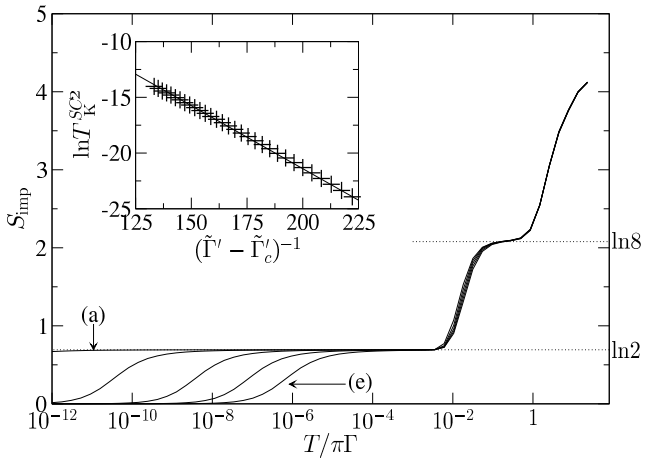


Figure 6.10: Entropy $S_{\rm imp}$ vs $T/\pi\Gamma$ for systems approaching the phase boundary between the SC2 and LM phases, with $\tilde{U} = 10$, $\tilde{t} = 4 \times 10^{-1}$ and $\tilde{t}' = 2 \times 10^{-1}$. $\Gamma = 10^{-2}D$ and Γ' is varied, with $\Gamma' = 6{\times}10^{-3}D$ for (a), $7{\times}10^{-3}D$ for (b), $8{\times}10^{-3}D$ for (c), $9{\times}10^{-3}D$ for (d) and $10^{-2}D$ for (e). The inset shows $\ln T_{\rm K}^{SC2}$ (defined via $S_{\rm imp}(T_{\rm K}^{SC2}) = 0.5 \ln 2$) as a function of $(\tilde{\Gamma}' - \tilde{\Gamma}'_c)^{-1}$, with $\Gamma'_c = \frac{1}{4}\Gamma$.

on an energy scale $T \sim U$. On an energy scale $T \sim J$ the quartet and even parity doublet are projected out, and the system then flows to the local moment fixed point, characterised by $S_{\rm imp} = \ln 2$ and $T\chi_{\rm imp} = \frac{1}{4}$, which is the ultimate low temperature fixed point of the system.

Our low energy effective model, Eq. 6.16, predicts that a Kosterlitz-Thouless transition between the SC2 and LM phases should be observed when $\Gamma' = \Gamma'_c = \frac{1}{4}\Gamma$. As shown in Fig. 6.10 this is exactly what is seen in the NRG, with the Kondo temperature, $T_{\rm K}^{SC2}$ (defined via $S_{\rm imp}(T_{\rm K}^{SC2}) = 0.5 \ln 2$), vanishing exponentially as the transition is approached: this is illustrated in the inset to the figure.

6.6.2.4 The SC1/SC2 and SC1/LM Phase Boundaries

We now consider the behaviour of the system close to the phase boundary between the doublet states — that is the phase boundary between the SC1 and SC2 phases, when $J'_{\rm K} > \frac{1}{4}J_{\rm K}$, and between the SC1 and LM phases otherwise. We first examine the special case $J_{\rm K} = J'_{\rm K}$. Here the two doublet states are exactly degenerate when $t = t'$, and we find that $T_{\rm K}^{SC1} = T_{\rm K}^{SC2} \simeq T_{\rm K}$ at this point: this is in agreement with the low energy effective model Eq. 6.17 and gives rise to the behaviour seen

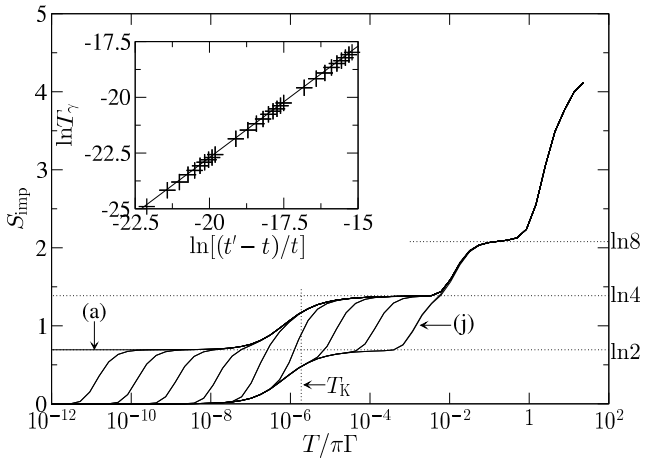


Figure 6.11: Entropy $S_{\rm imp}$ vs $T/\pi\Gamma$ for systems approaching the phase boundary between the SC1 and SC2 phases. $\tilde{U} = 10$, $\Gamma = \Gamma' = 10^{-2}D$ and $\tilde{t} = 4 \times 10^{-1}$. $\tilde{t}'$ is varied about $\tilde{t}'_c = \tilde{t}$, with $\tilde{t}' = \tilde{t} \pm \lambda$ with $\lambda = 0$ for (a), 10^{-10} for (b), 10^{-9} for (c), 10^{-8} for (d), 10^{-7} for (e), 10^{-6} for (f), 10^{-5} for (g), 10^{-4} for (h), 10^{-3} for (i) and 10^{-2} for (j). The inset plots $\ln[(t'-t)/t]$ against $\ln T_\gamma$ where we define T_γ via $S_{\rm imp}(T_\gamma) = 0.5 \ln 2$.

in line (a) of Fig. 6.11. The system here is initially at the free orbital fixed point ($S_{\rm imp} = \ln 4^3$ and $T\chi_{\rm imp} = 3 \times \frac{1}{8}$, not shown), but the empty and doubly occupied states of the TQD become thermally inaccessible on an energy scale $T \sim U$. At this point the entropy falls to $\ln 8$ and $T\chi_{\rm imp} = 3 \times \frac{1}{4}$, characteristic of three free spins. On an energy scale $T \sim J$ the quartet state is projected out, and the entropy falls to $\ln 4$ ($T\chi_{\rm imp} = \frac{1}{4}$), characteristic of two degenerate doublet states. On an energy scale $T_{\rm K}$ both the doublets are screened, and $T\chi_{\rm imp}$ falls to 0. However, as the ground state is still degenerate, $S_{\rm imp} = \ln 2$ here. This is the behaviour of the system exactly at the phase boundary, where $E_\Delta = 0$ and the system lies exactly on the transition fixed point. When $E_\Delta \neq 0$ the system will ultimately flow away from the transition fixed point on an energy scale $T \sim |E_\Delta|$. If $|E_\Delta| < T_{\rm K}$ then the system flows to the SC1 (if $E_\Delta < 0$) or SC2 (if $E_\Delta > 0$) fixed points. This will cause the entropy to fall from $\ln 2$ to 0. If $|E_\Delta| > T_{\rm K}$ however the system flows to the local moment fixed point on an energy scale $T \sim |E_\Delta|$, and so $S_{\rm imp}$ falls from $\ln 4$ to $\ln 2$ on this scale, before ultimately flowing to a strong coupling fixed point on an energy scale $T \sim T_{\rm K}$ (the sign of E_Δ determines whether the system ultimately flows to the SC1 or SC2 fixed point). This behaviour is shown in lines (b)-(j) of Fig. 6.11.

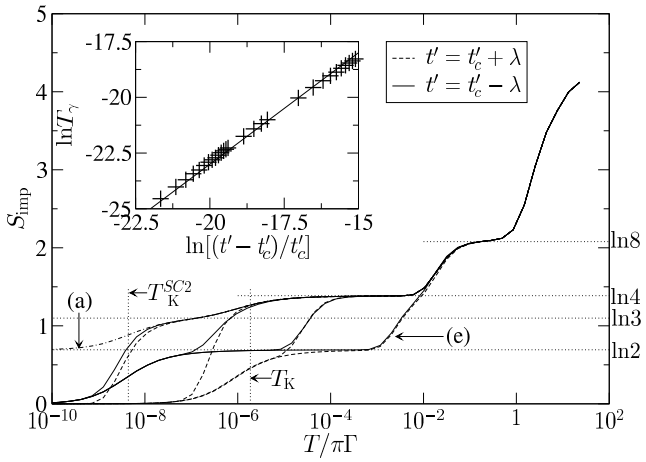


Figure 6.12: Entropy $S_{\rm imp}$ vs $T/\pi\Gamma$ for systems approaching the phase boundary between the SC1 and SC2 phases. $\tilde{U} = 10$, $\tilde{t} = 4 \times 10^{-1}$, $\Gamma = 10^{-2}D$ and $\Gamma' = 8 \times 10^{-3}D$. $\tilde{t}'$ is varied about $\tilde{t}'_c \simeq 3.81824 \times 10^{-1}$, with $\tilde{t}' = \tilde{t}'_c \pm \lambda$ with $\lambda = 0$ for (a), 2×10^{-8} for (b), 2×10^{-6} for (c), 2×10^{-4} for (d) and 2×10^{-2} for (e). The inset shows $\ln[(t' - t'_c)/t'_c]$ vs $\ln T_\gamma$ where we define T_γ via $S_{\rm imp}(T_\gamma) = 0.5 \ln 2$.

$T\chi_{\rm imp}$ is unaffected by this, being $1/4$ when $T > T_{\rm K}$ and 0 when $T < T_{\rm K}$. We find that the transition between these two phases is always a first order quantum phase transition, as is shown in the inset to Fig. 6.11, exactly as one would expect from the low energy effective model, Eq. 6.17.

We next consider a system close to the SC1/SC2 phase boundary where $\Gamma \neq \Gamma'$. Such a system is shown in Fig. 6.12. Here the two Kondo scales $T_{\rm K}^{SC1}$ and $T_{\rm K}^{SC2}$ are distinct, although we still find that $T_{\rm K}^{SC1} \simeq T_{\rm K}$, in agreement with Eq. 6.17, and as we concentrate on the case $\Gamma \geq \Gamma'$, we also find that $T_{\rm K}^{SC2} < T_{\rm K}$. Exactly at the phase boundary ($E_\Delta = 0$, corresponding to $t \approx t'$) the system lies on the transition fixed point (this is line (a) in Fig. 6.12). The system behaves exactly as in the $\Gamma = \Gamma'$ case until an energy scale $T \sim T_{\rm K}$ is reached. On this scale the (+)-parity doublet is screened, but the (−)-parity doublet is not, and so the entropy falls to $\ln 3$ and $T\chi_{\rm imp}$ (not shown) to $\frac{1}{6}$, just as seen in the transition fixed point for the apex coupled trimer model (Sec. 4.6). When an energy scale $T \sim T_{\rm K}^{SC2}$ is reached, the (−)-parity doublet is also screened and the system flows to the transition fixed point; the entropy falls to $\ln 2$ (as the ground state is degenerate) and $T\chi_{\rm imp} = 0$. The system is described down to zero temperature by this transition fixed point

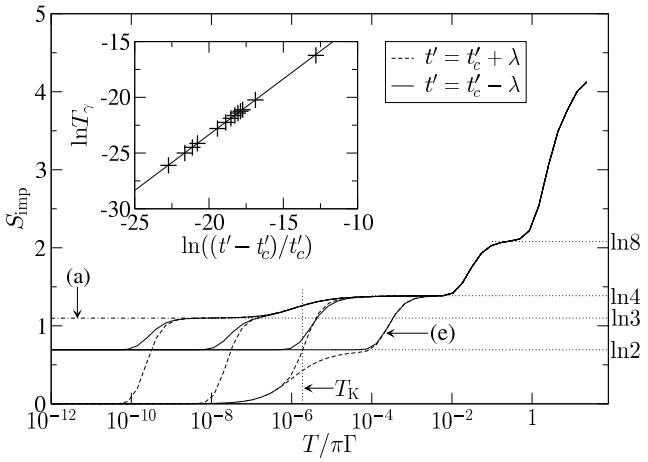


Figure 6.13: Entropy $S_{\rm imp}$ vs $T/\pi\Gamma$ for systems approaching the phase boundary between the SC1 and LM phases. $\tilde{U} = 10$, $\tilde{t} = 4 \times 10^{-1}$, $\Gamma = 10^{-2}D$ and $\Gamma' = 5 \times 10^{-3}D$. $\tilde{t}'$ is varied about $\tilde{t}'_c \simeq 3.71172 \times 10^{-1}$, with $\tilde{t}' = \tilde{t}'_c \pm \lambda$ with $\lambda = 0$ for (a), 2×10^{-9} for (b), 2×10^{-7} for (c), 2×10^{-5} for (d) and 2×10^{-3} for (e). The inset shows $\ln[(t' - t'_c)/t'_c]$ vs $\ln T_\gamma$ where we define T_γ via $S_{\rm imp}(T_\gamma) = 0.5 \ln 2$.

only when $E_\Delta = 0$.

When $E_\Delta < 0$ the system ultimately flows away from the transition fixed point on an energy scale $T \sim |E_\Delta|$, as shown in lines (b)-(e) of Fig. 6.12: if $|E_\Delta| < T_{\rm K}$ then the system flows directly to the SC1 fixed point, causing the entropy to fall from $\ln 2$ to 0 (if $|E_\Delta| < T_{\rm K}^{SC2}$) or from $\ln 3$ to 0 (if $T_{\rm K}^{SC2} < |E_\Delta| < T_{\rm K}$). However, if $|E_\Delta| > T_{\rm K}$ the the system flows away from the transition fixed point and to the local moment fixed point when $T \sim |E_\Delta|$, and so the entropy falls from $\ln 4$ to $\ln 2$ when $T \sim |E_\Delta|$, before ultimately falling to 0 on an energy scale $T \sim T_{\rm K}$ (the energy scale upon which the (+)-parity doublet is screened, and on which the system flows to the SC1 fixed point). When $E_\Delta > 0$ on the other hand the system ultimately flows to the SC2 fixed point, causing the entropy to fall from $\ln 2$ to 0 (if $E_\Delta < T_{\rm K}^{SC2}$), $\ln 3$ to $\ln 2$ (if $T_{\rm K}^{SC2} < E_\Delta < T_{\rm K}$) or $\ln 4$ to $\ln 2$ (if $E_\Delta > T_{\rm K}$) on an energy scale $T \sim |E_\Delta|$: in the latter two cases the (−)-parity doublet is then screened on an energy scale $T \sim T_{\rm K}^{SC2}$, at which point the system flows to the SC2 fixed point. In all cases we find that the transition between these two phases is a first order quantum phase transition, as is shown in the inset to Fig. 6.12, exactly as one would expect from the low energy effective model, Eq. 6.17.

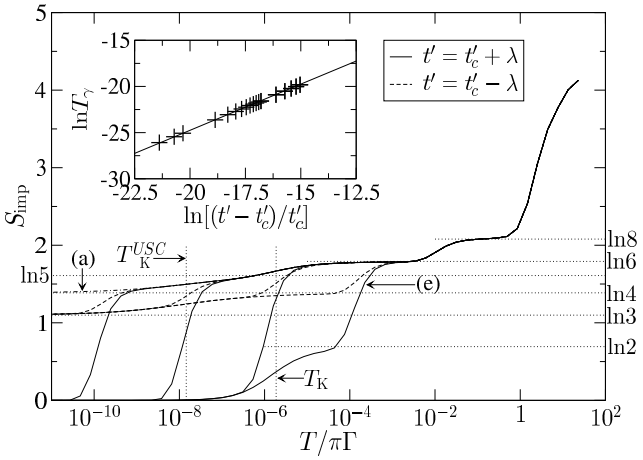


Figure 6.14: Entropy $S_{\rm imp}$ vs $T/\pi\Gamma$ for systems approaching the phase boundary between the SC1 and USC phases. $\tilde{U} = 10$, $\tilde{t} = 10^{-1}$, $\Gamma = 10^{-2}D$ and $\Gamma' = 5 \times 10^{-3}D$. $\tilde{t'}$ is varied about $\tilde{t'}_c \simeq 2.03521 \times 10^{-1}$, with $\tilde{t'} = \tilde{t'}_c \pm \lambda$: $\lambda = 0$ for (a), 2×10^{-9} for (b), 2×10^{-7} for (c), 2×10^{-5} for (d) and 2×10^{-3} for (e). The inset shows $\ln[(t' - t'_c)/t'_c]$ vs $\ln T_\gamma$, where we define T_γ via $S_{\rm imp}(T_\gamma) = 0.5 \ln 2$ in the SC1 phase.

Finally, we consider a system close to the SC1/LM phase boundary. Such a system is shown in Fig. 6.13. We again observe a first order quantum phase transition (as shown in the inset to the figure), and exactly on the phase boundary the system is described down to zero temperature by a transition fixed point characterised by $S_{\rm imp} = \ln 3$ and $T\chi_{\rm imp} = \frac{1}{6}$ (line (a)). The behaviour of the system here is identical to that of regime II of the apex coupled trimer model, flowing to the same fixed points on the same energy scales, exactly as one would expect from Eq. 6.17 and Eq. 4.12: compare Fig. 6.13 with Fig. 4.3. The behaviour of the system in this region is therefore described in Sec. 4.6.2, and is not repeated here.

6.6.2.5 The SC1/USC Phase Boundary

We now consider the behaviour of the TQD device close to the SC1/USC phase boundary. It is found that, due to the parity change across the phase boundary here, a first order quantum phase transition is seen in all cases (as one would expect from Eq. 6.19, the low energy effective model), and the underlying physics of the $\Gamma = \Gamma'$ case is indistinguishable from that seen when $\Gamma \neq \Gamma'$. The relevant results are shown in Fig. 6.14. When $E_\Delta = 0$, the system is described by a transition fixed

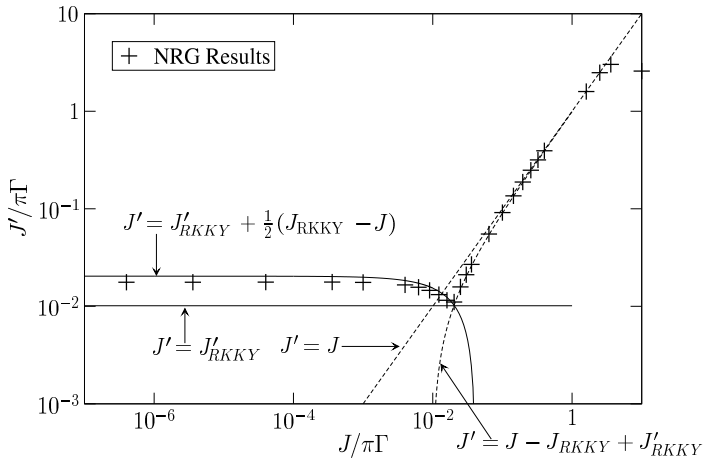


Figure 6.15: The phase boundary between the odd and even parity states of the TQD as a function of $\tilde{J}$ and $\tilde{J}'$ for a system with $\tilde{U} = 10$, $\Gamma = 10^{-2}D$ and $\Gamma' = 5 \times 10^{-3}D$.

point down to zero temperature. This is line (a) in Fig. 6.14. At high temperature, the system is initially at the free orbital fixed point, characterised by $S_{\rm imp} = \ln 4^3$ and $T\chi_{\rm imp} = 3 \times \frac{1}{8}$, not shown, but on an energy scale $T \sim U$ the empty and doubly occupied states of the dots are projected out, and the entropy flows to $\ln 8$ ($T\chi_{\rm imp} = 3 \times \frac{1}{4}$), characteristic of three free spins. On a temperature scale $T \sim J$ the $(-)$-parity doublet becomes thermally inaccessible, and the entropy drops to $\ln 6$ ($T\chi_{\rm imp} = \frac{11}{12}$). On an energy scale $T \sim T_{\rm K}$ the doublet state is screened, and the entropy falls to $\ln 5$ ($T\chi_{\rm imp} = 1$). Finally, on an energy scale $T_{\rm K}^{USC}$ (which is $\leq T_{\rm K}$ — see Eq. 6.14) the quartet is underscreened to give a triplet state, and the entropy falls to $\ln 4$ ($T\chi_{\rm imp} = \frac{1}{2}$). This transition fixed point describes the system at zero-temperature only when $E_\Delta = 0$. In all other cases the system will ultimately flow away from the transition fixed point on an energy scale $T \sim |E_\Delta|$, ultimately flowing to either the USC (if $E_\Delta < 0$) or SC1 (if $E_\Delta > 0$) fixed points, as shown in lines (b)-(e) of Fig. 6.14.

From Eq. 6.19 we expect the phase boundary to follow the line $E_\Delta = 0$, corresponding to $J' = J'_{\rm RKKY} + \frac{1}{2}(J_{\rm RKKY} - J)$. As shown in Fig. 6.15 this line describes the phase boundary in this region well, confirming the results of the low energy effective model (this figure also shows that the phase boundary between the SC1 and SC2

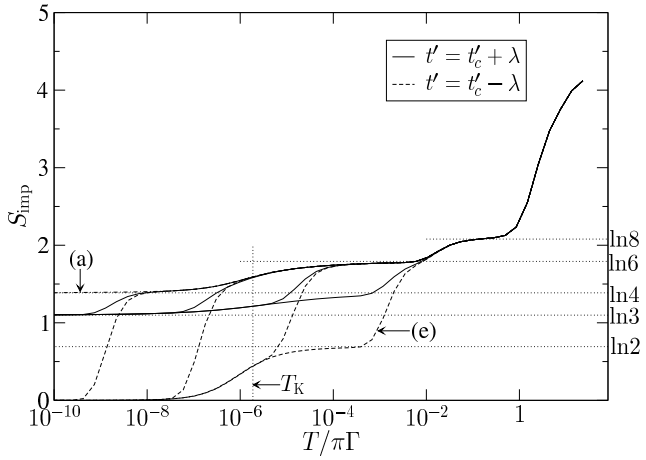


Figure 6.16: Entropy $S_{\rm imp}$ vs $T/\pi\Gamma$ for systems approaching the phase boundary between the SC2 and USC phases. $\tilde{U} = 10$, $\tilde{t'} = 10^{-1}$ and $\Gamma = \Gamma' = 10^{-2}D$. $\tilde{t}$ is varied about $\tilde{t}_c \simeq 3.08213 \times 10^{-1}$, with $\tilde{t} = \tilde{t}_c \pm \lambda$: $\lambda = 0$ for (a), 10^{-8} for (b), 10^{-6} for (c), 10^{-4} for (d) and 10^{-2} for (e).

phases is well described by $J' = J - J_{RKKY} + J'_{RKKY}$, as discussed in Sec. 6.6.1.4).

6.6.2.6 The SC2/USC and LM/USC Phase Boundaries

Finally, we consider the behaviour of a TQD close to the phase boundary between the USC phase and the odd parity doublet (i.e. between the USC phase and either the SC2 or LM phases). As one would expect from the low energy effective model, Eq. 6.20, we find that the behaviour of the system in the special case $\Gamma = \Gamma'$ is distinct from that seen when $\Gamma \neq \Gamma'$ (unlike the USC/SC1 phase boundary discussed above). In the $\Gamma = \Gamma'$ case, due to the conservation of TQD spin by the spin Hamiltonian (see Sec. 6.3), no mixing between the quartet and doublet states is permitted, and so a first order quantum phase transition, effectively identical to that described in Sec. 6.6.2.5, is seen, just as one would expect from Eq. 6.21. This is illustrated in Fig. 6.16, where the transition fixed point is identical to that in Fig. 6.14. We note that in this case $T_{\rm K}^{SC2} = T_{\rm K}^{USC} = T_{\rm K}$, and so the quartet and doublet states are quenched on the same energy scale, leading to a direct entropy flow from $\ln 6$ to $\ln 4$ at an energy scale $T \sim T_{\rm K}$, the physics being otherwise as described in Sec. 6.6.2.5.

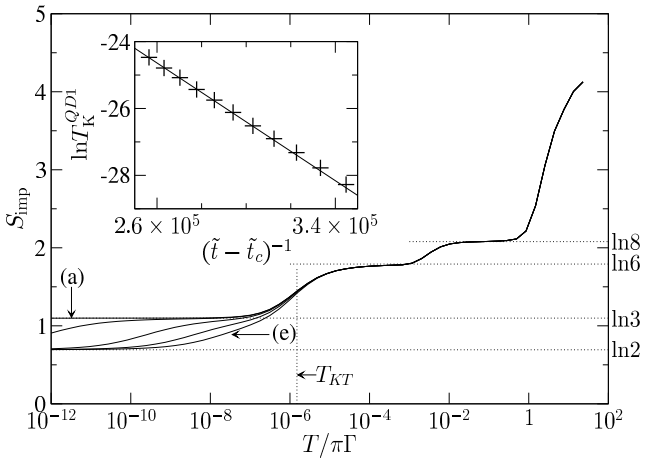


Figure 6.17: Entropy $S_{\rm imp}$ vs $T/\pi\Gamma$ for systems approaching the phase boundary between the LM and USC phases. $\tilde{U} = 10$, $\tilde{t}' = 10^{-1}$, $\Gamma = 10^{-2}D$ and $\Gamma' = 5 \times 10^{-3}D$. $\tilde{t}$ is varied with $\tilde{t} = 2.17672 \times 10^{-1}$ for (a), 2.17674×10^{-1} for (b), 2.17676×10^{-1} for (c), 2.17678×10^{-1} for (d) and 2.1768×10^{-1} for (e). The inset shows a plot of $\ln T_{\rm K}^{QD1}$ against $(t - t_c)^{-1}$, where $\tilde{t}_c = 2.17671 \times 10^{-1}$ and we define $T_{\rm K}^{QD1}$ via $S_{\rm imp}(T_{\rm K}^{QD1}) = 0.5 \ln 6$, suitably between $\ln 3$ and $\ln 2$. T_{KT} is defined via $S_{\rm imp}(T_{KT}) = 0.5 \ln 18$ for line (a).

In the case where $\Gamma \neq \Gamma'$ the Hamiltonian does permit mixing between the doublet and quartet states, and as a result a Kosterlitz-Thouless transition is seen, rather than the first order quantum phase transition observed in the $\Gamma = \Gamma'$ case. There are two distinct cases we must consider here: the first is the USC/LM case, illustrated in Fig. 6.17. Here we see a simple Kosterlitz-Thouless transition, which occurs when $J \simeq J_{\rm RKKY}$, corresponding to $E_\Delta = 0$ in our low energy effective model, Eq. 6.20. At high temperature, the system is initially at the free orbital fixed point ($S_{\rm imp} = \ln 4^3$ and $T\chi_{\rm imp} = 3 \times \frac{1}{8}$, not shown): the empty and doubly occupied states of the dot become thermally inaccessible on an energy scale $T \sim U$, causing the entropy to flow to $\ln 8$ and $T\chi_{\rm imp}$ to $3 \times \frac{1}{4}$, characteristic of three free spins. On an energy scale $T \sim J$ the (+)-parity doublet is projected out, and the system flows to a fixed point with $S_{\rm imp} = \ln 6$ and $T\chi_{\rm imp} = \frac{11}{12}$, only the quartet and doublet states being retained in the low energy manifold. In Fig. 6.17 on an energy scale $T \sim T_{KT}$ (which we make no attempt to quantify) the system flows away from this fixed point to the USC fixed point ($S_{\rm imp} = \ln 3$ and $T\chi_{\rm imp} = \frac{2}{3}$): however in the case where $T_{\rm K}^{USC} > T_{KT}$ (not shown) the system flows to a transition fixed point

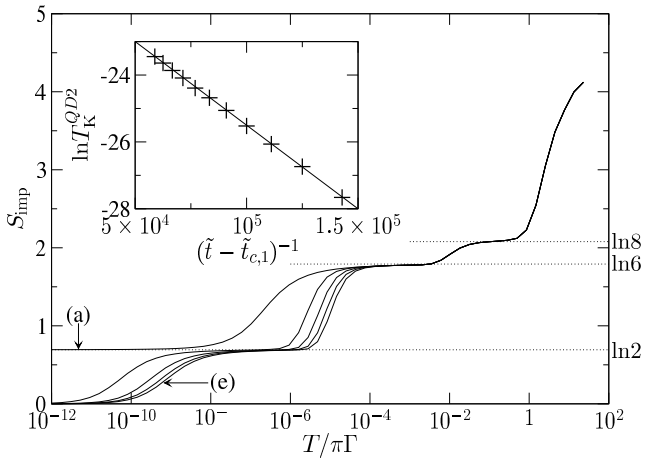


Figure 6.18: Entropy $S_{\rm imp}$ vs $T/\pi\Gamma$ for systems approaching the phase boundary between the LM and SC2 phases. $\tilde{U} = 10$, $\tilde{t}' = 10^{-1}$, $\Gamma = 10^{-2}D$ and $\Gamma' = 8 \times 10^{-3}D$. $\tilde{t}$ is varied with $\tilde{t} = 2.7552 \times 10^{-1}$ for (a), 2.7554×10^{-1} for (b), 2.7556×10^{-1} for (c), 2.7558×10^{-1} for (d) and 2.756×10^{-1} for (e). The inset shows a plot of $\ln T_{\rm K}^{QD2}$ against $(t - t_{c,1})^{-1}$, where $\tilde{t}_{c,1} = 2.75523 \times 10^{-1}$ ($\tilde{t}_c = 2.75516 \times 10^{-1}$) and we define $T_{\rm K}^{QD2}$ via $S_{\rm imp}(T_{\rm K}^{QD2}) = 0.5 \ln 2$.

characterised by $S_{\rm imp} = \ln 5$ and $T\chi_{\rm imp} = \frac{1}{2}$ on an energy scale $T \sim T_{\rm K}^{USC}$ before flowing to the USC fixed point on an energy scale $T \sim T_{KT}$. If the system lies in the region $t > t_c$ it will ultimately flow to the LM fixed point on an energy scale $T_{\rm K}^{QD1}$ (which we define via $S_{\rm imp}(T_{\rm K}^{QD1}) = 0.5 \ln 6$, suitably between $\ln 3$ and $\ln 2$), which vanishes exponentially as the phase boundary at $t = t_c$ is approached, as shown in the inset to Fig. 6.17. In the region $t > t_c$ the LM fixed point is therefore the ultimate low temperature fixed point of the system, whilst in the region $t < t_c$ the USC fixed point is the ultimate low temperature fixed point.

The second, and more complex, case is the USC/SC2 phase boundary. Here we apparently see two sequential Kosterlitz-Thouless transitions. The first transition, occurring at $t = t_c$, is effectively identical to that described above, and shown in Fig. 6.17; as the phase boundary is approached (from the doublet side) the energy scale $T_{\rm K}^{QD1}$, on which the entropy flows from $\ln 3$ to $\ln 2$, vanishes exponentially. The second transition, which occurs when $t = t_{c,1}$, is illustrated in Fig. 6.18. The behaviour down to a temperature $T \sim T_{KT}$ (where the entropy flows from $\ln 6$ to $\ln 2$) is very similar to that seen in Fig. 6.17 and Fig. 6.16, described above. Below

this temperature the system flows to the local moment fixed point ($S_{\rm imp} = \ln 2$ and $T\chi_{\rm imp} = 1/4$, not shown). If $t > t_{c,1}$ the system then flows to the SC2 fixed point on an energy scale $T \sim T_{\rm K}^{QD2}$, which vanishes exponentially as the phase boundary at $t = t_{c,1}$ is approached, as shown in the inset to Fig. 6.18. The stable fixed point of the system would therefore appear to be the local moment fixed point when $t_c < t < t_{c,1}$, indicating that the system enters a local moment phase in this region. However, t_c is typically extremely close to $t_{c,1}$ in parameter space: for example, in the system shown in Fig. 6.18 we find that $\tilde{t}_c = 2.75516 \times 10^{-1}$ and $\tilde{t}_{c,1} = 2.75523 \times 10^{-1}$, and the 'local moment phase' therefore has a width of 7×10^{-6} in units of $\pi\Gamma$. As there is an inherent uncertainty in our determination of the position of the phase boundary when a Kosterlitz-Thouless transition occurs (as discussed in Sec 5.4.1) we cannot state with certainty that $t_c \neq t_{c,1}$: the apparent 'local moment phase' may be a product of our inability to accurately determine t_c.

6.6.3 Dynamics

We now consider the dynamic properties of the trimer in parallel, concentrating upon the single particle spectrum, $\pi\Gamma_s D_{s\sigma}(\omega)$, and the differential conductance which may be derived from it, just as we did for the apex coupled trimer model.

6.6.3.1 The Underscreened Phase

In the USC phase the ground state quartet is underscreened by coupling to the conduction band on an energy scale $T_{\rm K}^{USC}$, giving rise to a triplet state. This underscreening gives rise to an enhanced conductance at temperatures below $T_{\rm K}^{USC}$, as shown in Fig. 6.19 (for the parameters used in Fig. 6.19 $T_{\rm K}^{USC} = T_{\rm K}$). The Kondo resonance here does not have the same functional form as the resonance seen for the SIAM (Fig. 3.7) — rather a more gradual approach to the unitarity limit is seen, which takes the form $\pi\Gamma_s D_{s\sigma}(\omega) = 1 - a/\ln^2(\omega/T_0)$ at small ω, approaching the unitarity fixed point with logarithmic corrections, as is expected for an under-

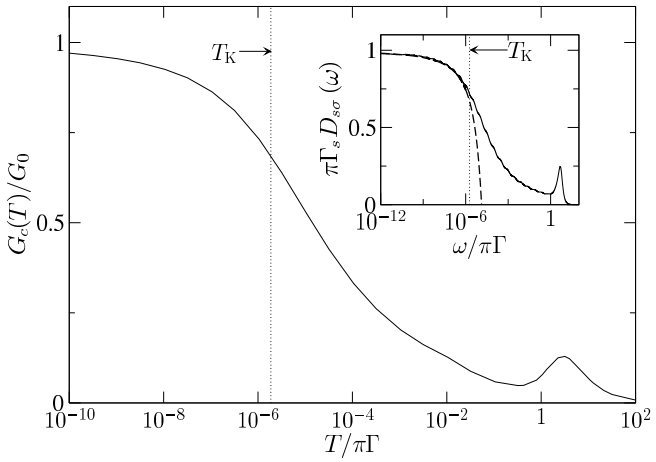


Figure 6.19: The conductance through a TQD device in the USC phase. $\tilde{U} = 10$, $\tilde{t}' = \tilde{t} = 10^{-1}$ and $\Gamma = \Gamma' = 10^{-2}D$. The inset shows the $T = 0$ single particle spectrum, $\pi\Gamma_s D_{s\sigma}(\omega)$, for the same system, and $T_{\rm K}(= T_{\rm K}^{USC})$, the Kondo temperature, is shown in both graphs. The dashed line on the inset is $\pi\Gamma_s D_{s\sigma}(\omega) = 1 - a/\ln^2(\omega/T_0)$.

screened spin-$\frac{3}{2}$ [21,126,127] — although the ultimate zero-temperature conductance is the same in both cases. Similar behaviour is seen in the zero-temperature single particle spectrum, $\pi\Gamma_s D_{s\sigma}(\omega)$, (inset to Fig. 6.19) which rises to the unitarity limit on an energy scale $\omega \sim T_{\rm K}^{USC}$. We generically find (via direct calculation using the NRG) that the Luttinger integral $I_{\rm L} = \mathrm{Im}\,\mathrm{Tr}\int_{-\infty}^{0} d\omega \frac{\partial \mathbf{\Sigma}_\sigma}{\partial \omega}\mathbf{G}_\sigma = 0$ in this phase, and so Eq. 6.11 may be used to determine the zero-temperature conductance.

6.6.3.2 The SC1 and SC2 Phases

Both the SC1 and SC2 phases exhibit a conductance extremely similar to that seen in the strong coupling phase of regime II of the apex coupled trimer model (see Sec. 4.6.3), and to that of the Anderson model (see Sec. 3.7). We find that the conductance rises to the unitarity limit on an energy scale $T \sim T_{\rm K}^{SC1} \simeq T_{\rm K}$ in the SC1 phase, and $T \sim T_{\rm K}^{SC2}$ in the SC2 phase, and that the Kondo resonance has the same functional form as in the single impurity Anderson model, as shown in Fig. 6.20 (SC1) and Fig. 6.21 (SC2). The single particle spectrum, $\pi\Gamma_s D_{s\sigma}(\omega)$, exhibits similar behaviour, as shown in the insets to the figures. In both these examples $\Gamma = \Gamma'$, and we therefore expect from our low energy effective models (Eq. 6.15 and Eq. 6.16)

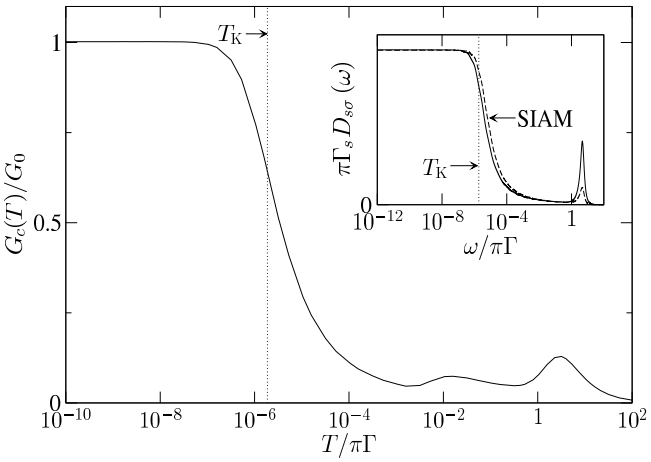


Figure 6.20: The conductance through a TQD deep within the SC1 phase, with $\tilde{U} = 10$, $\tilde{t} = 10^{-1}$, $\tilde{t}' = 4 \times 10^{-1}$ and $\Gamma = \Gamma' = 10^{-2}D$. The inset shows the $T = 0$ single particle spectrum, $\pi\Gamma_s D_{s\sigma}(\omega)$, for the same system, as well as the $T = 0$ single particle spectrum ($\pi\Gamma D_\sigma(\omega)$) for a SIAM with the same values of Γ and U.

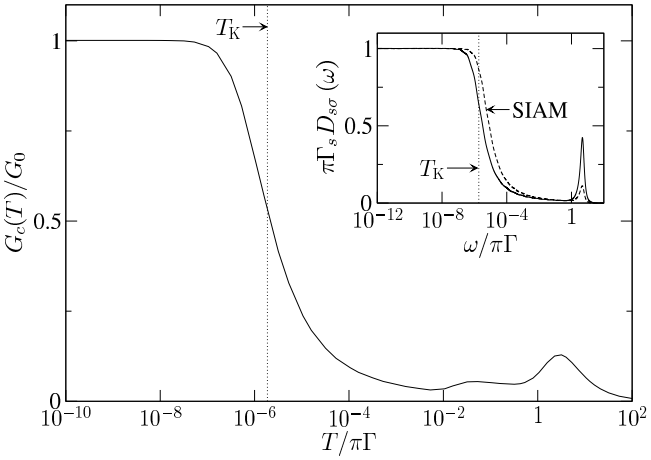


Figure 6.21: The conductance through a TQD deep within the SC2 phase, with $\tilde{U} = 10$, $\tilde{t} = 4 \times 10^{-1}$, $\tilde{t}' = 10^{-1}$ and $\Gamma = \Gamma' = 10^{-2}D$. The inset shows the $T = 0$ single particle spectrum, $\pi\Gamma_s D_{s\sigma}(\omega)$, for the same system, as well as the $T = 0$ single particle spectrum ($\pi\Gamma D_\sigma(\omega)$) for a SIAM with the same values of Γ and U.

that $T_K^{SC1} = T_K^{SC2} = T_K$. However, as we can see from the insets to Fig. 6.20 and Fig. 6.21 although T_K does give the scale upon which an enhancement of the low temperature conductance is seen, the spectra at low frequency ($\omega \lesssim T_K$) are not exactly coincident with the corresponding SIAM, contrary to what one would expect; as we discuss in Sec. 6.8, this is a result of the TQD approaching the boundary between the spin and orbital regimes (see Fig. 6.2). It is generically found that the

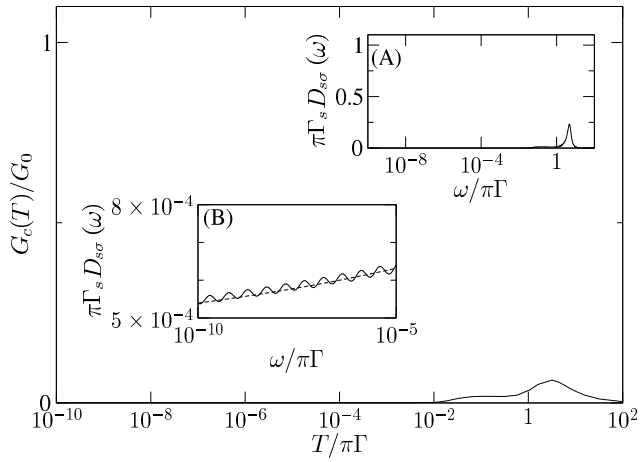


Figure 6.22: The conductance through a TQD deep within the LM phase, with $\tilde{U} = 10$, $\tilde{t} = 4 \times 10^{-1}$, $\tilde{t}' = 10^{-1}$, $\Gamma = 10^{-2}D$ and $\Gamma' = 2 \times 10^{-3}D$. Inset (A) shows the $T = 0$ single particle spectrum, $\pi\Gamma_s D_{s\sigma}(\omega)$, for the same system, whilst inset (B) shows the low frequency region of the spectrum in more detail. The dashed black line is $D_{s\sigma} \sim 1/[\ln(\omega/T_0)]^2$.

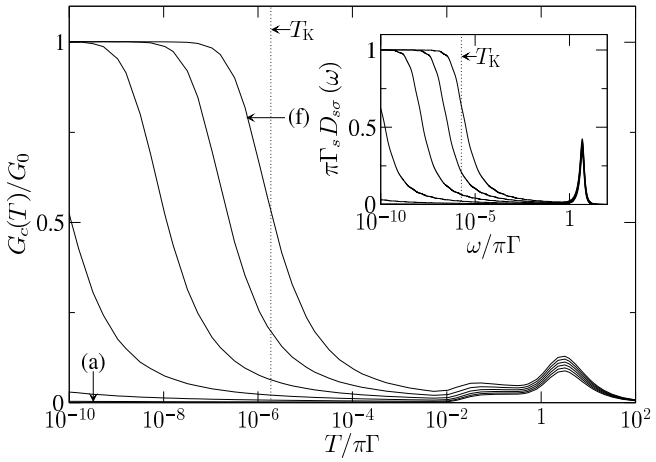


Figure 6.23: The conductance through a TQD approaching the phase boundary between the LM and SC2 phases, with $\tilde{U} = 10$, $\tilde{t} = 4\times10^{-1}$, $\tilde{t}' = 10^{-1}$ and $\Gamma = 10^{-2}D$. Γ' is varied with $\Gamma' = 5 \times 10^{-3}D$ for (a), $6 \times 10^{-3}D$ for (b), $7 \times 10^{-3}D$ for (c), $8 \times 10^{-3}D$ for (d), $9 \times 10^{-3}D$ for (e) and $10^{-2}D$ for (f). The inset shows the $T = 0$ single particle spectra, $\pi\Gamma_s D_{s\sigma}(\omega)$, for the same parameters.

Luttinger integral $I_{\rm L} = \mathrm{Im}\,\mathrm{Tr}\int_{-\infty}^{0} d\omega \frac{\partial \mathbf{\Sigma}_\sigma}{\partial \omega}\mathbf{G}_\sigma = 0$ in both the SC1 and SC2 phases here, as one would expect for a Fermi liquid, and so Eq. 6.11b may be used to determine the zero-temperature zero-bias conductance of the system.

6.6.3.3 The LM and SC2 Phases

The conductance in the LM phase is identical to that seen in the local moment phase of regime II of the apex coupled trimer model, that regime being the limiting case $J'_{\rm K} = 0$ of the trimer in parallel spin Hamiltonian, Eq. 6.5. We therefore see a conductance which decays to zero at zero temperature with logarithmic corrections, as discussed in Sec. 4.6.3 and shown in Fig. 6.22. Similar behaviour is seen in the single particle spectrum, $\pi\Gamma_s D_{s\sigma}(\omega)$, as shown in inset (A) to the figure; inset (B) shows detail on the low frequency region of the single particle spectrum, which decays to zero with logarithmic corrections; $D_{s\sigma}(\omega) \sim 1/[\ln(\omega/T_0)]^2$ (the dashed black line). We generically find that the Luttinger integral, $|I_{\rm L}| = |{\rm Im\,Tr}\int_{-\infty}^{0} d\omega \frac{\partial \mathbf{\Sigma}_\sigma}{\partial \omega}\mathbf{G}_\sigma| = \frac{\pi}{2}$ in the local moment phase ($I_{\rm L} = 0$ throughout both the strong coupling phases).

As discussed in Sec. 6.6.1.3 and 6.6.2.3 above, varying Γ' gives rise to a Kosterlitz-Thouless transition between the LM and SC2 phases. This naturally leads to a vanishing of the Kondo resonance seen in the SC2 phase as the transition is approached. This behaviour is illustrated in Fig. 6.23. The vanishing Kondo resonance is also observed in the zero-temperature single particle spectrum, $\pi\Gamma_s D_{s\sigma}(\omega)$, as shown in the inset to the figure.

6.6.3.4 The SC1/SC2 and SC1/LM Phase Boundaries

We consider first the SC1/SC2 phase boundary. In this case, as discussed in Sec. 6.6.3.2, the zero-temperature conductance rises to the unitarity limit on both sides of the phase boundary. We find that in the limiting case $\Gamma = \Gamma'$ the conductance as a function of temperature at the transition fixed point is indistinguishable from that in the SC1 and SC2 phases (conductance graphs which are coincident in that case as $T_{\rm K}^{SC1} = T_{\rm K}^{SC2}$). More interesting behaviour is seen in the case where $\Gamma \neq \Gamma'$; this leading of course to $T_{\rm K}^{SC1} > T_{\rm K}^{SC2}$ (see Eq. 6.15 and 6.16; we place an upper bound of Γ on the possible values of Γ' as we have throughout this chapter). At the transition fixed point (line (e) in Fig. 6.24) the conductance is seen to rise

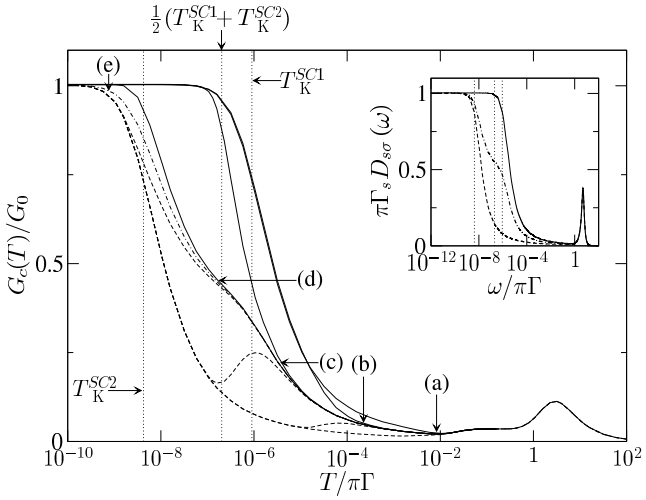


Figure 6.24: The zero-bias conductance through a TQD close to the SC1/SC2 phase boundary with $\tilde{U}=10$, $\tilde{t}=4\times10^{-1}$, $\Gamma=10^{-2}D$ and $\Gamma'=8\times10^{-3}D$. $\tilde{t}'$ is varied about $\tilde{t}'_c=3.81825\times10^{-1}$, with $\tilde{t}'=\tilde{t}'_c\pm\lambda$; $\lambda=2\times10^{-2}$ for (a), 2×10^{-4} for (b), 2×10^{-6} for (c), 2×10^{-8} for (d) and 0 for (e). The solid line denotes $\tilde{t}'=\tilde{t}'_c+\lambda$ and the dashed line $\tilde{t}'=\tilde{t}'_c-\lambda$. The scales $T_{\rm K}^{SC1}$, $T_{\rm K}^{SC2}$ and $\frac{1}{2}(T_{\rm K}^{SC1}+T_{\rm K}^{SC2})$ are also shown on the figure. The inset shows the $T=0$ single particle spectrum, $\pi\Gamma_s D_{s\sigma}(\omega)$, for the same system.

to a value of $G_c(T)/G_0\approx\frac{1}{2}$ on an energy scale $T_{\rm K}^{SC1}$, reflecting Kondo quenching of the (+)-parity doublet. A plateau in the conductance is then observed, which terminates at $T\sim T_{\rm K}^{SC2}$, the energy scale on which the (−)-parity doublet is Kondo quenched; at $T_{\rm K}^{SC2}$ the conductance rises to the unitarity limit. Systems close to the phase boundary (lines (b)-(e) of Fig. 6.24) flow close to the transition fixed point until an energy scale $T\sim|E_\Delta|$ is reached, at which point the higher energy doublet state is projected out and the system behaves as if it were deep in the SC1 or SC2 phase (depending upon the sign of E_Δ), exhibiting behaviour indistinguishable from that shown in Fig. 6.20 and Fig. 6.21. We note that for $|E_\Delta|\ll T_{\rm K}^{SC2}$ the conductance graph for both the SC1 and SC2 phases and at the transition fixed point is identical and so the conductance may not be used to distinguish the different phases on these (very small) energy scales.

It may initially appear that the conductance at the phase boundary, $G_c^{TFP}(T)=\frac{1}{2}(G_c^{SC1}(T)+G_c^{SC2}(T))$, an argument arising naturally from the Lehmann representation of the spectrum and Eq. 3.41, but this does not describe the conductance well in the region $T_{\rm K}^{SC2}<T<T_{\rm K}^{SC1}$ as in this region the (+)-parity doublet has been Kondo

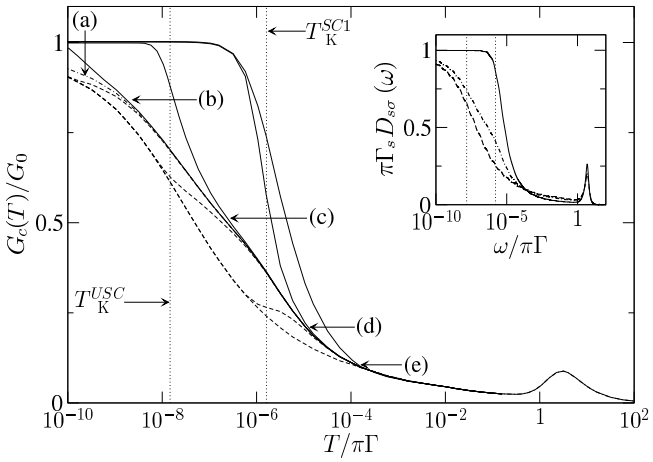


Figure 6.25: The zero-bias conductance through a TQD approaching the phase boundary between the SC1 and USC phases. $\tilde{U} = 10$, $\tilde{t} = 10^{-1}$, $\Gamma = 10^{-2}D$ and $\Gamma' = 5 \times 10^{-3}D$. $\tilde{t}'$ is varied about $\tilde{t}'_c \simeq 2.03521 \times 10^{-1}$, with $\tilde{t}' = \tilde{t}'_c \pm \lambda$: $\lambda = 0$ for (a), 2×10^{-9} for (b), 2×10^{-7} for (c), 2×10^{-5} for (d) and 2×10^{-3} for (e), with $\tilde{t}' = \tilde{t}'_c + \lambda$ plotted as solid lines, and $\tilde{t}' = \tilde{t}'_c - \lambda$ plotted as dashed lines. The inset shows the $T = 0$ single particle spectra, $\pi\Gamma_s D_{s\sigma}(\omega)$, for the same systems. $T_{\rm K}^{SC1}$ and $T_{\rm K}^{USC}$ are plotted in both the main figure and the inset.

quenched, whilst the $(-)$-parity doublet has not; the transition fixed point conductance in this region is therefore described by $G_c^{TFP}(T) = \frac{1}{3}(G_c^{SC1}(T) + 2G_c^{SC2}(T))$, reflecting the degeneracy of the two states within the low energy manifold in that temperature range.

As is shown in the inset to Fig. 6.24 the zero-temperature single particle spectrum, $\pi\Gamma_s D_{s\sigma}(\omega)$, deviates from that seen deep in the SC1 and SC2 phases only when the system lies exactly at the transition fixed point. The spectrum at the transition fixed point is well described by a weighted average of the spectra in the SC1 and SC2 phases, just as was the case for the conductance.

We again find that the behaviour of the TQD close to the SC1/LM phase boundary is identical to the behaviour of a system in regime II of the apex coupled trimer model; the conductance and single particle spectrum of a system in this region is described in detail in Sec. 4.6.3 and is therefore not repeated here.

6.6.3.5 The SC1/USC Phase Boundaries

In both the SC1 and USC cases the zero-temperature zero-bias conductance rises to the unitarity limit, but as discussed above the functional form of the conductance is different in the two phases, taking the characteristic functional form of the conductance in the SIAM in the SC1 case, and rising to the unitarity limit with the logarithmic corrections expected for an underscreened fixed point in the USC phase.

Close to the phase boundary we find that the conductance is described by the transition fixed point — line (a) in Fig. 6.25 — until an energy scale $T \sim |E_\Delta|$ is reached, at which point the system flows to the SC1 (if $E_\Delta > 0$) or USC (if $E_\Delta < 0$) fixed points (lines (b)-(e) in Fig. 6.25), the transition fixed point persisting to zero temperature only when $E_\Delta = 0$. We find that the transition fixed point conductance, initially small, rises to $G_c/G_0 \approx \frac{1}{2}$ on an energy scale $T \sim T_{\rm K}^{SC1}$ (when the (+)-parity doublet is screened), at which value it plateaus, before ultimately rising to the unitarity limit on an energy scale $T \sim T_{\rm K}^{USC}$ (when the quartet is underscreened).

Just as at the SC1/SC2 phase boundary, the conductance at the transition fixed point is described well by a weighted average of the conductance in the two phases[2]; $G_c^{TFP}(T) = \frac{1}{3}(G_c^{SC1}(T) + 2G_c^{USC}(T))$ when $T > T_{\rm K}^{SC1}$, $G_c^{TFP}(T) = \frac{1}{5}(G_c^{SC1}(T) + 4G_c^{USC}(T))$ when $T_{\rm K}^{USC} < T < T_{\rm K}^{SC1}$ and $G_c^{TFP}(T) = \frac{1}{4}(G_c^{SC1}(T) + 3G_c^{USC}(T))$ when $T < T_{\rm K}^{USC}$. This behaviour is illustrated in Fig. 6.25; as shown in the inset to that figure, the zero-temperature single particle spectrum, $\pi\Gamma_s D_{s\sigma}(\omega)$, deviates from that seen in the USC and SC1 phases far from the phase boundary only when $E_\Delta = 0$. The spectrum at the transition fixed point is well described by a weighted average of the spectra in the SC1 and USC phases, just as was the case for the conductance.

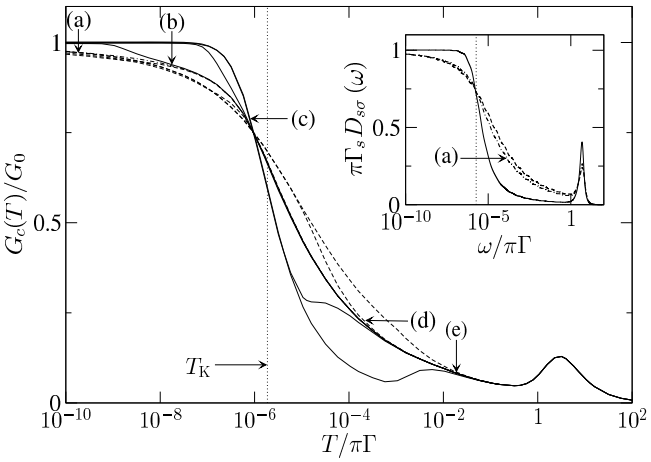


Figure 6.26: The zero-bias conductance through a TQD approaching the phase boundary between the SC2 and USC phases. $\tilde{U} = 10$, $\tilde{t}' = 10^{-1}$ and $\Gamma = \Gamma' = 10^{-2}D$. $\tilde{t}$ is varied about $\tilde{t}_c \simeq 3.08213 \times 10^{-1}$, with $\tilde{t} = \tilde{t}_c \pm \lambda$: $\lambda = 0$ for (a), 10^{-8} for (b), 10^{-6} for (c), 10^{-4} for (d) and 10^{-2} for (e); the solid black lines are $\tilde{t} = \tilde{t}_c + \lambda$, and the dashed lines $\tilde{t} = \tilde{t}_c - \lambda$. The inset shows the $T = 0$ single particle spectra, $\pi\Gamma_s D_{s\sigma}(\omega)$, for the same systems.

6.6.3.6 The SC2/USC and LM/USC Phase Boundaries

When $\Gamma = \Gamma'$, as discussed above (Sec. 6.6.1.6 and 6.6.2.6), the spin Hamiltonian conserves the total TQD spin, and as such the phase boundary between the USC and SC2 phases is found to be a first order quantum phase transition. The behaviour of the conductance close to the phase boundary is therefore very similar to that of the SC1/USC phase boundary, as discussed in the previous section and shown in Fig. 6.26: however as the two Kondo scales $T_{\rm K}^{USC}$ and $T_{\rm K}^{SC2}$ are the same (and equal to $T_{\rm K}$) no plateau in the conductance at $G_c(T)/G_0 \approx \frac{1}{2}$ is observed.

We find that the conductance at the transition is described well by $G_c^{TFP}(T) = \frac{1}{3}(G_c^{SC2}(T) + 2G_c^{USC}(T))$ when $T > T_{\rm K}$ and by $G_c^{TFP}(T) = \frac{1}{4}(G_c^{SC2}(T) + 3G_c^{USC}(T))$ when $T < T_{\rm K}$, as one would expect from the results of the previous section. Just as in that case, the system is described by the transition fixed point at zero temperature only when $E_\Delta = 0$, the system otherwise ultimately flowing away from the transition fixed point on an energy scale $T \sim |E_\Delta|$. This behaviour is illustrated in Fig. 6.26; the inset shows the corresponding zero-temperature single particle spec-

[2]Recall that we consider the parameter regime $\Gamma' \leq \Gamma$ and therefore $T_{\rm K}^{USC} \leq T_{\rm K}^{SC1}$.

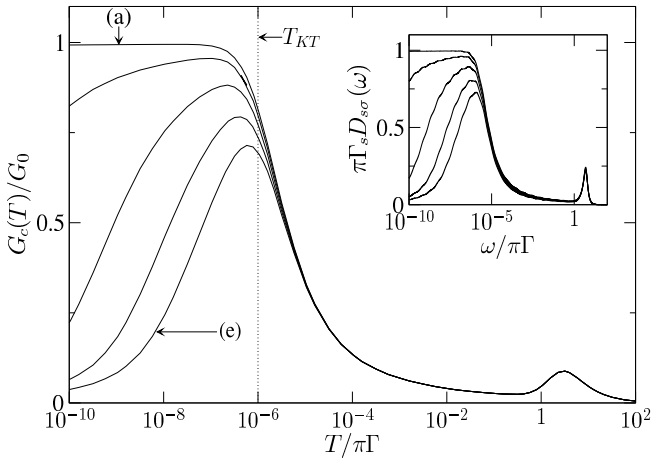


Figure 6.27: The zero-bias conductance through a TQD approaching the phase boundary between the LM and USC phases. $\tilde{U} = 10$, $\tilde{t'} = 10^{-1}$, $\Gamma = 10^{-2}D$ and $\Gamma' = 5 \times 10^{-3}D$. $\tilde{t}$ is varied with $\tilde{t} = 2.17672 \times 10^{-1}$ for (a), 2.17674×10^{-1} for (b), 2.17676×10^{-1} for (c), 2.17678×10^{-1} for (d) and 2.1768×10^{-1} for (e) ($\tilde{t}_c = 2.17671 \times 10^{-1}$). The inset shows the $T = 0$ single particle spectra, $\pi\Gamma_s D_{s\sigma}(\omega)$, for the same systems.

tra, $\pi\Gamma_s D_{s\sigma}(\omega)$, which exhibit similar behaviour, although the spectra deviate from that seen in the USC and SC2 phases only when $E_\Delta = 0$.

We next turn our attention to the more general case where $\Gamma \neq \Gamma'$. As discussed above, the phase boundary between the USC and LM phases takes the form of a line of Kosterlitz-Thouless transitions. As shown in Fig. 6.27, we find that the conductance rises towards the unitarity limit on an energy scale $T \sim T_{KT}$ (the energy scale at which the system flows to the USC fixed point), but as the phase boundary is approached the Kondo resonance vanishes, with the conductance falling to zero on a scale $T \sim T_{\rm K}^{QD1}$ (which we define via $S_{\rm imp}(T_{\rm K}^{QD1}) = 0.5 \ln 6$ — see Sec. 6.6.2.6), which vanishes as the phase boundary is approached. As a result, in this case cooling a system close to the phase boundary can lead to suppression of the Kondo effect and a decreased conductance. This behaviour is illustrated in Fig. 6.27; as shown in the inset to that figure, similar behaviour is seen in the single particle spectra, $\pi\Gamma_s D_{s\sigma}(\omega)$.

When $\Gamma \neq \Gamma'$ we find that the transition between the USC and SC2 phases is apparently a two-stage process, just as was the case in the thermodynamic data (Sec. 6.6.2.6). There is first a transition between the USC and LM phases, identi-

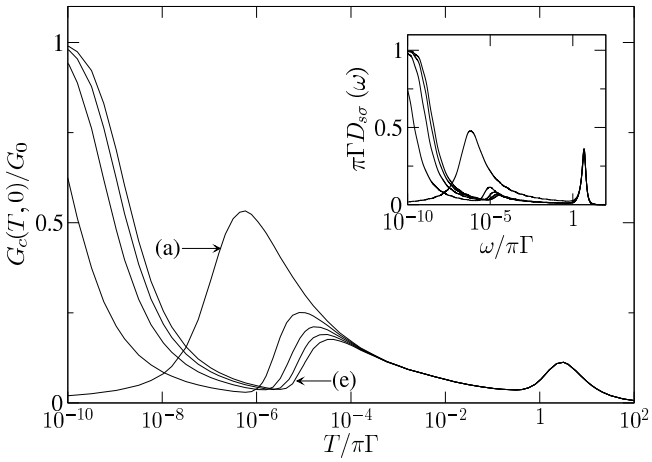


Figure 6.28: The zero-bias conductance for a system approaching the phase boundary between the LM and SC2 phases. $\tilde{U} = 10$, $\tilde{t}' = 10^{-1}$, $\Gamma = 10^{-2}D$ and $\Gamma' = 8 \times 10^{-3}D$. $\tilde{t}$ is varied with $\tilde{t} = 2.7552 \times 10^{-1}$ for (a), 2.7554×10^{-1} for (b), 2.7556×10^{-1} for (c), 2.7558×10^{-1} for (d) and 2.756×10^{-1} (e) ($\tilde{t}_{c,1} = 2.75523 \times 10^{-1}$). The inset shows the $T = 0$ single particle spectra, $\pi\Gamma_s D_{s\sigma}(\omega)$, for the same systems.

cal to that shown in Fig. 6.27, followed by a second Kosterlitz-Thouless transition between the LM and SC2 phases, as shown in Fig. 6.28, in which we find that the conductance initially increases on an energy scale T_{KT}, before decaying on an energy scale $T_{\rm K}^{QD1}$, and then finally increasing to the unitarity limit on an energy scale $T_{\rm K}^{QD2}$ (which we define via $S_{\rm imp}(T_{\rm K}^{QD2}) = 0.5 \ln 2$ — see Sec. 6.6.2.6). In this case we therefore see a conductance of $G_c(T = 0)/G_0 = 1$ on either side of the transition, but which appears to fall to zero in the immediate vicinity of the phase boundary (when $t_c < t < t_{c,1}$).

6.7 The Orbital Regime

We now consider the orbital regime of the trimer in parallel (see Fig. 6.2) — a weakly interacting regime ($t \sim \mathcal{O}(U)$ or larger) where the effective spin model $\hat{H}_{spin}$ is no longer valid. As we shall see, this regime is equivalent to regime III of the apex coupled trimer model, discussed in Sec. 4.8. We concentrate on the region close to the phase boundary ($t' \leq U$), and aim to provide intuitive physical arguments for the low energy effective model in this regime (Eq. 6.24) and the phase boundary

associated with it.

6.7.1 Effective Low Energy Model

Deep within the orbital regime $t \gg U$, and so a natural starting point for understanding the physics of this system is provided by the non-interacting TQD, described by the Hamiltonian $\hat{H}_{NITiP} = \hat{H}_{NITQD} + \hat{H}_{hyb} + \hat{H}_L$, where $\hat{H}_{NITQD}$ is $\hat{H}_{TQD}$ (as given in Eq. 6.2) with $\tilde{U} = 0$, and we no longer require that $\epsilon = -U/2$ (although we do specify that $t \gg |\epsilon|, t'$);

$$\hat{H}_{NITQD} = \sum_{\sigma,i=1,2,3} \epsilon \hat{n}_{i\sigma} + \sum_{\sigma} t[(c^{\dagger}_{1\sigma} + c^{\dagger}_{3\sigma})c_{2\sigma} + H.c] + \sum_{\sigma} t'(c^{\dagger}_{1\sigma}c_{3\sigma} + H.c.). \quad (6.22)$$

Eq. 6.22 is, of course, identical to Eq. 4.18. As described in detail in Sec. 4.8.1, $\hat{H}_{NITQD}$ may be written as a three level system, where the three levels, l, o and u, are defined such that $E_l < E_o < E_u$. $E_o = \epsilon - t'$, and so the o level lies closest to the Fermi level. The ground state of $\hat{H}_{TQD}$ is then the four electron singlet state of $(+)$-parity, $|0;+;0\rangle = c^{\dagger}_{o\uparrow}c^{\dagger}_{o\downarrow}c^{\dagger}_{l\uparrow}c^{\dagger}_{l\downarrow}|Vac\rangle$, with the lowest lying excited state being a three electron doublet of $(-)$-parity, $|\frac{1}{2};-;\sigma\rangle = c^{\dagger}_{o\sigma}c^{\dagger}_{l\uparrow}c^{\dagger}_{l\downarrow}|Vac\rangle$. Taking account of electron-electron correlations by treating $\hat{H}_U = \sum_i U\hat{n}_{i\uparrow}\hat{n}_{i\downarrow}$ as a perturbation to these states to first order, as described in Sec. 4.8.1 and Appendix D, we find that the three electron doublet state is stabilised, such that it is the ground state when $E'_{\Delta} = \epsilon - t' + \frac{U}{2}(1+\gamma^2) > 0$ (see Eq. 4.26 and 4.23). When $E'_{\Delta} < 0$, on the other hand, the four electron singlet is the ground state of the TQD. As these states have distinct parities, mixing between them is forbidden.

The behaviour of the system as described so far is identical to that of the ACTM in regime III (Sec. 4.8). Indeed, the only difference between the ACTM and the TiP model in this regime is found in the coupling between the TQD and the conduction

band:

$$\hat{H}_{hyb} = \sum_{\mathbf{k},\sigma}[(V\nu + \sqrt{2}V'\gamma)c^{\dagger}_{l\sigma}c_{\mathbf{k}\sigma} + H.c.] + \sum_{\mathbf{k},\sigma}[(\sqrt{2}V'\nu - \gamma V)c^{\dagger}_{u\sigma}c_{\mathbf{k}\sigma} + H.c.], \quad (6.23)$$

where γ and ν are defined in Eq. 4.23. This has a significant effect upon the low temperature physics of the system when a magnetic field is applied to the TQD in this regime (discussed in Sec. 6.11), but no effect upon the physics of the system in the absence of a field, as the o orbital is still decoupled from the conduction band. In the limit $t \gg U$ the doublet state is therefore effectively decoupled from the conduction band; as discussed in Sec. 6.8 we find that when not in that limit, the doublet state couples ferromagnetically to the conduction band. If the singlet state is the ground state, we naturally expect the system to flow to the frozen impurity fixed point at low temperature. The low energy effective model then follows naturally (using identical arguments to Sec. 4.8.1) as

$$\hat{H}_{\text{eff}} = -\frac{|J^{\ddagger}_{\text{K}}|}{2}(1 - 2\hat{\mathcal{T}}^z)\hat{\mathbf{S}} \cdot \hat{\mathbf{S}}(0) + E'_{\Delta}\hat{\mathcal{T}}^z + \hat{H}_L, \quad (6.24)$$

where $\hat{\mathbf{S}}$ is a spin-$\frac{1}{2}$ operator for the TQD as a whole, $-|J^{\ddagger}_{\text{K}}|$ is a weak ferromagnetic coupling which may be quantified using second order perturbation theory in V and V' (as described in Sec. 6.8), and we define a pseudospin, $\hat{\mathcal{T}}^z = \frac{1}{2}(|0;+;0\rangle\langle 0;+;0| - \sum_{S^z}|\frac{1}{2};-;S^z\rangle\langle\frac{1}{2};-;S^z|)$, such that $|0;+;0\rangle$ and $|\frac{1}{2};-;S^z\rangle$ are eigenstates of $\hat{\mathcal{T}}^z$ with eigenvalues $\pm\frac{1}{2}$, respectively. As was the case for Eq. 4.29 the Hamiltonian may be separated into distinct pseudospin sectors, reflecting the strict conservation of $1 \leftrightarrow 3$ parity. E'_{Δ} acts as an effective field upon the pseudospin, picking out the parity sector containing the ground state: this is the $(+)$-parity singlet when $E'_{\Delta} < 0$ and the $(-)$-parity doublet when $E'_{\Delta} > 0$. The singlet corresponds to the frozen impurity fixed point ($S_{\text{imp}} = 0$ and $T\chi_{\text{imp}} = 0$), whilst the doublet is ferromagnetically coupled to the conduction band, giving rise to a free local moment ($S_{\text{imp}} = \ln 2$ and $T\chi_{\text{imp}} = 1/4$) at low temperature. When $E'_{\Delta} = 0$ the system undergoes a first

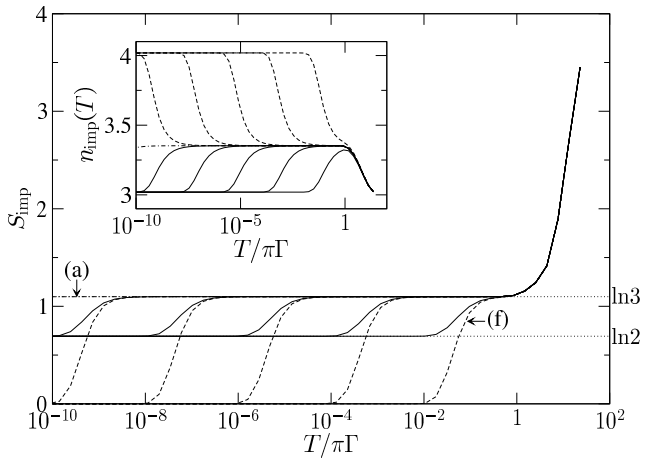


Figure 6.29: Entropy $S_{\rm imp}$ vs $T/\pi\Gamma$ for systems approaching the phase boundary in the orbital regime; $\tilde{U} = 10$, $\tilde{t} = 20$ and $\Gamma = \Gamma' = 10^{-2}D$. $\tilde{t}'$ is varied about $\tilde{t}'_c \simeq 2.44049$, with $\tilde{t}' = \tilde{t}'_c \pm \lambda$; $\lambda = 0$ for (a), 10^{-9} for (b), 10^{-7} for (c), 10^{-5} for (d), 10^{-3} for (e) and 10^{-1} for (f). Solid lines indicate $\tilde{t}' = \tilde{t}'_c - \lambda$ and dashed lines $\tilde{t}' = \tilde{t}'_c + \lambda$. The inset shows the electron population of the TQD, $n_{\rm imp}(T)$, for the same systems.

order quantum phase transition, and the full Eq. 6.24 is required to describe the system. This system is characterised here by a transition fixed point ($S_{\rm imp} = \ln 3$ and $T\chi_{\rm imp} = 1/6$), which reflects the degeneracy of the singlet and doublet states: the transition fixed point persists to zero temperature only in the limit $E'_\Delta = 0$. In all other cases, the system flows away from the transition fixed point when $T \sim |E_\Delta|$. In addition, Eq. 6.24 predicts that the phase boundary between the strong coupling and local moment phases of the orbital regime should follow the line $\epsilon - t' + \frac{U}{2}(1+\gamma^2) = 0$, corresponding to $t' = U/4$ in the limit of large t: as we can see from Fig. 6.2, 6.3 and 6.4 this is an accurate description of the phase boundary.

6.7.2 Thermodynamics

As we find that the low energy effective model in the orbital regime (Eq. 6.24) is identical to that in regime III of the apex coupled trimer model (Eq. 4.29) we expect to see identical behaviour at low temperature; as illustrated in Fig. 6.29 and Fig. 6.30 we find that this is indeed the case in both the $\Gamma = \Gamma'$ and $\Gamma \neq \Gamma'$ cases; compare these figures with Fig 4.16 and Fig. 4.17. After flowing away from the free

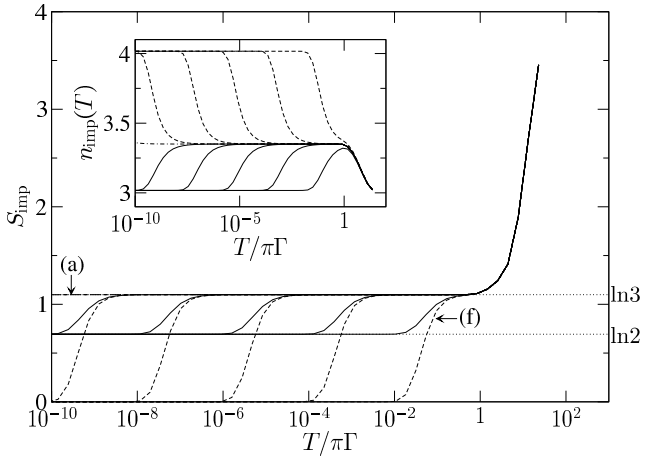


Figure 6.30: Entropy $S_{\rm imp}$ vs $T/\pi\Gamma$ for systems approaching the phase boundary in the orbital regime; $\tilde{U} = 10$, $\tilde{t} = 20$, $\Gamma = 10^{-2}D$ and $\Gamma' = 8 \times 10^{-3}D$. $\tilde{t}'$ is varied about $\tilde{t}'_c \simeq 2.4388$, with $\tilde{t}' = \tilde{t}'_c \pm \lambda$; $\lambda = 0$ for (a), 10^{-9} for (b), 10^{-7} for (c), 10^{-5} for (d), 10^{-3} for (e) and 10^{-1} for (f). Solid lines indicate $\tilde{t}' = \tilde{t}'_c - \lambda$ and dashed lines $\tilde{t}' = \tilde{t}'_c + \lambda$. The inset shows the electron population of the TQD, $n_{\rm imp}(T)$, for the same systems.

orbital fixed point ($S_{\rm imp} = \ln 64$ and $T\chi_{\rm imp} = \frac{3}{8}$, not shown) on an energy scale $T \sim t$, the system flows close to the transition fixed point ($S_{\rm imp} = \ln 3$, $T\chi_{\rm imp} = \frac{1}{6}$ and $n_{\rm imp} = \frac{10}{3}$) until an energy scale $T \sim E_\Delta$ is reached, at which point the system flows to the frozen impurity fixed point (if $E_\Delta < 0$), or the local moment fixed point (if $E_\Delta > 0$). We find that the the frozen impurity fixed point is characterised by $S_{\rm imp} = 0$, $T\chi_{\rm imp} = 0$ and $n_{\rm imp} = 4$, and the local moment fixed point by $S_{\rm imp} = \ln 2$, $T\chi_{\rm imp} = 1/4$ and $n_{\rm imp} = 3$. The transition fixed point, which persists to zero temperature only when $E_\Delta = 0$, is characterised by $S_{\rm imp} = \ln 3$, $T\chi_{\rm imp} = \frac{1}{6}$ and $n_{\rm imp} = 10/3$ as the singlet and doublet states are degenerate here.

6.7.3 Dynamics

Just as was the case for the thermodynamic properties, we find that the dynamic properties of the orbital regime are very similar to those of regime III of the apex coupled trimer model (see Sec. 4.8.3). We generically find that the Luttinger integral, $I_{\rm L} = {\rm Im\,Tr} \int_{-\infty}^{0} d\omega \frac{\partial \mathbf{\Sigma}_\sigma}{\partial \omega} \mathbf{G}_\sigma = 0$ in the strong coupling phase and $|I_{\rm L}| = \frac{\pi}{2}$ in the local moment phase and, as discussed above, $n_{\rm imp} = 4$ in the strong coupling phase and

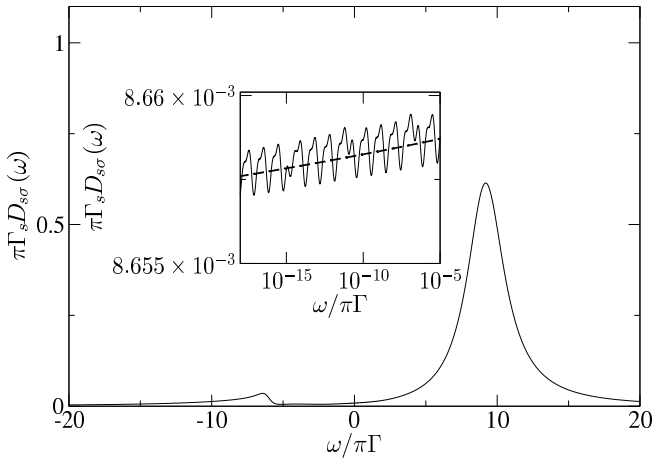


Figure 6.31: The $T = 0$ single particle spectrum, $\pi\Gamma D_{s\sigma}(\omega)$, for a system in the local moment phase of the orbital regime. $\tilde{U} = 10$, $\tilde{t} = 5$, $\tilde{t}' = 2.4$ and $\Gamma = \Gamma' = 10^{-2}D$. The inset shows the low frequency behaviour, fitted to a line of form $\pi\Gamma_s D_{s\sigma}(\omega) = a/\ln^2(|\omega|/T_0)$.

3 in the local moment phase. Using these results in combination with Eq. 6.11, we naturally expect to find that $G_c(0)/G_0 = 0$ and $\pi\Gamma_s D_{s\sigma}(\omega) = 0$ in *both* the local moment and strong coupling phases here, and this is indeed what we observe. Just as in Sec. 4.8.3, however, we find that the approach to $\pi\Gamma_s D_{s\sigma}(\omega = 0) = 0$ is characterised by logarithmic corrections in the local moment phase, as shown in the inset to Fig. 6.31, which are absent in the corresponding case for the strong coupling phase, and also that the positive and negative frequency Hubbard satellites are no longer equivalent, as the full model Hamiltonian, unlike the effective spin model, is not particle-hole symmetric. This behaviour is illustrated in Fig. 6.31.

6.8 The Intermediate Regime

We now consider the behaviour of the TQD device in the intermediate regime — between the spin and orbital regimes (see Fig. 6.2) — in more detail. We concentrate upon the phase transition between the SC2 and LM phases seen when $t \approx U/4$ and $\Gamma' > \frac{1}{4}\Gamma$ — as seen in the phase diagrams Fig. 6.2 and 6.3. In both the SC2 phase and the local moment phase of the orbital regime, the ground state of $\hat{H}_{TQD}$ is a doublet of $(-)$-parity with three electrons on the TQD; we label this state $|\frac{1}{2}; -; S^z\rangle$.

Projecting into the low energy manifold where only the doublet state is accessible (and so the unity operator for the reduced Hilbert space of the low energy manifold is $\hat{1} = \sum_{S^z} |\frac{1}{2}; -; S^z\rangle\langle\frac{1}{2}; -; S^z|$), a Schrieffer-Wolff transformation [13] may be used to generate an effective spin model for the system,

$$\hat{H}_{eff} = \hat{1}\hat{H}_{hyb}(E_0 - \hat{H}_0)^{-1}\hat{P}\hat{H}_{hyb}\hat{1} + \hat{H}_L, \tag{6.25}$$

just as in Sec. 4.8.1. Here $\hat{H}_0 = \hat{H}_{TQD} + \hat{H}_L$, $\hat{P} = \hat{1}_{full} - \hat{1}$, where $\hat{1}_{full}$ is the unity operator for the complete Hilbert space, and E_0 is the energy of $|\frac{1}{2}; -; S^z\rangle$ under $\hat{H}_0$. We find that $\hat{H}_{eff}$ can be written as a simple (isotropic) Kondo model,

$$\hat{H}_{eff} = J_{\mathrm{K}}^{\ddagger}\hat{\mathbf{S}} \cdot \hat{\mathbf{S}}(0) + \hat{H}_L, \tag{6.26}$$

where the value of $J_{\mathrm{K}}^{\ddagger}$ may be determined numerically, as described in Appendix E. This calculation, being conducted only to second order, obviously neglects the effect of RKKY interactions between neighbouring dots (which are fourth order processes), but as we concentrate on the region close to the phase boundary between the SC2 and LM phases, where $t \sim U$ (and $U \gg \Gamma$), one would not expect the RKKY interactions to have a significant effect upon the physics of the system.

Fig. 6.32 shows the results of these second order perturbation theory calculations. The two limiting cases here are $\Gamma' = \Gamma$ (line (a)) and $\Gamma' = 0$ (line (k)). In the $\Gamma' = \Gamma$ case we find that for small $\tilde{t}$ ($t \ll U$) $J_{\mathrm{K}}^{\ddagger} = J_{\mathrm{K}}$, in agreement with Eq. 6.16, but as $\tilde{t}$ approaches U we see a continuous fall in the value of $J_{\mathrm{K}}^{\ddagger}$, which eventually becomes negative, before increasing again and approaching zero asymptotically as $t \to \infty$ (as one would expect from the discussion of the local moment phase of the orbital regime in Sec. 6.7.1). As $J_{\mathrm{K}}^{\ddagger}$ changes continuously from antiferromagnetic to ferromagnetic coupling here we anticipate a Kosterlitz-Thouless transition will be observed. In the $\Gamma' = 0$ case, by contrast, the coupling of the doublet state to the conduction band is always ferromagnetic, although the magnitude of this coupling changes,

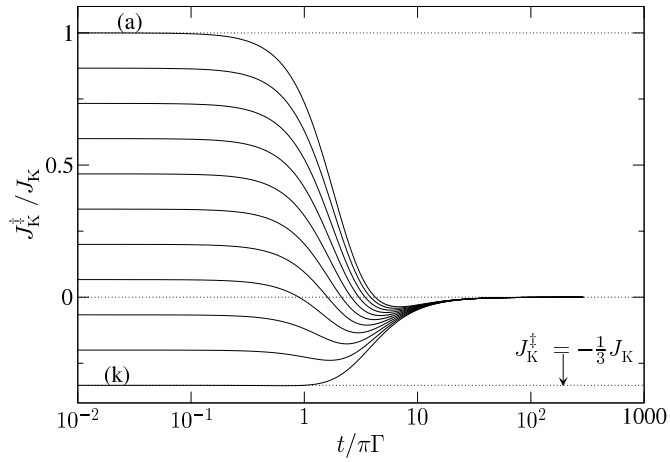


Figure 6.32: Perturbation theory results for the variation of $J_{\rm K}^{\ddagger}/J_{\rm K}$ as a function of $\tilde{t}$ for systems with $\tilde{U} = 10$, $\tilde{t}' = 10^{-2}$ and $\Gamma = 10^{-2}D$. Γ' is varied in equal steps of $10^{-3}D$ between $10^{-2}D$ (line (a)) and 0 (line (k)).

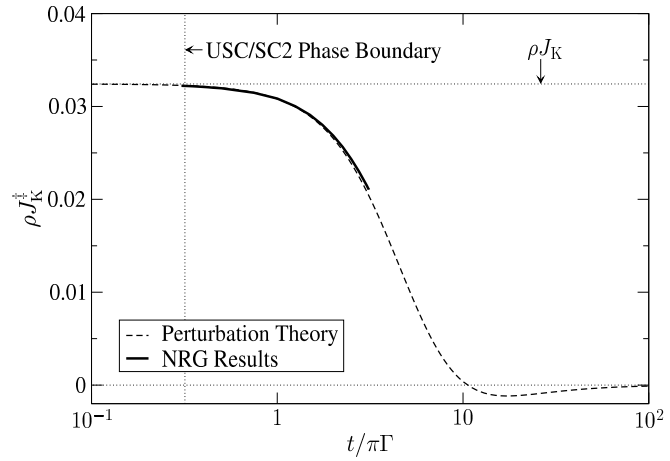


Figure 6.33: $\rho J_{\rm K}^{\ddagger}$ as a function of $\tilde{t}$ for a system with $\tilde{U} = 25$, $\tilde{t}' = 2.5 \times 10^{-2}$ and $\Gamma = \Gamma' = 4 \times 10^{-3}D$. The results of both perturbation theory (dashed line) and the NRG (solid line) are shown on the figure, along with the value of $J_{\rm K}$. The value of $J_{\rm K}^{\ddagger}$ is determined from the NRG results using the relationship $\ln T_{\rm K}^{SC2} = -\frac{1}{\rho J_{\rm K}^{\ddagger}} + A$.

again approaching zero asymptotically in the limit of large t. This behaviour was discussed in Sec. 4.8.1. For values of Γ' intermediate between these two limits we see a continuous decline in the value of $J_{\rm K}^{\ddagger}$ at small t — exactly as one would expect from Eq. 6.16 — and when $\Gamma' < \Gamma/4$ the coupling is ferromagnetic for all t.

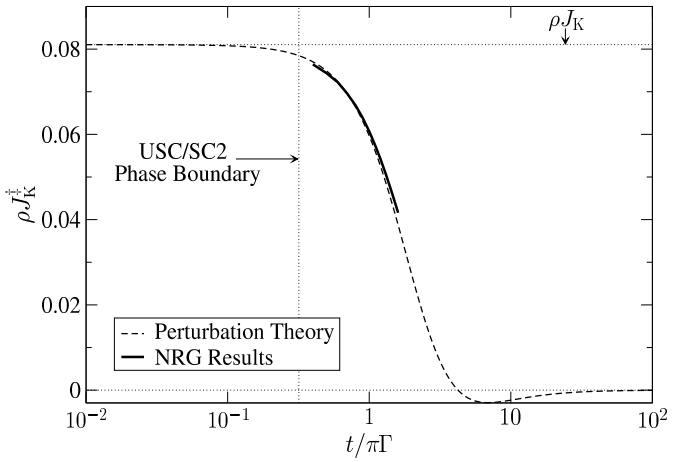


Figure 6.34: $\rho J_{\rm K}^{\ddagger}$ as a function of $\tilde{t}$ for a system with $\tilde{U} = 10$, $\tilde{t}' = 10^{-2}$ and $\Gamma = \Gamma' = 10^{-2}D$. The results of both perturbation theory (dashed line) and the NRG (solid line) are shown on the figure, along with the value of $J_{\rm K}$. The value of $J_{\rm K}^{\ddagger}$ is determined from the NRG results using the relationship $\ln T_{\rm K}^{SC2} = -\frac{1}{\rho J_{\rm K}^{\ddagger}} + A$.

6.8.1 Thermodynamics

Fig. 6.33 and 6.34 show $\rho J_{\rm K}^{\ddagger}$ as a function of $\tilde{t}$ for two systems with the same value of U/D and t'/D, but different values of $\Gamma = \Gamma'$. Both the $J_{\rm K}^{\ddagger}$ calculated directly using second order perturbation theory and the $J_{\rm K}^{\ddagger}$ which may be derived from the NRG using the relationship $T_{\rm K}^{SC2} \propto \exp(-1/\rho J_{\rm K}^{\ddagger})$ are shown: there is a good agreement between the two values. In addition, Fig. 6.34 helps to explain the apparent inconsistency noted in Sec. 6.6.2.2 that in the limit $\Gamma = \Gamma'$ we do not generically find that $T_{\rm K}^{SC2} = T_{\rm K}$, in (apparent) contradiction of our low energy effective model. The explanation is simple however: the energy scale on which the transition between the USC and SC2 phases occurs is very close to the energy scale of the intermediate regime, as is shown on the figure. This means that in the parameter space where the SC2 phase is accessible the effective coupling $J_{\rm K}^{\ddagger}$ has already begun to flow away from it's small-t value ($J_{\rm K}$ in the $\Gamma = \Gamma'$ case). As shown in Fig. 6.33 this problem disappears if much smaller values of Γ and Γ' are used, as this increases the energy separation between the USC/SC2 and SC2/LM (intermediate regime) phase boundaries, allowing the region where $T_{\rm K}^{SC2} = T_{\rm K}$ to be accessed. However, smaller values of Γ also lead to much smaller Kondo scales, and

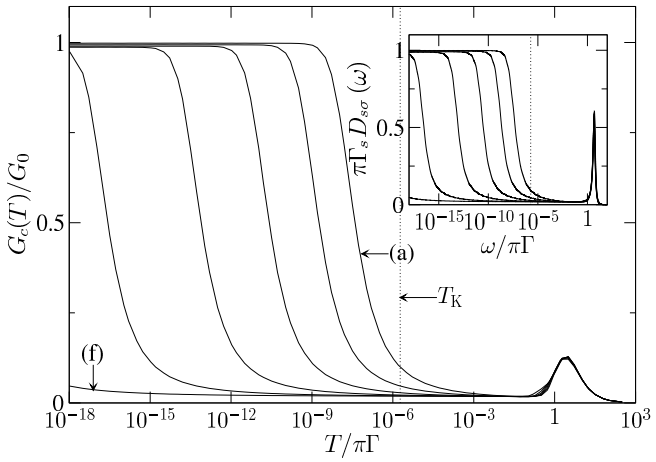


Figure 6.35: The zero-bias conductance for systems approaching the phase boundary between the spin and orbital regimes. $\tilde{U} = 10$, $\tilde{t}' = 10^{-1}$ and $\Gamma = \Gamma' = 10^{-2}D$. $\tilde{t}$ is varied, with $\tilde{t} = 1$ for (a), 1.25 for (b), 1.5 for (c), 1.75 for (d), 2 for (e) and 2.25 for (f). The inset shows the $T = 0$ single particle spectra, $\pi\Gamma_s D_{s\sigma}(\omega)$, for the same systems.

therefore increase the difficulty of observing the lowest temperature physics of the system. It is because of this that we typically consider systems with $\Gamma \sim \mathcal{O}(10^{-2}D)$.

In addition, as shown in Fig. 6.2, 6.3 and 6.4, we may use our perturbation theory results for $J_K^\ddagger$ to predict the position of the phase boundary between the SC2 phase and the local moment phase of the orbital regime (which should be found when $J_K^\ddagger = 0$). As seen in those figures, the shape of the phase boundary is predicted accurately, although there is an apparent small error in the position; however the phase boundary here is found to be a line of Kosterlitz-Thouless transitions, and as discussed above (Sec. 5.4.1) we generally find that this gives rise to an uncertainty in our determination of the position of the phase boundary; in addition, as discussed above, RKKY interactions are neglected here. As a result, a slight discrepancy between the results of perturbation theory and the NRG is not unexpected.

6.8.2 Dynamics

The Kosterlitz-Thouless transition observed between the SC2 phase and the local moment phase of the orbital regime is associated with a vanishing of the Kondo resonance in the zero-bias conductance of the system, as illustrated in Fig. 6.35; similar

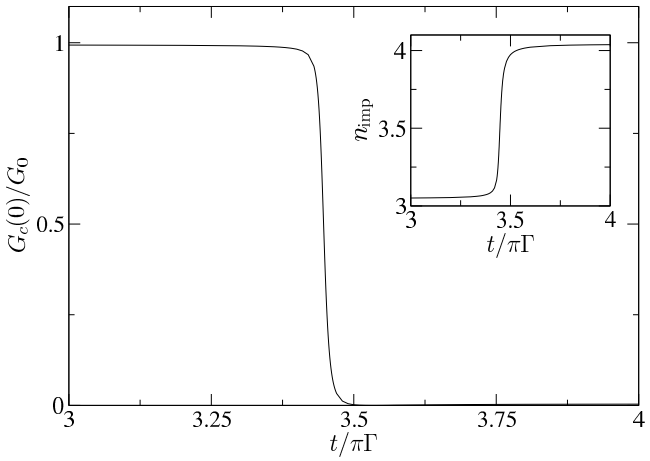


Figure 6.36: The zero-temperature zero-bias conductance as a function of $\tilde{t}$ for a system crossing between the SC1 phase and the strong coupling phase of the orbital regime; $\tilde{U} = 10$, $\tilde{t}' = 6$, $\Gamma = 10^{-2}D$ and $\Gamma' = 8 \times 10^{-3}D$. The inset shows $n_{\rm imp}$ as a function of $\tilde{t}$ for the same systems.

behaviour is seen in the zero-temperature single particle spectrum, $\pi\Gamma_s D_{s\sigma}(\omega)$, as shown in the inset to that figure. A discontinuous change in $I_{\rm L} = \mathrm{Im\,Tr} \int_{-\infty}^{0} d\omega \frac{\partial \mathbf{\Sigma}_\sigma}{\partial \omega} \mathbf{G}_\sigma$, the Luttinger integral, from 0 to $\pm\frac{\pi}{2}$ is seen across the phase boundary. In the SC1 phase, by contrast, no quantum phase transition is observed as t is increased, but a gradual increase in the value of $n_{\rm imp}$ from 3 to 4 is seen: as the Luttinger integral is zero in both the SC1 phase and the strong coupling phase of the orbital regime, this gives rise to a fall in the conductance, from the unitarity limit to zero, as the system enters the orbital regime. This behaviour, illustrated in Fig. 6.36, is, of course, the result of a change in the zero temperature fixed point of the system from a strong coupling fixed point to a frozen impurity fixed point.

6.9 Magnetic Fields

We consider now the effect of a magnetic field ($h \neq 0$ in Eq. 4.1) upon the TQD, with the aim of providing simple physical arguments and intuitive low energy effective models to accurately explain the behaviour of the system under a field in all regimes. We discuss the regimes in the same order as in the preceding work, considering first the spin regime and then the orbital regime (see Fig. 6.2).

6.10 Magnetic Fields: The Spin Regime

We now consider the effect of an applied field upon the TQD in the spin regime (see Fig. 6.2). A magnetic field introduces an additional term into the spin Hamiltonian, Eq. 6.5, viz. $\hat{H}_h = -2h\hat{S}^z = -2h(\hat{S}^z_1 + \hat{S}^z_2 + \hat{S}^z_3)$. The spin Hamiltonian is now therefore $\hat{H}^h_{spin} = \hat{H}_{spin} + \hat{H}_h$. We assume $h > 0$ throughout.

6.10.1 Effective Low Energy Models

A weak field ($h \ll T_{\rm K}^{SCi}$) will have no effect upon the physics of a system in either of the SC phases, and so these will continue to be described by the relevant low energy effective model for the system in the absence of a field (Eq. 6.15 for the SC1 phase and Eq. 6.16 for the SC2 phase). Larger fields ($h \gtrsim T_{\rm K}^{SCi}$) will suppress the zero-field Kondo effect, and so for fields $h \gg T_{\rm K}^{SCi}$ only the $S^z = +\frac{1}{2}$ component of the lowest energy doublet of the isolated trimer will be thermally accessible at the lowest temperatures.

Any field $h \neq 0$ will lift the degeneracy of the ground state of a system in the LM or USC phase in the absence of a field, such that only the highest spin component of the degenerate $h = 0$ ground state is accessible at the lowest temperatures. In the case of a system in the LM phase in the absence of a field this is the $|\frac{1}{2};-;+\frac{1}{2}\rangle$ state of the $(-)$-parity doublet of the isolated trimer. For the USC phase, when $h \ll T_{\rm K}^{USC}$ it is the $S^z = +1$ component of the triplet which arises as a result of underscreening of the quartet state. At larger fields ($h \gtrsim T_{\rm K}^{USC}$) underscreening of the quartet will be suppressed, and therefore only the $|\frac{3}{2};-;+\frac{3}{2}\rangle$ state of the isolated trimer will be accessible at the lowest temperatures.

If we consider a field $h \gg T_{\rm K}^{SC1}, T_{\rm K}^{SC2}, T_{\rm K}^{USC}$ such that any zero-field Kondo effects are suppressed, it is clear (using identical arguments to Sec. 4.10.1) that the ground state of the isolated trimer must be one of three states: $|\frac{3}{2};-;+\frac{3}{2}\rangle$ ($E_Q = \frac{J}{2} - \frac{1}{2}J_{RKKY} + \frac{J'}{4} - \frac{1}{4}J'_{RKKY} - 3h$), $|\frac{1}{2};-;+\frac{1}{2}\rangle$ ($E_- = \frac{J'}{4} - \frac{1}{4}J'_{RKKY} - J + J_{RKKY} - h$) or $|\frac{1}{2};+;+\frac{1}{2}\rangle$ ($E_+ = -\frac{3}{4}J' + \frac{3}{4}J'_{RKKY} - h$). Just as in Sec. 4.10.1, we may divide the

parameter space of the TQD here into two regions, which exhibit distinct physics. In the first (the region $J > J'$) the ground state is either $|\frac{1}{2};-;+\frac{1}{2}\rangle$ or $|\frac{3}{2};-;+\frac{3}{2}\rangle$. By analogy with the corresponding case in the apex coupled trimer model (Sec. 4.10.1) we refer to this as the 'local moment case'. In the second case (the region $J' > J$) the ground state is $|\frac{1}{2};+;+\frac{1}{2}\rangle$ or $|\frac{3}{2};-;+\frac{3}{2}\rangle$. By analogy with the corresponding case in the apex coupled trimer model, we refer to this as the 'strong coupling case'.

6.10.1.1 The Local Moment Case

First, let us consider the local moment case. Here the system lies either in the USC phase or the SC2/LM phase in the absence of a field, and we consider explicitly fields $h \gg T_{\rm K}^{USC}, T_{\rm K}^{SC2}$. As the $|\frac{3}{2};-;+\frac{3}{2}\rangle$ state of the trimer is stabilised more by an applied field than the $|\frac{1}{2};-;+\frac{1}{2}\rangle$ state (as is shown by the energies given above) a system in the USC phase when $h = 0$ will not undergo a phase transition at $h \gg T_{\rm K}^{USC}$. However, it also follows immediately that a system in the SC2/LM phase when $h = 0$ (i.e. where the ground state of the trimer in the absence of a field is $|\frac{1}{2};-;S^z\rangle$) will, at some 'critical' field ($h_c = \frac{3}{4}(J - J_{RKKY})$, as easily determined from the energies of the isolated states) have a crossover between a $|\frac{1}{2};-;+\frac{1}{2}\rangle$ trimer ground state and a $|\frac{3}{2};-;+\frac{3}{2}\rangle$ trimer ground state. As these states have the same parity, one would naturally expect to see a field-induced Kondo effect here.

In the region $h \sim h_c$, the low energy manifold spans the $|\frac{1}{2};-;+\frac{1}{2}\rangle$ and $|\frac{3}{2};-;+\frac{3}{2}\rangle$ states, as illustrated schematically in Fig. 4.20, and as such the unity operator spanning the reduced Hilbert space of the low energy manifold is $\hat{1} = \hat{1}_+ + \hat{1}_- = |\frac{3}{2};-;+\frac{3}{2}\rangle\langle\frac{3}{2};-;+\frac{3}{2}| + |\frac{1}{2};-;+\frac{1}{2}\rangle\langle\frac{1}{2};-;+\frac{1}{2}|$. Projecting into this low energy manifold, it follows immediately that the low energy effective model is given by

$$\hat{H}_{eff} = \hat{1}\hat{H}^h_{spin}\hat{1} = J_{\rm K}\hat{1}\hat{\mathbf{S}}_2\hat{1}\cdot\hat{\mathbf{S}}(0) + J'_{\rm K}\hat{1}(\hat{\mathbf{S}}_1 + \hat{\mathbf{S}}_3)\hat{1}\cdot\hat{\mathbf{S}}(0) + \hat{1}\hat{H}^h_s\hat{1} + \hat{H}_L, \qquad (6.27)$$

where $\hat{H}^h_s = J(\hat{\mathbf{S}}_1 + \hat{\mathbf{S}}_3)\cdot\hat{\mathbf{S}}_2 + J'\hat{\mathbf{S}}_1\cdot\hat{\mathbf{S}}_3 + \hat{H}_h$. Evaluating $\hat{1}\hat{H}^h_s\hat{1}$, $\hat{1}\hat{\mathbf{S}}_2\hat{1}$ and $\hat{1}(\hat{\mathbf{S}}_1 + \hat{\mathbf{S}}_3)\hat{1}$

gives

$$\begin{aligned}\hat{H}_{eff} = &\frac{2}{\sqrt{6}}(J'_{\mathrm{K}} - J_{\mathrm{K}})\frac{1}{2}\hat{\mathcal{T}}^{+}\hat{S}^{-}(0) + \frac{2}{\sqrt{6}}(J'_{\mathrm{K}} - J_{\mathrm{K}})\frac{1}{2}\hat{\mathcal{T}}^{-}\hat{S}^{+}(0) \\ &+ \left(\frac{2}{3}J_{\mathrm{K}} + \frac{1}{3}J'_{\mathrm{K}}\right)\hat{\mathcal{T}}^{z}\hat{S}^{z}(0) + E_{\Delta}\hat{\mathcal{T}}^{z} + \hat{H}_{L}\end{aligned} \tag{6.28}$$

where potential scattering is neglected for clarity, $E_{\Delta} = E_Q - E_- = \frac{3}{2}(J - J_{\mathrm{RKKY}}) - 2h$ is the energy separation between the quartet and doublet states and we define a pseudospin, $\hat{\mathcal{T}}$, with components

$$\hat{\mathcal{T}}^{z} = \frac{1}{2}(\hat{1}_{+} - \hat{1}_{-}), \tag{6.29a}$$

$$\hat{\mathcal{T}}^{+} = |\tfrac{3}{2};-;+\tfrac{3}{2}\rangle\langle\tfrac{1}{2};-;+\tfrac{1}{2}|, \tag{6.29b}$$

$$\hat{\mathcal{T}}^{-} = |\tfrac{1}{2};-;+\tfrac{1}{2}\rangle\langle\tfrac{3}{2};-;+\tfrac{3}{2}|, \tag{6.29c}$$

such that $|\frac{3}{2};-;+\frac{3}{2}\rangle$ and $|\frac{1}{2};-;+\frac{1}{2}\rangle$ are eigenstates of $\hat{\mathcal{T}}^{z}$ with eigenvalues $\pm\frac{1}{2}$, respectively. Eq. 6.28 takes the form of a spin-anisotropic Kondo model under an effective magnetic field, E_{Δ}, with $J_{\mathrm{K},z} = \frac{2}{3}J_{\mathrm{K}} + \frac{1}{3}J'_{\mathrm{K}}$ and $J_{\mathrm{K},\perp} = \frac{2}{\sqrt{6}}(J'_{\mathrm{K}} - J_{\mathrm{K}})$. We therefore expect to see a field-induced Kondo effect when $E_{\Delta} \approx 0$ (in practice, $|E_{\Delta}| < T^{h}_{\mathrm{K}}$, where T^{h}_{K} is the Kondo temperature associated with the field-induced Kondo effect). As discussed in Appendices F and G, we may use the Poor Man's Scaling technique of Anderson [2, 14] to estimate the Kondo temperature T^{h}_{K} here, and we find that it is given by

$$\frac{T^{h}_{\mathrm{K}}}{D} = \exp\left[-\frac{1}{\rho\sqrt{|C|}}\left\{\frac{\pi}{2} - \arctan\left(\frac{\frac{2}{3}J_{\mathrm{K}} + \frac{1}{3}J'_{\mathrm{K}}}{\sqrt{|C|}}\right)\right\}\right], \tag{6.30}$$

when $J'_{\mathrm{K}}/J_{\mathrm{K}} < 0.1303$, where $C = J^{2}_{\mathrm{K},z} - J^{2}_{\mathrm{K},\perp}$. This reduces to Eq. 4.36 in the limit $J'_{\mathrm{K}} = 0$, and gives rise to the behaviour discussed in Sec. 4.10.2. In the case where $J'_{\mathrm{K}}/J_{\mathrm{K}} > 0.1303$ the Kondo temperature is given by

$$\frac{T^{h}_{\mathrm{K}}}{D} = \left|\frac{J_{\mathrm{K},z} + \sqrt{C}}{J_{\mathrm{K},z} - \sqrt{C}}\right|^{\left\{\frac{-1}{2\rho\sqrt{C}}\right\}}. \tag{6.31}$$

We also note that in the limit $J'_{\rm K} = 0$ Eq. 6.28 reduces to Eq. 4.34, the result for the apex coupled trimer model, whilst when $J'_{\rm K} = J_{\rm K}$ Eq. 6.28 reduces to

$$\hat{H}_{eff} = J_{\rm K}\hat{\mathcal{T}}^z\hat{S}^z(0) + E_\Delta\hat{\mathcal{T}}^z + \hat{H}_L, \tag{6.32}$$

and $J_{\rm K,\perp}$ vanishes. As a result, at this point the field induced Kondo effect is suppressed, and $T_{\rm K}^h$, as given by Eq. 6.31, goes to zero (we know from Poor Man's Scaling that the ultimate low temperature fixed point of a spin anisotropic Kondo model with $J_{\rm K,\perp} = 0$ is the local moment fixed point — see Sec. 2.2 and Ref. [2, 14]). This is a natural result of the TQD spin symmetry conservation by the spin Hamiltonian at this point (see Sec. 6.3). In this particular case we therefore expect the transition between a $|\frac{3}{2};-;+\frac{3}{2}\rangle$ and $|\frac{1}{2};-;+\frac{1}{2}\rangle$ ground state to take the form of a simple level crossing.

6.10.1.2 The Strong Coupling Case

In the strong coupling case, similar arguments to those given in the preceding section apply, and we again consider only the region where $h \gg T_{\rm K}^{SC1}, T_{\rm K}^{USC}$. We do not expect to see any kind of phase transition when the system is in the USC phase in the absence of a field, but for a system in the SC1 phase when $h = 0$ at some 'critical' field ($h_c = \frac{1}{4}(J - J_{RKKY}) + \frac{1}{2}(J' - J'_{RKKY}) \gg T_{\rm K}$, as easily determined from the energies of the isolated states) there will be a change in the ground state of the trimer (from $|\frac{1}{2};+;+\frac{1}{2}\rangle$ to $|\frac{3}{2};-;+\frac{3}{2}\rangle$). As these two states have distinct parities, mixing between them is not permitted, and so we do not expect to see a field-induced Kondo effect.

When $h \sim h_c$ the low energy manifold spans $|\frac{1}{2};+;+\frac{1}{2}\rangle$ and $|\frac{3}{2};-;+\frac{3}{2}\rangle$, and so the unity operator spanning the reduced Hilbert space of the low energy manifold is $\hat{1} = \hat{1}_+ + \hat{1}_- = |\frac{3}{2};-;+\frac{3}{2}\rangle\langle\frac{3}{2};-;+\frac{3}{2}| + |\frac{1}{2};+;+\frac{1}{2}\rangle\langle\frac{1}{2};+;+\frac{1}{2}|$. Projecting into this manifold, the low energy effective model is again given by Eq. 6.27 (although the unity operator is of course different). Evaluating $\hat{1}\hat{H}_s^h\hat{1}$, $\hat{1}\hat{\mathbf{S}}_2\hat{1}$ and $\hat{1}(\hat{\mathbf{S}}_1 + \hat{\mathbf{S}}_3)\hat{1}$ we

find that the low energy effective model here is

$$\hat{H}_{eff} = J'_{\rm K}\hat{\mathcal{T}}^z\hat{S}^z(0) + E_\Delta\hat{\mathcal{T}}^z + \hat{H}_L, \tag{6.33}$$

where we define a pseudospin, $\hat{\mathcal{T}}^z = \frac{1}{2}(\hat{1}_+ - \hat{1}_-)$, such that $|\frac{3}{2};-;+\frac{3}{2}\rangle$ and $|\frac{1}{2};+;+\frac{1}{2}\rangle$ are eigenstates of it with eigenvalues $\pm\frac{1}{2}$, and $E_\Delta = E_Q - E_+ = \frac{1}{2}(J - J_{\rm RKKY}) + J' - J'_{\rm RKKY} - 2h$ is the energy separation between the $|\frac{3}{2};-;+\frac{3}{2}\rangle$ and $|\frac{1}{2};+;+\frac{1}{2}\rangle$ states; potential scattering is neglected for clarity. Eq. 6.33 is a spin-anisotropic Kondo model under an effective magnetic field, E_Δ, with $J_{{\rm K},\perp} = 0$, a model which we know from Poor Man's Scaling [2,14] will flow to the local moment fixed point when $E_\Delta = 0$.

Due to the conservation of parity by the Hamiltonian field-induced Kondo physics are suppressed here, and a simple level crossing transition is expected; the transition fixed point here being, of course, the local moment fixed point ($S_{\rm imp} = \ln 2$ and $T\chi_{\rm imp} = 1/4$), which will persist down to zero temperature only when $E_\Delta = 0$. In addition we note that in the limit $J'_{\rm K} = 0$ we recover Eq. 4.32, the corresponding result for the apex coupled trimer model (and in any case, the two models predict identical behaviour for the system).

6.10.2 Thermodynamics and Dynamics

As shown in Fig. 6.37, for a system in the USC phase in the absence of a field, any applied field $h \neq 0$ lifts the degeneracy of the triplet state which arises when the quartet state is underscreened, giving $m = 2$ for all fields $0 < h < T_{\rm K}^{USC}$. Increasing the field through $h \sim T_{\rm K}^{USC}$ suppresses the Kondo effect, causing m to rise towards 3, and suppressing the Kondo resonance: as a result the zero-temperature conductance falls to zero for $h \gg T_{\rm K}^{USC}$.

The behaviour of m and $n_{\rm imp}$ in this case is illustrated in Fig. 6.37, and in the inset to that figure the behaviour of the zero-temperature conductance as a function of the applied field is shown. We generically find (via direct calculation using the

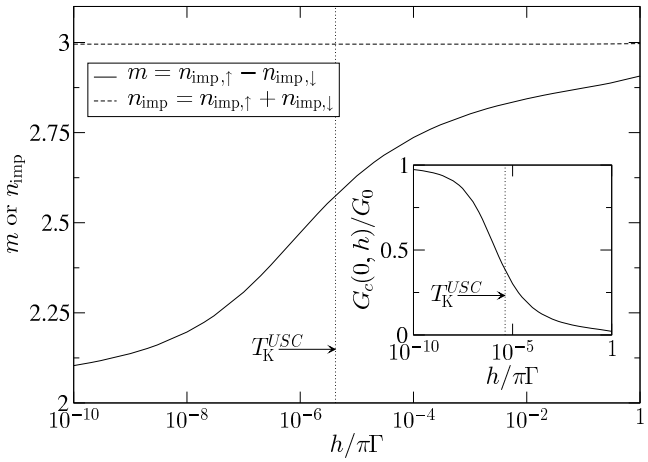


Figure 6.37: m and n_{imp} as a function of $\tilde{h}$ for a system in the USC phase in the absence of a field; $\tilde{U} = 10$, $\tilde{t}' = \tilde{t} = 10^{-1}$ and $\Gamma = \Gamma' = 10^{-2}D$. The inset shows the zero-temperature zero-bias conductance for the same system.

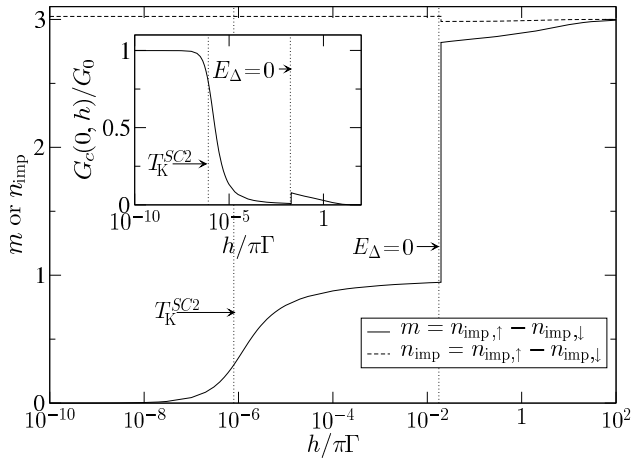


Figure 6.38: m and n_{imp} as a function of $\tilde{h}$ for a system in the SC2 phase in the absence of a field; $\tilde{U} = 10$, $\tilde{t} = 4 \times 10^{-1}$, $\tilde{t}' = 10^{-1}$ and $\Gamma = \Gamma' = 10^{-2}D$. The inset shows the zero-temperature zero-bias conductance for the same system.

NRG) that the Luttinger integral $I_{\mathrm{L}} = \mathrm{Im}\,\mathrm{Tr}\int_{-\infty}^{0} d\omega \frac{\partial \mathbf{\Sigma}_\sigma}{\partial \omega}\mathbf{G}_\sigma = 0$ here, and that $S_{\mathrm{imp}}(T=0) = 0$ and $T\chi_{\mathrm{imp}}|_{T=0} = 0$.

6.10.2.1 The Local Moment Case

If we now consider a system which lies in the SC2 phase in the absence of a field, we find that the behaviour of the system under an applied field is very different in the $\Gamma = \Gamma'$ (Fig. 6.38) and $\Gamma \neq \Gamma'$ (Fig. 6.38) cases; we consider the former first. In

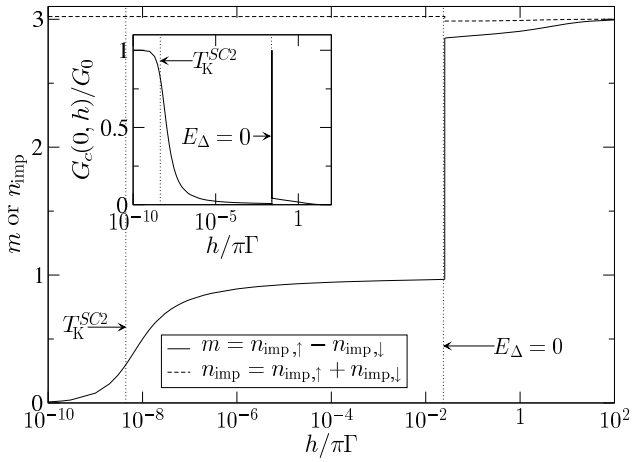


Figure 6.39: m and $n_{\rm imp}$ as a function of $\tilde{h}$ for a system in the SC2 phase in the absence of a field; $\tilde{U} = 10$, $\tilde{t} = 4 \times 10^{-1}$, $\tilde{t}' = 10^{-1}$, $\Gamma = 10^{-2}D$ and $\Gamma' = 8 \times 10^{-3}D$. The inset shows the zero-temperature, zero-bias conductance for the same system.

this case we find that very small fields ($h < T_{\rm K}^{SC2}$) have no discernible effect upon the system. Increasing the field through $h \sim T_{\rm K}^{SC2}$ suppresses Kondo quenching of the doublet state, causing m to rise asymptotically towards 1, and the conductance to fall to zero. As $\Gamma = \Gamma'$ here, the spin Hamiltonian conserves total TQD spin, and as such mixing between the quartet and doublet states is suppressed. The transition which we observe at $E_\Delta \simeq 0$ ($h \simeq h_c = \frac{3}{4}(J - J_{RKKY})$, as accurately predicted in Sec. 6.10.1.1) is therefore discontinuous, with m rising from $m \sim 1$ to $m \sim 3$, and so any field-induced Kondo effect is suppressed, exactly as one would expect from Eq. 6.32, the low energy effective model. This behaviour is illustrated in Fig. 6.38, and the inset to that figure, which shows the zero-temperature, zero-bias conductance.

The behaviour of the $\Gamma \neq \Gamma'$ case is shown in Fig. 6.39. Here we find, just as in the $\Gamma = \Gamma'$ case, that a field smaller than $T_{\rm K}^{SC2}$ has no discernible effect upon the system, and that increasing h through $h \sim T_{\rm K}^{SC2}$ suppresses the Kondo effect, causing the zero-temperature conductance to fall to zero. When $E_\Delta \simeq 0$ ($h \simeq h_c$, as accurately predicted in Sec. 6.10.1.1) the doublet and quartet states are near degenerate, but in this case mixing between them is not suppressed (as the spin Hamiltonian no longer conserves total TQD spin), and so a field induced Kondo effect is observed, giving

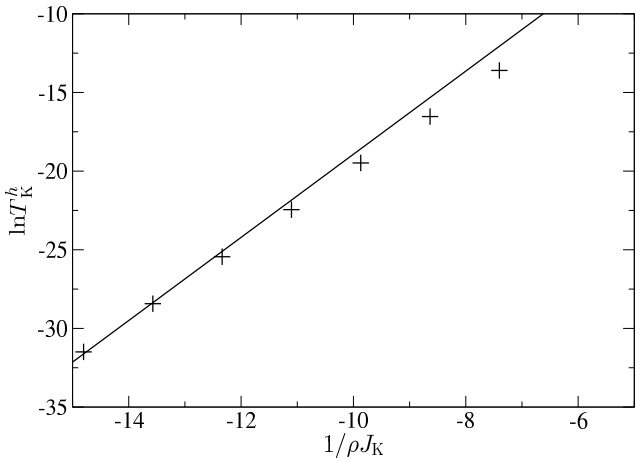


Figure 6.40: $\ln T_{\rm K}^h$ plotted against $1/\rho J_{\rm K}$ for a range of systems with $E_\Delta = 0$, $\tilde{J} = 6.4 \times 10^{-2}$ and $\tilde{J}' = 4 \times 10^{-3}$. $\tilde{U}$ is varied and $T_{\rm K}^h$ is defined via $S_{\rm imp}(T_{\rm K}^h) = 0.5 \ln 2$. The solid line is $\ln(T_{\rm K}^h/D) = -\frac{1}{2\rho\sqrt{C}} \ln \left| \frac{J_{{\rm K},z}+\sqrt{C}}{J_{{\rm K},z}-\sqrt{C}} \right|$, the expression for $T_{\rm K}^h$ derived from Poor Man's Scaling.

rise to a narrow peak in the conductance, which rises to the unitarity limit when $E_\Delta = 0$; this is in agreement with Eq. 6.28, our low energy effective model for the system in this case. A Kondo resonance, rising to the unitarity limit on an energy scale $\omega \sim T_{\rm K}^h$, is also seen in the single particle spectrum, $\pi\Gamma_s D_{s\sigma}(\omega)$, when $E_\Delta \approx 0$. In both the $\Gamma = \Gamma'$ and $\Gamma \neq \Gamma'$ cases we generically find that the Luttinger integral, $I_{\rm L} = {\rm Im\,Tr} \int_{-\infty}^{0} d\omega \frac{\partial \mathbf{\Sigma}_\sigma}{\partial \omega} \mathbf{G}_\sigma = 0$, as one would expect from our results in Sec. 4.10, 5.9 and the results of Wright *et al.* for a two-level quantum dot device [133]. Fig. 6.40 shows that the Kondo temperature of the field induced Kondo effect, $T_{\rm K}^h$, is well described by Eq. 6.31 in the region $J'_{\rm K}/J_{\rm K} > 0.1303$, with the description becoming more accurate as $T_{\rm K}^h$ becomes smaller.

The behaviour of a system in the LM phase in the absence of a field is, as one would expect from the form of the low energy effective model (Eq. 6.28) identical to that seen in the local moment case of regime II of the apex coupled trimer (see Sec. 4.10): we find that any non-zero field lifts the degeneracy of the local moment, causing m to rise to 1. m plateaus at this value until $h \simeq h_c$ ($E_\Delta \simeq 0$), at which point m increases (sharply but continuously) to ~ 3 as the $S^z = +\frac{3}{2}$ component of the quartet becomes the ground state of the trimer. As mixing between the doublet

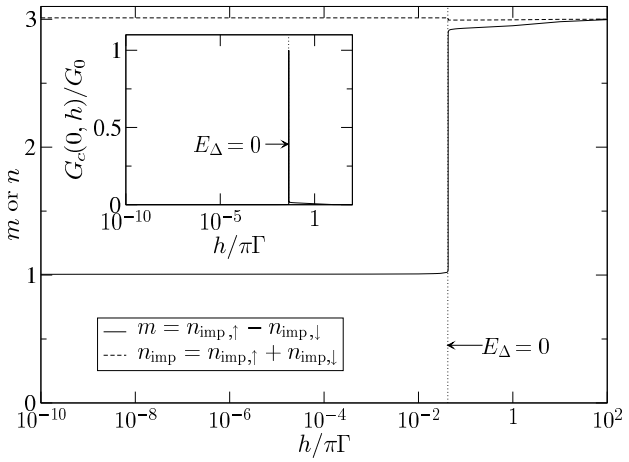


Figure 6.41: m and n_{imp} as a function of $\tilde{h}$ for a system in the LM phase in the absence of a field; $\tilde{U} = 10$, $\tilde{t} = 4 \times 10^{-1}$, $\tilde{t}' = 10^{-1}$, $\Gamma = 10^{-2}D$ and $\Gamma' = 2 \times 10^{-3}D$. The inset shows the zero-temperature, zero-bias conductance for the same system.

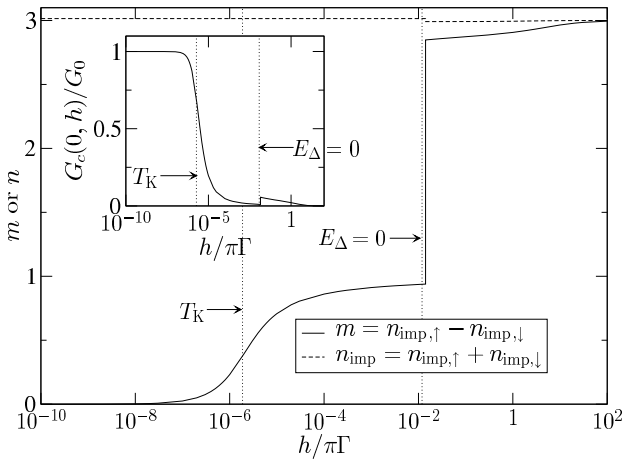


Figure 6.42: m and n_{imp} as a function of $\tilde{h}$ for a system in the SC1 phase in the absence of a field: $\tilde{U} = 10$, $\tilde{t} = 10^{-1}$, $\tilde{t}' = 4 \times 10^{-1}$, $\Gamma = 10^{-2}D$ and $\Gamma' = 8 \times 10^{-2}D$. The inset shows the zero-temperature zero-bias conductance for the same system.

and quartet states is not suppressed we see a field-induced Kondo effect at this point, and so the conductance through the TQD rises to the unitarity limit. This behaviour is illustrated in Fig. 6.41 and the inset to that figure. We generically find that the Luttinger integral $I_{\mathrm{L}} = 0$ in this case, and that $S_{\mathrm{imp}}(T = 0) = 0$ and $T\chi_{\mathrm{imp}}|_{T=0} = 0$ for all $h \neq 0$.

6.10.2.2 The Strong Coupling Case

The behaviour of a system in the SC1 phase when $h = 0$, under an applied field, is shown in Fig. 6.42, and is generally found to be very similar to the $\Gamma = \Gamma'$ case of a system in the SC2 phase in the absence of a field (Fig. 6.38), as one would expect; a field smaller than the Kondo temperature, $T_{\rm K}$, has no discernible impact upon the system, and increasing the applied field through $h \sim T_{\rm K}$ is found to suppress the Kondo effect. At this point m increases asymptotically towards 1 and the conductance falls to zero. When $E_\Delta \simeq 0$ ($h \simeq h_c = \frac{1}{4}(J - J_{RKKY}) + \frac{1}{2}(J' - J'_{RKKY})$, as accurately predicted in Sec. 6.10.1.2) there is a phase transition, characterised by a discontinuous change in m from $m \sim 1$ to ~ 3 as the $S^z = +\frac{3}{2}$ component of the quartet state becomes the ground state. Due to the change in parity here any mixing between the doublet and quartet states is suppressed, and hence no field-induced Kondo effect is observed. As expected, we generically find that the Luttinger integral $I_{\rm L} = {\rm Im\,Tr} \int_{-\infty}^{0} d\omega \frac{\partial \mathbf{\Sigma}_\sigma}{\partial \omega} \mathbf{G}_\sigma = 0$ here, and $S_{\rm imp}(T = 0) = 0$ and $T\chi_{\rm imp}|_{T=0} = 0$, except when $E_\Delta = 0$, where, as predicted by the low energy effective model, Eq. 6.33, the system is described down to zero temperature by the local moment fixed point ($S_{\rm imp} = \ln 2$ and $T\chi_{\rm imp} = \frac{1}{4}$).

6.11 Magnetic Fields: The Orbital Regime

Finally, we consider the effect of an applied field upon the orbital regime of the trimer in parallel (see Fig. 6.2). As discussed in Sec. 6.7.1 in the absence of a field the low energy effective models for the orbital regime of the trimer in parallel and regime III of the apex coupled trimer model are identical, and we find that the two models exhibit similar behaviour in the presence of an applied field.

6.11.1 Effective Low Energy Models

Just as for regime III of the ACTM (Sec. 4.12), under an applied field we find that the ground state of the trimer is one of four states, as illustrated schematically in Fig. 4.32;

$$|0;+;0\rangle = c^\dagger_{o\uparrow}c^\dagger_{o\downarrow}c^\dagger_{l\uparrow}c^\dagger_{l\downarrow}|Vac\rangle, \tag{6.34a}$$

$$|\tfrac{1}{2};-;+\tfrac{1}{2}\rangle = c^\dagger_{o\uparrow}c^\dagger_{l\uparrow}c^\dagger_{l\downarrow}|Vac\rangle, \tag{6.34b}$$

$$|1;-;+1\rangle = c^\dagger_{o\uparrow}c^\dagger_{l\uparrow}|Vac\rangle, \tag{6.34c}$$

$$|\tfrac{3}{2};-;+\tfrac{3}{2}\rangle = c^\dagger_{u\uparrow}c^\dagger_{o\uparrow}c^\dagger_{l\uparrow}|Vac\rangle = c^\dagger_{1\uparrow}c^\dagger_{2\uparrow}c^\dagger_{3\uparrow}|Vac\rangle. \tag{6.34d}$$

The $|0;+;0\rangle$ state has $(+)$-parity, and the other three $(-)$-parity. When the field is weak ($h < t$) the ground state is either $|0;+;0\rangle$ or $|\frac{1}{2};-;+\frac{1}{2}\rangle$, corresponding to the four electron singlet state and the $S^z = +\frac{1}{2}$ component of the three electron doublet state, respectively; the singlet and doublet states are, of course, the lowest energy states of the system in the absence of a field. $|1;-;+1\rangle$ and $|\frac{3}{2};-;+\frac{3}{2}\rangle$ are high spin states which become accessible only at large fields ($h > t$).

When $h < t$, the behaviour of the system should be indistinguishable from that of the ACTM, described in Sec. 4.12: for a system in the local moment phase when $h = 0$ the ground state of the trimer is $|\frac{1}{2};-;+\frac{1}{2}\rangle$ for all $0 < h < t$, whilst for a system in the strong coupling phase there is a crossover between the $|0;+;0\rangle$ and $|\frac{1}{2};-;+\frac{1}{2}\rangle$ states of the trimer when $h = h_{c,1} = t' - \epsilon - \frac{U}{2}(1+\gamma^2)$. As these two states have distinct parities, there is no mixing between them, and we therefore expect to see a level crossing transition when $h = h_{c,1}$.

In the region $h \sim h_{c,1}$ the low energy manifold spans $|0;+;0\rangle$ and $|\frac{1}{2};-;+\frac{1}{2}\rangle$, and so the unity operator for the reduced Hilbert space of the low energy manifold is $\hat{1} = \hat{1}_+ + \hat{1}_- = |0;+;0\rangle\langle 0;+;0| + |\frac{1}{2};-;+\frac{1}{2}\rangle\langle\frac{1}{2};-;+\frac{1}{2}|$. Using identical arguments to Sec. 4.12.1 it follows that the low energy effective model for the region $h \sim h_{c,1}$

is then

$$\hat{H}_{eff} = E'_{\Delta}\hat{\mathcal{T}}^{z} + \hat{H}_{L}, \tag{6.35}$$

where $E'_{\Delta} = \epsilon - t' + \frac{U}{2}(1+\gamma^2) + h$ is the energy separation between the two states (with electron-electron correlations taken into account by treating $\hat{H}_U = \sum_i U\hat{n}_{i\uparrow}\hat{n}_{i\downarrow}$ as a perturbation to first order of the states $|0;+;0\rangle$ and $|\frac{1}{2};-;+\frac{1}{2}\rangle$), and we define a pseudospin operator

$$\hat{\mathcal{T}}^{z} = \frac{1}{2}(\hat{1}_{+} - \hat{1}_{-}), \tag{6.36}$$

such that $|0;+;0\rangle$ and $|\frac{1}{2};-;+\frac{1}{2}\rangle$ are eigenstates of it with eigenvalues $\pm\frac{1}{2}$, respectively. This model describes a simple level crossing transition, just as in the corresponding case of the apex coupled trimer model.

At larger fields ($h \geq t$) the $S^z = +\frac{3}{2}$ component of the quartet state and the $S^z = +1$ component of the triplet state are stabilised and become thermally accessible, just as in Sec. 4.12. As in that case, the behaviour of the system at large fields depends upon the relative sizes of the two energy scales,

$$h_{c,2A} = \frac{1}{2}\sqrt{8t^2 + t'^2} - \epsilon - \frac{t'}{2} - U - \frac{3U}{2}(\gamma^4 - \gamma^2) \tag{6.37}$$

and

$$h_{c,2B} = \epsilon + \frac{1}{2}t' + \frac{1}{2}\sqrt{8t^2 + t'^2}, \tag{6.38}$$

as illustrated schematically in Fig. 4.33 and 4.34. When $h_{c,2A} < h_{c,2B}$ a two-stage transition will be observed, the first (at $h \sim h_{c,2A}$) between the $|\frac{1}{2};-;+\frac{1}{2}\rangle$ and $|1;-;+1\rangle$ states, and the second (at $h \sim h_{c,2B}$) between the $|1;-;+1\rangle$ state and the $|\frac{3}{2};-;+\frac{3}{2}\rangle$ state which is the ultimate ground state of the trimer at high field. As this two stage process involves a change in n_{imp} (from 3 to 2 at $h_{c,2A}$ and then from 2 back up to 3 at $h_{c,2B}$), any field induced Kondo effects will be suppressed, just as was the case in Sec. 4.12.

When $h_{c,2A} > h_{c,2B}$ on the other hand the transition between $|\frac{1}{2};-;+\frac{1}{2}\rangle$ and

$|\frac{3}{2};-;+\frac{3}{2}\rangle$ TQD ground states is direct, occurring at $h \sim h_{c,2} = \frac{1}{2}(\sqrt{8t^2+t'^2} - U - \frac{3U}{2}(\gamma^4 - \gamma^2))$, at which field the two states are degenerate. As there is no parity change across the transition here, we expect to see a finite field Kondo effect. As discussed in Sec. 4.12.1 the low energy effective model for such a system is generically a spin-anisotropic Kondo model [134]. In the region $h \sim h_{c,2}$ the unity operator spanning the reduced Hilbert space of the low energy manifold is $\hat{1} = \hat{1}_+ + \hat{1}_- = |\frac{3}{2};-;+\frac{3}{2}\rangle\langle\frac{3}{2};-;+\frac{3}{2}| + |\frac{1}{2};-;+\frac{1}{2}\rangle\langle\frac{1}{2};-;+\frac{1}{2}|$, and it immediately follows that the low energy effective model in this case is

$$\hat{H}_{eff} = \frac{1}{2}J_{\mathrm{K},\perp}\hat{\mathcal{T}}^+\hat{\mathbf{S}}^-(0) + \frac{1}{2}J_{\mathrm{K},\perp}\hat{\mathcal{T}}^-\hat{\mathbf{S}}^+(0) + J_{\mathrm{K},z}\hat{\mathcal{T}}^z\hat{\mathbf{S}}(0) + E_\Delta\hat{\mathcal{T}}^z + \hat{H}_L, \tag{6.39}$$

where we define the components of the pseudospin $\hat{\mathcal{T}}$

$$\hat{\mathcal{T}}^+ = |\tfrac{3}{2};-;+\tfrac{3}{2}\rangle\langle\tfrac{1}{2};-;+\tfrac{1}{2}|, \tag{6.40a}$$

$$\hat{\mathcal{T}}^- = |\tfrac{1}{2};-;+\tfrac{1}{2}\rangle\langle\tfrac{3}{2};-;+\tfrac{3}{2}|, \tag{6.40b}$$

$$\hat{\mathcal{T}}^z = \frac{1}{2}(\hat{1}_+ - \hat{1}_-), \tag{6.40c}$$

such that $|\frac{3}{2};-;+\frac{3}{2}\rangle$ and $|\frac{1}{2};-;+\frac{1}{2}\rangle$ are eigenvectors of the operator $\hat{\mathcal{T}}^z$ with eigenvalues $\pm\frac{1}{2}$, respectively. $E_\Delta = \sqrt{8t^2+t'^2} - U - \frac{3U}{2}(\gamma^4-\gamma^2) - 2h$ is the energy separation between $|\frac{3}{2};-;+\frac{3}{2}\rangle$ and $|\frac{1}{2};-;+\frac{1}{2}\rangle$. This is, of course, again identical to the corresponding low energy effective model in Sec. 4.12, and just as in that case we may numerically calculate $J_{\mathrm{K},\perp}$ and $J_{\mathrm{K},z}$ (as described in Appendix E), although the hybridisation term in this model is different:

$$\hat{H}_{hyb} = \sum_{\mathbf{k},\sigma}(V\nu + \sqrt{2}V'\gamma)[c^\dagger_{l\sigma}c_{\mathbf{k}\sigma} + H.c.] + \sum_{\mathbf{k},\sigma}(\sqrt{2}V'\nu - \gamma V)[c^\dagger_{u\sigma}c_{\mathbf{k}\sigma} + H.c.]. \tag{6.41}$$

This difference in $\hat{H}_{hyb}$ has a substantial effect on the low temperature physics of the system; in Sec. 4.12.1 we found that in the limit $t \gg t'$ the coupling between the conduction band and the u and l orbitals was identical, causing Eq. 6.39 to reduce

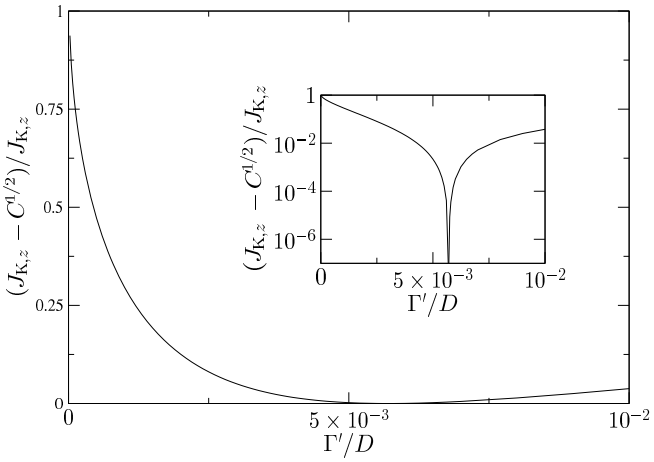


Figure 6.43: $(J_{\mathrm{K},z} - \sqrt{C})/J_{\mathrm{K},z}$ (as derived from perturbation theory) as a function of Γ' for a system with $\tilde{U} = 4$, $\tilde{t} = 6$, $\tilde{t}' = 5 \times 10^{-1}$ and $\Gamma = 10^{-2}D$. The inset shows the same data on a logarithmic scale.

to an isotropic Kondo model under those conditions. As the coupling between the conduction band and the u and l orbitals is distinct for all values of t and t' here, the model does *not* reduce to an isotropic Kondo model, and is instead found to be spin-anisotropic throughout the parameter space of the problem. We find that when $\Gamma' > 0$ the value of $J_{\mathrm{K},\perp}$ quickly becomes very small, and so $\sqrt{C} \approx J_{\mathrm{K},z}$, as shown in Fig. 6.43. As we find that $J_{\mathrm{K},z}^2 - J_{\mathrm{K},\perp}^2 = C > 0$ here the relevant expression for the Kondo temperature, T_{K}^h, is that derived in Appendix G,

$$T_{\mathrm{K}}^h = \left| \frac{J_{\mathrm{K},z} + \sqrt{C}}{J_{\mathrm{K},z} - \sqrt{C}} \right|^{\left\{ -\frac{1}{2\rho\sqrt{C}} \right\}} . \tag{6.42}$$

At the point $\sqrt{\Gamma/\Gamma'} = \gamma/\sqrt{2}\nu$ ($\Gamma = 2\Gamma'$ in the limit $t \gg t'$) the u orbital decouples from the conduction band, and so at this point the field-induced Kondo effect should be suppressed; our perturbation theory results show $J_{\mathrm{K},\perp}$ vanishing at this point, and as such $J_{\mathrm{K},z} = \sqrt{C}$ (this is shown in Fig. 6.43).

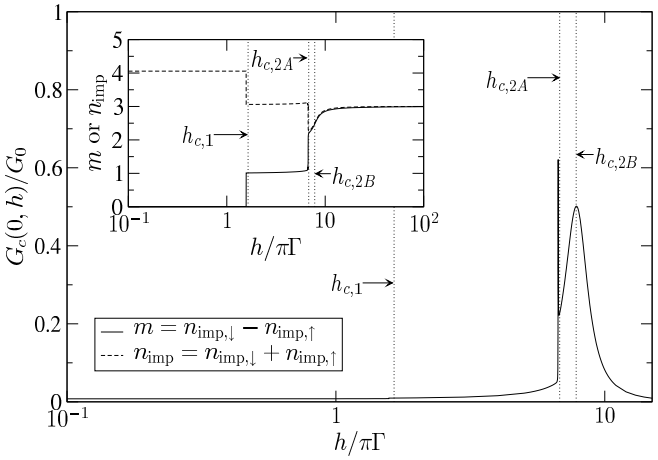


Figure 6.44: The zero-temperature conductance as a function of $\tilde{h}$ for a system in the strong coupling phase of the orbital regime when $h = 0$ with $\tilde{U} = 4$, $\tilde{t} = 6$, $\tilde{t}' = 2.5$ and $\Gamma = \Gamma' = 10^{-2}D$. Here $h_{c,2A} < h_{c,2B}$, and the 'critical' fields $h_{c,1}$, $h_{c,2A}$ and $h_{c,2B}$ are shown on the figure. The inset shows m and $n_{\rm imp}$ for the same system.

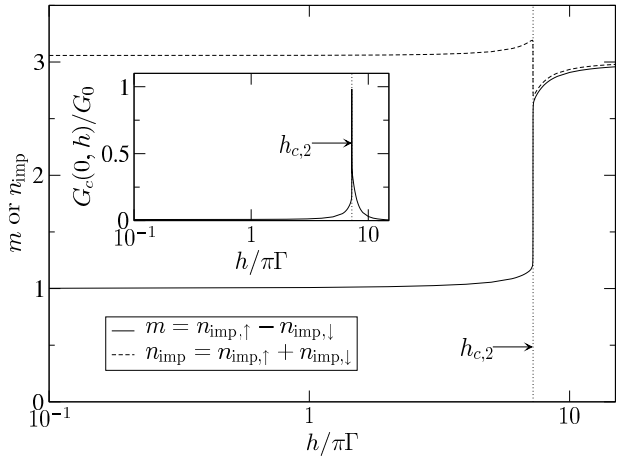


Figure 6.45: m and $n_{\rm imp}$ as a function of $\tilde{h}$ for a system in the local moment phase of the orbital regime when $h = 0$ with $\tilde{U} = 4$, $\tilde{t} = 6$, $\tilde{t}' = 5 \times 10^{-1}$, $\Gamma = 10^{-2}D$ and $\Gamma' = 8 \times 10^{-3}D$. Here $h_{c,2A} > h_{c,2B}$, and the 'critical' field $h_{c,2}$ is shown on the figure. The inset shows the zero-temperature zero-bias conductance for the same system.

6.11.2 Thermodynamics and Dynamics

The behaviour of systems in the orbital regime subject to an applied field is illustrated in Fig. 6.44 and 6.45 and in the insets to those figures. We find that if the system lies in the strong coupling phase in the absence of a field (Fig. 6.44 and inset) the values of m and $n_{\rm imp}$ are initially unchanged upon application of a weak ($h < h_{c,1}$) field, but that there is a discontinuous change in $n_{\rm imp}$ (from 4 to 3)

and m (from 0 to 1) when $h \simeq h_{c,1}$, in agreement with the predictions of our low energy effective model. There is no increase in the zero-temperature conductance through the system associated with this quantum phase transition, as there is a parity change across the phase boundary. This behaviour is shown in Fig. 6.44 and the inset to that figure. The degeneracy of a system in the local moment phase in the absence of a field will, by contrast, be lifted by any applied field, and so $m = 1$ and $n_{\mathrm{imp}} = 3$ is seen for all $h \neq 0$. We generically find that the Luttinger integral $I_{\mathrm{L}} = \mathrm{Im}\,\mathrm{Tr}\int_{-\infty}^{0} d\omega \frac{\partial \mathbf{\Sigma}_\sigma}{\partial \omega}\mathbf{G}_\sigma = 0$ here (as expected given our results in Sec. 4.12.3 and 5.11.3), and that $S_{\mathrm{imp}}(T = 0) = 0$ and $T\chi_{\mathrm{imp}}|_{T=0} = 0$, except when $h = h_{c,1}$, where the system is described by the local moment fixed point ($S_{\mathrm{imp}} = \ln 2$) down to zero temperature.

The $S^z = +\frac{3}{2}$ component of the quartet state and the $S^z = +1$ component of the triplet state are stabilised sufficiently by larger applied fields that they may become the ground state of the trimer. In agreement with our low energy effective models, we find that when $h_{c,2A} < h_{c,2B}$ a two stage transition is observed, just as was the case in Sec. 4.12, which suppresses the field-induced Kondo effect, but does give rise to Coulomb blockade peaks which lead to an enhanced zero-temperature conductance when $h \simeq h_{c,2A}$ and $h_{c,2B}$. This is shown in Fig. 6.44 and the inset to that figure. We find here that the doublet to triplet transition (at $h \simeq h_{c,2A}$) is typically much sharper than the triplet to quartet transition (at $h \simeq h_{c,2B}$), unlike the apex coupled trimer model: this gives rise to the wider peak at $h_{c,2B}$ seen Fig. 6.44. This naturally arises from the different magnitudes of the couplings between the l and u orbitals and the conduction band, discussed in Sec. 6.11.1.

By contrast, when $h_{c,2A} > h_{c,2B}$ (corresponding to $t' < \frac{3}{8}U$ in the limit of large t; Fig. 6.45) the transition between the doublet and quartet states is direct, and a field-induced Kondo effect may be observed, giving rise to an enhanced zero-temperature conductance at a critical field $h_{c,2}$, again in good agreement with our low energy effective model, Eq. 6.39, and with the results of Sec. 4.12. This behaviour

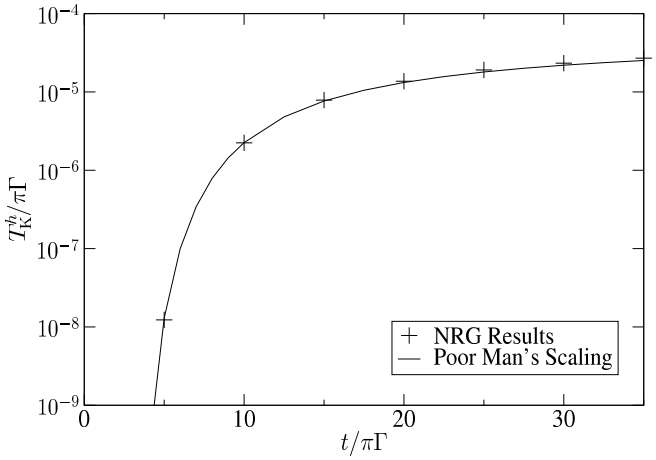


Figure 6.46: The field-induced Kondo temperature, $T_{\rm K}^h$ as a function of $\tilde{t}$ for systems with $\tilde{U} = 10$, $\tilde{t'} = 1$, $\Gamma = 10^{-2}D$, $\Gamma' = 8 \times 10^{-3}D$ and $h \simeq h_{c,2}$. Both the NRG results and the Poor Man's scaling result of Eq. 6.42, $T_{\rm K}^h \propto \left|\frac{J_{{\rm K},z}+\sqrt{C}}{J_{{\rm K},z}-\sqrt{C}}\right|^{\left\{-\frac{1}{2\rho\sqrt{C}}\right\}}$, are shown on the figure, where we define $T_{\rm K}^h$ via $S_{\rm imp}(T_{\rm K}^h) = 0.5 \ln 2$, and determine $J_{{\rm K},z}$ via perturbation theory, as described in the text.

is illustrated in Fig. 6.45 and the inset to that figure. We also find, as is predicted by our low energy effective model, that when $\sqrt{\Gamma/\Gamma'} \approx \gamma/\sqrt{2}\nu$ (corresponding to $\Gamma = 2\Gamma'$ in the limit $t \gg t'$) the field-induced Kondo effect is suppressed as the u orbital decouples from the conduction band. We find that the Kondo temperature is described well by Eq. 6.42, as one would expect from the low energy effective model. This is shown in Fig. 6.46.

6.12 Summary

In this chapter we investigate a mirror symmetric model in which all three quantum dots are attached to a single conduction band ('the trimer in parallel'). In Sec. 6.1 we discuss the model Hamiltonian. We find that in the regime where all three dots are singly occupied at low temperature we may derive an effective spin model for the system, and this process is described in Sec. 6.2. In this case, unlike the apex coupled trimer model, an RKKY interaction between the dots arises, and this suppresses the physics described as 'regime I' ($J < 10T_{\rm K}$) in Chapters 4 and 5.

In Sec. 6.3 we discuss the symmetry properties of the bare model Hamiltonian, and of the effective spin model derived in Sec. 6.2. Both of these are found to conserve parity under $1 \leftrightarrow 3$ interchange, and so all states of the system may be classified according to their parity. In addition, in the special case where all three dots have identical couplings to the conduction band ($V = V'$) the effective spin model is found to conserve total TQD spin. We follow this in Sec. 6.4 with a discussion of the relevant Friedel-Luttinger sum rule for this model.

Sec. 6.5 discusses the phase diagram for the trimer in parallel. We find the system has four possible phases — two strong coupling phases, one (SC1) of (+)-parity and one (SC2) of (−)-parity, a local moment (LM) phase of (−)-parity and an underscreened quartet phase (USC) of (−)-parity, which has no analogue in the apex coupled trimer model — although not all phases are present in every phase diagram. The phase diagram may in addition be divided into two distinct regimes, one (the 'spin regime') in which the system is described by the spin model at low temperature, and a second in which this description is not valid (the 'orbital regime'). We find that the phase boundaries between the SC1 and SC2 phases, the SC1 and LM phases and the SC1 and USC phases are a line of first order quantum phase transitions for all parameter sets, but that the phase boundaries between the USC and LM phases, and between the SC2 and LM phases are a line of Kosterlitz-Thouless transitions. The phase boundary between the USC and SC2 phase is found to be a line of first order quantum phase transitions when $V = V'$, and otherwise to be a line of Kosterlitz-Thouless transitions.

In Sec. 6.6 we discuss the physics of the spin regime, and in Sec. 6.7 the physics of the orbital regime. We derive a number of low energy effective models, which, we find, explain both the position and type (first order quantum phase transition or Kosterlitz-Thouless transition) of all the phase boundaries observed in the system. The behaviour of the system in the orbital regime is found to be identical to that of regime III of the apex coupled trimer model. We find that in the spin regime

the special case $V = V'$ (where the all three dots have identical couplings to the conduction band) has an additional symmetry in the effective Hamiltonian, and as such total spin on the TQD is conserved in that case. As a result, the system exhibits an atypical physics when $V = V'$. We also find that the results of the apex coupled trimer model (Chapter 4) are recovered by taking the limit $V' = 0$ in both the spin and orbital regimes.

Sec. 6.8 discusses the crossover between the spin and orbital regimes — a crossover which is associated, in the odd parity subsector (for sufficiently large V') with a Kosterlitz-Thouless transition between the SC2 and LM phases. We show that the system may be modelled as an effective Kondo model here, and that semi-analytic methods may be used to determine the effective coupling to the conduction band. This allows both the Kondo temperature in the SC2 phase and the position of the phase boundary between the SC2 and LM phases to be determined.

We investigate the behaviour of the spin regime under an applied field in Sec. 6.10, and the behaviour of the orbital regime under an applied field in Sec. 6.11. In both cases we derive effective low energy models, and find that for certain parameter regimes a field-induced Kondo effect may be observed in both the spin and orbital regimes.

Chapter 7

Conclusion

In this thesis we investigate the behaviour of a triple quantum dot device attached to a single conduction band. We examine the case where only a single dot is attached to the conduction band with both a mirror symmetric and an asymmetric arrangement of quantum dots, and also investigate a mirror symmetric arrangement of quantum dots in which all three dots are connected to the conduction band. Motivated by both recent experiments on TQD devices, and the opportunity to examine the effects of frustration upon coupled quantum dot systems, we examine all three models over a wide parameter range, and in both the presence and absence of a field. The three results chapters — Chapters 4, 5 and 6 — each finish with a summary of the key results of that chapter, and we do not repeat these here, but rather attempt to draw some general conclusions about our work.

We derived a number of low energy effective models, which were found to describe the behaviour of the TQD well over a large range of parameter space, accurately predicting both the behaviour of Kondo temperatures and the positions of phase boundaries. This is indeed one of the key results of this thesis, that we may use relatively simple models to provide an accurate description of the low temperature behaviour of these complex and subtle coupled quantum dot devices.

We find, quite generally, that the type of phase boundary observed is determined by the symmetry properties of the two phases it separates: when there is a change in

one of the symmetry labels of the system (parity for a mirror symmetric system, and total TQD spin for the spin regime of the trimer in parallel when $V = V'$) across the phase boundary a first order quantum phase transition is observed, with the system being described at the phase boundary by a transition fixed point (where the system is frustrated), distinct from the phases on either side of the phase boundary. When there is no change in the symmetry labels a Kosterlitz-Thouless transition is observed. It is not immediately apparent why this should be the case, although there is a simple physical explanation for why a first order quantum phase transition is *not* observed under these conditions.

We also generally find that when symmetry breaking leads to a Kosterlitz-Thouless transition, even when extremely close to the phase boundary the TQD behaves as it does in the symmetric case until an energy scale T_{KT}, which may be related directly to the asymmetry of the model, is reached. Away from the phase boundaries, we find that the behaviour of an asymmetric TQD is essentially indistinguishable from that of the corresponding mirror symmetric system when the asymmetry is small. This has implications for experimental results: we predict that on energy scales much larger than the asymmetry present in the system that asymmetry is effectively 'invisible'.

It is, of course, the potential for frustration inherent in the triangular triple quantum dot arrangement which allows us to observe such a large range of different quantum phase transitions — in many of which we see a discontinuous change in the zero-temperature zero-bias conductance through the triple quantum dot. This is perhaps the most important result of this thesis, that under a wide range of different geometries and conditions a triple quantum dot device may be tuned such that a very small change in the parameters of the system can give rise to a dramatic enhancement in the conductance.

This naturally leads one to think of triple quantum dot devices such as the one examined here as potential components in nanoelectronic systems. However, we also

find that the position of the phase boundaries is very sensitive to the parameters of the system — although we may accurately predict the position of the phase boundary using our low energy effective models. This accurate prediction of phase boundaries is another major result of this thesis, and one that again potentially has experimental relevance: for example, we find that plotting the three lines $J' = J^2/10T_{\mathrm{K}}$, $J' = J$ and $t' = U/4$ accurately describes the phase diagram for every case of the symmetric apex coupled trimer model.

We find, quite generally, that the phases of all the models studied in this thesis may be divided into three types; 'strong coupling' (Fermi liquid) phases, 'underscreened' phases and 'local moment' (singular Fermi liquid) phases. Within a strong coupling phase, we find that the Luttinger integral, $I_{\mathrm{L}} = 0$, as predicted by Luttinger's integral theorem [2]; we also find the $I_{\mathrm{L}} = 0$ in the underscreened phase. Within a local moment phase we find that the Luttinger integral is again constant, but that in this case $|I_{\mathrm{L}}| = \frac{\pi}{2}$. We can provide no theoretical justification for this numerical result, but we do note that it is in extremely good agreement with the results of Logan *et al.* [55] and Wright *et al.* [133] for a two level quantum dot system, and suggest that this would be a fruitful topic for further research.

Any scientific work naturally leaves some questions unanswered, and we therefore conclude this chapter with a discussion of possible future work in this area. A natural extension of this work would be to consider the effect of breaking the mirror symmetry of the triple quantum dot coupled in parallel, but we do not believe this would give rise to any particularly interesting physics beyond that described in Chapters 5 and 6, although a study of the region where $V' > V$ for the trimer in parallel model might prove rewarding. Likewise, a detailed examination of the effect of varying the level energies, ϵ_i, away from the point $\epsilon_i = \epsilon = -U/2$ would be possible, as would a study of the effect of placing a different charging energy upon each dot. Indeed, although it would be an ambitious project, an investigation of Kondo effects in a TQD connected to a single channel across the whole region of

electron filling (analogous to the work by Numata *et al.* [74] and Oguri *et al.* [77] on the TQD attached to two conduction channels) would be very informative. An examination of the system outside of equilibrium, or at finite bias, might also be of interest. In addition an experimental investigation and confirmation (or refutation) of the results presented here would be very welcome.

Appendix A

Elements of the $\mathbf{F}_\sigma$ Matrix

In this thesis we directly calculate the electron self-energy matrix, using the method of Bulla *et al.* [116]. As discussed in Sec. 3.6 direct calculation of the self-energy may be used to reduce the error in the calculation of the Green function matrix. The initial work by Bulla *et al.* considered a model (the single impurity Anderson model [6]) which contained only a single Green function. In that case direct calculation of the electron self-energy is a scalar problem. A recent work by Logan *et al.* [55] derived a more general (matrix) form of this result. We build upon that work here.

A general form of the Hamiltonian for the triple quantum dot device attached to a single conduction channel which we study is

$$\begin{aligned}\hat{H}_G = &\sum_{i,\sigma}(\epsilon_i - \sigma h)\hat{n}_{i\sigma} + \sum_i U\hat{n}_{i\uparrow}\hat{n}_{i\downarrow} + \sum_{i,j\neq i,\sigma} t_{ij}c^\dagger_{i\sigma}c_{j\sigma} \\ &+ \sum_{\mathbf{k},i,\sigma} V_i\,(c^\dagger_{i\sigma}c_{\mathbf{k}\sigma} + H.c.) + \sum_{\mathbf{k},\sigma}\epsilon_{\mathbf{k}}c^\dagger_{\mathbf{k}\sigma}c_{\mathbf{k}\sigma},\end{aligned} \tag{A.1}$$

where $c^\dagger_{i\sigma}$ ($c_{i\sigma}$) is the creation (destruction) operator for an electron with spin σ ($\sigma = \uparrow\ /\ \downarrow$) on dot i, $\hat{n}_{i\sigma} = c^\dagger_{i\sigma}c_{i\sigma}$ the counting operator for spin σ on dot i, ϵ_i the level energy for dot i and U the on-site Coulomb repulsion term. t_{ij} and V_i are hopping terms (we assume V_i is independent of $\mathbf{k}$ for simplicity) and $c^\dagger_{\mathbf{k}\sigma}$ ($c_{\mathbf{k}\sigma}$)

is the creation (destruction) operator for an electron in the conduction band with spin σ and wavevector $\mathbf{k}$. $\epsilon_{\mathbf{k}}$ is the energy of an electron in the conduction band with wavevector $\mathbf{k}$, and h is the applied magnetic field. Using equation of motion methods on $\hat{H}_G$ gives a simple equation for the retarded propagators[1] [2, 117]

$$\sum_{l=1}^{l=3}[\delta_{il}(\omega^+ - (\epsilon_i - \sigma h)) - \Gamma_{il}(\omega) - (1-\delta_{il})t_{il}]G_{ljs\sigma}(\omega) = \delta_{ij} + \langle\langle[c_{i\sigma}, \hat{H}_I]; c^\dagger_{j\sigma}\rangle\rangle \quad \text{(A.2)}$$

where $\omega^+ = \omega + i\eta$ with ω the frequency and η an infinitesimal,

$$\Gamma_{ij}(\omega) = \sum_{\mathbf{k}} \frac{V_i\, V_j}{\omega^+ - \epsilon_{\mathbf{k}}} = \Gamma^R_{ij}(\omega) - i\Gamma^I_{ij}(\omega), \quad \text{(A.3)}$$

and $G_{ij\sigma}(\omega)$ is the spin-σ retarded Green function connecting dots i and j. $[A, B]$ denotes a commutator and $\hat{H}_I$ is the interacting part of the Hamiltonian — $\hat{H}_I = \sum_i U\hat{n}_{i\uparrow}\hat{n}_{i\downarrow}$ in this case. $\langle\langle\hat{A}; \hat{B}\rangle\rangle$ is the Fourier transform of the retarded correlator $\langle\langle\hat{A}(t_1); \hat{B}(t_2)\rangle\rangle = -i\theta(t_1 - t_2)\langle\{\hat{A}(t_1), \hat{B}(t_2)\}\rangle$. It follows immediately that in the non-interacting limit $\hat{H}_I = 0$, and so Eq. A.2 may equivalently be written

$$[\mathbf{G}^0_\sigma(\omega)]^{-1}\mathbf{G}_\sigma(\omega) = \mathbf{I} + \mathbf{F}_\sigma(\omega) \quad \text{(A.4)}$$

where $\mathbf{G}_\sigma(\omega)$ is the (3×3) Green function matrix and $\mathbf{G}^0_\sigma(\omega)$ the non-interacting Green function matrix such that

$$[\mathbf{G}^0_\sigma]^{-1}_{ij} = \delta_{ij}[\omega^+ - (\epsilon_i - \sigma h)] - \Gamma_{ij}(\omega) - (1-\delta_{ij})t_{ij}, \quad \text{(A.5)}$$

and $\mathbf{F}$ is a 3×3 matrix with elements [55]

$$F_{ij\sigma} = \langle\langle[c_{i\sigma}, \hat{H}_I]; c^\dagger_{j\sigma}\rangle\rangle \quad \text{(A.6a)}$$

$$= U\langle\langle\hat{n}_{i-\sigma}c_{i\sigma}; c^\dagger_{j\sigma}\rangle\rangle. \quad \text{(A.6b)}$$

[1] As discussed in Sec. 3.6 there is a direct relationship between the advanced and retarded Green functions and so we only need calculate one of the two.

Using the Dyson equation,

$$[\mathbf{G}_{\sigma}^{0}]^{-1} = \mathbf{G}_{\sigma}^{-1} + \mathbf{\Sigma}_{\sigma}, \tag{A.7}$$

in combination with Eq. A.4 leads directly to the result

$$\mathbf{\Sigma}_{\sigma}(\omega) = \mathbf{F}_{\sigma}(\omega)[\mathbf{G}_{\sigma}(\omega)]^{-1} \tag{A.8}$$

which is used to calculate the self energy matrix.

Appendix B

Parity Operators

A number of the Hamiltonians studied in this thesis are found to have a parity symmetry — that is, the states of the Hamiltonian may be classified by their symmetry under interchange of the labels on dots 1 and 3;

$$\hat{P}_{1,3}c^{\dagger}_{1\sigma} = c^{\dagger}_{3\sigma}\hat{P}_{1,3}, \tag{B.1a}$$

$$\hat{P}_{1,3}c^{\dagger}_{3\sigma} = c^{\dagger}_{1\sigma}\hat{P}_{1,3}. \tag{B.1b}$$

Now, building on the work presented in the appendix to Ref [88], we may formally define the parity operator via

$$\hat{P}_{1,3} = 2(\hat{n}_o - 1)^2 - 1, \tag{B.2}$$

where $\hat{n}_o = \sum_\sigma c^{\dagger}_{o\sigma}c_{o\sigma}$ and $c^{\dagger}_{o\sigma} = \frac{1}{\sqrt{2}}(c^{\dagger}_{1\sigma} - c^{\dagger}_{3\sigma})$ is the antisymmetric linear combination of $c^{\dagger}_{1\sigma}$ and $c^{\dagger}_{3\sigma}$. The operator $\hat{P}_{1,3}$, as defined by Eq. B.2, is both self-adjoint and involutory ($\hat{P}^2_{1,3} = 1$), having eigenvalues ± 1 — corresponding to even and odd parity, respectively. It is a simple matter to show that the operator as defined in Eq. B.2 fulfils both parts of Eq. B.1.

A general form of the triple quantum dot Hamiltonian investigated in this thesis

is

$$\begin{aligned}\hat{H}_G = &\sum_{\sigma,i=1,2,3}(\epsilon_i - \sigma h)\hat{n}_{i\sigma} + \sum_{i=1,2,3} U\hat{n}_{i\uparrow}\hat{n}_{i\downarrow} \\ &+ \sum_{\sigma} t[(c^\dagger_{1\sigma} + c^\dagger_{3\sigma})c_{2\sigma} + H.c] + \sum_{\sigma} t'(c^\dagger_{1\sigma}c_{3\sigma} + H.c.) + \sum_{\sigma} x(c^\dagger_{2\sigma}c_{3\sigma} + H.c.) \\ &+ \sum_{\mathbf{k},\sigma} V(c^\dagger_{2\sigma}c_{\mathbf{k}\sigma} + H.c.) + \sum_{\mathbf{k},\sigma} V'[(c^\dagger_{1\sigma} + c^\dagger_{3\sigma})c_{\mathbf{k}\sigma} + H.c.] \\ &+ \sum_{\mathbf{k},\sigma} \epsilon_{\mathbf{k}} c^\dagger_{\mathbf{k}\sigma}c_{\mathbf{k}\sigma},\end{aligned} \tag{B.3}$$

where $c^\dagger_{i\sigma}$ ($c_{i\sigma}$) is the creation (destruction) operator for an electron in dot i, with level energy ϵ_i and an on-site Coulomb repulsion, U. t, t' and x are hopping terms, as are V and V'. $c^\dagger_{\mathbf{k}\sigma}$ ($c_{\mathbf{k}\sigma}$) is the creation (destruction) operator for an electron in the conduction band with spin σ and wavevector $\mathbf{k}$, which has energy $\epsilon_{\mathbf{k}}$, whilst h is the applied field. If we evaluate the commutator of this Hamiltonian with $\hat{P}_{1,3}$ we find that

$$[\hat{P}_{1,3}, \hat{H}_G] = -\sqrt{2}x\sum_{\sigma}(c^\dagger_{2\sigma}c_{o\sigma} + H.c.)\hat{P}_{1,3} + \sum_{\sigma}(\epsilon_3 - \epsilon_1)(c^\dagger_{1\sigma}c_{3\sigma} + H.c.), \tag{B.4}$$

which shows that the parity operator *does not*, in general, commute with the Hamiltonian for the models we study. The states of the system cannot, therefore, be classified using parity as a quantum number, *except* in the specific case in which both $x = 0$ *and* $\epsilon_1 = \epsilon_3$. In that particular case the system does contain a plane of mirror symmetry, and the Hamiltonian does not mix states of distinct parity.

Appendix C

The Friedel Sum Rule

Here we describe the derivation of a Friedel-Luttinger sum rule for a triple quantum dot device. Our derivation here builds heavily on the original proof of the Friedel Sum Rule for a single impurity Anderson model by Langreth [22] and the derivation of the Friedel-Luttinger sum rule for a two level quantum dot presented in Ref. [55]. Such a sum rule may be used to relate the zero-frequency value of the single particle spectrum of the device to the electronic population of the TQD, n_{imp}. We begin with a very general derivation of the sum rule;

$$\arg\det \mathbf{G}_\sigma(\omega=0) - \arg\det \mathbf{G}_\sigma(\omega=-\infty) = \int_{-\infty}^{0} d\omega \frac{\partial}{\partial\omega} \arg(\det \mathbf{G}_\sigma(\omega)) \tag{C.1a}$$

$$= \text{Im} \int_{-\infty}^{0} d\omega \frac{\partial}{\partial\omega} \ln|\det \mathbf{G}_\sigma(\omega)| \tag{C.1b}$$

$$= \text{Im} \int_{-\infty}^{0} d\omega \frac{1}{\det \mathbf{G}(\omega)} \frac{\partial}{\partial\omega} \det \mathbf{G}_\sigma(\omega) \tag{C.1c}$$

where $\mathbf{G} = \mathbf{G}(\omega, T, h)$ is the Green function matrix, and we take $T = 0$ as implicit. From Jacobi's Formula [137]

$$\frac{\partial}{\partial\omega} \det \mathbf{G}_\sigma(\omega) = \text{Tr}\left[\text{adj}\, \mathbf{G}_\sigma(\omega) \frac{\partial}{\partial\omega} \mathbf{G}_\sigma(\omega)\right], \tag{C.2}$$

and using this result in Eq. C.1c gives

$$\arg\det \mathbf{G}_\sigma(0) - \arg\det \mathbf{G}_\sigma(-\infty) = \mathrm{Im\,Tr} \int_{-\infty}^{0} d\omega \frac{1}{\det \mathbf{G}_\sigma(\omega)} \,\mathrm{adj}\, \mathbf{G}_\sigma(\omega) \frac{\partial}{\partial \omega} \mathbf{G}_\sigma(\omega), \tag{C.3a}$$

$$= \mathrm{Im\,Tr} \int_{-\infty}^{0} d\omega \mathbf{G}_\sigma^{-1}(\omega) \frac{\partial}{\partial \omega} \mathbf{G}_\sigma(\omega). \tag{C.3b}$$

Integrating Eq. C.3b by parts gives

$$\arg\det \mathbf{G}_\sigma(0) - \arg\det \mathbf{G}_\sigma(-\infty) = -\mathrm{Im\,Tr} \int_{-\infty}^{0} d\omega \mathbf{G}_\sigma(\omega) \frac{\partial}{\partial \omega} \mathbf{G}_\sigma^{-1}(\omega) = \tilde{\delta}_\sigma, \tag{C.4}$$

where Eq. C.4 provides the definition of $\tilde{\delta}_\sigma$, the phase shift. Our results thus far are entirely general. We now consider a specific Hamiltonian,

$$\begin{aligned} \hat{H}_G = &\sum_{i,\sigma} (\epsilon_i - \sigma h) \hat{n}_{i\sigma} + \sum_i U \hat{n}_{i\uparrow} \hat{n}_{i\downarrow} + \sum_{i, j \neq i, \sigma} t_{ij} c_{i\sigma}^\dagger c_{j\sigma} \\ &+ \sum_{\mathbf{k}, i, \sigma} V_i \left(c_{i\sigma}^\dagger c_{\mathbf{k}\sigma} + H.c. \right) + \sum_{\mathbf{k}, \sigma} \epsilon_{\mathbf{k}} c_{\mathbf{k}\sigma}^\dagger c_{\mathbf{k}\sigma}, \end{aligned} \tag{C.5}$$

where $c_{i\sigma}^\dagger$ ($c_{i\sigma}$) is the creation (destruction) operator for an electron with spin σ on dot i ($i = 1, 2, 3$), $\hat{n}_{i\sigma} = c_{i\sigma}^\dagger c_{i\sigma}$, ϵ_i the level energy for dot i and U the on-site Coulomb repulsion term. t_{ij} and V_i are hopping terms and $c_{\mathbf{k}\sigma}^\dagger$ ($c_{\mathbf{k}\sigma}$) is the creation (destruction) operator for an electron in the conduction band with spin σ, wavevector $\mathbf{k}$ and level energy $\epsilon_{\mathbf{k}}$. h is the applied magnetic field. Eq. C.5 is a general form of the Hamiltonian of a triple quantum dot attached to a single conduction channel. As discussed in Appendix A the inverse of the Green function matrix for a system described by Eq. C.5 can be determined using equation of motion methods;

$$\mathbf{G}_\sigma^{-1}(\omega) = [\mathbf{G}_\sigma^0]^{-1} + \mathbf{\Sigma}_\sigma, \tag{C.6}$$

where $\mathbf{G}^0_\sigma$ is the non-interacting Green function matrix, and $\mathbf{\Sigma}_\sigma$ is the spin-σ self-energy matrix. Combining this with Eq. A.5 it follows immediately that

$$\mathbf{G}^{-1}_\sigma = \begin{bmatrix} (\omega^+ - \epsilon_{1\sigma} - \Gamma_{11} - \Sigma_{11\sigma}) & -\Sigma_{12\sigma} - \Gamma_{12} - t_{12} & -\Sigma_{13\sigma} - \Gamma_{13} - t_{13} \\ -\Sigma_{12\sigma} - \Gamma_{12} - t_{12} & (\omega^+ - \epsilon_{2\sigma} - \Gamma_{22} - \Sigma_{22\sigma}) & -\Sigma_{23\sigma} - \Gamma_{23} - t_{23} \\ -\Sigma_{13\sigma} - \Gamma_{13} - t_{13} & -\Sigma_{23\sigma} - \Gamma_{23} - t_{23} & (\omega^+ - \epsilon_{3\sigma} - \Sigma_{33\sigma} - \Gamma_{33}) \end{bmatrix}, \tag{C.7}$$

where $\omega^+ = \omega + i\eta$, with η an infinitesimal, and $\Sigma_{ij\sigma}$ is the spin-σ self-energy for dots i and j; $\epsilon_{i\sigma} = (\epsilon_i - \sigma h)$. From Eq. C.7 it follows that

$$\mathbf{G}^{-1}_\sigma(\omega) = \omega^+ \mathbf{I} - \boldsymbol{\epsilon}_\sigma - \mathbf{\Gamma} - \mathbf{\Sigma}_\sigma - \mathbf{t}, \tag{C.8a}$$

$$\therefore \frac{\partial \mathbf{G}^{-1}_\sigma(\omega)}{\partial \omega} = \mathbf{I} - \frac{\partial \mathbf{\Gamma}}{\partial \omega} - \frac{\partial \mathbf{\Sigma}_\sigma}{\partial \omega}, \tag{C.8b}$$

where $\mathbf{I}$ is the identity matrix, whilst $\boldsymbol{\epsilon}_\sigma$ is a 3×3 matrix with elements $\epsilon_{ij\sigma} = \delta_{ij}(\epsilon_i - \sigma h)$. $\mathbf{\Sigma}_\sigma$, $\mathbf{t}$ and $\mathbf{\Gamma}$ are also 3×3 matrices with elements Γ_{ij}, t_{ij} ($t_{ii} = 0$) and $\Sigma_{ij\sigma}$, respectively, where Γ_{ij} is defined in Eq. A.3. From Eq. C.4,

$$\tilde{\delta}_\sigma = -\operatorname{Im}\operatorname{Tr}\int_\omega^0 \partial\omega \mathbf{G}_\sigma \left[\mathbf{I} - \frac{\partial \mathbf{\Gamma}}{\partial \omega} - \frac{\partial \mathbf{\Sigma}_\sigma}{\partial \omega}\right] \tag{C.9a}$$

$$= -\operatorname{Im}\operatorname{Tr}\int_{-\infty}^0 d\omega \mathbf{G}_\sigma \left[\mathbf{I} - \frac{\partial \mathbf{\Gamma}}{\partial \omega}\right] + \operatorname{Im}\operatorname{Tr}\int_{-\infty}^0 d\omega \frac{\partial \mathbf{\Sigma}_\sigma}{\partial \omega}\mathbf{G}_\sigma \tag{C.9b}$$

$$= \pi n_{\mathrm{imp},\sigma}|_{T=0} + I_{\mathrm{L}}, \tag{C.9c}$$

where Eq. C.9b is the Friedel-Luttinger Sum Rule. Eq. C.9c makes use of the two definitions

$$\pi n_{\mathrm{imp},\sigma}|_{T=0} = -\operatorname{Im}\operatorname{Tr}\int_{-\infty}^0 d\omega \mathbf{G}_\sigma \left[\mathbf{I} - \frac{\partial \mathbf{\Gamma}}{\partial \omega}\right], \tag{C.10a}$$

$$I_{\mathrm{L}} = \operatorname{Im}\operatorname{Tr}\int_{-\infty}^0 d\omega \frac{\partial \mathbf{\Sigma}_\sigma}{\partial \omega}\mathbf{G}_\sigma, \tag{C.10b}$$

where I_{L} is the Luttinger integral [120, 125, 138]. Eq. C.10a directly relates the thermodynamic quantity, $n_{\mathrm{imp},\sigma}|_{T=0}$ (corresponding to the difference between the

electronic population of the system calculated in the presence and in the absence of the quantum dots), to the matrix of Green functions [2, 22].

We next relate $\tilde{\delta}_\sigma$ to the single particle spectrum of the triple quantum dot device, which may be calculated using the NRG, and related directly to the conductance through the TQD, as described in Sec. 3.6. It may easily be shown that $\arg(\det \mathbf{G}_\sigma(-\infty)) = 0$ ($\det \mathbf{G}_\sigma(-\infty) = \arctan(-1/\omega)_{\omega\to-\infty}$). We therefore only need to consider the value of $\arg\det \mathbf{G}_\sigma(0)$. Inverting $\mathbf{G}_\sigma^{-1}$, as defined in Eq. C.7, we find that the elements of $\mathbf{G}_\sigma$ may be written

$$G_{ij\sigma} = G^{\alpha}_{ij\sigma} \det \mathbf{G}_\sigma, \tag{C.11a}$$

$$= \frac{1}{\det \mathbf{G}^{-1}_\sigma} G^{\alpha}_{ij\sigma}, \tag{C.11b}$$

where $\mathbf{G}^\alpha_\sigma$ is a 3×3 matrix. We then define

$$G_{s\sigma}(0) = G^R_{s\sigma}(0) - i\pi D_{s\sigma}(0) = \frac{1}{\Gamma^I_{11}+\Gamma^I_{22}+\Gamma^I_{33}} \sum_{i,j} \Gamma^I_{ij} G_{ij\sigma}(0), \tag{C.12a}$$

$$= \frac{\det \mathbf{G}_\sigma(0)}{\Gamma^I_{11}+\Gamma^I_{22}+\Gamma^I_{33}} \sum_{i,j} \Gamma^I_{ij} G^{\alpha}_{ij\sigma}(0), \tag{C.12b}$$

$$= \frac{\det \mathbf{G}_\sigma(0)}{\Gamma^I_{11}+\Gamma^I_{22}+\Gamma^I_{33}} [\gamma - i\eta\beta], \tag{C.12c}$$

where η is an infinitesimal and γ and β are real quantities. We may also show that

$$\det \mathbf{G}_\sigma(0) = \frac{1}{\alpha+\eta\beta+i[\gamma+\eta\theta]} = \frac{\alpha+\eta\beta-i[\gamma+\eta\theta]}{[\alpha+\eta\beta]^2+[\gamma+\eta\theta]^2} \tag{C.13a}$$

$$\therefore \arg\det \mathbf{G}_\sigma(0) = \arctan\left[\frac{-[\gamma+\eta\theta]}{[\alpha+\eta\beta]}\right], \tag{C.13b}$$

where α and θ are real. It follows immediately that

$$(\Gamma^I_{11}+\Gamma^I_{22}+\Gamma^I_{33})[G^R_{s\sigma}(0) - i\pi D_{s\sigma}(0)] = \frac{\alpha+\eta\beta-i[\gamma+\eta\theta]}{[\alpha+\eta\beta]^2+[\gamma+\eta\theta]^2}[\gamma - i\eta\beta]. \tag{C.14}$$

Now, in the (physically relevant) case where $\alpha \neq 0$ and/or $\gamma \neq 0$ $\tilde{\delta}_\sigma = \arg\det \mathbf{G}_\sigma(0) =$

$\arctan[-\gamma/\alpha]$ and

$$(\Gamma^I_{11} + \Gamma^I_{22} + \Gamma^I_{33})\pi D_s(0) = \frac{\gamma^2}{\alpha^2 + \gamma^2} \tag{C.15a}$$

$$= \sin^2 \tilde{\delta}_\sigma \tag{C.15b}$$

$$= \sin^2(\pi n_{\mathrm{imp},\sigma}|_{T=0} + I_{\mathrm{L}}). \tag{C.15c}$$

Eq. C.15b arises from Eq. C.15a via

$$\frac{\gamma^2}{\alpha^2 + \gamma^2} = \frac{1}{1 + \frac{\alpha^2}{\gamma^2}} = \frac{1}{1 + \left(\frac{\gamma^2}{\alpha^2}\right)^{-1}} \tag{C.16a}$$

$$= \frac{1}{1 + \cot^2 \tilde{\delta}_\sigma} = \sin^2 \tilde{\delta}_\sigma. \tag{C.16b}$$

Additionally, in the special case where $\alpha = \gamma = 0$ we may show that

$$(\Gamma^I_{11} + \Gamma^I_{22} + \Gamma^I_{33})\pi D_{s\sigma}(0) = \cos^2 \delta. \tag{C.17}$$

We also note that in the limit $\Gamma_{11} = \Gamma_{33} = 0$ $D_{s\sigma}(0) = D_{2\sigma}(0)$ — and we therefore need only consider the single particle spectrum of dot 2 when evaluating the Friedel-Luttinger sum rule for the ACTM and AACTM (see Sec. 4.4 and 5.3).

Appendix D

Perturbation Theory In The Orbital Regime

In Sec. 4.8, 5.7 and 6.7, where the orbital regimes of the ACTM, AACTM and TiP models are investigated and low energy effective models are constructed, we treat $\hat{H}_U$ as a perturbation to the ground state and first excited state of the non-interacting TQD Hamiltonians, so that the energy difference between the two states can be more accurately determined. The details of that calculation are given in this appendix.

We initially consider the more general case of the asymmetric ACTM; as shown at the end of this appendix, the results for the symmetric ACTM and TiP model arise naturally as the limiting case $x = 0$ of the AACTM result. As discussed in Sec. 5.7 the non-interacting TQD Hamiltonian, $\hat{H}_{NITQD}$, may be written in the form of a three level system,

$$\hat{H}_{NITQD} = \sum_{\sigma} E_{\alpha} c^{\dagger}_{\alpha\sigma} c_{\alpha\sigma} + \sum_{\sigma} E_{\beta} c^{\dagger}_{\beta\sigma} c_{\beta\sigma} + \sum_{\sigma} E_{\gamma} c^{\dagger}_{\gamma\sigma} c_{\gamma\sigma} \tag{D.1}$$

where

$$c^\dagger_{\alpha\sigma} = \alpha_1 c^\dagger_{e\sigma} + \alpha_2 c^\dagger_{o\sigma} + \alpha_3 c^\dagger_{2\sigma}, \tag{D.2a}$$

$$c^\dagger_{\beta\sigma} = \beta_1 c^\dagger_{e\sigma} + \beta_2 c^\dagger_{o\sigma} + \beta_3 c^\dagger_{2\sigma}, \tag{D.2b}$$

$$c^\dagger_{\gamma\sigma} = \gamma_1 c^\dagger_{e\sigma} + \gamma_2 c^\dagger_{o\sigma} + \gamma_3 c^\dagger_{2\sigma}, \tag{D.2c}$$

and (again, as discussed in Sec. 5.7) the two lowest energy states of this system are given by

$$|0;0\rangle = c^\dagger_{\beta\uparrow} c^\dagger_{\beta\downarrow} c^\dagger_{\gamma\uparrow} c^\dagger_{\gamma\downarrow} |Vac\rangle, \tag{D.3a}$$

$$|\tfrac{1}{2};\sigma\rangle = c^\dagger_{\beta\sigma} c^\dagger_{\gamma\uparrow} c^\dagger_{\gamma\downarrow} |Vac\rangle. \tag{D.3b}$$

If we consider $\hat{H}_U = \sum_i U \hat{n}_{i\uparrow} \hat{n}_{i\downarrow}$ as a perturbation to these states to first order, the energy separation between them is given by

$$E'_\Delta = \langle 0;0|[\hat{H}_{NITQD} + \hat{H}_U]|0;0\rangle - \langle \tfrac{1}{2};S^z|[\hat{H}_{NITQD} + \hat{H}_U]|\tfrac{1}{2};S^z\rangle \tag{D.4a}$$

$$= 2E_\beta + 2E_\gamma + \langle 0;0|\hat{H}_U|0;0\rangle - E_\beta - 2E_\gamma - \langle \tfrac{1}{2};S^z|\hat{H}_U|\tfrac{1}{2};S^z\rangle \tag{D.4b}$$

$$= E_\beta + \langle 0;0|\hat{H}_U|0;0\rangle - \langle \tfrac{1}{2};S^z|\hat{H}_U|\tfrac{1}{2};S^z\rangle. \tag{D.4c}$$

E_β is a known quantity and so we only need determine

$$E''_\Delta = \langle 0;0|\hat{H}_U|0;0\rangle - \langle \tfrac{1}{2};S^z|\hat{H}_U|\tfrac{1}{2};S^z\rangle. \tag{D.5}$$

As the $S^z = \pm\frac{1}{2}$ states of the $|\frac{1}{2};S^z\rangle$ doublet are (in the absence of a field) indistinguishable, we shall from this point on set $S^z = -\frac{1}{2}$; a choice of $S^z = +\frac{1}{2}$ would, of

course, give identical results. Therefore

$$E''_\Delta = \langle 0;0|\hat{H}_U|0;0\rangle - \langle \tfrac{1}{2};-\tfrac{1}{2}|\hat{H}_U|\tfrac{1}{2};-\tfrac{1}{2}\rangle \tag{D.6a}$$

$$= \sum_i \langle Vac|c_{\gamma\downarrow}c_{\gamma\uparrow}c_{\beta\uparrow}c_{\beta\downarrow}U\hat{n}_{i\uparrow}\hat{n}_{i\downarrow}c^\dagger_{\beta\uparrow}c^\dagger_{\beta\downarrow}c^\dagger_{\gamma\uparrow}c^\dagger_{\gamma\downarrow}|Vac\rangle \tag{D.6b}$$

$$- \sum_i \langle Vac|c_{\gamma\downarrow}c_{\gamma\uparrow}c_{\beta\downarrow}U\hat{n}_{i\uparrow}\hat{n}_{i\downarrow}c^\dagger_{\beta\downarrow}c^\dagger_{\gamma\uparrow}c^\dagger_{\gamma\downarrow}|Vac\rangle.$$

Now

$$[c_{\beta\uparrow}, \hat{n}_{i\uparrow}\hat{n}_{i\downarrow}] = c_{\beta\uparrow}\hat{n}_{i\uparrow}\hat{n}_{i\downarrow} - \hat{n}_{i\uparrow}\hat{n}_{i\downarrow}c_{\beta\uparrow}, \tag{D.7a}$$

$$c_{\beta\uparrow}\hat{n}_{i\uparrow}\hat{n}_{i\downarrow} = [c_{\beta\uparrow}, \hat{n}_{i\uparrow}\hat{n}_{i\downarrow}] + \hat{n}_{i\uparrow}\hat{n}_{i\downarrow}c_{\beta\uparrow}. \tag{D.7b}$$

Substituting Eq. D.7b into Eq. D.6b gives

$$E''_\Delta = \sum_i U\langle Vac|c_{\gamma\downarrow}c_{\gamma\uparrow}c_{\beta\downarrow}[c_{\beta\uparrow}, \hat{n}_{i\uparrow}\hat{n}_{i\downarrow}]c^\dagger_{\beta\uparrow}c^\dagger_{\beta\downarrow}c^\dagger_{\gamma\uparrow}c^\dagger_{\gamma\downarrow}|Vac\rangle \tag{D.8a}$$

$$+ \sum_i U\langle Vac|c_{\gamma\downarrow}c_{\gamma\uparrow}c_{\beta\downarrow}\hat{n}_{i\uparrow}\hat{n}_{i\downarrow}c_{\beta\uparrow}c^\dagger_{\beta\uparrow}c^\dagger_{\beta\downarrow}c^\dagger_{\gamma\uparrow}c^\dagger_{\gamma\downarrow}|Vac\rangle$$

$$- \sum_i U\langle Vac|c_{\gamma\downarrow}c_{\gamma\uparrow}c_{\beta\downarrow}\hat{n}_{i\uparrow}\hat{n}_{i\downarrow}c^\dagger_{\beta\downarrow}c^\dagger_{\gamma\uparrow}c^\dagger_{\gamma\downarrow}|Vac\rangle$$

$$= \sum_i U\langle Vac|c_{\gamma\downarrow}c_{\gamma\uparrow}c_{\beta\downarrow}[c_{\beta\uparrow}, \hat{n}_{i\uparrow}\hat{n}_{i\downarrow}]c^\dagger_{\beta\uparrow}c^\dagger_{\beta\downarrow}c^\dagger_{\gamma\uparrow}c^\dagger_{\gamma\downarrow}|Vac\rangle \tag{D.8b}$$

$$+ \sum_i U\langle Vac|c_{\gamma\downarrow}c_{\gamma\uparrow}c_{\beta\downarrow}\hat{n}_{i\uparrow}\hat{n}_{i\downarrow}c^\dagger_{\beta\downarrow}c^\dagger_{\gamma\uparrow}c^\dagger_{\gamma\downarrow}|Vac\rangle$$

$$- \sum_i U\langle Vac|c_{\gamma\downarrow}c_{\gamma\uparrow}c_{\beta\downarrow}\hat{n}_{i\uparrow}\hat{n}_{i\downarrow}c^\dagger_{\beta\downarrow}c^\dagger_{\gamma\uparrow}c^\dagger_{\gamma\downarrow}|Vac\rangle$$

$$= \sum_i U\langle Vac|c_{\gamma\downarrow}c_{\gamma\uparrow}c_{\beta\downarrow}[c_{\beta\uparrow}, \hat{n}_{i\uparrow}\hat{n}_{i\downarrow}]c^\dagger_{\beta\uparrow}c^\dagger_{\beta\downarrow}c^\dagger_{\gamma\uparrow}c^\dagger_{\gamma\downarrow}|Vac\rangle. \tag{D.8c}$$

The next step is clearly to evaluate

$$[c_{\beta\uparrow}, \hat{n}_{i\uparrow}\hat{n}_{i\downarrow}] = [c_{\beta\uparrow}, \hat{n}_{i\uparrow}]\hat{n}_{i\downarrow}. \tag{D.9}$$

Now, the creation/destruction operators for dots 1, 2 and 3 may be written in terms

of the α, β and γ orbitals, viz.

$$c^\dagger_{1\sigma} = \frac{1}{\sqrt{2}}(\alpha_1+\alpha_2)c^\dagger_{\alpha\sigma} + \frac{1}{\sqrt{2}}(\beta_1+\beta_2)c^\dagger_{\beta\sigma} + \frac{1}{\sqrt{2}}(\gamma_1+\gamma_2)c^\dagger_{\gamma\sigma}, \tag{D.10a}$$

$$c^\dagger_{2\sigma} = \alpha_3 c^\dagger_{\alpha\sigma} + \beta_3 c^\dagger_{\beta\sigma} + \gamma_3 c^\dagger_{\gamma\sigma}, \tag{D.10b}$$

$$c^\dagger_{3\sigma} = \frac{1}{\sqrt{2}}(\alpha_1-\alpha_2)c^\dagger_{\alpha\sigma} + \frac{1}{\sqrt{2}}(\beta_1-\beta_2)c^\dagger_{\beta\sigma} + \frac{1}{\sqrt{2}}(\gamma_1-\gamma_2)c^\dagger_{\gamma\sigma} \tag{D.10c}$$

expressions which have the general form $c^\dagger_{x\sigma} = Ac^\dagger_{\alpha\sigma} + Bc^\dagger_{\beta\sigma} + Cc^\dagger_{\gamma\sigma}$ $(x = 1, 2, 3)$, and it follows immediately that

$$[c_{\beta\uparrow}, \hat{n}_{x\uparrow}] = c_{\beta\uparrow}[Ac^\dagger_{\alpha\uparrow} + Bc^\dagger_{\beta\uparrow} + Cc^\dagger_{\gamma\uparrow}][Ac_{\alpha\uparrow} + Bc_{\beta\uparrow} + Cc_{\gamma\uparrow}] \tag{D.11a}$$

$$-[Ac^\dagger_{\alpha\uparrow} + Bc^\dagger_{\beta\uparrow} + Cc^\dagger_{\gamma\uparrow}][Ac_{\alpha\uparrow} + Bc_{\beta\uparrow} + Cc_{\gamma\uparrow}]c_{\beta\uparrow}$$

$$= ABc_{\alpha\uparrow} + B^2 c_{\beta\uparrow}\hat{n}_{\beta\uparrow} + BCc_{\gamma\uparrow} + AB\hat{n}_{\beta\uparrow}c_{\alpha\uparrow} + BC\hat{n}_{\beta\uparrow}c_{\gamma\uparrow} \tag{D.11b}$$

and also that

$$\hat{n}_{x\downarrow} = [Ac^\dagger_{\alpha\downarrow} + Bc^\dagger_{\beta\downarrow} + Cc^\dagger_{\gamma\downarrow}][Ac_{\alpha\downarrow} + Bc_{\beta\downarrow} + Cc_{\gamma\downarrow}] \tag{D.12a}$$

$$= A^2\hat{n}_{\alpha\downarrow} + B^2\hat{n}_{\beta\downarrow} + C^2\hat{n}_{\gamma\downarrow} + AB(c^\dagger_{\alpha\downarrow}c_{\beta\downarrow} + H.c.) + AC(c^\dagger_{\alpha\downarrow}c_{\beta\uparrow} + H.c.) + BC(c^\dagger_{\beta\downarrow}c_{\gamma\downarrow} + H.c.), \tag{D.12b}$$

where $\hat{n}_{\nu\sigma} = c^\dagger_{\nu\sigma}c_{\nu\sigma}$, $\nu = \alpha, \beta, \gamma$. Using Eq. D.11 and D.12 we may easily show that

$$\langle Vac|c_{\gamma\downarrow}c_{\gamma\uparrow}c_{\beta\downarrow}[c_{\beta\uparrow}, \hat{n}_{x\uparrow}]\hat{n}_{x\downarrow}c^\dagger_{\beta\uparrow}c^\dagger_{\beta\downarrow}c^\dagger_{\gamma\uparrow}c^\dagger_{\gamma\downarrow}|Vac\rangle = B^2(B^2 + C^2), \tag{D.13}$$

from which it follows that E''_Δ as given by Eq. D.8c may be written

$$E''_\Delta = \frac{U}{4}(\beta_1+\beta_2)^2[(\beta_1+\beta_2)^2+(\gamma_1+\gamma_2)^2] + U\beta_3^2(\beta_3^2+\gamma_3^2) + \frac{U}{4}(\beta_1-\beta_2)^2[(\beta_1-\beta_2)^2+(\gamma_1-\gamma_2)^2], \tag{D.14}$$

and so

$$\begin{aligned} E'_{\Delta} =& E_{\beta} + \frac{U}{4}(\beta_1 + \beta_2)^2[(\beta_1 + \beta_2)^2 + (\gamma_1 + \gamma_2)^2] + U\beta_3^2(\beta_3^2 + \gamma_3^2) \\ &+ \frac{U}{4}(\beta_1 - \beta_2)^2[(\beta_1 - \beta_2)^2 + (\gamma_1 - \gamma_2)^2]. \end{aligned} \tag{D.15}$$

In the mirror symmetric case ($x = 0$), $E_{\beta} = \epsilon - t'$, $\alpha_2 = \gamma_2 = \beta_1 = \beta_3 = 0$, $\beta_2 = 1$ and $\gamma_1 = \gamma$. Eq. D.15 therefore reduces to

$$E'_{\Delta} = \epsilon - t' + \frac{U}{2}(1 + \gamma^2). \tag{D.16}$$

Appendix E

Schrieffer-Wolff Transformations with Numerically Evaluated Elements

In the sections of this thesis which discuss regime III of the ACTM and AACTM (Sec. 4.8.1, 4.12.1, 5.7 and 5.11.1), and the equivalent orbital regime of the TiP model (Sec. 6.7.1, 6.8 and 6.11.1) we find that some of the low energy effective models, arising as a result of Schrieffer-Wolff transformations [2, 13], take the form of a Kondo model with a coupling between the TQD and the conduction band which we can determine by evaluating the matrix elements of the low energy effective model numerically. In this appendix a general description of this technique is provided, illustrated by a simple model.

Let us consider a system described by the general Hamiltonian

$$\hat{H} = \hat{H}_0 + \hat{H}_1 \tag{E.1}$$

where we will treat $\hat{H}_1$ as a perturbation to the states of $\hat{H}_0$. The eigenstates of $\hat{H}_0$

are constructed from the orthonormal basis states of the system, $|\phi_i\rangle$,

$$|\psi_A\rangle = \sum_i \lambda_i^A |\phi_i\rangle, \tag{E.2}$$

where λ_i^A is a constant and $\hat{H}_0|\psi_A\rangle = E_A|\psi_A\rangle$. The unity operator which spans the low energy manifold here is

$$\hat{1} = \sum_x |\psi_x\rangle\langle\psi_x| \tag{E.3}$$

where $\hat{1}\hat{H}_0\hat{1} = E_0$, and we also define $\hat{P} = \hat{1} - \hat{1}_{full}$, where $\hat{1}_{full}$ is the unity operator for the complete Hilbert space. We further assume that $\hat{1}\hat{H}_1\hat{1} = 0$ (i.e. that $\hat{H}_1$ cannot, to first order, connect states within the low energy manifold: this is the case for all the Schrieffer-Wolff transformations in this thesis). Therefore, using Brillouin-Wigner perturbation theory [93] to treat $\hat{H}_1$ as a perturbation to the states of $\hat{H}_0$ (to second order), the effective Hamiltonian of the system is given by

$$\begin{aligned}
\hat{H}_{eff} =& \hat{1}\hat{H}_0\hat{1} + \hat{1}\hat{H}_1(E_0 - \hat{H}_0)^{-1}\hat{P}\hat{H}_1\hat{1} && \text{(E.4a)}\\
=& E_0 + \sum_{x,x'} |\psi_x\rangle\langle\psi_x|\hat{H}_1(E_0 - \hat{H}_0)^{-1}\hat{P}\hat{H}_1|\psi_{x'}\rangle\langle\psi_{x'}| && \text{(E.4b)}\\
=& E_0 + \sum_{x,x'}\sum_i |\psi_x\rangle\langle\psi_x|\hat{H}_1(E_0 - \hat{H}_0)^{-1}\hat{P}\hat{H}_1\lambda_i^{x'}|\phi_i\rangle\langle\psi_{x'}| && \text{(E.4c)}\\
=& E_0 + \sum_{x,x'}\sum_i \lambda_i^{x'}|\psi_x\rangle\langle\psi_x|\hat{H}_1(E_0 - \hat{H}_0)^{-1}\hat{P}\hat{H}_1|\phi_i\rangle\langle\psi_{x'}|. && \text{(E.4d)}
\end{aligned}$$

Now

$$\hat{P}\hat{H}_1|\phi_i\rangle = \hat{H}_1|\phi_i\rangle = \sum_j \alpha_{ij}|\phi_j\rangle, \tag{E.5}$$

($\hat{P}$ has no effect as $\hat{H}_1$ cannot connect states within the low energy manifold to first order) and substituting this into Eq. E.4d gives

$$\begin{aligned}
\hat{H}_{eff} =& E_0 + \sum_{x,x'}\sum_{i,j} \lambda_i^{x'}|\psi_x\rangle\langle\psi_x|\hat{H}_1(E_0 - \hat{H}_0)^{-1}\alpha_{ij}|\phi_j\rangle\langle\psi_{x'}|\\
=& E_0 + \sum_{x,x'}\sum_{i,j} \lambda_i^{x'}\alpha_{ij}|\psi_x\rangle\langle\psi_x|\hat{H}_1(E_0 - \hat{H}_0)^{-1}|\phi_j\rangle\langle\psi_{x'}|.
\end{aligned} \tag{E.6}$$

We may write the basis states of the system in terms of linear combinations of the eigenstates of $\hat{H}_0$,

$$|\phi_j\rangle = \sum_k \beta_k^j |\psi_k\rangle \tag{E.7}$$

and substituting this into Eq. E.6 gives

$$\begin{aligned}
\hat{H}_{eff} =& E_0 + \sum_{x,x'}\sum_{i,j,k} \alpha_{ij}\lambda_i^{x'}|\psi_x\rangle\langle\psi_x|\hat{H}_1(E_0-\hat{H}_0)^{-1}\beta_k^j|\psi_k\rangle\langle\psi_{x'}| && \text{(E.8a)}\\
=& E_0 + \sum_{x,x'}\sum_{i,j,k} \alpha_{ij}\lambda_i^{x'}\beta_k^j|\psi_x\rangle\langle\psi_x|\hat{H}_1(E_0-\hat{H}_0)^{-1}|\psi_k\rangle\langle\psi_{x'}| && \text{(E.8b)}\\
=& E_0 + \sum_{x,x'}\sum_{i,j,k} \alpha_{ij}\lambda_i^{x'}\beta_k^j|\psi_x\rangle\langle\psi_x|\hat{H}_1(E_0-E_k)^{-1}|\psi_k\rangle\langle\psi_{x'}| && \text{(E.8c)}\\
=& E_0 + \sum_{x,x'}\sum_{i,j,k} \alpha_{ij}\lambda_i^{x'}\beta_k^j(E_0-E_k)^{-1}|\psi_x\rangle\langle\psi_x|\hat{H}_1|\psi_k\rangle\langle\psi_{x'}| && \text{(E.8d)}\\
=& E_0 + \sum_{x,x'}\sum_{i,j,k,l} \alpha_{ij}\lambda_i^{x'}\beta_k^j(E_0-E_k)^{-1}|\psi_x\rangle\langle\psi_x|\hat{H}_1\lambda_l^k|\phi_l\rangle\langle\psi_{x'}| && \text{(E.8e)}\\
=& E_0 + \sum_{x,x'}\sum_{i,j,k,l} \alpha_{ij}\lambda_i^{x'}\beta_k^j(E_0-E_k)^{-1}\lambda_l^k|\psi_x\rangle\langle\psi_x|\hat{H}_1|\phi_l\rangle\langle\psi_{x'}| && \text{(E.8f)}\\
=& E_0 + \sum_{x,x'}\sum_{i,j,k,l,m} \alpha_{ij}\lambda_i^{x'}\beta_k^j(E_0-E_k)^{-1}\lambda_l^k|\psi_x\rangle\langle\psi_x|\alpha_{lm}|\phi_m\rangle\langle\psi_{x'}| && \text{(E.8g)}\\
=& E_0 + \sum_{x,x'}\sum_{i,j,k,l,m} \alpha_{ij}\lambda_i^{x'}\beta_k^j(E_0-E_k)^{-1}\lambda_l^k\alpha_{lm}|\psi_x\rangle\langle\psi_x||\phi_m\rangle\langle\psi_{x'}| && \text{(E.8h)}\\
=& E_0 + \sum_{x,x'}\sum_{i,j,k,l,m,n} \alpha_{ij}\lambda_i^{x'}\beta_k^j(E_0-E_k)^{-1}\lambda_l^k\alpha_{lm}|\psi_x\rangle\langle\phi_n|\lambda_n^x|\phi_m\rangle\langle\psi_{x'}| && \text{(E.8i)}\\
=& E_0 + \sum_{x,x'}\sum_{i,j,k,l,m,n} \lambda_n^x\alpha_{lm}\lambda_l^k(E_0-E_k)^{-1}\beta_k^j\alpha_{ij}\lambda_i^{x'}|\psi_x\rangle\langle\phi_n||\phi_m\rangle\langle\psi_{x'}| && \text{(E.8j)}\\
=& E_0 + \sum_{x,x'}\sum_{i,j,k,l,m,n} \lambda_n^x\alpha_{lm}\lambda_l^k(E_0-E_k)^{-1}\beta_k^j\alpha_{ij}\lambda_i^{x'}|\psi_x\rangle\delta_{mn}\langle\psi_{x'}| && \text{(E.8k)}\\
=& E_0 + \sum_{x,x'}\sum_{i,j,k,l,m} \lambda_m^x\alpha_{lm}\lambda_l^k(E_0-E_k)^{-1}\beta_k^j\alpha_{ij}\lambda_i^{x'}|\psi_x\rangle\langle\psi_{x'}| && \text{(E.8l)}\\
=& E_0 + \sum_{x,x'} A_{xx'}|\psi_x\rangle\langle\psi_{x'}|. && \text{(E.8m)}\\
& && \text{(E.8n)}
\end{aligned}$$

In order to calculate the matrix elements $A_{xx'}$ one therefore needs to know the

eigenstates and eigenvalues of $\hat{H}_0$ (from which one can determine the unity operator for the low energy manifold and the coefficients β_k^j), and the coefficients α_{ij}. Calculating these values may be a lengthy process, but is not usually complex; armed with this information, the calculation of the matrix elements $A_{xx'}$ is essentially trivial, and can quickly be done by computer.

Appendix F

Scaling in the Anisotropic Kondo Model

In this appendix we derive the Kondo Temperature for the specific case of the anisotropic Kondo model which is the low energy effective model for regime II ($J > 10T_{\mathrm{K}}$) of the apex coupled trimer model under a magnetic field in both the mirror symmetric (ACTM) and asymmetric (AACTM) cases (Sec. 4.10 and 5.9). We consider the (more complex) asymmetric case, and as such our effective Hamiltonian is

$$\hat{H}_{eff} = \frac{1}{2}J^0_{\mathrm{K},\perp}\hat{\mathcal{T}}^+\hat{S}^-(0) + \frac{1}{2}J^0_{\mathrm{K},\perp}\hat{\mathcal{T}}^-\hat{S}^+(0) + J^0_{\mathrm{K},z}\hat{\mathcal{T}}^z\hat{S}^z(0) + E_\Delta\hat{\mathcal{T}}^z + \hat{H}_L, \qquad \text{(F.1)}$$

where

$$J^0_{\mathrm{K},\perp} = -\frac{2}{\sqrt{6}}\alpha J_{\mathrm{K}}, \qquad \text{(F.2a)}$$

$$J^0_{\mathrm{K},z} = \frac{2}{3}\alpha^2 J_{\mathrm{K}}, \qquad \text{(F.2b)}$$

are the bare model parameters, and where α is defined in Eq. 5.12, and $\alpha = 1$ in the local moment case of the mirror symmetric model (Sec. 4.10). Our scaling equations

are (from Ref. [14] and Sec. 2.2)

$$\frac{dJ_{\mathrm{K},z}}{d\ln D} = -\rho J_{\mathrm{K},\perp}^2, \tag{F.3a}$$

$$\frac{dJ_{\mathrm{K},\perp}}{d\ln D} = -\rho J_{\mathrm{K},\perp} J_{\mathrm{K},z}, \tag{F.3b}$$

$$J_{\mathrm{K},z}^2 - J_{\mathrm{K},\perp}^2 = 4\alpha^2 J_{\mathrm{K}}^2 \left[\frac{\alpha^2}{9} - \frac{1}{6}\right] < 0. \tag{F.3c}$$

Substituting Eq. F.3c into Eq. F.3a we obtain the result

$$\frac{dJ_{\mathrm{K},z}}{d\ln D} = -\rho \left[J_{\mathrm{K},z}^2 + 4\alpha^2 J_{\mathrm{K}}^2 \left(\frac{1}{6} - \frac{\alpha^2}{9}\right)\right], \tag{F.4a}$$

$$\frac{dJ_{\mathrm{K},z}}{\left[J_{\mathrm{K},z}^2 + 4\alpha^2 J_{\mathrm{K}}^2 \left(\frac{1}{6} - \frac{\alpha^2}{9}\right)\right]} = -\rho d\ln D, \tag{F.4b}$$

which we may then integrate along the scaling trajectory such that

$$\frac{1}{\left|2\alpha J_{\mathrm{K}}\sqrt{\frac{1}{6} - \frac{\alpha^2}{9}}\right|} \arctan\left[\frac{J_{\mathrm{K},z}}{\left|2\alpha J_{\mathrm{K}}\sqrt{\frac{1}{6} - \frac{\alpha^2}{9}}\right|}\right]\Bigg|_{J_{\mathrm{K},z}^0}^{\tilde{J}_{\mathrm{K},z}} = -\rho \ln(T_{\mathrm{K}}^h/D), \tag{F.5}$$

where $\tilde{J}_{\mathrm{K},z}$ is defined as the value of $J_{\mathrm{K},z}$ when $\tilde{D} = T_{\mathrm{K}}^h$, where $\tilde{D}$ is the renormalised bandwidth[1]. Rearranging Eq. F.5 we obtain the result

$$\frac{T_{\mathrm{K}}^h}{D} = \exp\left\{-\frac{1}{\rho\left|2\alpha J_{\mathrm{K}}\sqrt{\frac{1}{6} - \frac{\alpha^2}{9}}\right|}\left(\arctan\left[\frac{\tilde{J}_{\mathrm{K},z}}{\left|2\alpha J_{\mathrm{K}}\sqrt{\frac{1}{6} - \frac{\alpha^2}{9}}\right|}\right] - \arctan\left[\frac{J_{\mathrm{K},z}^0}{\left|2\alpha J_{\mathrm{K}}\sqrt{\frac{1}{6} - \frac{\alpha^2}{9}}\right|}\right]\right)\right\}. \tag{F.6}$$

[1]It is only necessary that our choice of $\tilde{J}_{\mathrm{K},z}$ be internally consistent, and $\gg J_{\mathrm{K}}$: a different choice of $\tilde{J}_{\mathrm{K},z}$ will result in a constant shift in the calculated value of T_{K}^h, which is irrelevant as our calculated T_{K}^h is in any case only proportional to the value determined using the NRG.

Substituting Eq. F.2b into Eq. F.6, and making use of the relationship $\arctan[a/b] = \frac{\pi}{2} - \frac{b}{a}$ for $a \gg b$ (valid in this case as we choose $\tilde{J}_{\mathrm{K},z} \gg J_{\mathrm{K}}$), we obtain the result

$$\frac{T_{\mathrm{K}}^h}{D} = \exp\left\{ -\frac{1}{\rho\left|2\alpha J_{\mathrm{K}}\sqrt{\frac{1}{6}-\frac{\alpha^2}{9}}\right|}\left(\frac{\pi}{2} - \arctan\left[\frac{|\alpha|}{3\sqrt{\frac{1}{6}-\frac{\alpha^2}{9}}}\right]\right)\right\}, \tag{F.7}$$

where we assume that the terms $\mathcal{O}(\frac{J_{\mathrm{K}}}{\tilde{J}_{\mathrm{K},z}})$ and higher in the expansion of $\arctan(A\tilde{J}_{\mathrm{K},z}/J_{\mathrm{K}})$ are negligible. Finally, taking $\alpha = 1$ we find the mirror symmetric result

$$\frac{T_{\mathrm{K}}^h}{D} = \exp\left\{ -\frac{3}{\sqrt{2}\rho J_{\mathrm{K}}}\left(\frac{\pi}{2} - \arctan\sqrt{2}\right)\right\}. \tag{F.8}$$

Appendix G

Scaling in the Anisotropic Kondo Model II

In this appendix we derive the Kondo temperature for the specific case of the anisotropic Kondo model which is the low energy effective model for the spin regime of the trimer in parallel under a magnetic field (see Sec. 6.10). We will build heavily upon the results presented in Appendix F. Our effective Hamiltonian is

$$\hat{H}_{eff} = \frac{1}{2}J^0_{\mathrm{K},\perp}\hat{\mathcal{T}}^+\hat{S}^-(0) + \frac{1}{2}J^0_{\mathrm{K},\perp}\hat{\mathcal{T}}^-\hat{S}^+(0) + J^0_{\mathrm{K},z}\hat{\mathcal{T}}^z\hat{S}^z(0) + E_\Delta\hat{\mathcal{T}}^z + \hat{H}_L, \quad \text{(G.1)}$$

where

$$J^0_{\mathrm{K},\perp} = \frac{2}{\sqrt{6}}(J'_{\mathrm{K}} - J_{\mathrm{K}}), \quad \text{(G.2a)}$$

$$J^0_{\mathrm{K},z} = \frac{2}{3}J_{\mathrm{K}} + \frac{1}{3}J'_{\mathrm{K}}, \quad \text{(G.2b)}$$

are the bare model parameters. Our scaling equations are (from Ref. [14] and Sec. 2.2)

$$\frac{dJ_{\mathrm{K},z}}{d\ln D} = -\rho J_{\mathrm{K},\perp}^2, \tag{G.3a}$$

$$\frac{dJ_{\mathrm{K},\perp}}{d\ln D} = -\rho J_{\mathrm{K},\perp} J_{\mathrm{K},z}, \tag{G.3b}$$

$$J_{\mathrm{K},z}^2 - J_{\mathrm{K},\perp}^2 = -\frac{2}{9}J_{\mathrm{K}}^2 - \frac{5}{9}J_{\mathrm{K}}' + \frac{16}{9}J_{\mathrm{K}}J_{\mathrm{K}}' = C. \tag{G.3c}$$

We find that C, as defined in Eq. G.3c, can be both positive and negative: these two cases must be treated separately. We assume that $J_{\mathrm{K}}' = \lambda J_{\mathrm{K}}$, and we may therefore write

$$C = \frac{1}{9}(16\lambda - 2 - 5\lambda^2)J_{\mathrm{K}}^2. \tag{G.4}$$

Solving this quadratic, we find that $C < 0$ when $\lambda < \frac{1}{5}(8 - 3\sqrt{6}) \simeq 0.1303$ and $\lambda > \frac{1}{5}(8 + 3\sqrt{6}) \simeq 3.0697$ (the latter case is irrelevant, as we restrict ourselves to the region $0 < \lambda < 1$). When $C < 0$ we may use identical arguments to those given in Appendix F, which gives rise to a very similar expression for the Kondo temperature;

$$\frac{T_{\mathrm{K}}^h}{D} = \exp\left[-\frac{1}{\rho\sqrt{|C|}}\left\{\frac{\pi}{2} - \arctan\left(\frac{\frac{2}{3}J_{\mathrm{K}} + \frac{1}{3}J_{\mathrm{K}}'}{\sqrt{|C|}}\right)\right\}\right]. \tag{G.5}$$

This expression is not however valid when $C > 0$. If we now consider that case, we may begin by substituting Eq. G.3c into Eq. G.3a. This gives the result

$$\frac{dJ_{\mathrm{K},z}}{d\ln D} = -\rho(J_{\mathrm{K},z}^2 - C), \tag{G.6a}$$

$$\frac{dJ_{\mathrm{K},z}}{J_{\mathrm{K},z}^2 - C} = -\rho d\ln D, \tag{G.6b}$$

$$\frac{dJ_{\mathrm{K},z}}{(J_{\mathrm{K},z} + \sqrt{C})(J_{\mathrm{K,z}} - \sqrt{C})} = -\rho d\ln D, \tag{G.6c}$$

which we may integrate along the scaling trajectory, such that

$$\frac{1}{2\sqrt{C}}\left[\ln\left|\frac{J_{\mathrm{K},z}-\sqrt{C}}{J_{\mathrm{K},z}+\sqrt{C}}\right|\right]\Bigg|_{J^0_{\mathrm{K},z}}^{\tilde{J}_{\mathrm{K},z}} = -\rho\ln(T^h_{\mathrm{K}}/D). \tag{G.7}$$

where $\tilde{J}_{\mathrm{K},z}$ is defined as the value of $J_{\mathrm{K},z}$ for which $\tilde{D} = T^h_{\mathrm{K}}$, where $\tilde{D}$ is the renormalised bandwidth. Now $\tilde{J}_{\mathrm{K},z} \gg C$, such that $(\tilde{J}_{\mathrm{K},z}+\sqrt{C})/(\tilde{J}_{\mathrm{K},z}-\sqrt{C}) \simeq 1$. We may therefore write the Kondo temperature here as

$$\ln(T^h_{\mathrm{K}}/D) = -\frac{1}{2\rho\sqrt{C}}\ln\left|\frac{J^0_{\mathrm{K},z}+\sqrt{C}}{J^0_{\mathrm{K},z}-\sqrt{C}}\right|, \tag{G.8a}$$

$$\frac{T^h_{\mathrm{K}}}{D} = \left|\frac{J^0_{\mathrm{K},z}+\sqrt{C}}{J^0_{\mathrm{K},z}-\sqrt{C}}\right|^{\left\{-\frac{1}{2\rho\sqrt{C}}\right\}}, \tag{G.8b}$$

results which (as discussed in Sec. 6.10.2) we find in good agreement with the NRG.

Bibliography

[1] L. Kouwenhoven and L. Glazman, Physics World **14**, 33 (2001).

[2] A. C. Hewson, *The Kondo Problem to Heavy Fermions* (Cambridge University Press, Cambridge, 1993).

[3] J. Kondo, Prog. Theor. Phys. **32**, 37 (1964).

[4] K. G. Wilson, Rev. Mod. Phys. **47**, 773 (1975).

[5] D. Goldhaber-Gordon *et al.*, Nature **391**, 156 (1998).

[6] P. W. Anderson, Phys. Rev. **124**, 41 (1961).

[7] H. R. Krishnamurthy, J. W. Wilkins, and K. G. Wilson, Phys. Rev. B **21**, 1003 (1980).

[8] H. R. Krishnamurthy, J. W. Wilkins, and K. G. Wilson, Phys. Rev. B **21**, 1044 (1980).

[9] K. Yosida and K. Yamada, Prog. Theor. Phys. Suppl. **46**, 244 (1970).

[10] K. Yamada, Prog. Theor. Phys. **53**, 970 (1975).

[11] K. Yosida and K. Yamada, Prog. Theor. Phys. **53**, 1286 (1975).

[12] C. Zener, Phys. Rev. **81**, 440 (1951).

[13] J. R. Schrieffer and P. A. Wolff, Phys. Rev. **149**, 491 (1966).

[14] P. W. Anderson, J. Phys. C **3**, 2436 (1970).

[15] N. Andrei, Phys. Rev. Lett. **45**, 379 (1980).

[16] V. Filyov, A. Tzvelik, and P. Wiegmann, Phys. Lett. A **81**, 175 (1981).

[17] N. Andrei, K. Furuya, and J. H. Lowenstein, Rev. Mod. Phys. **55**, 331 (1983).

[18] P. Wiegmann, Phys. Lett. A **80**, 163 (1980).

[19] N. Kawakami and A. Okiji, Phys. Lett. A **86**, 483 (1981).

[20] N. Kawakami and A. Okiji, Prog. Theor. Phys. Suppl. **101**, 429 (1990).

[21] Ph. Nozières and A. Blandin, J. Phys. France **41**, 193 (1980).

[22] D. C. Langreth, Phys. Rev. **150**, 516 (1966).

[23] D. Newns and N. Read, Adv. in Phys. **36**, 799 (1987).

[24] I. Affleck, Acta Phys. Pol. B **26**, 1869 (1995).

[25] D. E. Logan, M. P. Eastwood, and M. A. Tusch, J. Phys.: Condens. Matter **10**, 2673 (1998).

[26] D. E. Logan and N. L. Dickens, J. Phys.: Condens. Matter **14**, 3605 (2002).

[27] M. R. Galpin, A. B. Gilbert, and D. E. Logan, J. Phys.: Condens. Matter **21**, 375602 (2009).

[28] A. C. Hewson, Phys. Rev. Lett. **70**, 4007 (1993).

[29] K. Edwards and A. C. Hewson, J. Phys.: Condens. Matter **23**, 045601 (2011).

[30] Y. Nishikawa, D. J. G. Crow, and A. C. Hewson, Phys. Rev. B **82**, 245109 (2010).

[31] Y. Nishikawa, D. J. G. Crow, and A. C. Hewson, Phys. Rev. B **82**, 115123 (2010).

[32] M. R. Galpin, DPhil Thesis, University of Oxford, 2005.

[33] K. Grove-Rasmussen *et al.*, Nano Lett. **8**, 1055 (2008).

[34] F. B. Anders, D. E. Logan, M. R. Galpin, and G. Finkelstein, Phys. Rev. Lett. **100**, 086809 (2008).

[35] M. A. Kastner, Physics Today **46**, 24 (1993).

[36] L. Kouwenhoven and C. Marcus, Physics World **11**, 35 (1998).

[37] H. Jeong, A. M. Chang, and M. R. Melloch, Science **293**, 2221 (2001).

[38] R. H. Blick *et al.*, Phys. Rev. B **53**, 7899 (1996).

[39] A. Vidan *et al.*, J. Supercond. **18**, 223 (2005).

[40] D. Schröer *et al.*, Phys. Rev. B **76**, 075306 (2007).

[41] L. Gaudreau *et al.*, Phys. Rev. Lett. **97**, 036807 (2006).

[42] L. Gaudreau *et al.*, Nature Physics **8**, 54 (2012).

[43] M. C. Rogge and R. J. Haug, Phys. Rev. B **77**, 193306 (2008).

[44] K. Kikoin and Y. Avishai, Phys. Rev. Lett. **86**, 2090 (2001).

[45] M. Vojta, R. Bulla, and W. Hofstetter, Phys. Rev. B **65**, 140405 (2002).

[46] L. Borda *et al.*, Phys. Rev. Lett. **90**, 026602 (2003).

[47] M. R. Galpin, D. E. Logan, and H. R. Krishnamurthy, Phys. Rev. Lett. **94**, 186406 (2005).

[48] A. K. Mitchell, M. R. Galpin, and D. E. Logan, Europhys. Lett. **76**, 95 (2006).

[49] R. López *et al.*, Phys. Rev. B **71**, 115312 (2005).

[50] G. Zaránd, C.-H. Chung, P. Simon, and M. Vojta, Phys. Rev. Lett. **97**, 166802 (2006).

[51] L. G. G. V. Dias da Silva, K. Ingersent, N. Sandler, and S. E. Ulloa, Phys. Rev. B **78**, 153304 (2008).

[52] R. Žitko and J. Bonča, Phys. Rev. B **76**, 241305 (2007).

[53] R. Žitko and J. Bonča, Phys. Rev. B **74**, 045312 (2006).

[54] R. Žitko and J. Bonča, Phys. Rev. B **73**, 035332 (2006).

[55] D. E. Logan, C. J. Wright, and M. R. Galpin, Phys. Rev. B **80**, 125117 (2009).

[56] F. W. Jayatilaka, M. R. Galpin, and D. E. Logan, Phys. Rev. B **84**, 115111 (2011).

[57] C.-H. Chung and W. Hofstetter, Phys. Rev. B **76**, 045329 (2007).

[58] B. Lazarovits, P. Simon, G. Zaránd, and L. Szunyogh, Phys. Rev. Lett. **95**, 077202 (2005).

[59] A. Oguri, Y. Nisikawa, and A. C. Hewson, J. Phys. Soc. Jpn. **74**, 2554 (2005).

[60] R. Žitko, J. Bonča, A. Ramšak, and T. Rejec, Phys. Rev. B **73**, 153307 (2006).

[61] K. Kikoin, T. Kuzmenko, and Y. Avishai, Physica B **378-380**, 906 (2006).

[62] T. Kuzmenko, K. Kikoin, and Y. Avishai, Phys. Rev. B **73**, 235310 (2006).

[63] T. Kuzmenko, K. Kikoin, and Y. Avishai, Phys. Rev. Lett. **96**, 046601 (2006).

[64] A. M. Lobos and A. A. Aligia, Phys. Rev. B **74**, 165417 (2006).

[65] A. Oguri, Y. Nisikawa, Y. Tanaka, and T. Numata, J. Magn. Magn. Mater. **310**, 1139 (2007).

[66] W.-z. Wang, Phys. Rev. B **76**, 115114 (2007).

[67] M. Ferrero, L. D. Leo, P. Lecheminant, and M. Fabrizio, J. Phys.: Condens. Matter **19**, 433201 (2007).

[68] M. Korkusinski *et al.*, Phys. Rev. B **75**, 115301 (2007).

[69] K. Kikoin, Low Temp. Phys. **33**, 105 (2007).

[70] F. Delgado and P. Hawrylak, J. Phys.: Condens. Matter **20**, 315207 (2008).

[71] R. Žitko and J. Bonča, Phys. Rev. B **77**, 245112 (2008).

[72] W.-z. Wang, Phys. Rev. B **78**, 235316 (2008).

[73] P. Trocha and J. Barnaś, J. Phys.: Condens. Matter **20**, 125220 (2008).

[74] T. Numata, Y. Nisikawa, A. Oguri, and A. C. Hewson, Phys. Rev. B **80**, 155330 (2009).

[75] G. Chiappe, E. V. Anda, L. Costa Ribeiro, and E. Louis, Phys. Rev. B **81**, 041310 (2010).

[76] E. Vernek, P. A. Orellana, and S. E. Ulloa, Phys. Rev. B **82**, 165304 (2010).

[77] A. Oguri *et al.*, Phys. Rev. B **83**, 205304 (2011).

[78] L. Gaudreau *et al.*, Appl. Phys. Lett. **95**, 193101 (2009).

[79] G. Granger *et al.*, Phys. Rev. B **82**, 075304 (2010).

[80] S. Amaha *et al.*, Appl. Phys. Lett. **94**, 092103 (2009).

[81] A. Mühle, W. Wegscheider, and R. J. Haug, Appl. Phys. Lett. **92**, 013126 (2008).

[82] S. Amaha *et al.*, Physica E **40**, 1322 (2008).

[83] A. Vidan *et al.*, Appl. Phys. Lett. **85**, 3602 (2004).

[84] T. Takakura *et al.*, Appl. Phys. Lett. **97**, 212104 (2010).

[85] S. Amaha *et al.*, Phys. Rev. B **85**, 081301 (2012).

[86] E. A. Laird *et al.*, Phys. Rev. B **82**, 075403 (2010).

[87] M. Busl, R. Sánchez, and G. Platero, Phys. Rev. B **81**, 121306 (2010).

[88] A. K. Mitchell and D. E. Logan, Phys. Rev. B **81**, 075126 (2010).

[89] E. Vernek *et al.*, Phys. Rev. B **80**, 035119 (2009).

[90] A. K. Mitchell, T. F. Jarrold, and D. E. Logan, Phys. Rev. B **79**, 085124 (2009).

[91] H.-H. Fu and K.-L. Yao, J. Appl. Phys. **108**, 084510 (2010).

[92] H.-H. Fu and K.-L. Yao, J. Appl. Phys. **110**, 094502 (2011).

[93] J. M. Ziman, *Elements of Advanced Quantum Theory* (Cambridge University Press, Cambridge, 1969).

[94] D. M. Cragg and P. Lloyd, J. Phys. C **12**, L215 (1979).

[95] D. M. Cragg, P. Lloyd, and P. Nozieres, J. Phys. C **13**, 803 (1980).

[96] H. B. Pang and D. L. Cox, Phys. Rev. B **44**, 9454 (1991).

[97] B. A. Jones and C. M. Varma, Phys. Rev. Lett. **58**, 843 (1987).

[98] B. A. Jones and C. M. Varma, Phys. Rev. B **40**, 324 (1989).

[99] O. Sakai, Y. Shimizu, and T. Kasuya, Solid State Commun. **75**, 81 (1990).

[100] O. Sakai and Y. Shimizu, J. Phys. Soc. Jpn. **61**, 2333 (1992).

[101] C. A. Paula, M. F. Silva, and L. N. Oliveira, Phys. Rev. B **59**, 85 (1999).

[102] M.-S. Choi, D. Sánchez, and R. López, Phys. Rev. Lett. **92**, 056601 (2004).

[103] J. Martinek *et al.*, Phys. Rev. Lett. **91**, 247202 (2003).

[104] K. Satori, H. Shiba, O. Sakai, and Y. Shimizu, J. Phys. Soc. Jpn. **61**, 3239 (1992).

[105] O. Sakai, Y. Shimizu, H. Shiba, and K. Satori, J. Phys. Soc. Jpn. **62**, 3181 (1993).

[106] M.-S. Choi, M. Lee, K. Kang, and W. Belzig, Phys. Rev. B **70**, 020502 (2004).

[107] R. Bulla, T. A. Costi, and T. Pruschke, Rev. Mod. Phys. **80**, 395 (2008).

[108] J. Binney, N. Dowrick, A. Fisher, and M. Newman, *The Theory of Critical Phenomena: An Introduction to the Renormalization Group* (Oxford University Press, Oxford, 1992).

[109] T. L. Hill, *An Introduction to Statistical Thermodynamics* (Dover, New York, 1986).

[110] A. Weichselbaum and J. von Delft, Phys. Rev. Lett. **99**, 076402 (2007).

[111] R. Peters, T. Pruschke, and F. B. Anders, Phys. Rev. B **74**, 245114 (2006).

[112] Y. Meir and N. S. Wingreen, Phys. Rev. Lett. **68**, 2512 (1992).

[113] T. A. Costi, A. C. Hewson, and V. Zlatic, J. Phys.: Condens. Matter **6**, 2519 (1994).

[114] R. Bulla, T. A. Costi, and D. Vollhardt, Phys. Rev. B **64**, 045103 (2001).

[115] F. B. Anders and A. Schiller, Phys. Rev. Lett. **95**, 196801 (2005).

[116] R. Bulla, A. C. Hewson, and T. Pruschke, J. Phys.: Condens. Matter **10**, 8365 (1998).

[117] D. N. Zubarev, Soviet Physics Uspekhi **3**, 320 (1960).

[118] W. C. Oliveira and L. N. Oliveira, Phys. Rev. B **49**, 11986 (1994).

[119] H. O. Frota and L. N. Oliveira, Phys. Rev. B **33**, 7871 (1986).

[120] J. M. Luttinger and J. C. Ward, Phys. Rev. **118**, 1417 (1960).

[121] T. A. Costi, Phys. Rev. Lett. **85**, 1504 (2000).

[122] W. Hofstetter, Phys. Rev. Lett. **85**, 1508 (2000).

[123] A. C. Hewson, J. Bauer, and W. Koller, Phys. Rev. B **73**, 045117 (2006).

[124] R. Žitko, R. Peters, and T. Pruschke, New J. Phys. **11**, 053003 (2009).

[125] J. M. Luttinger, Phys. Rev. **119**, 1153 (1960).

[126] W. Koller, A. C. Hewson, and D. Meyer, Phys. Rev. B **72**, 045117 (2005).

[127] P. Mehta *et al.*, Phys. Rev. B **72**, 014430 (2005).

[128] B. Su, V. J. Goldman, and J. E. Cunningham, Science **255**, 313 (1992).

[129] C. W. J. Beenakker, Phys. Rev. B **44**, 1646 (1991).

[130] R. C. Ashoori *et al.*, Phys. Rev. Lett. **71**, 613 (1993).

[131] T. A. Fulton and G. J. Dolan, Phys. Rev. Lett. **59**, 109 (1987).

[132] U. Meirav, M. A. Kastner, and S. J. Wind, Phys. Rev. Lett. **65**, 771 (1990).

[133] C. J. Wright, M. R. Galpin, and D. E. Logan, Phys. Rev. B **84**, 115308 (2011).

[134] M. Pustilnik, Y. Avishai, and K. Kikoin, Phys. Rev. Lett. **84**, 1756 (2000).

[135] P. Chaikin and T. Lubensky, *Principles of condensed matter physics* (Cambridge University Press, Cambridge, 1995).

[136] P. J. Bickel and K. A. Doksum, *Mathematical Statistics: Basic Ideas and Selected Topics* (Holden-Day, Oakland, 1977).

[137] J. R. Magnus and H. Neudecker, *Matrix Differential Calculus With Applications in Statistics and Econometrics* (John Wiley and Sons, Chichester, 1988).

[138] J. M. Luttinger, Phys. Rev. **121**, 942 (1961).